Advanced Light Source

ACTIVITY REPORT 1999

This report is dedicated to the memory of
WERNER MEYER-ILSE

∾

1998 ALS Users' Executive Committee Chair
Builder of the XM-1 x-ray microscope
Recipient of the 1994 Klaus Halbach Award for instrumentation
Staff Scientist in the Center for X-Ray Optics

whose unflagging efforts on behalf of the ALS and its user
community brought renewed vitality to the light source
at a crucial time in its development. Werner passed
away on July 14, 1999, after an automobile accident in
his native Germany. He is warmly remembered as
a gentle and thoughtful scientist who took joy in his work
and in every opportunity to share his expertise with
students and colleagues.

ADVANCED LIGHT SOURCE
ACTIVITY REPORT
1999

Contents

INTRODUCTION

Daniel Chemla
ALS Director

My second year as Director of the ALS has confirmed my belief that the ALS is an outstanding scientific enterprise. It is a pleasure to work with such talented users and such a dedicated and hardworking staff. If our Activity Report this year has a unifying theme, it is "activity, activity, activity." We have much to report in the areas of scientific accomplishments, building out the experiment floor, and improving the performance of the machine.

The major recent development is the recognition and applause that is starting to come in from our various advisory committees. Our Science Policy Board (SPB) and Scientific Advisory Committee (SAC) have been constructive and encouraging. An important milestone was the report of the Bader committee. Now that we are a full- fledged division within Berkeley Lab, we are required by our contractor, the University of California, to be reviewed annually. The 1999 review was chaired by Sam Bader of Argonne National Laboratory, and the report speaks of a vibrant scientific program that is "excellent to outstanding."

The culmination of our efforts, however, came with the review of the ALS for the U.S. Department of Energy's Basic Energy Sciences Advisory Committee by a panel chaired by Yves Petroff (Director General of the European Synchrotron Radiation Facility). The wide-ranging conclusions of the resulting report, subsequently accepted by BESAC, constitute ringing praise for the value of science in the VUV and soft x-ray region and for the leading role the ALS is playing in bringing the science to fruition. Specifically, the report notes the outstanding performance of the ALS storage ring, identifies important areas of scientific excellence at the ALS spanning a broad spectrum of disciplines, rates the management and staff as outstanding, and affirms a significant improvement both in the
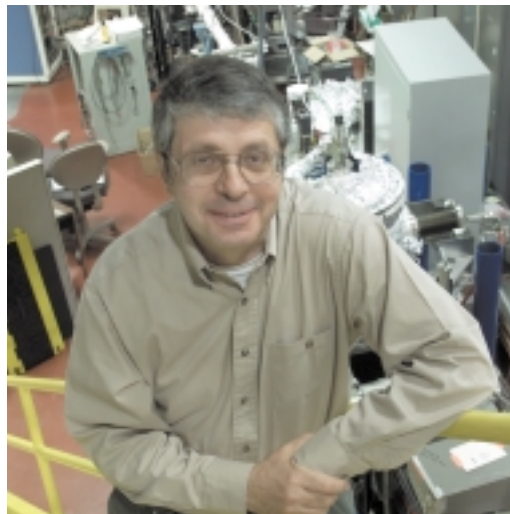
number of ALS users and the way in which the ALS provides support for them.

The panel also endorsed our scientific strategic plan. In addition to the superbend project for a substantial expansion of our structural biology program and other hard x-ray science, the plan highlights initiatives for building out the remaining straight sections, which will be dedicated to science in several key areas. It was recommended that the ALS (1) complete the molecular environmental science beamlines in Sector 11, (2) develop the next-generation photoemission electron microscope for the study of magnetic and polymer nanostructures in Sector 4, (3) develop femtosecond technology and science in Sector 6, and (4) enhance its capabilities in high-resolution spectroscopy of correlated systems with a low-energy elliptically polarizing undulator beamline in Sector 2. As evidenced by this list, the distinction between our core (ultraviolet and soft x-ray) and noncore areas is becoming blurred. The ALS is in fact a "universal machine" with which we can excel in our core region while being world class in the hard x-ray region.

With this emphasis on strategic planning, we now have a pretty clear picture of what the ALS should

look like five to ten years from now. The challenge is how to implement the plan. As a rule of thumb, the capital investment on the experiment floor of a mature synchrotron radiation facility (beamlines, monochromators, experimental chambers, etc.) is roughly equal to the investment in the accelerator itself. In round figures, the investment in the ALS accelerator was $150M, and the investment so far on the floor is about $50M. So we are about one-third built out. My main preoccupation now is finding the resources to go the rest of the way in a reasonable time.

Science Highlights

OVERVIEW

Neville Smith
Division Deputy for Science

Nobel laureate Richard Smalley is quoted in Science Magazine as having been "blown away" by what he saw at the ALS during his participation as a me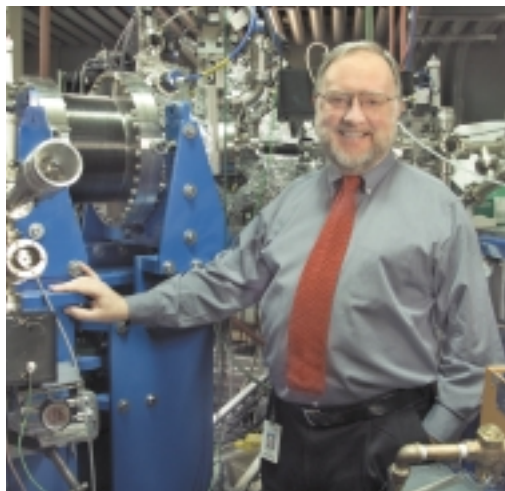mber of the recent BESAC review chaired by Yves Petroff. The panel identified the following areas of scientific excellence:

- structural biology
- femtosecond and picosecond dynamics in condensed matter and in the gas phase
- electronic processes and many-body effects in highly correlated systems, magnetic nanostructures, and correlation in small systems
- surface science, thin films, and microscopy
- ultrahigh-resolution spectroscopy of gas-phase atoms, ions, and molecules
- chemistry and catalysis (wet, heterogeneous, nanoscale chemistry and biochemistry; dynamics of radicals; and catalytic interfaces at atmospheric pressure)
- analytical sciences and metrology

The glowing evaluation by the Petroff panel is very gratifying, particularly to those of us who have always held that the scientific program at the ALS is fundamentally sound. The panel expressed surprise with the assessment of an earlier panel, which had asserted that "important scientific issues which require UV radiation have decreased in number compared to those which require hard x rays." An inspection of high-profile journals shows that, in solid-state physics and chemistry, the total number of papers obtained in the IR, UV, and soft x-ray region is roughly comparable with the number obtained in the hard x-ray region. Let us hope that we can put such comparisons behind us and just get on with delivering excellent science.

This section of our Activity Report presents 25 scientific highlights of work done by our users in 1999. The choice of the number 25 is arbitrary but is dictated primarily by a need to keep this volume down to a reasonable size. Some very meritorious accomplishments have consequently been left out. We hasten to point out that the selection was made prior to the visit of the Petroff panel and yet incorporates highlights in almost all of the areas of excellence that they identified. The moral is that our user community is already aligned in the directions in which the ALS has now been judged to excel.

We trust that you will find these scientific highlights interesting. We welcome your comments.

COMPLEX MATERIALS

Charge Stripes in High-Temperature Superconductors

Superconductivity is the property of carrying electrical current with no resistance. Owing in part to the requirement that they be cooled to a few degrees above absolute zero (0 K), applications of conventional metal and alloy superconductors have been comparatively limited. Electromagnet coils for magnetic resonance imaging machines represent one use of superconductors. Hopes for technological applications were raised dramatically beginning in late 1986 with a series of reports of new families of ceramic oxide superconductors, some exhibiting superconductivity above the temperature of liquid nitrogen (77 K), which would reduce the cooling requirement considerably. With the breakthrough came a brand new scientific puzzle, because the origin of high-temperature superconductivity in these materials remains unknown after more than a decade. In the experiments at the ALS described here, researchers confirm the self-assembling of charge carriers into one-dimensional stripes, a feature that will shed light on the mystery of high-temperature superconductivity.

One of the great unsolved problems of contemporary condensed-matter physics is the origin of superconductivity in the "high-temperature" superconductors (HTSCs). With a puzzling array of properties unlike those of ordinary superconductors, these materials have defied understanding since the discovery of the first HTSC compound in 1986. Now, we have evidence from angle-resolved photoelectron spectroscopy for still another surprising behavior, the self-assembling of charge carriers into spatially localized, one-dimensional stripes. While the stripes were already known from other work, the latest data raises new questions about the electronic structure associated with these entities and its relation to superconductivity.

Angle-resolved photoelectron spectroscopy (ARPES) probes the electronic structure (energy and momentum) of materials by measuring the energy and angle of the emitted electrons. In particular, ARPES can determine in momentum space the Fermi surface, which represents the locus of the momenta of the highest energy occupied electron states (Fermi energy). The Fermi surface is important because electrons near the Fermi surface are responsible for many physical properties, including superconductivity. From high-resolution measurements along the Fermi surface in HTSCs, ARPES has revealed several major departures from the behavior of conventional superconductors.

For our ARPES experiments, we studied a compound known to have stripes, $(La_{1.28}Nd_{0.6}Sr_{0.12})CuO_4$, whose "parent" compound, La_2CuO_4, is an insulator. Copper and some of the oxygen atoms are arranged on a square lattice in parallel copper–oxygen planes separated by block layers that act as charge reservoirs. Replacing some of the lanthanum in the La_2CuO_4 insulator with strontium (strontium doping), which has one less electron for bonding, to form $(La_{2-x}Sr_x)CuO_4$ results in the generation of positively charged holes (missing electrons) that end up in the copper–oxygen planes. Over a strontium concentration range (x) from around 6 to 27 percent, the material becomes superconducting, except at 12 percent where the superconductivity is suppressed.

Stripes, in which holes are confined to parallel lines of copper atoms in the copper–oxygen planes separated by insulating regions without holes, were first observed at this so-called one-eighth doping, suggesting a perhaps antagonistic, but in any case intimate, relationship between superconductivity and stripe formation. The replacement of some lanthanum with neodymium helps to pin down the stripes at low temperature. Stripes were later seen at other dopings and in other superconductors.

The ARPES spectra obtained for $(La_{1.28}Nd_{0.6}Sr_{0.12})CuO_4$ exhibited several unusual features. The Fermi surface implied by the data is highly one dimensional. It has a cross-like shape consisting of two sets of parallel lines that intersect at right angles. This pattern deviates significantly from
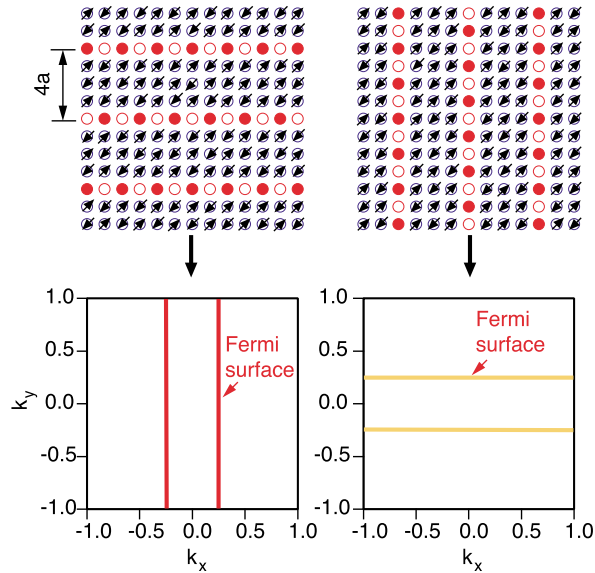
Figure 1

Model showing two orientations of charge stripes in the copper–oxygen planes and their associated Fermi surfaces for momentum (k) in the x and y directions. The stripes are separated by four times the lattice spacing a in the planes. Small arrows represent local magnetic moments in the antiferromagnetic insulator that separates the stripes. Red circles in stripes represent holes.

that calculated for the two-dimensional copper–oxygen planes but is consistent with the superposition of Fermi surfaces from stripes with two perpendicular orientations. The one-dimensionality seems to imply that the electrons are well confined in the stripes and move along them. However, the data also indicate that electrons very close to the Fermi energy show two-dimensional behavior, i.e., electrons can also move perpendicular to the stripes. The unusual behavior of the stripes may represent a new state of matter, and apparently a new theory is called for to understand this behavior.

These results provide new grist for the HTSC mill whose implications may reach farther than even superconductivity. The several families of HTSCs constitute one segment of a still larger class of so-called strongly correlated materials that are characterized by a powerful Coulomb repulsion between neighboring electrons. Many physicists believe that solution of the HTSC problem will require a new paradigm for strongly correlated materials.

Investigators

X.J. Zhou (ALS and Stanford University); P. Bogdanov, S.A. Kellar, and Z.-X. Shen (Stanford University); Z. Hussain (ALS); and T. Noda, H. Eisaki, and S. Uchida (University of Tokyo).
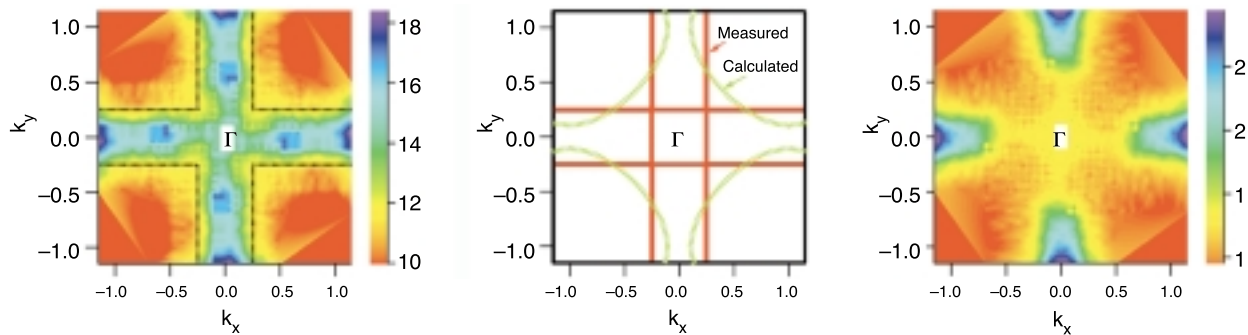
Figure 2

(left) Image of the photoemission intensity in momentum space integrated over a 500-meV energy window. The Fermi surface is the boundary between high (blue) and low (red) intensities. (center) Comparison of measured and calculated Fermi surfaces. The Fermi surface determined experimentally is consistent with a superposition of the Fermi surfaces of one-dimensional stripes (red) but differs significantly from that calculated for the two-dimensional copper–oxygen planes (green), thereby suggesting one-dimensional behavior for the electrons. (right) The photoemission intensity integrated over a 100-meV energy window. As compared to the intensity integrated over a 500-meV window, the reduced intensity at low momenta in this image reveals an anisotropic energy gap. Low-energy excitations across the gap indicate that electrons close to the Fermi energy also show two-dimensional behavior.

Publication

1. X.J. Zhou et al., "One-dimensional electronic structure and suppression of d-wave node state in $(La_{1.28}Nd_{0.6}Sr_{0.12})CuO_4$," *Science* **286**, 268 (1999).

Peierls Instability of Atomic-Scale Metallic Indium Chains on a Silicon Surface

Although the world as we experience it is three dimensional, mathematicians and theoreticians often find that one- or two-dimensional models are easier to solve than three-dimensional ones, yet they still produce important insights and sometimes even yield new physical phenomena. As it happens, with modern fabrication technology, researchers can also construct approximately one- and two-dimensional systems. For example, a line of atoms for many purposes is one dimensional and a layer of atoms is two dimensional, even though the atoms themselves do have a thickness. Studying materials with such reduced dimensionality is now at the forefront of materials physics. At the ALS, researchers have demonstrated one-dimensional behavior by chains of indium atoms on a silicon surface. A structural change as the chains are cooled to cryogenic temperature and characteristic electron behavior are tell-tale signs of one-dimensionality.

One-dimensional metallic systems are important for their exotic physical properties, such as an unusual form of superconductivity, formation of charge-density waves, and non-Fermi-liquid behavior. In addition, one-dimensional systems can be described by exactly soluble theoretical models. In principle, bulk three-dimensional and planar two-dimensional metals with anisotropic electronic band structures can exhibit quasi-one-dimensional properties, but up to now, only a very few bulk materials with anisotropic band structures have been shown to have quasi-one-dimensional properties.

On the other hand, among two-dimensional systems, the 4×1 indium overlayer on the Si(111)
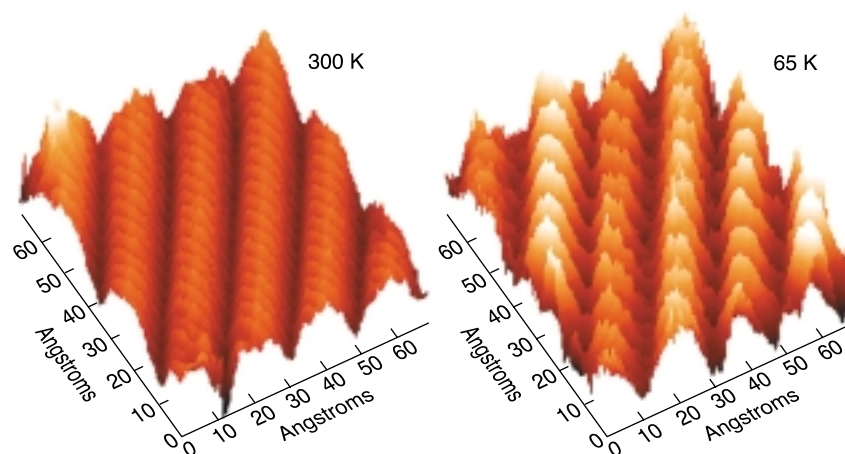
Figure 3

Surface charge-density maps of the indium chain structures on the Si(111) surface at room temperature (300 K) and at 65 K obtained by scanning tunneling microscopy (STM). The room temperature image shows the indium quantum chains of 13.4-Å width, whose fine charge-density modulation along the chains transforms into a doubled-periodicity strong charge modulation (i.e., into the one-dimensional charge-density wave) below about 100 K.

surface forms a well-ordered linear-chain structure, as shown in the scanning tunneling microscopy (STM) images (Figure 3), and has one-dimensional metallic bands. Based on reports that one of these surface metallic bands was almost half filled, we predicted this room-temperature metallic phase would undergo a phase transition on cooling, owing to the well-known Peierls instability of a one-dimensional metallic system. Indeed, we confirmed that this surface undergoes a phase transition at about 100 K into a 4×2 phase with a doubled periodicity along the linear chains as shown in low-temperature STM images (Figure 3) and by electron-diffraction data. An angle-resolved photoemission study of these one-dimensional metallic surface-state bands clearly showed the formation of a sizeable band gap at the Fermi level, thereby indicating that the phase transition is a reversible metal–insulator transition.

In order to verify that this phase transition is due to the Peierls instability, we have measured the Fermi contours and surface band structures in great detail for the room-temperature 4×1 phase. The experiments, conducted on the photoemission endstation of Beamline 7.0.1, fully utilized the ultrabright and high-resolution photon beams provided by an undulator. The Fermi contours obtained from the 4×1 phase (Figure 4) showed three electron pockets centered on the $\overline{X}$ point of the surface Brillouin zone that were due to three quasi-one-dimensional bands (m_1, m_2, and m_3). One of these three bands crosses the Fermi level at the zone center (middle of the $\overline{\Gamma}-\overline{X}$ line) $\overline{X}$ and has a virtually ideal one-dimensional Fermi contour (straight line), which yields a perfect nesting condition for the 4×1 → 4×2 Peierls transition. This finding provides evidence for a completely new type of one-dimensional Peierls system composed of well-ordered metallic chains on a solid surface, thereby opening up new possibilities for low-temperature one-dimensional physics research on solid surfaces. This result also carries important implications for the present technological quest of atomic-scale quantum-electronic devices on semiconductor surfaces.
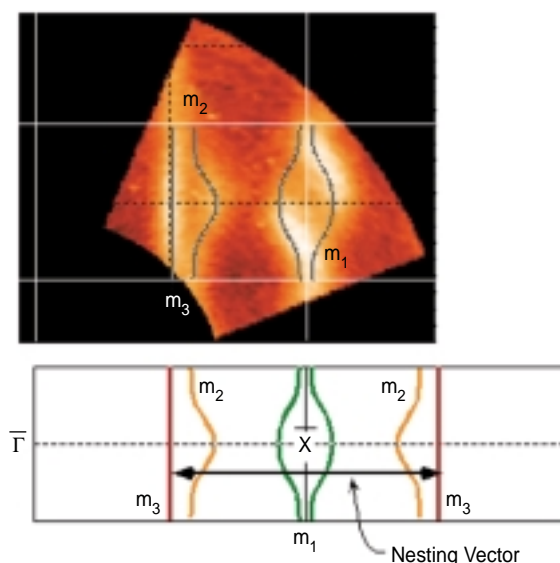
Figure 4

(top) Photoemission intensity map at the Fermi level of the room-temperature indium chain structure (the 4×1 phase) over a portion of momentum space that overlaps part of the surface Brillouin zone whose boundaries are marked by the solid lines (white). The bright features of the map correspond to the Fermi contours of the electronic states localized on the surface quantum chains. (bottom) Schematic depiction of the details of the Fermi contours.

Investigators

H.W. Yeom, I. Matuda, S. Takeda, and S. Hasegawa (University of Tokyo); E. Rotenberg (ALS); and J. Schaefer and S.D. Kevan (University of Oregon).

Funding

Japanese Ministry of Education and U.S. Department of Energy, Office of Basic Energy Sciences.

Publication

1. H. W. Yeom et al., "Instability and charge density wave of metallic quantum chains on a silicon surface," *Phys. Rev. Lett.* **82**, 4898 (1999).

Decay Mechanisms of 4d Core Holes in Dysprosium

Generally speaking, the most loosely bound or valence electrons in a compound dictate its physical and chemical properties, because they are the electrons that participate in chemical bonding and that interact with external stimuli, such as light, applied voltages, and the like. In the transition metals (e.g., iron, nickel, and cobalt) and the even heavier lanthanide elements, however, more tightly bound electrons designated as d and f electrons play an important role, particularly in magnetism, owing to a tendency for the quantum-mechanical spins of electrons in these elements to align themselves (thereby giving rise to an overall magnetic moment) or otherwise assume an ordered arrangement. Blessed with many novel magnetic and, researchers hope, useful properties, so-called "complex materials," particularly oxide compounds, are the focus of much of today's research. Working at the ALS, experimenters have been investigating the role of d and f electrons in the lanthanide compound dysprosium oxide.

The electronic properties of the d and f electrons cause a variety of phenomena, such as Kondo resonances, mixed valency, and magnetism in the lanthanides and in the transition metals. The magnetic polarization of the d and f electrons, for example, gives rise to magnetism. Therefore, the study of the electronic structure of materials containing these elements is essential in order to understand their magnetic properties. Here we report soft x-ray emission spectra (XES) of Dy_2O_3, where the features of spectra excited above and below the 4d–4f resonance provide information about the electronic structure.

Our experiments were performed at Beamline 8.0.1. In Figure 5, emission spectra of Dy_2O_3 are displayed for several excitation energies from below to above the 4d–4f resonance. Arrows in the total electron yield (TEY) absorption spectrum shown in the inset in Figure 5 indicate at which energies the emission spectra are excited. The dipole-forbidden absorption features below the 4d–4f resonance (i.e., below 158 eV) become weakly dipole allowed, owing to the spin-orbit interaction. The ionization thresholds lie at 152.6 eV and above.
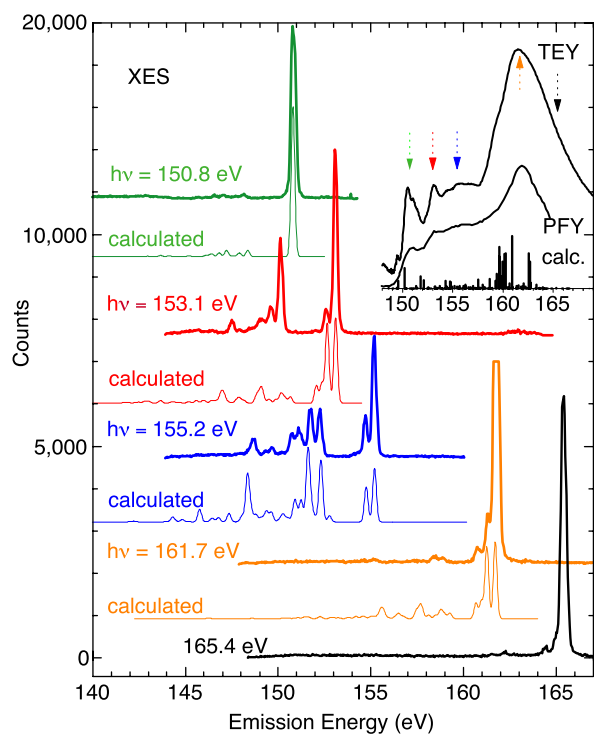
Figure 5

Soft x-ray emission (XES) spectra of Dy_2O_3 for excitations in the region of the dysprosium 4d–4f resonance. The excitation energy (hν) is given above each experimental spectrum. Total electron yield (TEY) and partial fluorescence yield (PFY) absorption spectra are shown in the top right insert. The arrows indicate the excitation energies selected for the XES spectra. For clarity, the spectra have been offset (in all figures), and the top of the elastic peak for the spectrum at 161.7 eV has been cut off.

The emission spectra show strong variations in intensity and structure, depending upon which intermediate states are excited. When exciting below 161.7 eV, the inelastic scattering is highly resonant, and the total number of inelastically scattered photons can exceed the number of elastically scattered photons. We have calculated the spectra excited at different photon energies using the Kramers–Heisenberg description for photon scattering and resonant fluorescence. The calculated emission spectra are shown below each measured spectrum. The energy-loss features are due to excitations within the 4f shell, $4d^{10} 4f^9 \rightarrow 4d^9 4f^{10} \rightarrow 4d^{10} (4f^9)^*$, in which the 4f shell remains in an excited state. Because of the large number of widely separated terms of the 4f shell

filled with nine electrons, these losses extend over a large energy range from about 0.2 to 7 eV below the elastic peak.

In order to compare the emission processes when exciting at and above the 4d–4f resonance, the emission spectra for excitation energies below (154 and 157.2 eV) and above (208.4 eV) the resonance are displayed in Figure 6 over a wide range of emission energies. When exciting through the resonance, the
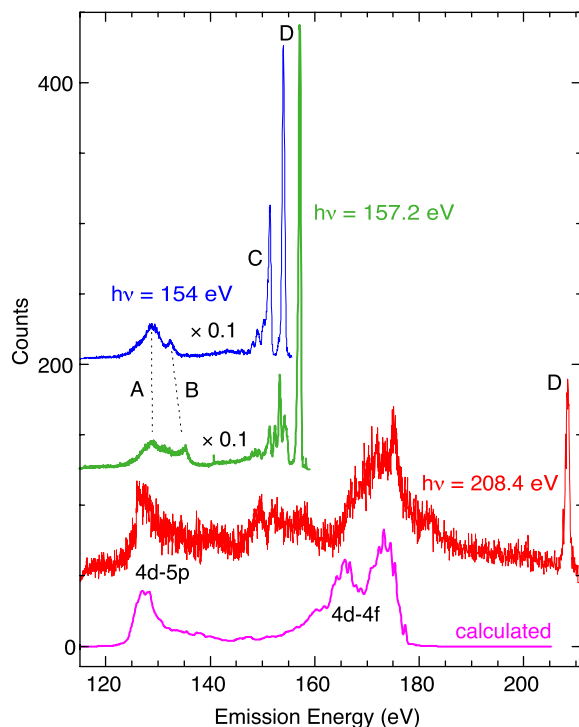
Figure 6

Emission spectra for excitation energies below (154 and 157.2 eV) and above (208.4 eV) the 4d–4f resonance. In order to display all data on the same scale, the spectra excited at energies below the resonance are divided by a factor of 10. Peak A is emission from the decay of the 4d hole via the 5p channel; peak B is the inelastic peak; peaks C are the energy losses due to the 4f inner-shell transitions, and peak D is the elastic peak.

elastic peak (D) and the energy losses due to 4f inner-shell excitations (C) dominate the emission. In addition, emission from the decay of the 4d hole via the 5p channel is observed (peak A). The inelastic peak (B) is due to the transition $4d^{10} 5p^6 4f^9 \rightarrow 4d^9 5p^6 4f^{10} \rightarrow 4d^{10} 5p^5 4f^{10}$, in which a 5p electron is promoted to the 4f shell.

The total number of emitted photons is much smaller for excitation above the resonance (208.4 eV) than when exciting at or below resonance. The reason is that the core hole decays predominantly by radiationless processes. The dominant radiationless decay processes are 5s, 5p, and valence band autoionization for excitation energies below the 4d resonance, and for energies at and above resonance the 4f autoionization becomes dominant. When exciting above resonance, the nonresonant fluorescence from the refill of the 4d hole via 5p and 4f is very weak because the excited states decay mainly by radiationless processes. We estimate the total number of emitted photons for excitation above the resonance to be at least a factor of six smaller than for excitation below.

Investigators

A. Moewes (CAMD at Louisiana State University); M.M. Grush and T.A. Callcott (University of Tennessee); and D.L. Ederer (Tulane University).

Funding

Publication

1. A. Moewes et al., "Decay mechanisms of the 4d core hole through the 4d–4f resonance in dysprosium," *Phys. Rev. B* **60**, 15728 (1999).

MAGNETISM AND MAGNETIC MATERIALS

Observation of Antiferromagnetic Domains in Epitaxial Thin Films

Atoms are like tiny magnets. Antiferromagnetic magnetic materials have the peculiar property that the atomic magnets are aligned along an axis, but they alternately point in either direction along the axis, so that the material as a whole does not appear to be magnetic. Nonetheless, antiferromagnets play a key role in the operation of advanced magnetic data-storage and proposed memory devices composed of several layers of magnetic and nonmagnetic materials, each as thin as a few atoms. With an eye to improving their performance or to devising new devices, scientists want to probe each layer separately, as well the as boundaries between the layers. In the experiments described here, researchers working at the ALS used a type of x-ray microscopy to image for the first time areas with different antiferromagnetic behavior with high spatial resolution and sensitivity to the surface, thereby paving the way for future experiments with these important materials.

In atomically engineered magnetic thin-film structures, the antiferromagnetic layer magnetically pins (or exchange biases) the magnetization of a ferromagnetic layer, thereby providing a magnetic reference. In antiferromagnetic thin films, as in ferromagnets, small magnetic domains of micrometer or even nanometer size form during growth. Imaging the magnetic domain structure at the surface of the antiferromagnetic layer is a necessary step towards an understanding of exchange-coupling effects across the ferromagnet–antiferromagnet interface, an understanding that could help the magnetic-storage industry to further optimize its products. Up to now, however, the compensated magnetic structure and the consequent lack of a macroscopic moment has impeded the investigation of the magnetic properties of antiferromagnetic thin films, explaining the ongoing controversies on the origin of exchange biasing.

It has now been demonstrated for the first time that photoemission electron microscopy (PEEM) can determine the surface magnetic structure of antiferromagnets in experiments on two materials, NiO and $LaFeO_3$. The photoemission electron microscope, PEEM2, located at Beamline 7.3.1.1 offers high spatial resolution (< 50 nm) in conjunction with magnetic contrast to investigate ferro- and antiferromagnetic thin-film structures. Photoelectrons emitted from the sample, which is illuminated by intense monochromatic x rays, are imaged by electron optics onto a phosphor screen. Magnetic contrast arises from the dependence of the absorption coefficient and thereby the intensity of electron emission on the relative orientation of the x-ray polarization and the orientation of the magnetic axis. This effect is called x-ray magnetic dichroism (XMD).

X-ray magnetic linear dichroism (XMLD) contrast, obtained with linearly polarized x rays, has been applied in the investigation of two thin-film systems, NiO and $LaFeO_3$. NiO is of technological importance as an antiferromagnetic material in exchange-biasing applications and can be called a benchmark material. Figure 1 shows a magnetic XMLD image of the NiO(100) surface. In this image, the bright stripes, between 400 nm and 2000 nm wide, crisscrossing the surface are regions of reduced magnetization. A similarly locally reduced ordering temperature, the Néel temperature of the antiferromagnet, is correlated with the decreased magnetic moment in these stripes. These observations can be explained as finite size effects.

$LaFeO_3$ is an insulating antiferromagnet of technological interest because properties like its Néel temperature can be easily adapted to the demands of an application by doping with strontium. Figure 2 shows the boundary of a bicrystal sample consisting of two macroscopically joined $SrTiO_3$ substrate crystals with the antiferromagnetic $LaFeO_3$ layer epitaxially grown on top. The crystal lattices in the two substrate crystals are rotated with respect to each
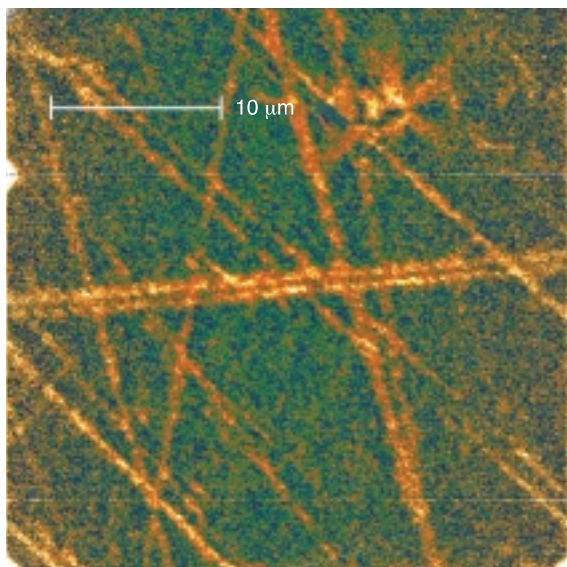
Figure 1

XMLD antiferromagnetic image of an 80-nm-thick NiO(100) film on MgO(100). In this image, bright stripes, between 400 nm and 2000 nm wide, crisscrossing the surface are regions of reduced magnetization.
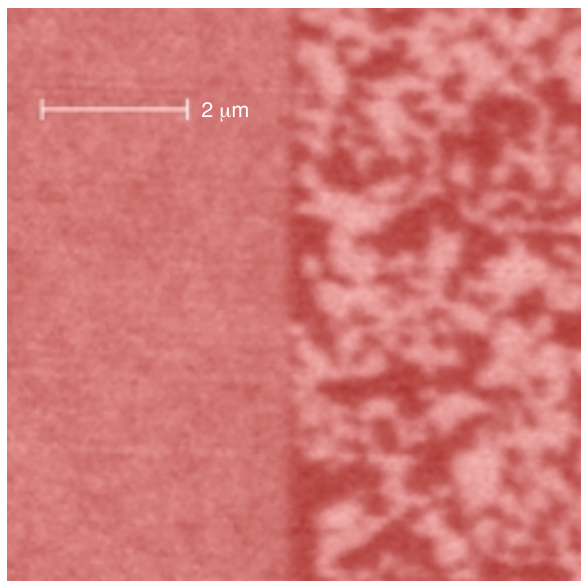
Figure 2

Antiferromagnetic domain structure of LaFeO$_3$ on a SrTiO$_3$(100) bicrystal. The XMLD magnetic-contrast image reveals striking antiferromagnetic domains on the right side of the junction and a uniform gray shade on the left.

other by 45° around the surface normal. The XMLD magnetic-contrast image reveals striking antiferromagnetic domains on the right side of the junction and a uniform gray shade on the left. The strong magnetic contrast on the right arises from magnetic domains with an in-plane projection of the antiferromagnetic axis parallel and perpendicular to the horizontal x-ray polarization vector. On the left, all domains have an equal projection of the antiferromagnetic axis onto the x-ray polarization vector and therefore cannot be distinguished.

This first observation of the antiferromagnetic domain structure in a thin film opens the door to the microscopic investigation of ferromagnet–antiferromagnet interfaces in order to develop a better understanding of exchange-biasing effects. In the future an improved photoemission electron microscope at the ALS (PEEM3) with a design resolution of 2 nm will allow the investigation of even smaller structures in ferro- and antiferromagnets, such as domain walls.

Investigators

A. Scholl, F. Nolting, S. Anders, and H.A. Padmore (Berkeley Lab); J. Stöhr, J. Lüning, and E.E Fullerton (IBM Almaden Research Center); J.W. Seo (University of Neuchâtel); J. Fompeyrine, H. Siegwart, and J.-P. Locquet (IBM Zürich Research Laboratory); and M.R. Scheinfein (Arizona State University)

Funding

Publications

1. S. Anders et al., "Photoemission electron microscope for the study of magnetic materials," *Rev. Sci. Instrum.* **70**, 3973 (1999).
2. J. Stöhr et al., "Images of the antiferromagnetic structure of a NiO(100) surface by means of x-ray magnetic linear dichroism spectromicroscopy," *Phys. Rev. Lett.* **83**, 1862 (1999).
3. A. Scholl et al., "Observation of antiferromagnetic domains in epitaxial thin films," *Science* **287**, 1014 (2000).

Surface Magnetism: A Spin-Density Wave as Quantum Mechanical Ground State with an Energy Gap

In the layered metallic systems known as magnetic nanostructures that are under development for data-storage devices and computer memory cells, two magnetic layers are separated by either a nonmagnetic or an antiferromagnetic spacer layer that mediates the magnetic coupling between the layers. The coupling is highly sensitive to the properties of the electrons, such as energy and the quantum-mechanical spin responsible for magnetism. A candidate antiferromagnetic material for the mediating spacer layer, chromium, when cooled to low temperature, exhibits a "phase change" in which there is a long-wavelength periodic alignment of the local magnetization due to the electrons, known as a spin-density wave. By studying the energy and direction of electrons emitted when x rays are absorbed (angle-resolved photoemission), researchers working at the ALS have observed a lowering of the energy of the electrons that stabilizes the spin density wave and, for the first time, have determined how this energy gain changes with temperature, a matter of fundamental scientific interest.

Either nonmagnetic or antiferromagnetic spacer layers can mediate magnetic coupling in the new miniature giant-magnetoresistance (GMR) spin devices. Chromium, which is one of the possible materials for spacer layers, changes from the paramagnetic to the antiferromagnetic state near room temperature (311 K). We have chosen to study this system at various temperatures because the paramagnetic-to-antiferromagnetic phase transition will affect the electronic properties drastically and hence any magnetic coupling as well.

In fact, chromium, when in the antiferromagnetic state, exhibits the fundamental phenomenon of a spin-density wave (SDW). As schematically depicted in Figure 3, in the SDW, the magnetic moment at a lattice point oscillates in magnitude and direction with a wavelength Λ. The formation of an SDW leads to an energy gap that lowers the total energy of the system, reminiscent of conventional superconductors. What is the actual magnitude and extent in momentum (reciprocal) space of the energy gap of the SDW that has such a pronounced impact? What happens in the vicinity of a surface, and what is the behavior with temperature? In this project, we used Beamline 7.0.1 to conduct
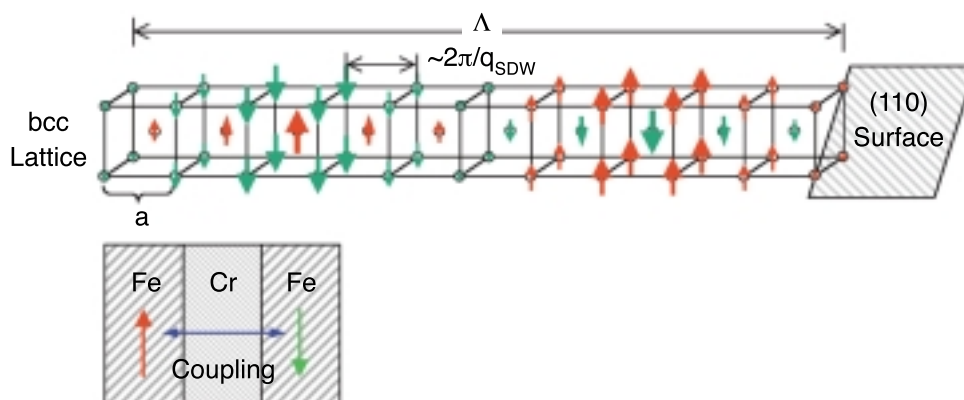

Figure 3

Schematic of the alternating spins in a spin-density-wave state of an antiferromagnet, such as chromium, in which the magnetic moment at a lattice point oscillates in magnitude and direction with a wavelength Λ. A layer of chromium can be interlayered between two iron films to form a magnetic sensor.

angle-resolved photoelectron spectroscopy (ARPES) measurements with high momentum and energy resolution on clean Cr(110) thin films to supply the answers. In particular, we have directly observed temperature-dependent changes in the energy gap for the first time.

Experimental band maps were made at temperatures far below (300 K) and above (570 K) the measured surface Néel temperature (440 K, see below). After subtraction of a smooth background, the raw data were divided by the Fermi distribution to allow observation of thermally excited states above the Fermi level (Figure 4). We observe at low temperature a diffuse intensity above the Fermi energy (E_F), which we identify with the band above the SDW gap. This identification is completely confirmed from measurements throughout reciprocal space. The band structure is thus exhibiting an almost direct gap, which we determine to be about 200 meV, at E_F. The observed magnitude of the energy gap is larger than the bulk value of 120 meV reported from infrared measurements.

Constant energy contours obtained from ARPES in the vicinity of E_F in the antiferromagnetic and paramagnetic states are presented in Figure 5. The data represent maps in reciprocal space of states at energies corresponding to (a) the lower edge, (b) the middle, and (c) the upper edge of the gap in the SDW phase, as well as (d) the middle of the gap region in the paramagnetic phase. These data show graphically that the energy gap opens almost isotropically and with a constant magnitude of 200 meV around this section of the electron bands at the center of the reciprocal-space unit cell.

We also monitored the temperature dependence of the energy gap. A surface transition temperature of about 440 K was determined, considerably above the bulk Néel temperature of 311 K. On the basis of an increase of the magnetic moments obtained in density functional calculations, SDW mean-field theory lets us qualitatively expect a larger energy gap and a higher transition temperature towards the surface, as is observed.
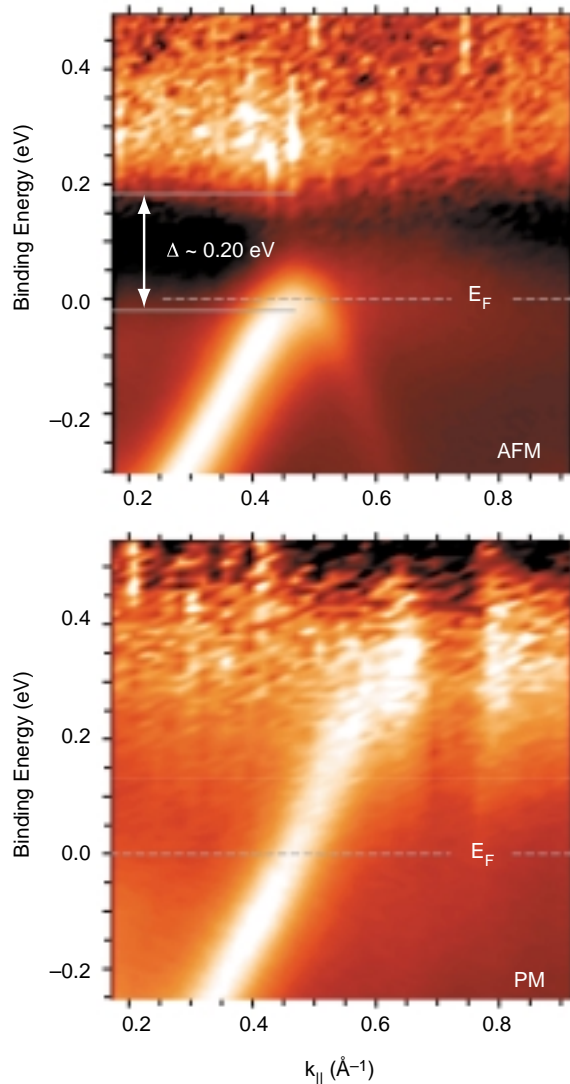
Figure 4

Band maps of chromium taken in the antiferromagnetic state (AFM) at 300 K (top) and the paramagnetic state (PM) at 570 K (bottom), with the Fermi distribution divided out. In the antiferromagnetic state, the energy gap is clearly seen, whereas there is no gap in the paramagnetic state.

Investigators

J. Schäfer and S.D. Kevan (University of Oregon); E. Rotenberg and G. Meigs (ALS); P. Blaha (Technische Universität Wien, Austria); and S. Hüfner (Universität des Saarlandes, Germany).

a) Lower branch
$E_B = E_F - 20$ meV

c) Upper branch
$E_B = E_F + 180$ meV

b) Energy gap
$E_B = E_F + 80$ meV

d) Closed gap
$E_B = E_F + 80$ meV

$\overline{S}$

$\overline{\Gamma}$

300 K

570 K

k_x (Å^{-1})
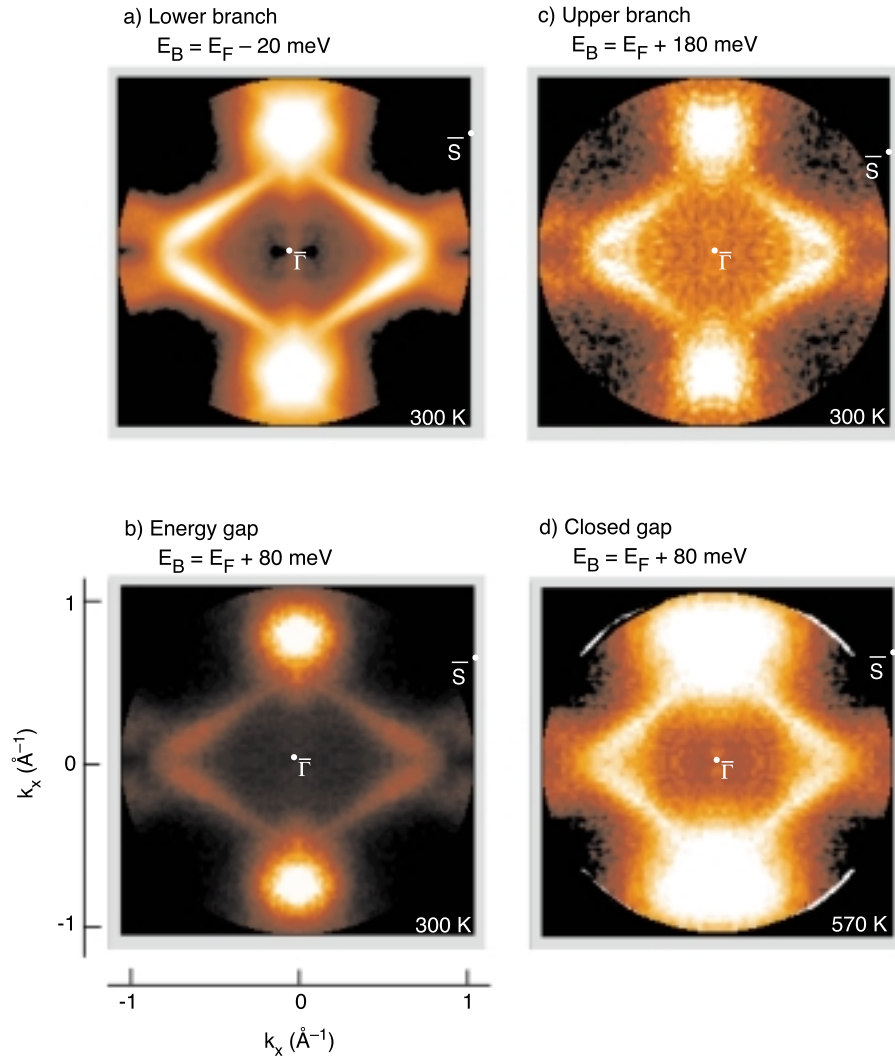
Figure 5

Constant-binding-energy ARPES contours. Images (a) and (c) of the SDW-nested AFM state show the edges of the bands that define the virtually isotropic SDW gap of about 200 meV seen in (b). There is no gap in the PM state (d).

Funding

Publications

1. J. Schäfer et al., "Energy gap of the spin density wave at the Cr(110) surface," *Surface Science*, in press.

2. J. Schäfer et al., "Direct spectroscopic observation of the energy gap formation in the spin density wave phase transition at the Cr(110) surface," *Phys. Rev. Lett.* **83**, 2069 (1999).

Quantum Well States Visualized in Copper Thin Films

"Wave-function engineering" refers to tailoring electron behavior by fabricating materials with controlled quantum-mechanical electron wave functions. For example, magnetic nanostructures comprising several layers of magnetic and nonmagnetic materials, each a few nanometers thick, are already in commercial production as high-sensitivity read heads in the newest data-storage disks. High-speed, low-power, nonvolatile magnetic random-access memories that retain their information when the power is turned off are under development that would dramatically change the architecture of computer design. A group working at the ALS has combined precision sample-fabrication technology and the spatial resolution achievable with the high brightness of the ALS to make "images" of the spatial variation of electron wave functions in thin copper films. The images qualitatively verify a proposed model and lend hope that wave-function engineering can become a practical tool for designing devices based on magnetic nanostructures.

By combining precision sample-fabrication technology and the spatial resolution achievable with the high brightness of the ALS, we have been able to make photoemission images of the spatial variation of electron wave functions (quantum well states) in thin copper films. The images qualitatively verify a proposed model in which a longer wavelength "envelope" function modulates a shorter wavelength component of the wave function. Quantum well states are believed to underlie the magnetic behavior of the layered metallic nanostructures now under intense development for advanced data-storage and memory applications, so understanding them is a major thrust of magnetic-materials research.

In a metal, an electron wave function can be represented by a short-wavelength component that is modulated by an envelope with a longer wavelength. In a large sample, the allowed electron energies fall into a series of bands within which the energy is quasi-continuous, but as the dimensions shrink, the allowed energies become widely separated and few in number. For a film, which is thin in only one

direction, the energy is quantized in this way for travel perpendicular to the film surface and is continuous for travel parallel to the surface. In the model for quantum well states, the envelope functions must fit an integer number of half wavelengths into roughly the film thickness.

Our group visualized the envelope function by means of photoemission measurements of a copper film, using a finely focused x-ray beam from the ALS to excite photoelectrons. The intensity in the photoemission spectrum oscillated, with maxima occurring when the photoelectron energies matched those of quantum well states. The researchers used a layer of nickel only one atom thick embedded in the quantum well to probe the wave function. Embedding the nickel between two wedge-shaped copper layers oriented at right angles made it possible either to continuously vary the position of the nickel layer in a film of fixed total thickness or to keep the nickel layer fixed in the middle of a quantum well of continually varying thickness, depending on the direction of travel across the sample surface (Figure 6).

Measuring the photoemission intensity at a fixed electron energy, corresponding to photoelectrons emitted from quantum well states at the Fermi level of copper, while scanning the x-ray beam across the sample, resulted in a pattern of light and dark oscillations (Figure 7). The nickel layer acted to suppress the quantum well states when it was near a node of
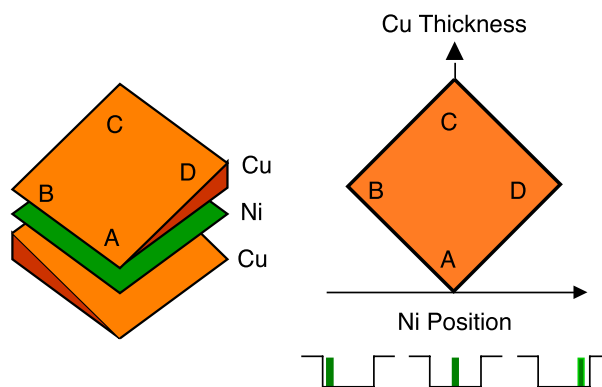
Figure 6

Double-wedge sample varies nickel-layer position in the horizontal direction and total copper thickness in the vertical.

the envelope function, thereby reducing the intensity of the photoemission. Therefore, scanning in the direction of fixed thickness and variable nickel position produced an image of the envelope with dark

areas representing nodes and bright areas representing antinodes. Scanning in the direction corresponding to an increasing well thickness and fixed nickel position gave bright bands as additional quantum well states became allowed in the thicker film.

Tailoring electron wave functions ("wave-function engineering") in magnetic nanostructures with layer thicknesses measured in nanometers may make it possible to control the spin-dependent behavior of electrons. We intend to test our qualitative analysis with quantitative theoretical calculations, and we hope to reach a level of understanding that will turn wave-function engineering in magnetic nanostructures into a practical tool.

Investigators

R.K. Kawakami, H. J. Choi, E.J. Escorcia-Aparicio, M. O. Bowen, J.-H. Wolfe, E. Arenholz, Z.D. Zhang, and Z.Q. Qiu (University of California, Berkeley); and E. Rotenberg and N.V. Smith (ALS).

Funding

Publication

1. R.K. Kawakami et al, "Quantum well states in copper thin films," *Nature* **398**, 132 (1999).

Figure 7

Image of the photoemission intensity at the Fermi level shows both horizontal and vertical oscillations. The horizontal oscillation in the photoemission intensity maps the spatial variation of the quantum-well envelope, whereas the vertical intensity variation shows the presence of additional envelope modes (denoted by the index v) as the quantum-well thickness increases.

POLYMERS, BIOMATERIALS, AND SOFT MATTER

Probing a Buried Buffer Layer between a Metal and a Polymer with Soft X-Ray Fluorescence

The adhesion between a metal and a polymer depends on the electronic and chemical properties of the interface and plays a key role in numerous applications of mechanical and electronic devices. Understanding the electronic and chemical structures at a buried interface is therefore crucial for eluci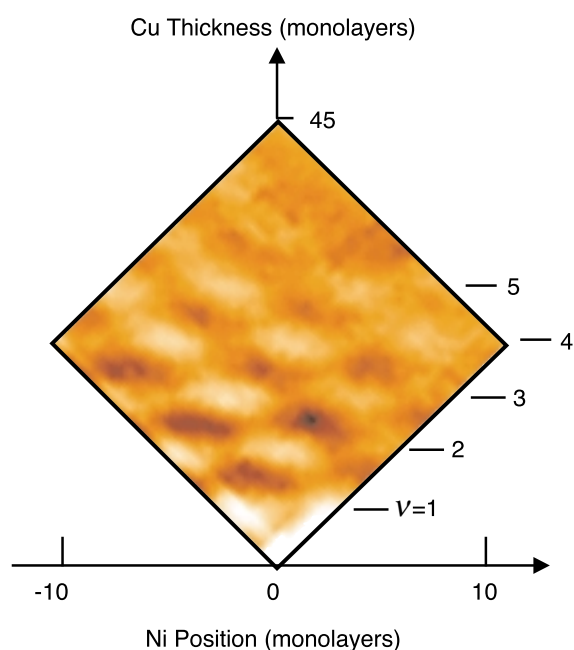dating the mechanism of interfacial adhesion of metal/polymer systems. Because x rays can emerge from deep below the surface, x-ray emission spectroscopy (XES), also known as soft x-ray fluorescence (SXF), provides an element-specific probe for examining changes in the local environment and chemical bonding of interface atoms caused by various chemical and physical treatments. With XES, a group working at the ALS has demonstrated the formation of a chemical compound at the interface between copper and polyimide (a polymer) that enhances the adhesion between these materials.

Metal/polymer structures have attracted considerable attention as good candidates for multilevel interconnections in very large scale integrated (VLSI) circuits and other highly miniaturized electronic devices, but a large adhesion strength at the interface is required. In a previous study, enhancement of the adhesion strength was obtained by ion irradiating a copper/aluminum/polyimide trilayer in which the aluminum served as a buffer; however, the mechanism of the enhancement remained controversial. By using x-ray emission spectroscopy (XES), we have successfully characterized the metal–polymer interface and demonstrated the key role played by the formation of a $CuAl_2O_4$ compound.

Photoelectron spectroscopy is a common technique for studying electronic structure and chemical properties, but it is surface sensitive, owing to the shallow escape depth of photoelectrons. To study

interfaces, therefore, sputtering of the overlayer is required, resulting in an unavoidable alteration of the original interfacial structure. As a photon-in–photon-out technique, XES provides a nondestructive, element-specific probe of the valence states at buried interfaces. Our experiments were carried out at Beamline 8.0.1 with the soft x-ray fluorescence (SXF) endstation, which is equipped with a five-meter-radius spectrometer of the Rowland-circle type. The spectrometer resolution was about 0.5 eV for the measurements. Ion-irradiated copper/aluminum/polyimide films, which have a larger adhesion strength than copper/polyimide without the aluminum buffer layer, were used for this study. The copper thickness was 40 nm and the aluminum thickness was 5 nm. Ion irradiation was performed at room temperature with N_2^+ at an incident energy of 80 keV.

Copper $L_{2,3}$ XES spectra of the ion-irradiated copper/aluminum/polyimide sample and of reference materials copper, CuO, and $CuAl_2O_4$ are shown in Figure 1. Comparison of the spectrum of the ion-irradiated sample with a superposition of copper and $CuAl_2O_4$ spectra demonstrate that 60 atomic percent of the copper atoms participate in the formation of a $CuAl_2O_4$ interlayer (upper panel), whereas the superposition of copper and CuO cannot reproduce the spectrum of the ion-irradiated sample (lower panel). The identity of the interlayer compound, known to be correlated with an enhanced adhesion strength between copper and polyimide, was confirmed for the first time. In addition, carbon K_α XES spectra of ion-irradiated polyimide (Figure 2) show that the structural transition in the polyimide from carbocyclic aromatic rings (benzene) to amorphous carbon occurs with increased ion dose. The decrease in adhesion strength at high ion dose, observed in a previous study, can be explained by creation of chemically inert amorphous carbon.

Soft x-ray emission valence spectra have shown that the formation of the interlayer compound
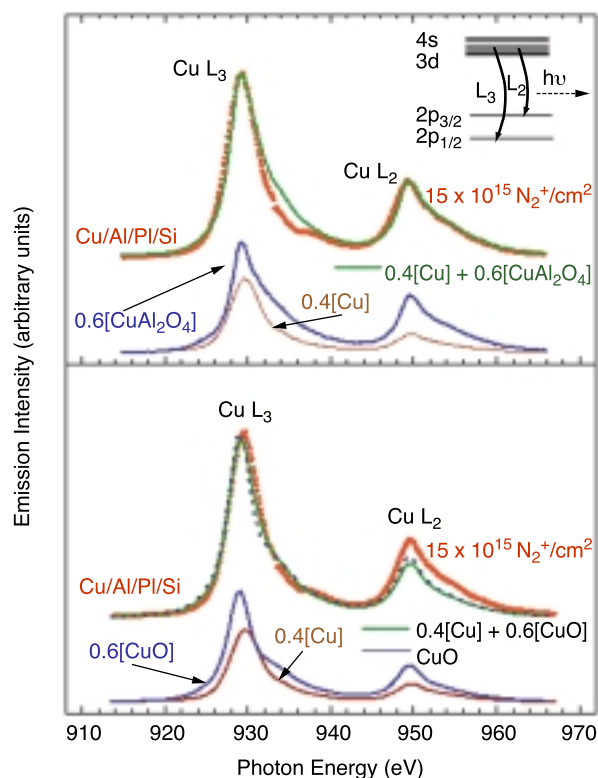
Figure 1

Copper $L_{2,3}$ XES spectra of ion-irradiated copper/aluminum/polyimide (PI) and reference samples copper, $CuAl_2O_4$, and CuO, where the intensity of the copper is reduced by 0.4 and those of the $CuAl_2O_4$ and CuO are reduced by 0.6. The spectrum of the ion-irradiated sample is compared with a superposition of the reduced spectra of copper and $CuAl_2O_4$ (upper panel) and of copper and CuO (lower panel).

Figure 2

Carbon K_α XES spectra of polyimide films on silicon irradiated by N_2^+ ions and of benzene and amorphous carbon reference samples.

$CuAl_2O_4$, which plays a crucial role in interfacial adhesion between copper and polyimide, results from ion irradiation, and the decrease in adhesion strength at excessive ion dose is caused by the formation of amorphous carbon. In spectroscopic studies to characterize buried interfaces or embedded nanoparticles, XES and SFX offer unique, nondestructive experimental tools that do not alter the electronic structure during the measurements.

Investigators

G.S. Chang and C.N. Whang (Yonsei University, Korea); E.Z. Kurmaev and D.A. Zatsepin (Russian Academy of Science–Ural Division, Russia); R.P. Winarski and D.L. Ederer (Tulane University); A. Moewes (Louisiana State University); and Y.P. Lee (Hanyang University, Korea)

Funding

Publications

1. G.S. Chang et al. "Mechanism for interfacial adhesion strength of an ion beam mixed Cu/polyimide with a thin buffer layer," *Appl. Phys. Lett.* **74**, 522 (1999).
2. E.Z. Kurmaev et al. "Soft x-ray fluorescence measurements of irradiated polyimide and polycarbonsilane films," *J. Electr. Spectr. Relat. Phenom.* **101**, 565 (1999).

NANOSTRUCTURES AND SEMICONDUCTORS

Ultrafast Lattice Dynamics Probed by Time-Resolved X-Ray Diffraction

We all know that one cannot record the flapping wings of a hummingbird in flight with a camera with a slow shutter speed. The same principle holds for scientific experiments. To record the progress of dynamic processes, whether physical, chemical, or biological, requires that the detector be faster than the process; otherwise, the "picture" is fuzzy. Many of the processes of interest to those at the frontiers of research take place on the time scale of molecular vibrations, typically around 100 femtoseconds. A group working at the ALS has directly observed atomic vibrations, as well as ultrafast structural changes, in a solid with a high-speed detector known as a streak camera. During recording, the camera places data gathered at each instant along a line (hence the streak camera name), thereby converting temporal information to spatial and effectively recording the time evolution of the process all at once.

X rays have long been used as structural probes of complex molecules and solids on the atomic scale, but only recently have these techniques been extended into the time domain. In this experiment, we watched—in real time—the motion of atoms in the semiconductor indium antimonide on picosecond time scales. Following a "kick" from a short laser pulse, we directly observed large-amplitude coherent atomic vibrations, in which the atoms collectively oscillate about their equilibrium positions. At higher laser powers, the structural phase transition from an ordered to a disordered state was followed in real time.

The experiment was performed at Beamline 7.3.3. A femtosecond laser pulse synchronized to the individual electron bunches in the storage ring with a jitter of less than 5 picoseconds was made to overlap—in both space and time—a single x-ray pulse on the crystal. A monochromator selected

x rays of wavelength 2.4 Å to be diffracted from the crystal onto the detector, a streak camera with picosecond resolution. We then followed the structural dynamics of the crystal by monitoring the intensity of the diffracted x rays as a function of time with the camera. Since the length of the x-ray pulse was hundreds of times longer than the laser pulse, it served as a "continuous" source of x rays for diffraction before, during, and after the laser excitation of the sample (Figure 1).

Following impulsive excitation of the crystal, we discovered distinct temporal oscillations in the diffracted intensity, indicative of coherent lattice motion (Figure 2). By slightly changing the angle of the crystal with respect to the incident x rays, different vibrational modes, or phonons, could be selected, thus mapping out part of the acoustic phonon dispersion relation. This new technique thus allows one to probe the vibrational properties of solids, even under extreme, highly nonequilibrium conditions, by directly watching the atoms collectively ring. Because we were able to resolve in real time the transfer of energy
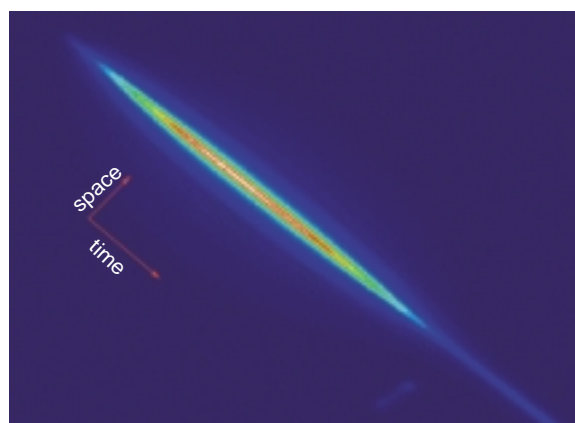

Figure 1

Streak camera image of a single 60-picosecond x-ray pulse. Time runs from the upper left to the lower right.
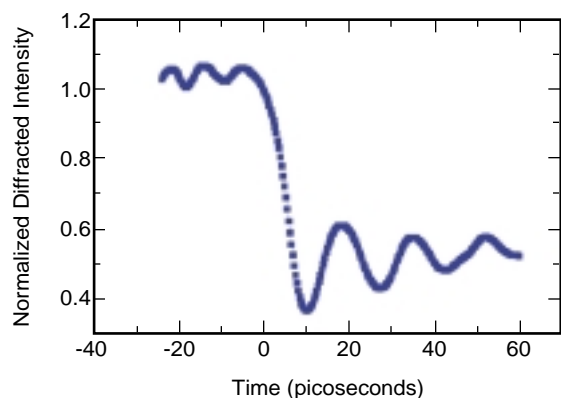
Figure 2

Time-resolved x-ray diffraction efficiency following laser excitation shows an initial decrease, representing a shift of the Bragg diffraction peak with lattice expansion, followed by an oscillatory signal indicative of coherent, large-amplitude lattice vibrations that induce an extra, time-dependent periodicity to the lattice.

from the carrier system to the lattice, important physical parameters such as the electron–phonon coupling time could be extracted. A significant contribution to the excitation of this coherent phonon state was found to be due to a direct coupling between the carriers and the acoustic phonons through the deformation potential interaction.

Furthermore, we found a close relationship between the excitation of this coherent phonon state and the disordering transition that occurred above a critical laser fluence. In particular, the diffracted x-ray signal disappeared on a time scale determined by a vibrational period, implying that each mode took one final collective swing in one direction before disordering. Further time-resolved observations of phase transitions in other materials (for example, strongly correlated systems) should lead to greater understanding of the driving mechanisms behind them.

Investigators

A.M. Lindenberg, I. Kang, and S.L. Johnson (University of California, Berkeley); T. Missalla (ALS and Lawrence Livermore National Laboratory); P.A. Heimann and H.A. Padmore (ALS); Z. Chang and P.H. Bucksbaum (University of Michigan); J. Larsson (Lund Institute of

Technology, Sweden); H.C. Kapteyn (University of Colorado); R.W. Lee (Lawrence Livermore National Laboratory); J.S. Wark (University of Oxford); and R.W. Falcone (University of California, Berkeley, and Berkeley Lab).

Funding

Publication

1. A.M. Lindenberg et al., "Time-resolved x-ray diffraction from coherent phonons during a laser-induced phase transition," *Phys. Rev. Lett.* **84**, 111 (2000).

Femtosecond Structural Dynamics Observed in Semiconductor Crystals

Physical, chemical, and biological processes are by nature dynamic; that is, they evolve with time. A common method used by scientists to study such processes is to illuminate the sample with pulses of light, both to stimulate the process and to probe it. To avoid smearing together data from a range of times, however, this approach requires that the light have a pulse length shorter than the time it takes for significant changes to occur. X-ray experiments to study structural changes that occur on a time scale of one molecular vibration are an emerging area of research. Lasers with pulses of 100 femtoseconds or less have been available for infrared and visible light but so far not for x rays. A group working at the ALS has now measured structural changes occurring over a few picoseconds or less by means of time-resolved x-ray diffraction with a novel femtosecond x-ray source.

We have measured ultrafast structural changes in indium antimonide crystals by means of time-resolved x-ray diffraction with a novel femtosecond x-ray source at the ALS. The experiments quantitatively resolved lattice expansion occurring over tens

of picoseconds after excitation with a high-power infrared laser. We have also demonstrated the sub-picosecond creation of a disordered region near the surface.

Femtosecond x-ray experiments are an emerging area of research in chemistry, solid-state physics, and biology. Dynamic processes in condensed matter occur on a time scale dictated by the period of a lattice vibration, typically about 100 femtoseconds. However, the time resolution of established techniques for determining atomic structure, such as x-ray diffraction and x-ray absorption fine structure, is limited by the pulse length of the x-ray source. For example, the ALS emits pulses 30 picoseconds in length, which is 300 times too long to resolve events lasting 100 femtoseconds. A number of ways to circumvent this limitation are under investigation at the ALS.

In one of these, the Beam Test Facility (BTF) makes use of the electron beam in the ALS linear accelerator rather than in the storage ring. In brief, firing a high-power infrared laser across the tightly focused linac beam at 90° generates femtosecond x-ray pulses by the process of Thomson scattering (Figure 3). The x-ray photon energy depends on the electron-beam energy. In the present experiments with a 100-femtosecond titanium-sapphire laser, 50-MeV electrons in the linac resulted in 300-femtosecond pulses of x rays with a photon energy of 30 keV, and 25-MeV electrons resulted in

500-femtosecond x rays at 7.3 keV. We used the BTF source to measure x-ray diffraction from an indium antimonide crystal every few picoseconds both before and after laser irradiation at intensities below the threshold for damage.

The data at 30 keV demonstrate that expansion of the lattice, which shifts the diffraction peak to lower photon energies, begins only after a delay of about 10 picoseconds after laser irradiation (Figure 4). This is the first direct evidence of such a delay, which we quantitatively modeled as a combination of energy-relaxation processes by which energy is transferred from the electrons excited by absorption of laser light to lattice vibrations and subsequent propagation of the resulting lattice expansion inward from the surface. A decrease in diffraction intensity from the surface was observed with 7.3-keV photons, which do not penetrate the sample as deeply as 30-keV photons. The decrease is due to the high concentration of photoexcited electrons near the surface, which causes a nonthermal disordering of the lattice in less than a picosecond, a time too short to invoke transfer of energy to lattice vibrations and subsequent bond breaking.

In collaboration with researchers from the Berkeley Lab Center for Beam Physics and the ALS, we are building a new bend-magnet beamline (Beamline 5.3.1) that will provide 100-femtosecond x-ray pulses via another laser-based technique,
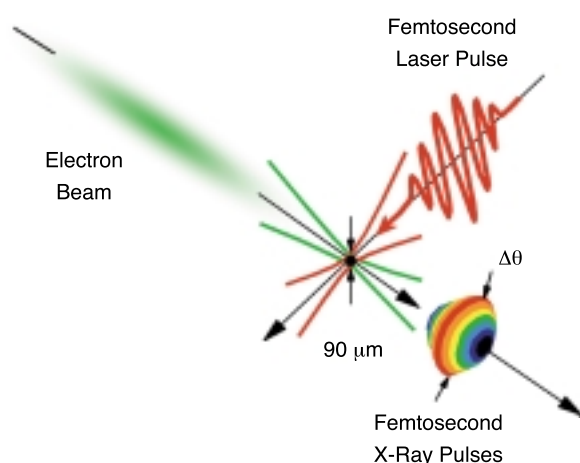

Figure 3

Firing a laser at 90° across a focused electron beam generates femtosecond pulses of x rays by Thomson scattering.
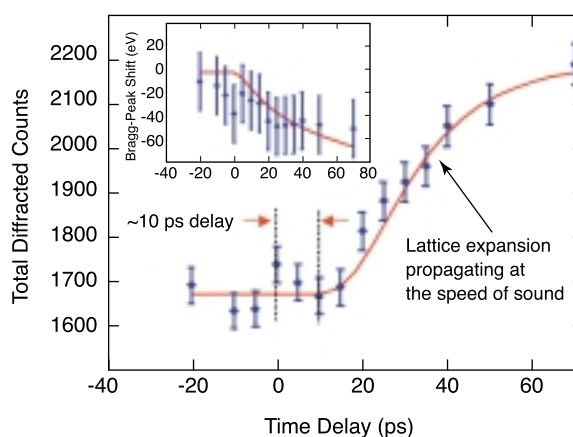

Figure 4

Shifts in peak position (inset) and intensity of diffracted x rays show that laser heating of InSb results in rapid lattice expansion after a 10-ps delay.

recently demonstrated at the ALS, called time slicing. In addition to the improved time resolution, this beamline will be about 10,000 times brighter than the BTF source and will cover the entire spectral range of the bend magnet, thereby opening up a wide range of scientific applications for time-resolved x-ray measurements.

Investigators

R.W. Schoenlein, T.E. Glover, and W.P. Leemans (Berkeley Lab); A.H Chin and C.V. Shank (University of California, Berkeley, and Berkeley Lab); and P. Balling (University of Aarhus, Denmark).

Funding

Publication

1. A.H. Chin et al., "Ultrafast structural dynamics in InSb probed by time-resolved x-ray diffraction," *Phys. Rev. Lett.* **83**, 336 (1999).

Structural Disorder in Colloidal InAs and CdSe Nanocrystals Observed by X-ray Absorption Near-Edge Spectroscopy

The properties of a solid material depend on the arrangement of the atoms inside and on the surface. As the size of the solid decreases toward a few nanometers, the number of surface atoms increases dramatically with respect to the total number of atoms in the resulting nanocrystal. As a consequence, the influence of the surface on the structure and hence the properties of the nanocrystal increases significantly. In the last few years, it has been possible to make nanocrystals with well-controlled sizes, but it has not been so easy to investigate their surface structure. Researchers at the ALS have successfully applied an x-ray technique called x-ray absorption near-edge spectroscopy (XANES) to this problem in semiconductor nanocrystals. They concluded that XANES is a suitable tool for monitoring structural rearrangements of surface atoms in nanocrystals.

The fundamental properties of nanocrystals are significantly different from those of the macrocrystalline bulk material. In particular, the size dependence of the electronic structure of semiconductor nanocrystals has attracted widespread interest during the last decade, resulting in a thorough investigation of their optical, electronic, and structural properties. Because the surface area in a nanocrystalline sample is dramatically increased as compared to that of the bulk material and because the surface influences various properties of nanocrystals, the determination of the surface structure is required for a detailed understanding of the properties of nanocrystals. However, it has been difficult to characterize the surface structure of these particles, in part because there was no suitable experimental technique sensitive to aperiodic parts of the nanocrystal structure, such as the surface. One technique that has the potential to provide information about the surface structure of nanocrystals is x-ray absorption near-edge spectroscopy (XANES), since it does not rely on long-range order, in contrast to techniques like x-ray diffraction. In addition, the increased contribution of multiple-scattering effects makes XANES sensitive to the relative arrangement of multiple atoms, so that this technique is particularly useful for studying complex surface reconstructions in nanocrystals.

In our study, we measured the x-ray absorption near-edge structure at the indium and cadmium $M_{4,5}$ edges of surfactant-capped InAs and CdSe nanocrystals at ALS Beamline 6.3.2. As shown in Figure 5 (dotted lines), the XANES spectra of InAs nanocrystals show a strong size-dependent broadening relative to the respective bulk material (bottom in Figure 5). Exactly the same trend was also observed for CdSe nanocrystals. X-ray photoelectron spectroscopy measurements of these samples (not shown) indicate that the size-dependent effects observed in XANES must be a result of changes in the final state of the excitation. In order to investigate the link between the size dependence of the XANES spectra and surface reconstructions in the nanocrystals, we simulated the indium $M_{4,5}$ spectra of InAs nanocrystals with the program FEFF7. Whereas simulations with a bulk-like crystal structure of InAs nanocrystals could not reproduce the observed XANES spectra, introducing a surface reconstruction in models of
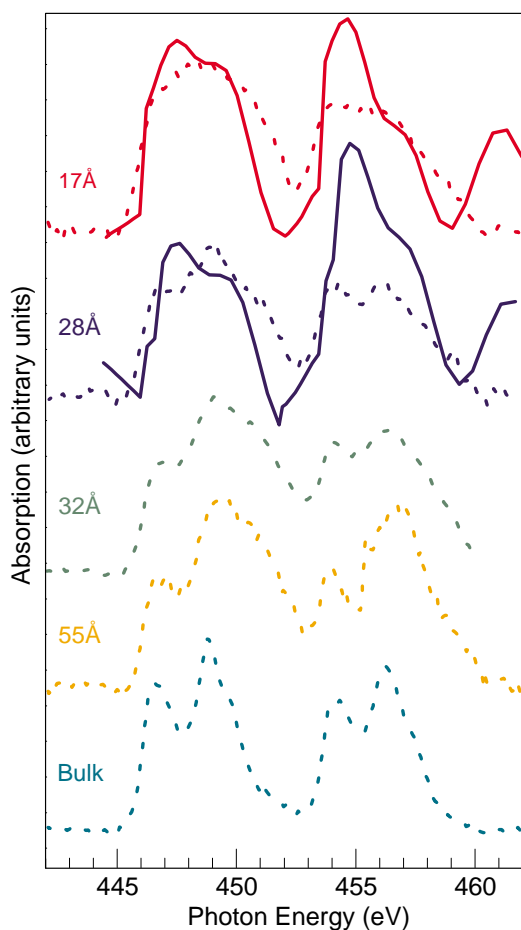
Figure 5

X-ray near-edge absorption spectra (XANES) at the indium $M_{4,5}$ edge for InAs nanocrystals of varying particle size (dashed lines) and for a bulk crystal (bottom dashed line). For the 17-Å and 28-Å InAs nanocrystals, the results of FEFF7 simulations (solid lines) that include a surface displacement of the two outermost atom layers by −0.85 Å (indium atoms) and +0.39 Å (arsenic atoms) relative to the bulk surface are plotted for comparison. Simulations lacking this surface reconstruction yield results very similar to the experimental bulk spectrum.

17-Å and 28-Å InAs nanocrystals led to a broadening of the simulated spectra (solid lines in Figure 5) similar to the experimental data. Other potential sources for the spectral broadening, such as a disordered surfactant shell, a slightly elliptical particle shape, or quantum size effects, could be excluded.

Therefore, we conclude that structural disorder in the nanocrystals induced by surface reconstructions is responsible for the broadening of the XANES spectra of InAs and CdSe nanocrystals. This study indicates that XANES spectroscopy can be a valuable tool in the investigation of surface reconstruction in nanocrystals, the knowledge of which can lead to a better understanding of the factors influencing the properties and stability of nanocrystals.

Investigators

J. Rockenberger, K.S. Hamad, R. Roth, and A.P. Alivisatos (University of California, Berkeley, and Berkeley Lab); and T. van Buuren (Lawrence Livermore National Laboratory).

Funding

Publications

1. K.S. Hamad et al., "Structural disorder in colloidal InAs and CdSe nanocrystals observed by x-ray absorption near-edge spectroscopy," *Phys. Rev. Lett.* **83**, 3474 (1999).

Layer-Specific Structure Determination: Anomalous Carbon Dimers on Silicon Carbide

Much of the action during fabrication of microcircuits and other electronic devices takes place at or near the surface. For example, carving out circuit patterns is a multistep process involving growing high-quality crystalline substrates and depositing and etching away thin layers on the substrate through a mask containing parts of the pattern. Sometimes a second material is first deposited on the substrate and serves as the active electronic material. Whatever the case, precise control of the growth and fabrication processes relies on understanding the surface structure at the atomic level. A group working at the ALS has used photoelectron diffraction, a technique in which the intensity of electrons emitted after absorption of x rays is measured in many directions and for many x-ray wavelengths, to resolve a controversy about the surface structure of silicon carbide (SiC), a semiconductor under development for several applications.

Silicon carbide is a promising material both for use as a substrate on which to grow diamond and for electronic devices that overcome the limitations of conventional silicon devices in high-temperature, high-frequency, and high-power applications. The growth of SiC thin films with high crystalline quality and the subsequent processing steps are the subject of substantial research and development programs. For both growth and process control, an atomic-scale understanding of the SiC surface structure is essential. Although cubic SiC is known to have three major surface phases (the carbon-terminated, the silicon-terminated, and the silicon-rich surfaces), their atomic structures have been uncertain.

In particular, for the carbon-terminated c(2×2) surface, a very unusual bridge-bonded dimer (BD) structure with a triple carbon–carbon bonding (Figure 1b), as in the C_2H_2 molecule, has been

discussed as an alternative to a conventional sp^3 dimer structure. However, the BD structure seems to violate the most important chemical rule of semiconductor surface reconstructions: minimization of the number of unsaturated dangling bonds. High-resolution scanning transmission microscope (STM) images on the c(2×2) surface have failed to resolve this structural issue because of strong electronic effects within the surface carbon dimers (Figure 1a).
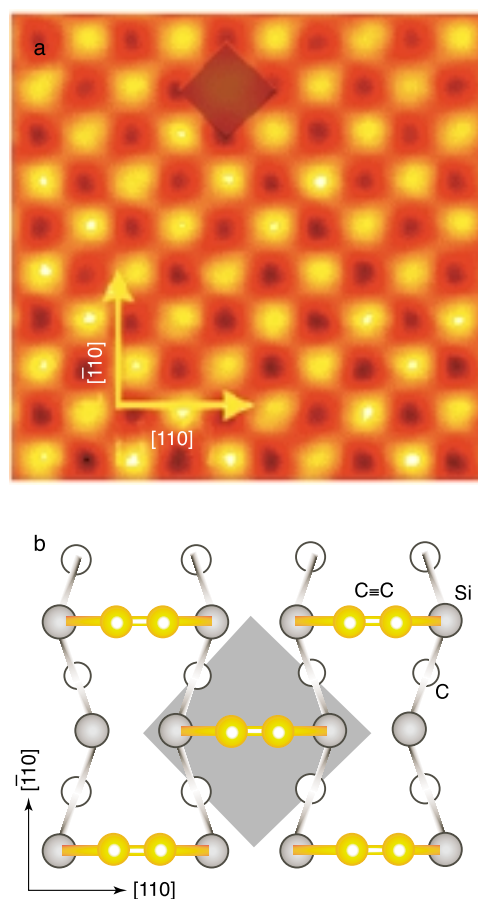
Figure 1

(a) Atomic-scale scanning tunneling microscopy (STM) image and (b) model of C_2H_2-like triple-bonded dimer (the so-called bridge-dimer model) of the carbon-terminated cubic SiC(001) surface. The surface unit cell of a c(2×2) periodicity is depicted by hatched diamonds.

This issue is unambiguously resolved by photo-electron diffraction (PED) measurements made by using the high-resolution soft x-ray synchrotron radiation provided by Beamline 9.3.2. The carbon 1s photoemission of the cubic SiC(001)c(2×2) surface clearly exhibits a surface core-level component (S in Figure 2a) that will be shown to be due to the carbon dimers on the surface. Several hundred similar high-resolution carbon 1s spectra emitted into a small cone of solid angles were taken at varying incident photon energy and emission angle. In this way, the intensity modulation of the surface carbon 1s component was measured as a function of the photoelectron wave vector. The resulting PED pattern

shown in Figure 2b is due to the scattering of the outgoing photoelectrons with the surrounding atoms and thus contains detailed local structural information of the near-surface layers around the atoms emitting photoelectrons, the surface carbon atoms in this case.

The simulated PED patterns were then calculated for two structure models: the BD model and a conventional model called the staggered-dimer (SD) model. The calculations were done with a full multiple-scattering simulation scheme (MCSD package) recently developed by Y. Chen and M.A. Van Hove of Berkeley Lab. Comparing the results of the simulations with the experimental data
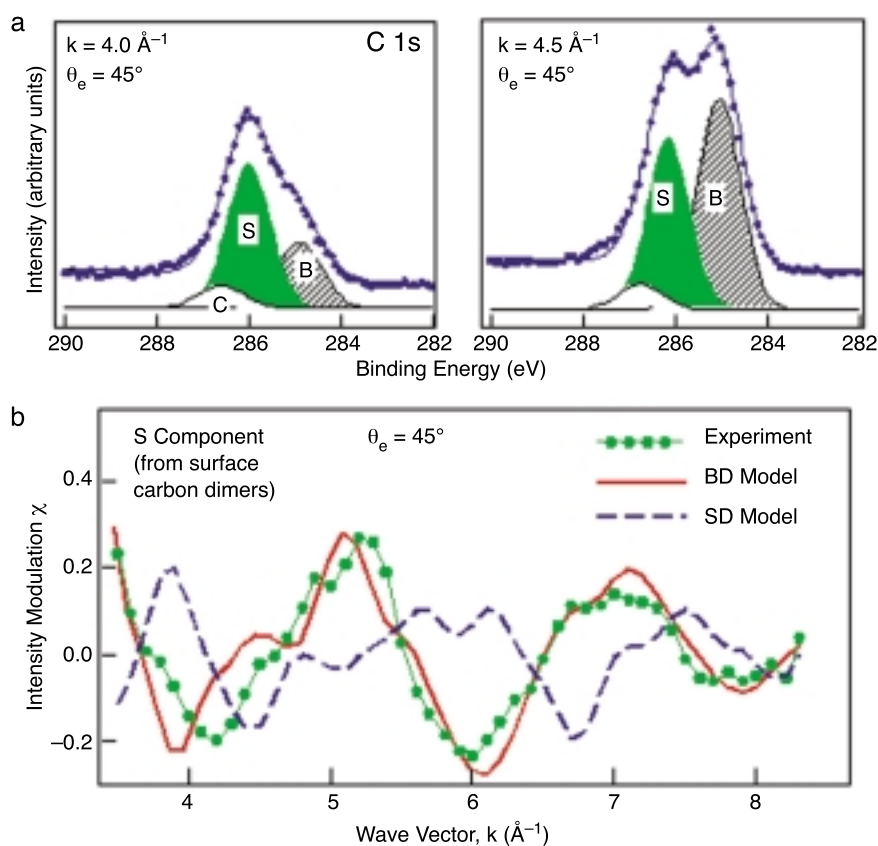
Figure 2

(a) Carbon 1s spectra of 3*C*–SiC(001)-c(2×2) for two different kinetic energies corresponding to photoelectron wave vectors k = 4.0 and 4.5 Å^{-1}. S and B denote the surface and bulk components, respectively. (b) Intensity modulation (χ) of the S component as function of photoelectron wave vector (k), where $\chi = (I - I_0)/I_0$, I is the photoelectron intensity, and I_0 is the smooth background. The dots connected by a thin green line represent the experimental data, and the thick red and dashed blue lines are the optimized results of theoretical simulations for the bridge-dimer and staggered-dimer structure models, respectively.

unambiguously confirmed the unusual BD model: Figure 2b clearly shows that only the simulation based on the BD model fits the experimental data well. In addition, detailed structural parameters were obtained by optimizing the fit between simulation and experiment. The carbon–carbon dimer bond length obtained in this way is 1.22 ± 0.05 Å, in close agreement with the predictions of *ab initio* calculations and with the bond length of the triple bonded C_2H_2 molecule.

Investigators

H.W. Yeom (University of Tokyo); M. Shimomura and S. Kono (Tohoku University); J. Kitamura and S. Hara (Electrotechnical Laboratory); B.S. Mun and C.S. Fadley (Berkeley Lab and University of California, Davis).

Funding

Publications

1. H.W. Yeom et al., "Surface reconstructions of 3*C*–SiC(001) studied by high-resolution core-level photoemission," *Surf. Sci.* **433**, 237 (1999).
2. H.W. Yeom et al., "Atomic and electronic-band structures of anomalous carbon dimers on 3*C*–SiC(001)-c(2×2)," *Phys. Rev. Lett.* **83**, 1640 (1998).
3. M. Shimomura et al., "Surface-core-level-shift photoelectron diffraction study of the β-SiC(001)-c(2×2) surface," *Surf. Sci.* **438**, 237 (1999).

Tuning the Spin-Orbit Coupling at a Metal Surface

One of the enduring questions about magnetic materials is the effect of surfaces and interfaces on the materials' magnetic properties. This is not just an academic question, because the current rapid development of magnetic data-storage devices relies in no small part on the use of very thin layered magnetic structures. As these device dimensions continue to shrink, the roles of the surfaces and interfaces become more and more important. And yet, as important as these effects are for understanding thin-film magnetic devices, it has been difficult to predict from theory how the important magnetic properties change in going from a bulk, three-dimensional magnet to a flat, two-dimensional one. A group working at the ALS has experimentally studied model systems in which the relative energies of electrons of opposite spins were tuned by judiciously modifying the interface. Ultimately, the improved understanding gained from this study may lead to creation of new and useful magnetic devices.

A lithium layer on a tungsten surface provides a good model system for studying interfaces because the tungsten surface has been studied in considerable detail. In this study, we have focused on the role of the interface in spin-orbit coupling, which is the coupling between an electron and the local electric field it experiences as it moves through a solid. This interaction leads to a local magnetic field, which even in the absence of normal magnetism can, under some conditions, cause electrons of opposite spins to have different energies. Although we are studying this effect for a nonmagnetic system, the same coupling is important for the interface magnetism that figures prominently in the layered magnetic nanostructures under rapid development for magnetic data-storage devices and other applications.

Figure 3 shows the basic result of our measurements, which were conducted by means of angle-resolved valence-band photoemission. The dots represent the energies of electronic states as a function of electron momentum along the indicated direction in the Brillouin zone. Figure 3a represents the states present at the clean (110) surface of tungsten. The most important feature is a pair of states (labeled 1 and 2) that are split because of the spin-orbit interaction. We would not be able to observe this splitting except that (1) the very existence of the surface breaks the symmetry and allows the bands to be split and (2) the relatively heavy tungsten nucleus enhances the splitting by increasing the importance of relativistic corrections. We could not see the splitting, for example, when we examined a similar molybdenum surface, which apart from the lightness
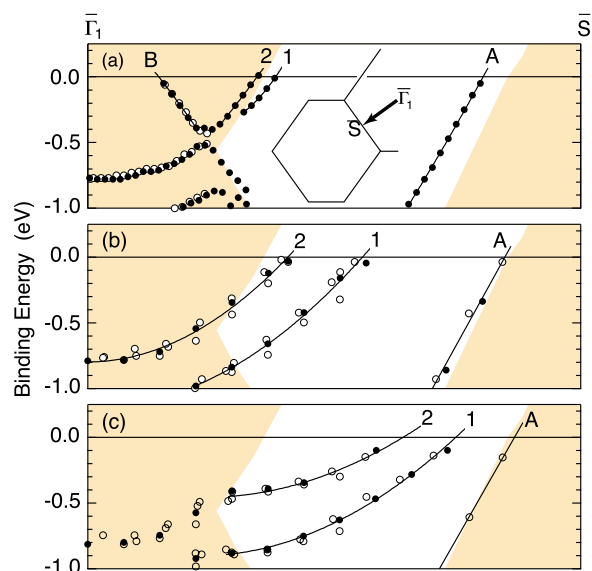
Figure 3

Angle-resolved surface-state valence bands for lithium on the (110) surface of tungsten for (a) clean surface, (b) about one-half of a monolayer of lithium, and (c) one monolayer of lithium. The shaded region is the projection of bulk states onto the (110) surface. The closed circles are for momenta indicated in the inset at the center of a; open circles are from other symmetry-equivalent directions. The spin-orbit splitting of the states labeled 1 and 2 increases with lithium coverage, and the states become more localized at the surface.

In addition to mapping the interface-state energy as a function of momentum in one direction, we can restrict the energy to that of the least bound electrons and map the density of electrons at that energy throughout momentum space, as shown in Figure 4. The contours that these states form in momentum space are the Fermi surfaces. We know that the Fermi surfaces associated with bands 1 and 2 have opposite spin, and we show one possible arrangement of spins in the figure. The point is that while there is no net spin polarization (since the system is not magnetic), in local regions of momentum space there is an in-plane polarization. There is an apparent handedness to the spin arrangements, and the sense of the hand-edness is fixed by the sign of the surface electric-field gradient. In principle, the photoelectrons emitted in a particular direction are highly spin-polarized, which we would like to check in future measure-ments using spin-resolved photoemission.

of the nucleus is electronically very similar to the tungsten surface, with nearly identical bands.

We modified the surface by adding one-half of a monolayer of lithium (Figure 3b) and a full mono-layer (Figure 3c). As we add lithium, the states move away from the gray region, which represents bulk-like electronic states with relatively weak binding to the surface, into the white region, which represents states more localized to the surface. This shift is due to the energy gain obtained when the electrons in these states interact with the overlying lithium atoms. An additional effect is that the splitting we observed in Figure 3a is enhanced as lithium is introduced. This shows that the symmetry breaking introduced when the surface was created is actually stronger when lithium is added.

Figure 4

Map of the Fermi intensity for one monolayer of lithium deposited on the (110) surface of tungsten. The straight white lines are the surface Brillouin zone boundaries. The remaining white lines are the Fermi crossings of the spin-polarized bands; the arrows indicate a proposed spin.

Investigators

E. Rotenberg (ALS), J.W. Chung (POSTECH, Korea), and S.D. Kevan (University of Oregon).
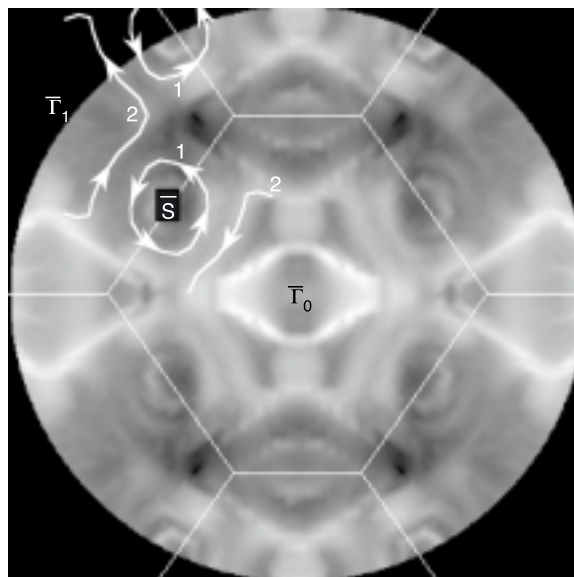
Publications

1. E. Rotenberg, J.W. Chung, and S.D. Kevan, "Spin-orbit coupling induced surface band splitting in Li/W(110) and Li/Mo(110)," *Phys. Rev. Lett.* **82**, 4066 (1999).
2. E. Rotenberg and S.D. Kevan, "Evolution of Fermi level crossings versus H coverage on W(110)," *Phys. Rev. Lett.* **80**, 2905 (1998).

Multi-Atom Resonant Photoemission: New Probe of Near-Neighbor Properties Applied to Metal Bilayers and Alloys

Although many existing experimental techniques can provide information on the elements present in a given sample of material, as well as on their local structural and bonding environment and their magnetic properties, we lack a broadly applicable probe that can determine whether an atom of a given element is actually located in close physical proximity to an atom of another element. Multi-atom resonant photoemission (MARPE), an effect recently discovered at the ALS, appears to provide such a probe. Application of the MARPE technique to a metal alloy of iron and chromium by the same group of experimenters has provided direct evidence for compositional clustering in which chromium atoms prefer to be near other chromium atoms rather than near iron atoms. Quantitative agreement between measured and calculated clustering makes MARPE look promising for the study of clustering and other types of compositional heterogeneity in more complex materials and at surfaces and interfaces between materials.

The multi-atom resonant photoemission (MARPE) effect, discovered at the ALS in experiments on Beamline 9.3.2, makes use of the well-known elemental specificity of core-electron excitation energies but takes this specificity one step further by involving two atoms at once. If the energy of a soft x ray that is exciting photoelectrons from a core level of a given atom "A" is tuned through an absorption edge or threshold for a core electron on a neighboring atom "B," the excitation strength on the neighbor atom is found to be transferred back to atom "A" via an interatomic resonant process. Increases of up to 100 percent in the resulting photoelectron intensity from "A" have been observed. The effect was first seen in photoelectron emission from various metal oxides, and it has by now also been observed in the secondary decay processes of Auger emission and soft x-ray emission, thus expanding its range of applicability. Groups elsewhere in the world have also begun to study the effect experimentally. Preliminary discussions of the theory of MARPE have also appeared.

We here present results of applying MARPE for the first time to metallic systems, in particular to chromium/iron bilayers and alloys. The chromium 2p intensity for both a thin chromium overlayer on a thick iron layer and an iron-rich alloy was found to be enhanced by up to 85 percent upon sweeping the x-ray energy through the iron 2p absorption edges, as shown in Figure 5a and in Figure 5b, respectively. In both cases, the MARPE enhancements closely followed the normal iron 2p x-ray absorption coefficient shown in Figure 5c, a similarity noted in previous experiments.

Similar data have been obtained over a broad range of chromium and iron thicknesses, as well as alloy compositions, with the resulting intensity enhancements summarized in Figures 6a and 6b. The solid blue curves in these panels represent the best fit to these data with an empirical model in which the short-range, near-neighbor contributions are much enhanced (about 5000 times) with respect to the long-range contributions that are fitted very well by an exponential decay with decay lengths of 25 to 30 Å. Near neighbors within about 3 Å of the emitting atom are thus found to contribute about half of the overall effect. However, the marked curvature in the alloy data of Figure 6b can only be
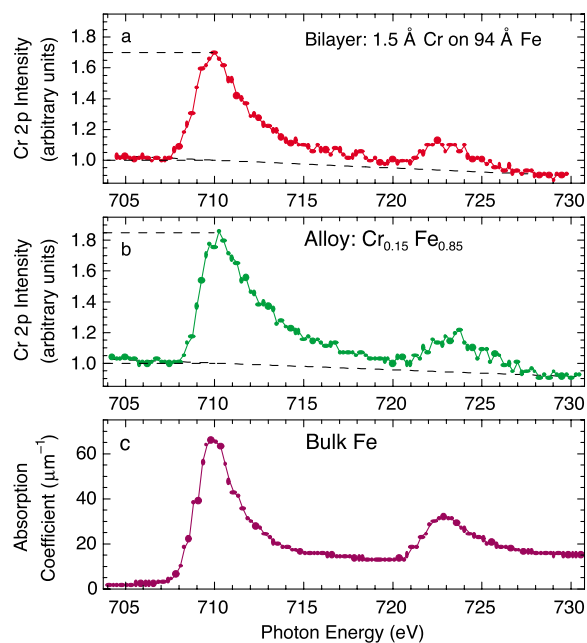
Figure 5

Multi-atom resonant photoemission (MARPE) and x-ray absorption results for chromium/iron bilayers and alloys. (a) Chromium 2p photoemission intensity for a thin 1.5-Å chromium layer on a thicker 94-Å iron layer as the photon energy is scanned through the iron $L_{3,2}$ edges. The dashed line below the curve indicates the expected chromium 2p intensity without interatomic effects. (b) chromium 2 p photoemission intensity as in (a) for an iron-rich $Cr_{0.15}Fe_{0.85}$ alloy. (c) X-ray absorption coefficient for pure iron at the iron $L_{3,2}$ absorption edges.

Figure 6

(a) MARPE enhancement of the chromium 2p photoemission intensity at the iron L_3 edge for chromium/iron bilayers with iron thickness t_{Fe}=94 Å and varying chrome thickness t_{Cr} (red squares) and t_{Cr}=4.5 Å and varying t_{Fe} (black squares). The blue curves are empirical fits to this data with enhanced near-neighbor contributions. (b) MARPE enhancement of the chromium 2p intensity at the iron L_3 edge for Cr_xFe_{1-x} alloys of varying composition x. The experimental results are displayed as green circles. Simulations of the data based on random mixing in the alloy (blue curve) and with empirically derived near-neighbor chromium compositional clustering via the parameter x_{nn} (red curve) are also shown. (c) Near-neighbor chromium composition x_{nn} as a function of alloy composition x: straight blue line = random mixing; red curve = experimental, as derived from our MARPE results; black curve = independent theoretical prediction.

described if we introduce compositional clustering in the alloy, with chromium preferring to have chromium near neighbors (red curve). This results in the experimentally determined near-neighbor composition x_{nn} shown in Figure 6c (red curve).

The extent of short-range compositional clustering in this system has also been calculated by a method that expands the free energy in inverse temperature, with effective interatomic interactions explicitly involved in the expansion. These results (black curve) are compared with the experimental short-range chromium concentration derived from MARPE in Figure 6c (red curve), and the agreement is excellent. These results thus better quantify the interaction range of MARPE, challenge theory to yield a quantitative prediction of the distance dependence observed, and provide a first application of the

effect to compositional clustering in alloys. Taken together with other work, a broad future utility of this type of measurement is suggested for studying various types of heterogeneity in alloys and complex materials, as well as at surfaces and buried interfaces.

Investigators

E. Arenholz and Z. Hussain (ALS); A.W. Kay, C.S. Fadley, and B.S. Mun (Berkeley Lab and University of California, Davis); M. Polak and L. Rubinovich (Ben Gurion University, Israel); F.J. García de Abajo (Berkeley Lab and Universidad del País Vasco/EHU, Spain); and M.A. Van Hove (Berkeley Lab).

Funding

Publications

1. F. J. García de Abajo, C.S. Fadley, and M.A. Van Hove, "Multiatom resonant photoemission: Theory and systematics," *Phys. Rev. Lett.* **82**, 4126 (1999).

2. E. Arenholz et al., "Multiatom resonant photoemission observed via secondary processes: Auger decay and x-ray fluorescence," *Phys. Rev. B* **61**, 7183 (2000).

3. C.S. Fadley et al., "Multiatom resonant photoemission," in *X-Ray and Inner-Shell Processes*, AIP Conference Proceedings No. 506, R.W. Dunford et al., Eds., (American Institute of Physics, New York, 2000) pp. 251-272.

ENVIRONMENTAL AND EARTH SCIENCE

Quantitative Zinc Speciation in Soils: Attacking Complexity with Complementary X-Ray Techniques

To help clean up polluted military, industrial, and agricultural sites, a new field of research has arisen that offers a scientific approach to waste remediation—molecular environmental science (MES). The transport of pollutants, such as heavy metals, from their source through soil and water to their final resting place and their impact on plants, animals, and humans along the way depends in detail on the chemical form of the polluting species. MES researchers aim to study at the molecular level the forms pollutants take in the environment, the processes by which they move through it, and the mechanisms by which they change from one form to another. In this study, a group of French researchers examined soils contaminated by zinc from decommissioned smelters. By combining new x-ray analysis techniques, they were able to identify the three main chemical forms taken by zinc in these soils and determine their relative proportions.

A scientific approach to cleaning up the environment requires basic chemical information at the molecular level about contaminants. Working at both the ALS and the European Synchrotron Radiation Facility (ESRF) in Grenoble, our team has shown how to use complementary x-ray techniques to identify zinc-containing compounds in contaminated French and Belgian soils located near smelters. In particular, we have combined spatially resolved (at the micrometer scale) x-ray fluorescence (μ-XRF) and extended x-ray absorption fine structure (μ-EXAFS) at the ALS and polarized EXAFS at the ESRF to make the key identification of important zinc constituents and their structural forms (i.e., their speciation).

Like other toxic metals, such as chromium and uranium, zinc undergoes many chemical transformations during its journey from the source to the final resting place. The Imperial Smelting Process used for many decades in Europe produced considerable amounts of dust and fumes rich in zinc and lead. When the zinc reached the soil, it was deposited in the form of a number of "primary" zinc-containing minerals. Weathering of these minerals resulted in the trapping of zinc in "secondary" minerals, predominantly clay minerals but to a lesser extent iron oxyhydroxides and manganese oxides that immobilize the zinc, rendering it less harmful.

In recent years, x-ray diffraction and EXAFS of powder samples have been replacing older chemical-extraction techniques for speciation of contaminants in the environment. Making EXAFS measurements for a large number of compounds in well-prepared forms results in a library of standards that can be used when a sample contains multiple chemical compounds containing the same element. Mathematically fitting a combination of the EXAFS spectra from standards with the measured spectrum, in principle, identifies and gives the concentration of each compound in the sample. However, the method does not work well when too many standards are required, so it is necessary to have some idea of what is present—a difficult task when some compounds exist in small concentrations against a larger background of other compounds.

We attacked this problem for soil samples by exploiting the newer third-generation synchrotron-radiation sources. Powder EXAFS suggested that zinc-containing clay minerals were the predominant species. Because of the layered structure of clays, EXAFS spectra with linearly polarized light have a distinctive angular dependence as an oriented sample is rotated in the beam, and this is what we observed at the ESRF, thereby confirming the presence of
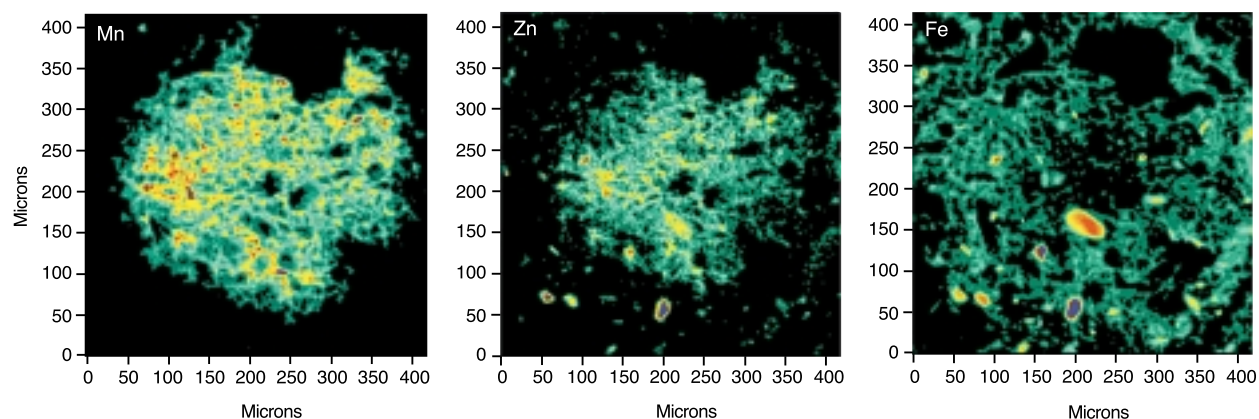
Figure 1

μ-XRF map of elemental distributions shows that zinc (center) is partitioned between large manganese-rich spherules (left) and smaller iron-rich grains (right) in a sample of soil contaminated by a decommissioned zinc smelter.

zinc-containing clay minerals. A detailed analysis of the spectra revealed the local structure around the zinc in the clay.

The two next most important zinc species (i.e., the iron oxyhydroxides and manganese oxides) were identified at the ALS. First, with μ-XRF, we located regions containing manganese, iron, and zinc in these inhomogeneous samples. In particular, we found iron-rich grains that typically were 10 to 20 μm in size and manganese-rich spherules that were much larger at 300 μm. Application of μ-EXAFS within these regions then revealed the identity and structure of the zinc species. For example, the zinc-containing manganese compound was birnessite, a layered compound in which the zinc is adsorbed in the interlayer space above and below vacant sites with either four- or six-fold coordination. Model compounds derived from polarized and μ-EXAFS data were then used to obtain good fits of powder-EXAFS data for all the soil samples studied.

Investigators

A. Manceau, B. Lanson, M.L. Schlegel, J.-C. Hargé, M. Musso, L. Eybert-Bérard, and J.-L. Hazemann (Université J. Fourier and CNRS, France); D. Chateigner (University of Maine-Le Mans, France); and G.M. Lamble (ALS).
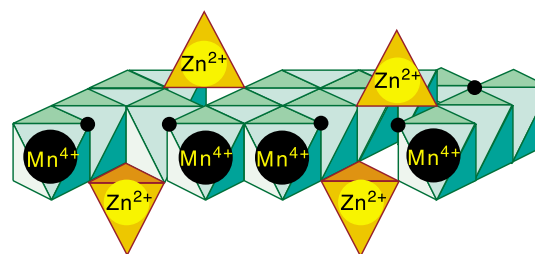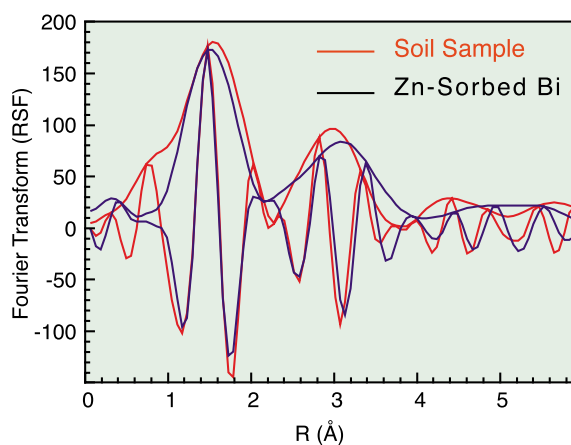
Figure 2

μ-EXAFS (red) of zinc in a manganese-rich area of a soil sample identifies the presence of zinc-sorbed birnessite (blue), a layered manganese compound with zinc above and below vacant sites, as shown in the model (bottom). Similar models for iron and clay minerals were obtained from μ-EXAFS (ALS) and polarized EXAFS (ESRF), respectively.
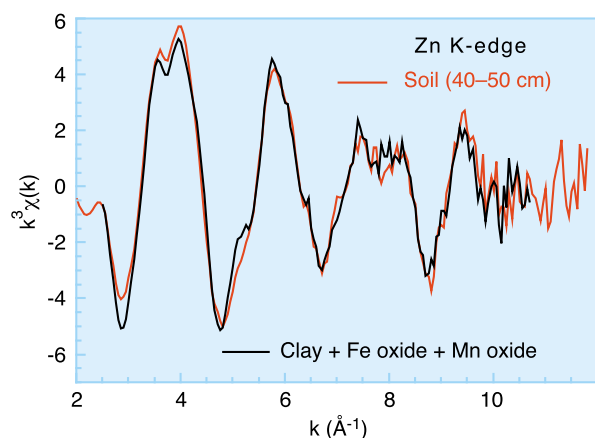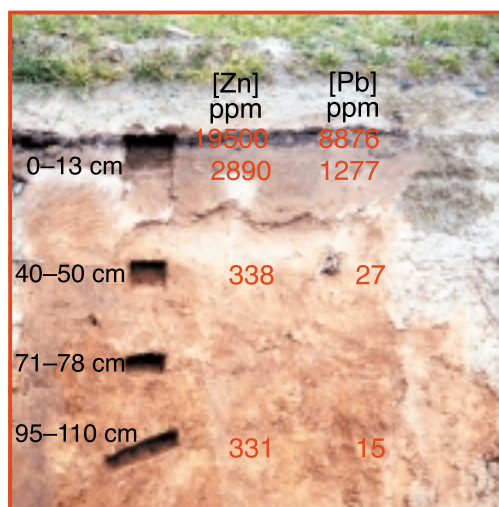
Figure 3

(top) Soil samples were taken at several depths from a contaminated site. (bottom) Model compounds derived from polarized-EXAFS data at the ESRF and µ-EXAFS data at the ALS provide a good fit with powder-EXAFS spectra from a soil sample, thereby confirming the identification of the contaminating species.

Publication

1. A. Manceau et al, "Quantitative Zn speciation in smelter-contaminated soils by EXAFS spectroscopy," *Am. J. Sci.* (in press, 2000).

Microbial Reduction of Hexavalent Chromium

Compounds containing chromium atoms are potentially hazardous contaminants in the environment. The degree of hazard depends on the chemical state of the chromium in the compounds in which it occurs. Chromium with a positive charge of +6 is highly soluble in water and therefore mobile in the environment, so the contamination spreads, and it is toxic and carcinogenic. However, chromium with a positive charge of +3 is relatively insoluble in water and significantly less harmful. Processes that convert chromium from the +6 to the +3 state are potentially useful for waste cleanup and environmental remediation. Berkeley Lab researchers working at the ALS have used an infrared microscope to demonstrate that certain bacteria found naturally in rocks are effective agents in the "biogeochemical" transformation of chromium from the undesirable +3 state to the less harmful +3 state, thereby resolving an on-going controversy about the nature of the conversion.

Hexavalent chromium (Cr^{6+}) is a widespread contaminant that enters the environment through various industrial processes. Cr^{6+} compounds are highly water soluble, toxic in the environment, and carcinogenic in mammals. However, recent studies have shown that certain bacterial species in geologic materials can detoxify the compounds by reducing them to relatively insoluble and hence significantly less harmful trivalent chromium (Cr^{3+}) compounds, a process known as biogeochemical transformation. We have used the Fourier-transform infrared (FTIR) spectromicroscopy beamline (Beamline 1.4.3) to obtain spatially resolved, time-dependent spectra that give evidence of the biogeochemical transformation of Cr^{6+}.

This is the first time that biogeochemical transformation of Cr^{6+} by microorganisms on a mineral surface has been nondestructively monitored and studied. Because infrared light does not kill bacteria, the transformation of Cr^{6+} can be monitored where it occurs. Distinct and relevant infrared absorption bands related to the transformation are used not

only as chemical markers to detect different chromium species, but also as biological markers to detect the presence and activity of microorganisms on specimen surfaces. In addition, the brightness of the infrared radiation from the beamline makes spatially resolved spectroscopy (spectromicroscopy) possible.

Two reduction mechanisms had previously been postulated for the reduction of Cr^{6+} compounds. The biological mechanism requires the presence of microorganisms to aerobically reduce the Cr^{6+}. The chemical mechanism relies on metal oxides, such as Fe(II) compounds, to catalyze the Cr^{6+}-reduction reaction. We conducted FTIR experiments to distinguish the relative significance of these two mechanisms. In addition, we evaluated the effects of common organic co-contaminants, such as toluene vapor, on the biotic reduction process.

For magnetite surfaces of mixed iron oxides that contain no living microorganisms, a five-day exposure to Cr^{6+} compounds resulted in no statistically significant changes in infrared chemical markers, indicating that no catalysis of Cr^{6+} reduction was occurring. On samples with living microorganisms, however, some Cr^{6+} reduction was detected. Moreover, when the samples with living microorganisms were incubated in dilute toluene vapor, statistically significant changes in both infrared-absorption

intensity and characteristic band shapes were observed for Cr^{6+}, as were new bands signaling the possible existence of intermediate Cr^{5+}. FTIR spectromicroscopy showed that the changes in the infrared absorption bands occurred at the sites of bacterial concentration. Imaging the surface at characteristic absorption bands showed a strong correlation between peak depletion of Cr^{6+} and toluene and peak concentration of biological molecules.

In a study to determine if this microbial reduction process could occur in real geologic samples, composite mineral surfaces of basalt rock chips containing resident communities of microbes were exposed to solutions of Cr^{6+} and toluene vapor. At the end of four months, FTIR spectromicroscopy showed that Cr^{6+}-tolerant and Cr^{6+}-reducing natural microorganisms were thriving in association with Cr^{3+} (Figure 4). The reduced Cr^{3+} state was confirmed by x-ray absorption fine structure (XAFS) spectroscopy at Beamline 10.3.2.

The nondestructive infrared spectromicroscopy studies, combined with XAFS spectroscopy and microbiological techniques, show that highly mobile and toxic Cr^{6+} contaminants can be biologically reduced into less soluble, less toxic Cr^{3+} compounds. The FTIR method can now be expanded to examine other infrared-amenable microbial/chemical contaminant systems.
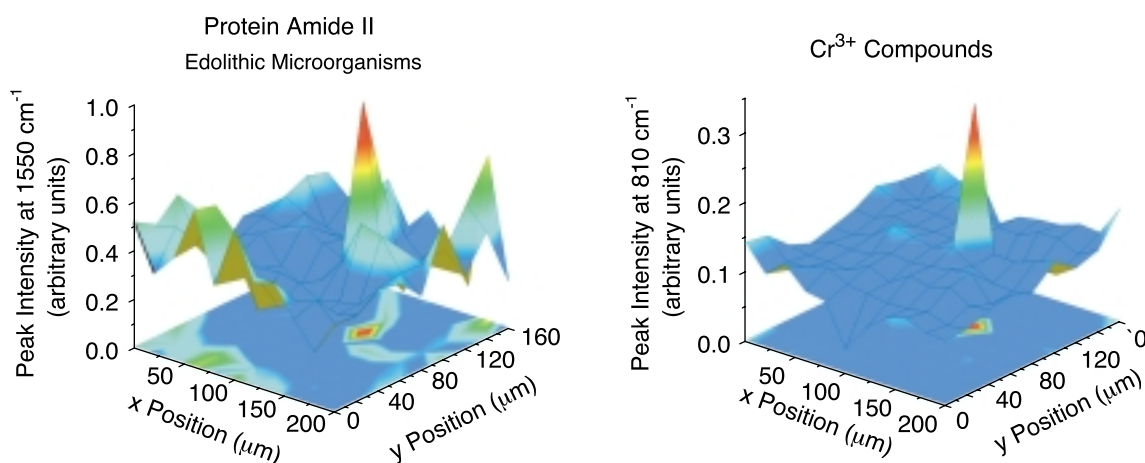
Figure 4

After a four-month exposure of basalt rock chips to solutions of Cr^{6+} and toluene vapor, SR-FTIR spectromicroscopy showed that Cr^{6+}-tolerant and Cr^{6+}-reducing natural microorganisms (left) were thriving in association with Cr^{3+} (right).

Investigators

H.-Y.N. Holman, D.L. Perry, G.M. Lamble, and J.C. Hunter-Cevera (Berkeley Lab) and M.C. Martin and W.R. McKinney (ALS).

Funding

Publication

1. H.-Y. N. Holman et al., "Real-time characterization of biogeochemical reduction of Cr(VI) on basalt surfaces by SR-FTIR imaging," *Geomicrobiology J.* **16**, 307(1999).

PROTEIN CRYSTALLOGRAPHY

Solving the Ribosome Puzzle

Ribosomes are ancient biological molecules with an overall structure that is common to all forms of life. They play an essential role by manufacturing proteins, thereby translating genetic information into an individual's observable characteristics. A group working at the ALS has now determined the overall molecular structure of the ribosome and how its parts fit together, a finding with practical and fundamental implications. On the practical side, bacterial infections are often treated by antibiotics that selectively target bacterial ribosomes while leaving mammalian ribosomes unaffected. Armed with the details of ribosomal structure, researchers can perhaps devise more effective strategies for inhibiting protein synthesis in disease-causing bacteria. Illumination of the ribosome's structure is also relevant to our quest to understand how life works. Detailed knowledge of the structure of this key molecule would represent a significant advancement in our understanding of the origins and evolution of life.

After decades of effort, techniques for crystallizing ribosomes and analyzing their structures have begun to yield rich dividends. Within the space of a month, several research groups recently reported on the solution of ribosome structures. While other groups focused on the component parts (subunits) of the ribosome, our group looked at the overall ribosome and how its parts fit together. About 2.5 million times more massive than a hydrogen atom, these ribosomes are the largest asymmetric structures solved by crystallography to date.

Ribosomes are the cell's protein manufacturing plants. In the ribosome, raw materials in the form of amino acids are combined according to blueprints provided by ribonucleic acid (RNA) to produce all the proteins necessary for life. To perform this complex task, the ribosome has evolved a complex structure, the rough outlines of which are already known.

Two subunits, one larger (50S) and one smaller (30S), together constitute the whole (70S) ribosome. The interface between the subunits contains several cavities where proteins (chains of amino acids) are assembled.

The order of the amino acids in the chain is determined by the sequence of nucleotides in a strand of messenger RNA (mRNA), a sequence that is transcribed from the cell's DNA. The mRNA then moves through the ribosome cavity like a conveyor belt. Each combination of three nucleotides (codon) in the mRNA strand forms base pairs with the complementary nucleotides (anticodon) in molecules of transfer RNA (tRNA). Each tRNA molecule carries a specific amino acid. Bonds are formed between adjacent amino acids and the growing chain exits the ribosome through a tunnel.

Bacterial ribosomes, which have the same basic structure as those of all life forms, are smaller than others and are therefore the most studied. Our team successfully crystallized 70S ribosome complexes (ribosomes plus various mRNA and tRNA fragments) from the bacterium *Thermus thermophilus*. Taking advantage of the high photon flux and collimation of Beamline 5.0.2, we used multiple-wavelength anomalous diffraction (MAD) techniques to obtain electron-density maps of the ribosome complexes with a resolution as good as 7.8 Å.

In addition to confirming features of ribosome structure already known through other types of studies, the electron-density maps reveal many interesting new details. For example, the images indicate how tRNAs are bound to various sites in the ribosome. At the site where codon–anticodon matches are recognized, only weak contacts between the ribosome and tRNA were observed, suggesting a degree of flexibility. In contrast, at the site where the amino acid chain begins to form, the ribosome rigidly grips the tRNA with six "fingers" of electron density, stabilizing and orienting both tRNA and mRNA components. Another striking feature seen in the images is
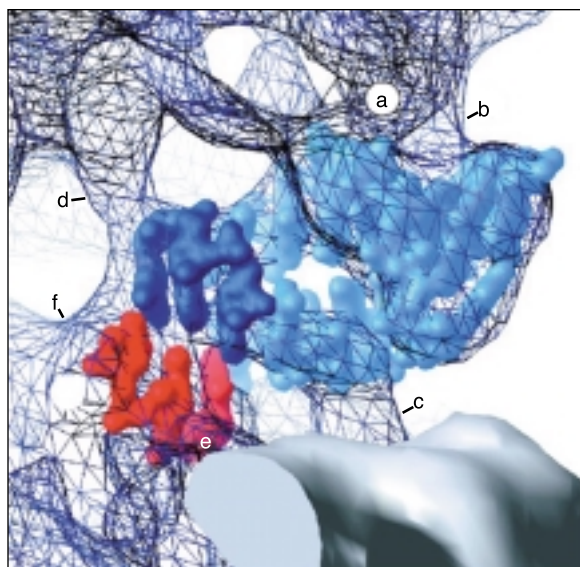
Figure 1

Six "fingers" of ribosomal electron density (labeled a–f) tightly grip mRNA (red) and tRNA (blue) components to facilitate protein synthesis.

an RNA helix that runs along the length of the 30S subunit. This single feature contributes about half of all the contacts between the two subunits and may function as a relay switch, linking events occurring in the two subunits by alternating between two different configurations.

These results reinforce the impression that the ribosome is a dynamic molecular machine with moving parts and a very complicated mechanism of action. Through these studies, we are, in a sense, reverse-engineering the ribosome: attempting to understand its function by examining how it is constructed. Toward this end, we are already working on improving their resolution and obtaining images of ribosomes at different stages of protein synthesis.

Investigators

H.F. Noller, M.M. Yusupov, and G.Zh. Yusupova (University of California, Santa Cruz); J.H. Cate (Whitehead Institute for Biomedical Research); and T.N. Earnest (Berkeley Lab).
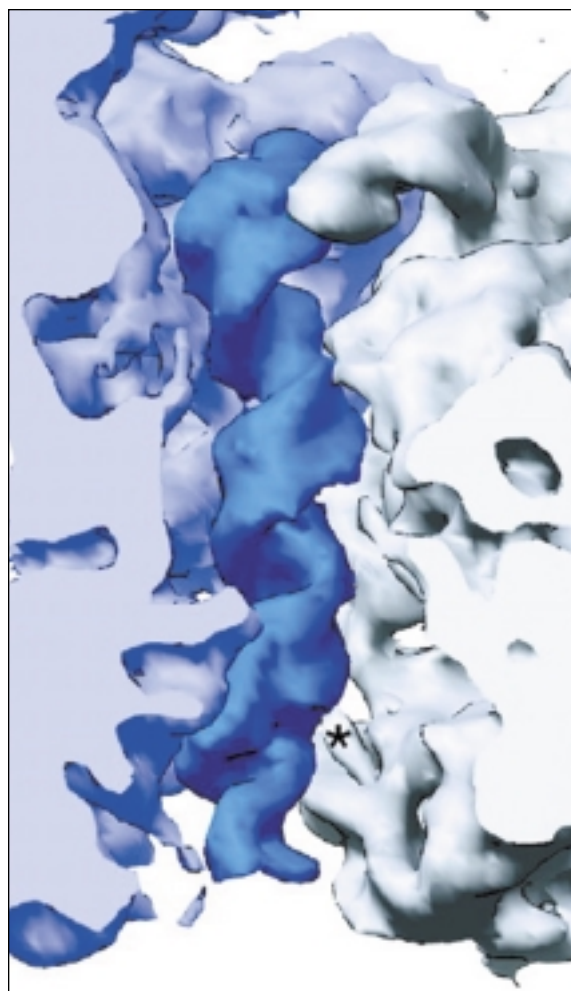
Figure 2

RNA helix (blue) packed into interface between the two ribosomal subunits (purple and gray). This feature may relay information from one subunit to the other.

Funding

Publication

1. J.H. Cate, et al., "X-ray crystal structures of 70S ribosome functional complexes," *Science* **285**, 2095 (1999).

Bacteriorhodopsin: Ion Transport is Net Result of Small Changes in Protein Structure

In addition to passively separating inside from outside, the skin on our bodies actively senses external conditions, helps regulate body temperature, and eliminates toxins. Similarly, on a much smaller scale, the membranes that define cells and organelles are more than just passive containers. Proteins embedded in the membranes are responsible for all forms of intercell signaling, sensing of external stimuli, and the transport of molecules and ions. A group working at the Macromolecular Crystallography Facility at the ALS has determined the structure of bacteriorhodopsin, a relatively small, simple bacterial membrane protein, before and during ion transport. Scientists believe that analysis of such membrane proteins in action will reveal a new world of channels, pumps, receptors, pores, and antigens that play large roles in disease and drug resistance. Consequently, an expanded database of membrane-protein structures is expected to facilitate the prediction, design, and discovery of new drugs.

Bacteriorhodopsin (BR) is a membrane-embedded protein that can actively "pump" ions from one side of the membrane to the other, against an electrochemical gradient. The energy for this process comes from a photon of visible light, which sets into motion a series of structural changes within the BR molecule that favor active ion transport. Our group has obtained atomic-resolution structures of BR crystals in two different states: one at the beginning of the ion-transport cycle and another in midstroke. Analysis of the small, but significant, structural differences between the two states provides insight into the mechanisms and forces that push and pull ions through the membrane, against the electrochemical tide.

The BR molecule contains seven helices that surround a channel through which ions can move. Charged amino-acid side chains (Glu^{204}, Glu^{194}, Arg^{82}, Asp^{85}, Asp^{96}) throughout the channel interact with the ions. Bound in a cavity roughly in the middle of the channel is a photosensitive molecule called retinal. The retinal divides the channel into a hydrophobic cytoplasmic side and a hydrophilic extracellular side. In the type of BR used in this study, the ions transported across the membrane are protons, and upon absorption of a photon of light, the retinal molecule flips toward the cytoplasmic side, losing a proton to the nearby Asp^{85} side chain. This, in turn, causes a proton to be released from the extracellular side (from Glu^{204} or Glu^{194}). Subsequently, a proton is taken up from the cytoplasmic side (via Asp^{96}), and sites that have lost a proton (such as the retinal site) are reprotonated to complete the photocycle.

In this study, we used a particular BR mutant (D96N) in which the uptake of a proton from the cytoplasmic side is hindered. This enabled us to freeze the action at the M_N state (just before reprotonation of the retinal) by illuminating "ground-state" crystals with yellow light, followed by cryo-trapping at 100 K. The structures of both ground-state and M_N-state crystals were then determined to 1.8 and 2.0 Å, respectively. This excellent resolution was made possible by the high quality of the crystals and the brightness, collimation, and small spot size of Beamline 5.0.2 at the Macromolecular Crystallography Facility.

The ground-state crystal structures show a network of amino-acid side chains and water molecules that provide a path for protons moving from the retinal to the extracellular surface (Figure 3). In the M_N state, the disappearance of key water molecules from this network and shifts in the locations of side chains (in response to the displacement of the retinal) raise or lower the proton affinity of the various binding sites (Figure 4). Thus, protons are released and captured by various sites, with the net result being that one proton is transported across the membrane.

This process moves in only one direction because the proton affinity of the Asp^{85}, which accepts the proton released by the retinal, remains high throughout most of the cycle. Also, there is no comparable network of side chains and water molecules on the cytoplasmic side to provide a continuous path from the retinal to the internal membrane surface. However, the images show the displacement of two side chains near the retinal on the cytoplasmic side, opening up a possible path for reprotonation of the retinal. Also, strong disorder in the cytoplasmic ends
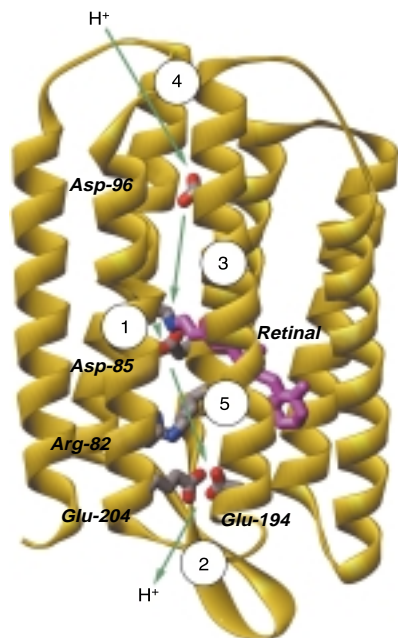
Figure 3

Overview of the structure of bacteriorhodopsin, including the photosensitive retinal molecule (purple) and the amino acids involved in ion transport. The arrows show the direction of transport, and the numbers represent the sequence of transport steps.
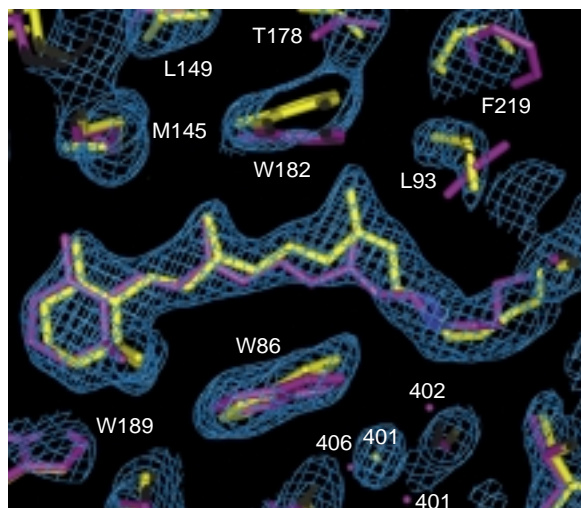
Figure 4

Comparison of ground-state (purple) and M_N-state (yellow) structures in the vicinity of the retinal. Small shifts in position and the disappearance of key water molecules (e.g., 402 and 406, near bottom) raise or lower the ion affinities of various ion binding sites, ensuring the unidirectionality of the ion pump. Displacements are on the order of 1 Å.

of two of the seven main helices suggests a possible role for these helices in the later stages of the photocycle.

Investigators

H. Luecke, B. Schobert, H.-T. Richter, J.-P. Cartailler, and J.K. Lanyi (University of California, Irvine).

Funding

Publications

1. H. Luecke et al., "Structural changes in bacteriorhodopsin during ion transport at 2 angstrom resolution," *Science* **286**, 255 (1999).
2. H. Luecke et al., "Structure of bacteriorhodopsin at 1.55 angstrom resolution," *J. Mol. Biol.* **291**, 899 (1999).

The Crystal Structure of Respiratory Complex II

We all have an instinctive feel for the necessity of breathing. Even in bacteria, respiration is not a thing to be taken lightly. As it happens, the protein complexes that catalyze respiration in cells are similar across species, all the way from bacteria to humans. Thus, information about how a microbe "breathes" helps humans understand how their own cells produce the energy needed for life. Researchers working at the Macromolecular Crystallography Facility at the ALS have grasped a big piece of the respiratory jigsaw puzzle by solving the structure of fumarate reductase, or respiratory complex II, from the bacterium Escherichia coli. *The new information about fumarate reductase provides a framework for understanding the function of an entire family of respiratory proteins. Together with recently solved structures within other complexes of the respiratory pathway, the new structure gives a more complete picture of respiration, for both aerobic (with oxygen) and anaerobic (without) processes.*

Our mitochondria require oxygen to help produce adenosine triphosphate (ATP), a molecule that can store chemical energy for later use. What makes the production of ATP possible? As we digest the food we eat, electrons are extracted from the chemical compounds that make up the food and are used to reduce oxygen. The energetically favorable process of oxygen reduction is indirectly coupled to the unfavorable process of ATP synthesis by a set of five protein complexes, numbered I through V, that bridge the mitochondrial membrane (Figure 5). However, some organisms, like the bacteria found in our digestive tracts, do not require oxygen for ATP synthesis; instead they can utilize the chemical fumarate ($C_4H_2O_4^{2-}$) in place of oxygen. Fumarate is normally a byproduct of aerobic respiration. By reversing the direction of one reaction and reducing fumarate, ATP synthesis can proceed in the absence of oxygen.

The reaction runs in either direction and is catalyzed by a protein complex called complex II. Because complex II is involved in such a fundamental metabolic process, genetic mutations are often lethal in the embryonic stage. In the cases where mutations are not lethal, they cause severe symptoms similar to those seen in multiple sclerosis. Although complex II has been extensively studied, there are still many mysteries as to how it functions. Understanding the mechanism of how proteins function requires knowledge of their structures.

X rays generated at Beamline 5.0.2 of the Macromolecular Crystallography Facility were used to determine the structure of complex II from the common bacterium *Escherichia coli*. The use of Beamline 5.0.2 was critical for several reasons. First, the wavelength is tunable, whereas it is fixed at most x-ray crystallography beamlines. Tunable radiation was important for determining structural information about complex II through the use of the anomalous scattering effect (multiple-wavelength anomalous diffraction, or MAD) at the iron K edge. Second, Beamline 5.0.2 focuses a higher useful intensity onto the sample than many other protein crystallography beamlines and therefore generated a higher signal in the diffraction data.

The structure of complex II revealed an essentially modular enzyme with two independently folded soluble domains and two transmembrane anchors (Figure 6). The active site of the enzyme is located in the flavoprotein subunit (Figure 6, blue domain) near a cofactor called a flavin. The understanding of the chemical composition of the amino acid residues and cofactors located near the reaction site allows us to better understand the mechanism of biological oxidation and reduction catalyzed by complex II. By looking at the cofactors attached to the protein chain (Figure 7), it is apparent how electrons can be transferred away from the food molecule bound at the active site of the enzyme and into the membrane where they can interact with complex III (Figure 5). This structure gives us insight into how aerobic respiration occurs in humans as well as how anaerobic respiration occurs in other organisms.
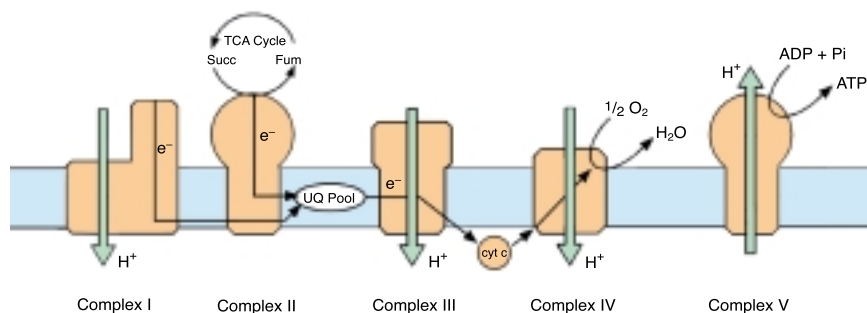
Figure 5

Schematic representation of the aerobic respiratory chain. Complexes I–V are labeled and the pathway of electron transfer is indicated.
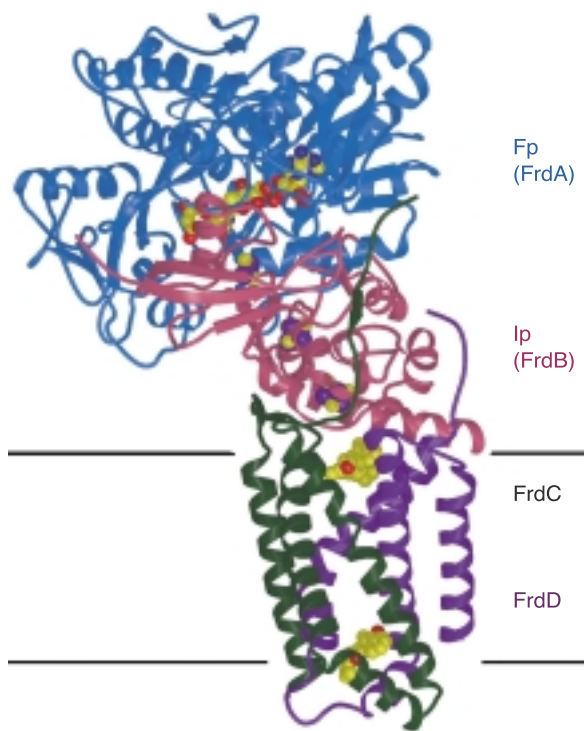
Figure 6

High-resolution structure of complex II. The ribbons shown in the figure follow the polypeptide chains of the protein. The flavoprotein subunit is colored blue, the iron protein is colored pink, and the two membrane anchors are green and purple. Black lines show where the boundaries of the membrane might be located.

Figure 7

Cofactors involved in electron transfer in complex II. The figure shows the same view of the structure as Figure 2 but with the protein stripped away. The distances shown are the closest distances between each redox cofactor. An electron likely follows the linear pathway along the arrows.

Investigators

T.M. Iverson and D.C. Rees (California Institute of Technology) and C. Luna-Chavez and G. Cecchini (VA Medical Center, San Francisco, and University of California, San Francisco).

Funding

Publications

1. T.M Iverson et al., "Structure of the *Escherichia coli* fumarate reductase respiratory complex," *Science* **284**, 1961 (1999).

2. C. Luna-Chavez, T.M. Iverson, D.C. Rees, and G. Cecchini, "Overexpression, purification and crystallization of the membrane-bound fumarate reductase from *Escherichia coli*," *Protein Expression Pur.*, (in press).

3. T.M. Iverson, C. Luna-Chavez, I. Schröder, G. Cecchini, and D.C. Rees, "Analyzing your complexes: Structure of the quinol–fumarate reductase respiratory complex," *Curr. Op. Str. Biol.*, (in press).

First Protein Structure of a Key Molecular Engine

Functioning of the cell requires the transport of molecules into and out of the cell through the cell membrane. For starters, nutrients must be ingested and waste products expelled. The family comprising several types of molecular machines that propel and guide biochemical compounds through cell membranes goes by the collective name "ABC transporters." Researchers from Berkeley Lab and the University of California, Berkeley, working at the ALS have obtained the first structure of a key subunit of an important ABC transporter, thereby providing clues about how these molecular machines work. In addition, mutations in ABC transporters appear to bring about genetic diseases in humans. The Berkeley researchers used their findings to propose a structural basis for the effects of mutations known to cause the lethal disease cystic fibrosis. Information of this type may someday lead to treatments for cystic fibrosis and other genetic diseases.

ABC transporters (also known as traffic ATPases) form a large family of proteins responsible for movement of biochemical compounds through cell membranes. We have used the Macromolecular Crystallography Facility at Beamline 5.0.2 to obtain the crystal structure of the HisP subunit of histidine permease, an ABC transporter from *Salmonella typhimurium*. The structure, obtained at a resolution of 1.5 Å, provides a basis for understanding properties of both normal and defective ABC transporters.

ABC transporters variously act as pumps that propel substances through membranes, as channels that allow the substances' passage, and as regulators that control other membrane proteins. Their general structural features, known from biochemical studies, include membrane-spanning domains between which the transported substances pass and nucleotide-binding domains, which are the molecular engines that drive the pumps or open and close the channels by using the energy released in the binding and hydrolysis of adenosine triphosphate (ATP). ABC transporters are increasingly recognized as the causes of human genetic diseases, such as cystic

fibrosis—a lethal disease that occurs in about 1 in 3,300 live births in the United States and Canada.

In *S. typhimurium*, histidine permease contains two identical nucleotide-binding domains, known as HisP, that together form a dimer (Figure 8). Using multiple-wavelength anomalous diffraction (MAD) methods to obtain phase information about a diffracted x-ray beam, we have solved the structure of HisP at a resolution of 1.5 Å. A four-wavelength MAD data set was obtained in just two hours at the ALS. The structure of the HisP monomer exhibits an unusual L shape with two thick arms, one of which holds the ATP binding site and the other of which is proposed to be in contact with membrane-spanning domains (Figure 9). It is possible that binding and hydrolysis of ATP in one arm results in conformational changes in the other arm that are passed on to the membrane-spanning domain, but the mechanism is not yet known in detail.

Because of the substantial similarity of the nucleotide-binding domains of ABC transporters in both prokaryotic cells (such as *S. typhimurium*) and eukaryotic cells (such as those in humans), structural details found in one type of organism are expected to apply to others. For example, our ability to correlate the properties of mutant forms of the cystic fibrosis transmembrane conductance regulator (CFTR), an
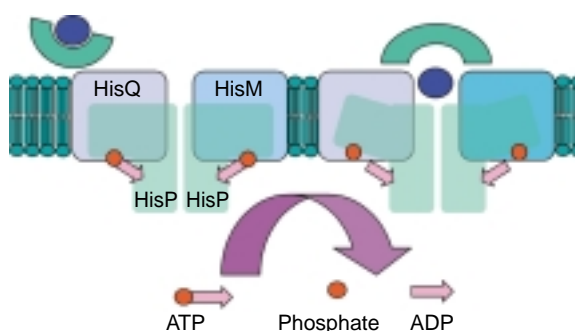
Figure 8

(left) Histidine permease (HisQMP2) molecular pump in a cell membrane (green) consists of two membrane-spanning domains (HisQ and HisM) and two identical nucleotide-binding domains (HisP). (right) Operation of the pump is driven by binding of ATP and hydrolysis to ADP, which are proposed to cause conformational changes in HisP that are transmitted to HisQ and HisP.

ABC transporter involved in cystic fibrosis, with the crystal structure of HisP indicates that HisP is a good model for the nucleotide-binding domains of ABC transporters in general.

We have used our HisP findings to propose a structural basis for the consequences of the known CFTR mutations. The most common mutation, found in 90% of all cystic fibrosis patients, leads to incorrect protein folding and transit. Other mutations may inhibit ATP binding or hydrolysis, thereby turning off the engine, or disrupt the interaction with the membrane-spanning domains, thereby putting the engine in neutral. This kind of information may eventually lead to a treatment for cystic fibrosis.

Arm II

Arm I

Figure 9

Ribbon representation of the structure of the HisP nucleotide-binding domain exhibits two arms in an L-shaped configuration. ATP (shown in ball-and-stick representation) resides in a binding pocket toward the bottom of Arm I. Two HisP units together form a dimer.

Investigators

L.-W. Hung (Berkeley Lab); I.X. Wang, K. Nikaido, P.-Q. Liu, and G.F.-L. Ames (University of California, Berkeley); and S.-H. Kim (University of California, Berkeley, and Berkeley Lab).

Funding

Publication

1. L.-W. Hung et al., "Crystal structure of the ATP-binding subunit of an ABC transporter," *Nature* **396**, 703 (1998).

ATOMIC AND MOLECULAR SCIENCE

A Momentum Microscope Views Many-Body Dynamics

How has nature created all the wonderful complexity surrounding us from such simple ingredients as positively charged nuclei and negatively charged electrons? What coordinates all the subtle motions and changes that animate our world on a microscopic level? The general answer to these questions comes from the fact that electrons do not move individually and independently of each other but mostly in a highly correlated fashion; that is, the motion of one electron affects the motions of the others through the Coulomb force that causes like charges to repel and opposite charges to attract. An international team working at the ALS has constructed a unique apparatus to study this correlated motion and applied it to the emission of two electrons from a deuterium molecule after absorption of an x ray. This is the first time that the correlated electron emission from a molecule has been mapped in complete detail.

Dynamical electron correlation—the fact that changes in electron motion, or more precisely their quantum-mechanical wavefunctions, occur in a highly correlated fashion—is determined by the complex, many-particle, momentum exchange via the Coulomb force between the charged particles (electrons and ions) in an atom or molecule. This momentum exchange is constrained by quantum-mechanical symmetry conditions imposed on all composite systems by their total angular momentum and parity.

A long-term project at the ALS is yielding new insight into this fundamental problem of electron correlation by investigating in as much detail as possible simple few-body processes that can serve as paradigms for more complicated cases. To do this, an endstation equipped with a novel momentum-space microscope (termed COLTRIMS) is used. It has been developed by a collaboration among

Universität-Frankfurt, Kansas State University, and Berkeley Lab. This device provides multidimensional images of the correlated momenta of all charged particles after photofragmentation of an atom or small molecule. Subatomic resolution and high detection efficiency are achieved for each electron and ion, no matter in which direction they may be moving.

Using this unique tool, we have investigated the ejection of two electrons from helium and neon. More recently, we have applied this technique to study the complete fragmentation of a hydrogen (deuterium) molecule by absorption of a single photon. The final state for this process consists of two protons and two electrons. The momentum vectors of each of the four particles have been measured in coincidence. The fact that a single photon can couple to two electrons at all is a remarkable consequence of electron correlation. In a world of isolated, uncorrelated electrons, the probability for coupling one photon to two electrons would be zero.

After absorption of the photon, the two electrons are emitted very quickly. On a much longer time scale, the two heavy nuclei then fly apart back-to-back along the molecular axis because of the repulsive Coulomb force between them. Thus, detecting the two nuclei yields the orientation of the molecular axis at the instant of ionization. With this trick one can map the correlated emission pattern of the two electrons from a "fixed-in-space" molecule.

In a first deuterium experiment at the old Beamline 9.0.1 (which later moved to become Beamline 10.0.1), we measured the energy and angular distribution of one of the two electrons with respect to the two heavy nuclei. Then, in two successive experiments at Beamline 7.0.1, both nuclei and both electrons were finally measured (Figures 1 and 2). This is the first time that the correlated electron emission from a molecule has been mapped in complete detail. Astonishingly, the gross features of the two electron wave functions do not depend strongly on the molecular orientation and are somewhat
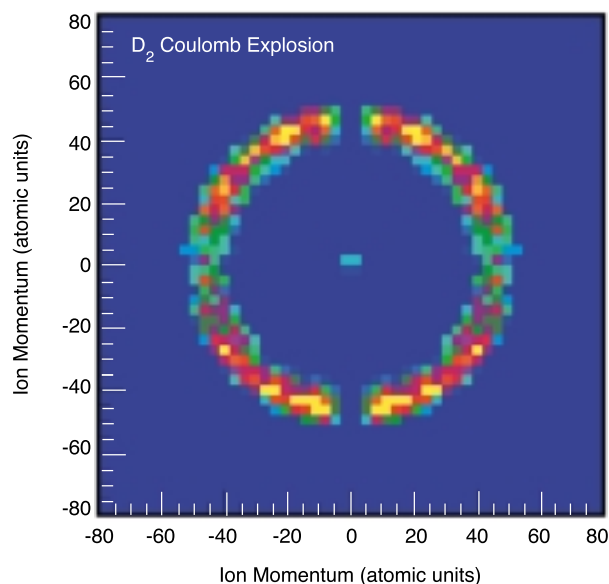
Figure 1

Momentum distribution of the D^+ fragments from photo-double-ionization of deuterium by 58.8-eV linearly polarized light. The electric field vector is horizontal, and the light propagates in the vertical direction. The gap in the "ring" is caused by inability to separate two ions arriving at the detector at nearly the same time.

Figure 2

Correlated two-electron momentum distribution after double ionization of deuterium by photons 25 eV above the double-ionization threshold. In this figure, the momentum vector of one electron points along the horizontal axis to the right (arrow), so the momentum distribution shown is that of the second electron. Electron repulsion is responsible for the dominant emission of the two electrons into opposite half spheres. The node for back-to-back emission is a result of the odd-parity symmetry of the final-state electron wave function. The data are integrated over all orientations of the molecule and all directions of the polarization axis.

similar to the emission pattern from a helium atom. The two new molecular effects to be seen are interference due to the two indistinguishable centers of the molecule and the consequences of a transfer of angular momentum from the electronic to the nuclear wave function.

The plot represented in Figure 2 is only one of many ways to visualize the results of these measurements using the COLTRIMS momentum microscope. The power of the technique allows investigators to view the correlations among the particle momenta without enforcing *a priori* restrictions on any of them.

Investigators

R. Dörner, Th. Weber, O. Jagutzki, L. Spielberger, V. Mergel, A. Bräuning-Demian, M. Achler, and H. Schmidt-Böcking (Universität Frankfurt); A. Czasch (Berkeley Lab and Universität Frankfurt);

M.H. Prior, J.D. Bozek, G. Meigs, and T. Warwick (Berkeley Lab); C.L. Cocke and T. Osipov (Kansas State University); H. Bräuning (Berkeley Lab, Kansas State University, and Universität Giessen); R. Moshammer (Universität Freiburg); J.M. Feagin (California State University at Fullerton); A. Landers (Western Michigan University and Kansas State University); and N. Berrah (Western Michigan University).

Funding

Publications

1. R. Dörner et al., "Photo-double-ionization of He: Fully differential and absolute electronic and ionic momentum distributions," *Phys. Rev. A* **57**, 1074 (1998).
2. H. Bräuning et al., "Absolute triple differential cross sections for photo-double-ionization of helium—Experiment and theory," *J. Phys. B* **31**, 5149 (1998).
3. R. Dörner et al., "Double photoionization of spatially aligned D_2," *Phys. Rev. Lett.* **81**, 5776 (1998).

Symmetry Resolution Yields Evidence for Shape Resonance

Many people are familiar with acetylene as a welding fuel, but it also plays an important role in industrial chemistry. Acetylene molecules that are fixed (adsorbed) onto a specially prepared surface serve as the foundation for the synthesis of certain types of plastics, such as polypropylene. To achieve the desired end result, the initial conditions of the acetylene molecules on the surface must be well understood. It would therefore be extremely useful to have a simple way to determine the properties of these molecular building blocks. Shape resonances are spectroscopic features that have shown promise for probing the geometry of molecules that are not in the gas phase. Now, the first convincing evidence for the existence of a shape resonance in acetylene has been obtained at the ALS through high-resolution photoelectron spectroscopy, where small differences in the energy of molecular orbitals can be resolved.

Shape resonances in photoelectron spectroscopy were first proposed to exist 15 years ago. Shape resonances occur when photoelectrons are temporarily trapped by a potential-energy barrier in the molecule. Because the shape of the potential depends upon the configuration of the molecule, it was initially thought that shape resonances might be a simple way to obtain information about molecular geometry. In particular, it was thought that the energy at which a shape resonance occurred could be correlated with the length of molecular bonds.

An attempt was made 15 years ago to quantify the relationship between shape-resonance energy and bond length for a number of molecules, including acetylene. However, shape resonances were manifested as broad, somewhat ambiguous peaks in the photoelectron cross section, and the criteria for identifying shape resonances in general were unclear. Subsequent studies found only weak evidence for a shape resonance in acetylene. But now symmetry-resolved photoelectron spectroscopy measurements have finally provided the first convincing evidence for the existence of a shape resonance in acetylene.

The high brightness of undulator radiation and the high resolution afforded by Beamline 10.0.1 (old Beamline 9.0.1 was moved to sector 10 in mid-1998; data were obtained before and after the move) made it possible to see features of the photoelectron spectrum that were not readily apparent in previous work. As a result, it was possible to resolve the carbon 1s peak of acetylene into contributions from electrons of g (symmetric) and u (antisymmetric) character (Figure 3).
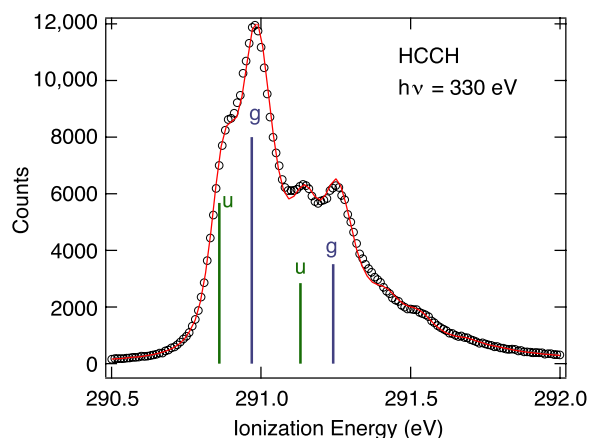
Figure 3

Symmetry-resolved photoelectron measurements show relative intensities of $1\sigma_u$ and $1\sigma_g$ ionization. The circles are experimental data, and the solid line is a fit to theory with the assumption that carbon–carbon stretching is the only vibrational mode contributing. The vertical bars indicate the position and intensity for ionization with vibrational quantum number $\nu = 0$ (left pair of bars) and $\nu = 1$ (right pair of bars).

According to dipole selection rules, transitions to the shape resonance can result only from ionization involving electrons of g character. Analysis of the symmetry-resolved data showed that the cross section for ionization of g-character electrons goes through a maximum at an incident photon energy of about 317 eV, coinciding with the location of the shape resonance indicated by previous investigations and slightly higher than that predicted by theory (Figure 4, top). These results also provide a test of calculations of the photoionization cross section near the photoionization threshold for both u and g ionization. It was found that the theory successfully reproduces the trend of the data, indicating that most of the basic physics has been included (Figure 4, bottom).

Although prospects for the original "molecular bond ruler" concept appear to be dim because of the difficulty involved in identifying shape resonances and because of the complexity of the correlation (if any), this result clearly demonstrates how the improvements in spectral resolution made possible by high-brightness synchrotron radiation can help resolve outstanding questions in the scientific literature and lead to better understanding of the inner workings of molecules.

Investigators

T.D. Thomas and J. Hahne (Oregon State University); N. Berrah (Western Michigan University); E. Kukk (Western Michigan University and Berkeley Lab); J. Bozek (Berkeley Lab); T.X. Carroll (Keuka College); and T. Karlsen and L.J. Såthre (University of Bergen, Norway).

Funding
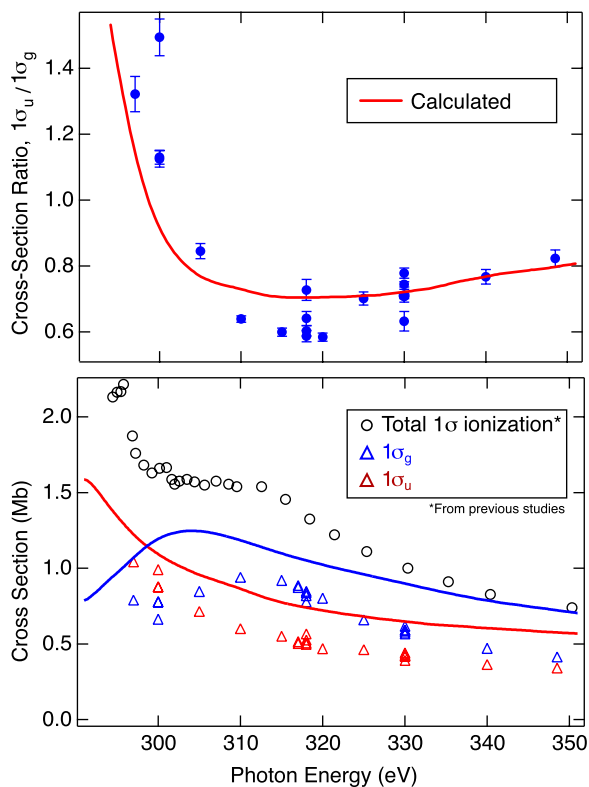
Figure 4

(top) $1\sigma_u/1\sigma_g$ as a function of photon energy goes through a minimum (i.e., $1\sigma_g$ is at a maximum) at about 317 eV, coinciding with the location of the shape resonance indicated by previous investigations and slightly higher than that predicted by theory. (bottom) Comparison of experimental (triangles) and calculated (solid lines) $1\sigma_g$ and $1\sigma_u$ cross sections shows that the theory successfully reproduces the trend of the data, indicating that most of the basic physics has been included. The circles represent the total single-electron cross section for ionization of HCCH.

Publication

1. T.D. Thomas et al., "Photon energy dependence of the $1\sigma_u/1\sigma_g$ intensity ratio in carbon 1s photoelectron spectroscopy of ethyne," *Phys. Rev. Lett.* **82**, 1120 (1999).

Bond-Length-Dependent Core-Hole Localization

One of the most powerful concepts in molecular physics is that of symmetry. For example, mirror symmetry means an object seen in a mirror cannot be distinguished from the actual object. A plain ball exhibits mirror symmetry, for example, whereas a person raising one hand does not because in the image it is the opposite hand that is raised. In molecules, the symmetry of interest is that of the orbitals that describe the electrons. Electronic transitions from one orbital in a molecule to another determine many properties of the molecule, but the symmetry of the orbitals restricts what transitions are allowed. In some cases, influences such as molecular vibrations can break (lower) the symmetry, thereby allowing otherwise "forbidden" molecular processes to occur. A Swedish team working at the ALS has shown that the distance between atoms in a molecule (the bond length) plays a key role in this kind of symmetry breaking in normally symmetric molecules.

Polyatomic symmetric molecules may have their symmetry broken when they are core excited. Symmetry breaking occurs because asymmetric vibrations can couple near-degenerate, core-excited states of different symmetry. In resonant soft x-ray emission spectroscopy (SXES), also known as resonant inelastic x-ray scattering (RIXS), this coupling and the accompanying core-hole localization lead to the appearance of "forbidden" transitions. In our experiments at the ALS, resonant SXE spectra from acetylene, ethylene, and ethane molecules show that the amount of symmetry breaking, and thus dynamic vibronic coupling, in a core-excited molecule is bond-length dependent.

Resonant SXES is based on a two-photon scattering process: an incoming x-ray photon excites a core electron, which results in a transition to an intermediate core-excited state. The intermediate state then decays by emission of an x-ray photon to a final valence-excited state or to the electronic ground state. The resonant SXE spectra were recorded at Beamline 7.0.1 with a grating spectrometer. Owing to the low fluorescence yield in this energy range and the low density of gas-phase targets as compared to

that of solid samples, the high brightness of the ALS and the good focus of Beamline 7.0.1 were necessary for carrying out these experiments.

Figures 5, 6, and 7 show absorption spectra and resonant and nonresonant SXE spectra for acetylene, ethylene, and ethane, respectively. For acetylene (Figure 5a) the excitation was to the unoccupied $1\pi_g$ orbital. If the parity selection rule were strictly valid,
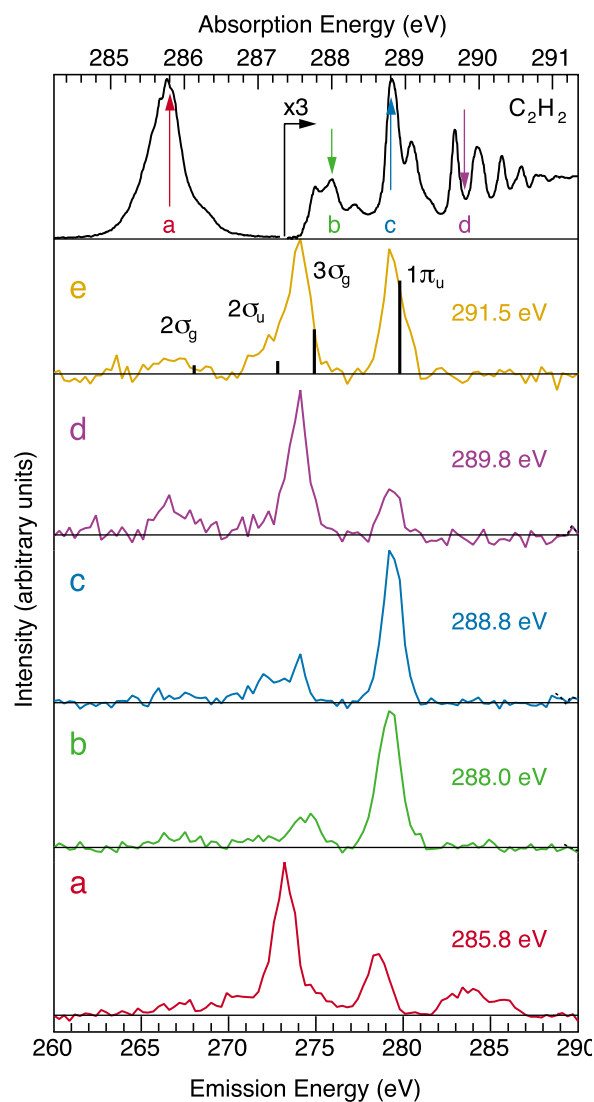
Figure 5

Absorption, resonant SXE, and nonresonant SXE spectra of C_2H_2. (top) Absorption spectrum from B. Kempgens et al., *Chem. Phys. Lett.* **277**, 436 (1997). Spectra (a–e) are emission spectra recorded at the excitation energies marked by arrows in the top panel. The transitions are labelled by the valence orbital from which the de-excitation takes place.
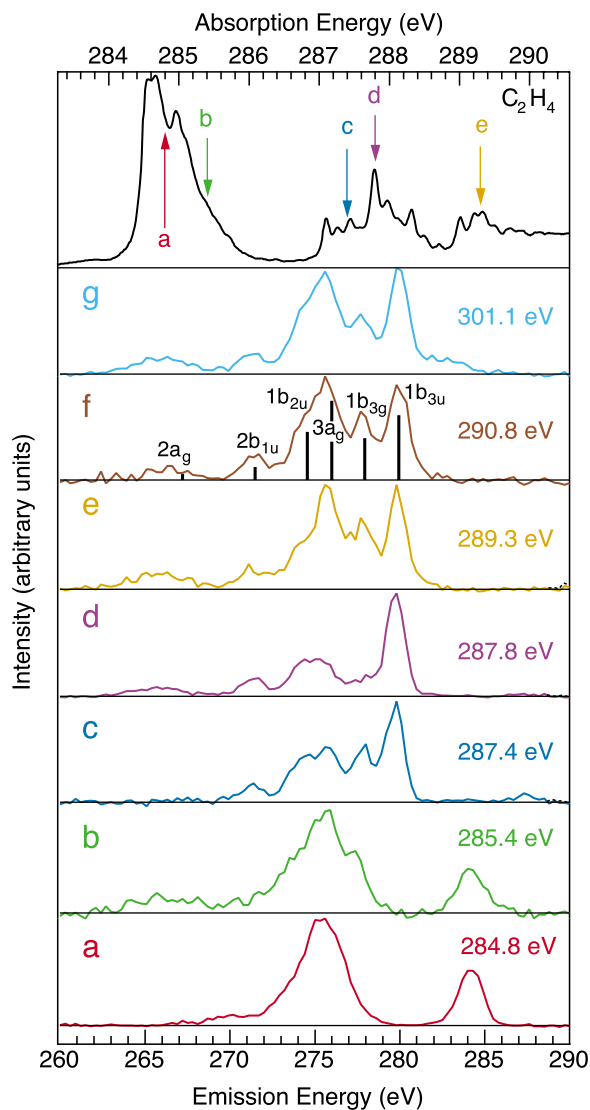
Figure 6

Absorption, resonant SXE, and nonresonant SXE spectra of C_2H_4. (top) Absorption spectrum from F.X. Gadea et al., *Phys. Rev. Lett.* **66**, 883 (1991). Spectra (a–g) as in Figure 5.

For ethane, on the other hand, Figure 7 shows that the relative intensities of gerade and ungerade (u) transitions in all spectra are practically the same as in the nonresonant case, so the selection rule is broken. Figure 7a is an exception, since the forbidden transitions are reduced. In this case, the excitation energy was detuned below the first absorption resonance. As we have shown previously, detuning leads to a quenching of the symmetry breaking. The spectra of ethylene in Figure 6 are more complicated
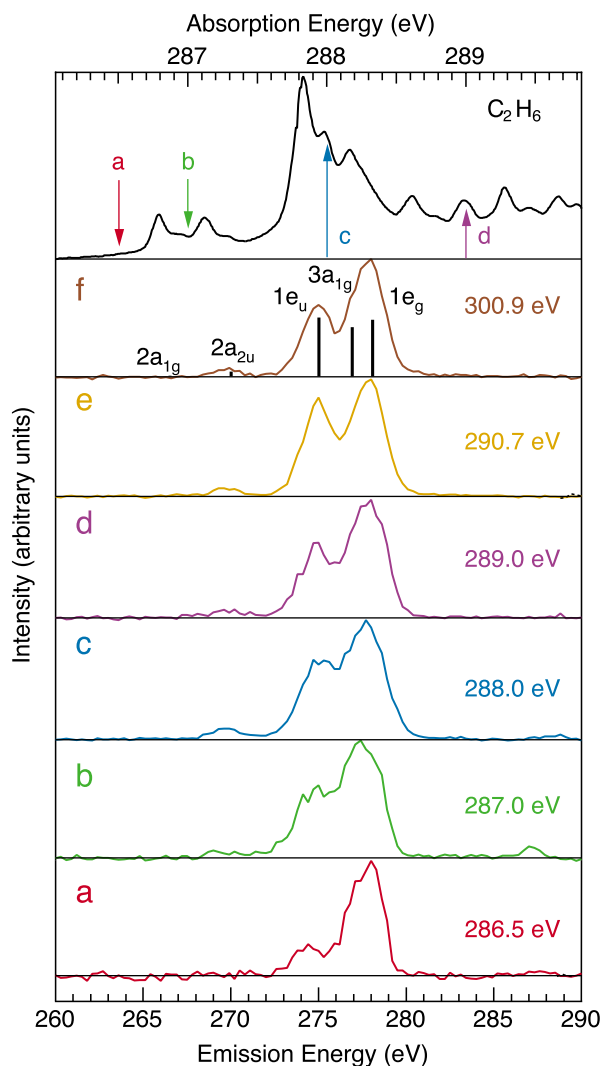
Figure 7

Absorption, resonant SXE, and nonresonant SXE spectra of C_2H_6. (top) Absorption spectrum from Y. Ma et al., *Phys. Rev. A* **44**, 1848 (1991). Spectra (a–f) as in Figure 5.

only de-excitations from gerade (g) valence orbitals would be seen. In the emission spectrum, however, both the allowed transition from the $3\sigma_g$ and the forbidden transition from the $1\pi_u$ orbitals are seen. However, the relative intensity of the forbidden transition is greatly reduced as compared to that in the nonresonant spectrum in Figure 5e, showing that the selection rule is still partially valid. The same is true for the spectra in Figures 5b–d.

than those of acetylene and ethane, representing an intermediate case between large symmetry conservation and large symmetry breaking.

In summary, the large suppression of the forbidden peaks in the resonant acetylene spectra, as compared to those in the nonresonant spectrum, indicates that symmetry is preserved to a large degree, whereas the ethane spectra show almost complete symmetry breaking. The different behavior is due to the different bond lengths. A shorter bond length means a larger energy splitting between the gerade and ungerade core orbitals, which in turn gives a smaller vibronic coupling and less symmetry breaking. The energy splittings for acetylene (shorter bond length) and ethane (longer bond length) differ by an order of magnitude, which is why the effect can be seen so clearly.

This is one example of how the symmetry selectivity of resonant SXES can be used to study the behavior of molecules during the x-ray scattering process. It can be used in a similar way to study the electronic structure and the dynamics of the scattering process in other situations.

Investigators

K. Gunnelin, P. Glans, J.-E. Rubensson, C. Såthe, and J. Nordgren (Uppsala University, Sweden); and Y. Li, F. Gel'mukhanov and H. Ågren (Linköping University, Sweden).

Funding

Publication

1. K. Gunnelin et al., "Bond length dependent core hole localization observed in simple hydrocarbons," *Phys. Rev. Lett.* **83**, 1315 (1999).

CHEMICAL DYNAMICS

Electronic Branching and Correlated Distributions in Molecular Photodissociation

One of the major research areas in the study of chemical reactions is the fragmentation of a molecule after the absorption of light. Known as photodissociation, this important type of reaction occurs widely and is, for example, a crucial step in many photochemical processes in the earth's atmosphere, including the destruction of ozone and the formation of urban smog. In the laboratory, experimenters typically use a laser to initiate the photodissociation and then measure the directions, velocities, and masses of the molecular fragments. Additional detail comes from identification of the orbitals occupied by the electrons in the fragments. At the ALS, chemists are using vacuum-ultraviolet (VUV) radiation as a new tool to ionize those fragments that have electrons in selected orbitals. The fragments can then be separated according to their mass with a mass spectrometer, thereby providing the most detailed look yet at the photodissociation process.

The study of multistate photodissociation is an important ongoing area of study in chemical dynamics. Two major types of experiments are in common use: those with state selectivity and those with universal detection. Numerous techniques allow the selective detection of specific electronic states of photofragments. These techniques permit the measurement of correlated-state distributions that can provide detailed information about the excited-state potential energy surfaces on which a dissociation process evolves. However, many of these methods sacrifice velocity resolution for state selectivity and are typically limited to probing only a subset of the final products. Foregoing state selectivity, traditional photofragment translational spectroscopy (PTS) experiments, based on electron-impact product ionization, provide high velocity resolution and permit the study of all possible reaction products. This

"universal detection" capability of electron-impact PTS is critical to investigations of complex reaction mechanisms and large polyatomic systems. The use of synchrotron radiation makes it possible to do both types of experiments. Ionization with tunable VUV radiation allows the experimentalist to choose between either state-selective detection, based on individual electronic states or internal energy, or universal detection.

The photodissociation of CS_2 provides the first demonstration of state-selective detection using VUV ionization at Beamline 9.0.2. Upon laser excitation at 193 nm, CS_2 dissociates via two different channels, resulting in CS and either $S(^3P)$ or $S(^1D)$ products. As CS_2 is a benchmark molecule, its photodissociation has been studied previously by many groups, and the $S(^3P)/S(^1D)$ branching ratio and the correlated-state distributions have been the subject of debate and conflicting reports. In PTS with synchrotron photoionization, we have discriminated against the $S(^3P)$ products, allowing the state-selective detection of the $S(^1D)$ products. Figure 1 shows two time-of-flight (TOF) spectra for m/z 32 (S^+) as a function of the photoionization energy. With 13.0-eV photons, both electronic states of sulfur are ionized. The resulting translational energy distribution, shown in the upper panel of Figure 2, is similar to previously determined distributions from electron-impact studies. At 10.1 eV, only the $S(^1D)$ electronic state can be ionized, allowing the direct determination of the vibrationally resolved translational energy distribution of the $CS + S(^1D)$ channel. The lower panel of Figure 2 shows the measured translational energy distribution for this channel. The spatial anisotropy of the angular distribution for each product channel was also determined. The measured anisotropies suggest that the two channels have similar origins and that the electronic branching may be decided at a point further along the dissociation coordinate. By simulating the vibrational distribution, we find that the partitioning of the vibrational energy peaks at $v = 3$ in coincidence with $S(^1D)$ fragments.
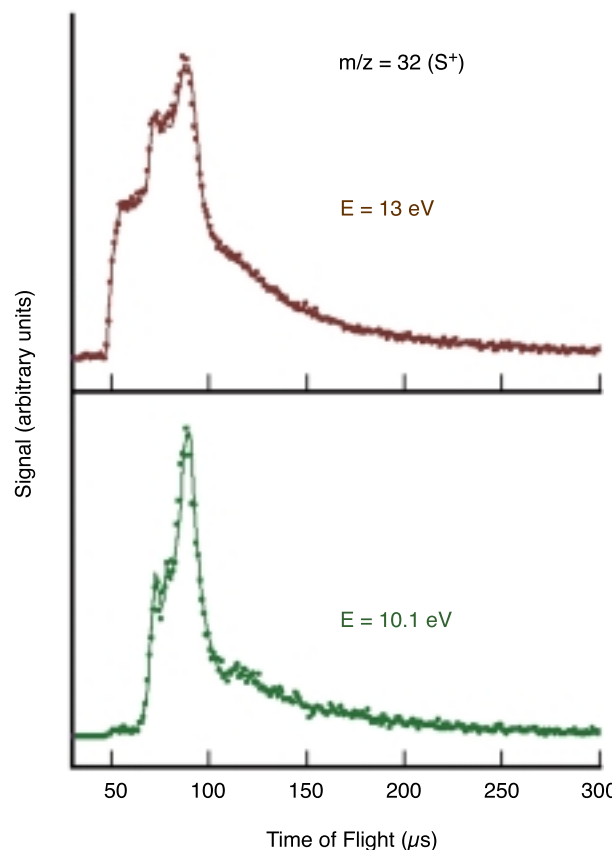
Figure 1

Time-of-flight spectra for m/z 32 (S$^+$) at ionization energies of 13.0 eV (upper) and 10.1 eV (lower). The circles represent the experimental data and the solid lines represent the forward convolution fits derived from the translational energy distributions. At lower photoionization energies, the fastest components of the TOF spectrum have disappeared, corresponding to a disappearance of the CS + S(^{3}P) channel contribution.

Figure 2

Translational energy distributions. The total translational energy distribution is shown in the upper panel. The two arrows represent the thermodynamic maxima for the CS + S(^{3}P) and CS + S(^{1}D) channels. Vibrational combs are shown for the coincident CS photoproduct. The lower panel shows the CS + S(^{1}D) translational energy distribution derived from the 10.1-eV TOF spectrum.

The ability to directly measure single electronic states by using PTS can provide a detailed view of complicated multistate photodissociation processes and should allow the photochemistry of atmospherically relevant molecules to be studied in significant detail.

Investigators

W.S. McGivern and S.W. North (Texas A&M University); and O. Sorkhabi, A. Rizvi, and A.G. Suits (Berkeley Lab).

Funding

Publication

1. W. S. McGivern et al., "Photofragment translational spectroscopy with state-selective 'Universal Detection': The ultraviolet photodissociation of CS$_2$," *J. Chem. Phys.* **112**, 5301 (2000).

Rotationally Resolved Studies of Highly Vibrationally Excited $O_2^+(X^2\Pi_{1/2,3/2g})$, $NO^+(X^1\Sigma^+)$, and $CO^+(X^2\Sigma^+)$

The chemistry of our planet's ionosphere, which begins about 50 miles above the Earth's surface, is dominated by reactions and other processes involving electrically charged molecules (ions) produced from neutral molecules by absorption of vacuum-ultraviolet light from the sun, a process called photoionization. The ionosphere not only plays an important role by reducing the flux of ultraviolet light reaching us on the ground, but is an active place chemically. Atmospheric auroras in the polar regions are highly visible results of chemical processes in the ionosphere. To examine what goes on in the ionosphere in detail, chemists need to measure the production of molecular ions with different energies, in the form of vibrations and rotations, resulting from photoionization of atmospheric gases. At the ALS, experimenters have developed a new spectroscopic technique and applied it to atmospheric gases, such as oxygen, nitrous oxide, and carbon monoxide, achieving unparalleled spectral resolution in the process.

Photoelectron spectroscopy is a major technique for research in the physical sciences. The development of the laser-based pulsed-field-ionization–photoelectron (PFI-PE) technique has revolutionized the field of photoelectron spectroscopy, demonstrating a resolution close to that of the laser itself. Nevertheless, the full potential of this technique has not been realized because of the limited photon-energy range accessible by lasers. To achieve a real impact with this technique in chemistry requires a high-resolution, broadly tunable vacuum-ultraviolet (VUV) source.

In the past few years, we have established an experimental station at the chemical dynamics beamline (Beamline 9.0.2.2) that provides such a high-resolution VUV source. This unique facility consists of a 6.65-m Eagle-mounted monochromator and a specially designed photoelectron–photoion apparatus. The monochromator has demonstrated a resolving power of 100,000 in the range from 6 to 30 eV and is currently the highest resolution scanning VUV monochromator in the world. This resolving power is close to that achieved with VUV laser systems. However,

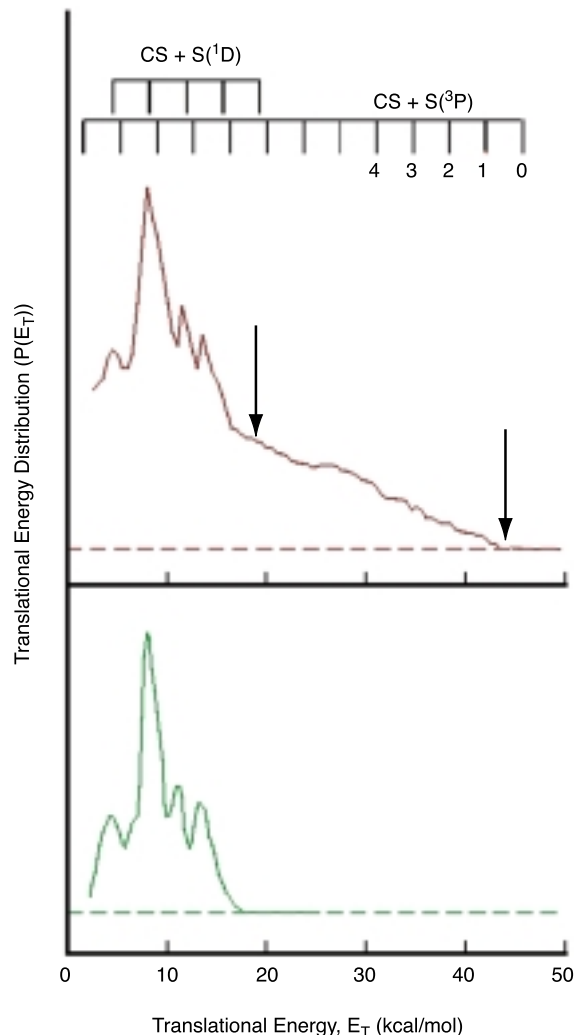the (pulsed) laser-based PFI-PE technique has traditionally required a delay of about 1 to 3 μs to allow time for the dispersion of prompt background electrons. Thus, this approach is not directly applicable to PFI-PE measurements using synchrotron radiation, where the pulses are more closely spaced. We have developed novel synchrotron-based PFI-PE schemes overcoming the delay requirement and have attained resolutions of 1 to 5 cm^{-1} (FWHM), which are similar to that attained in laser-based PFI-PE studies.

With these newly developed synchrotron-based PFI-PE schemes, we have measured the photoelectron spectra for O_2, NO, and CO. These are important atmospheric gases; the photoionization of these molecules by solar VUV is a main source of atmospheric ions in the planetary ionosphere. A major decay pathway of these ions involves dissociative recombination with electrons. The emission of excited neutral atoms resulting from the latter process is known to be responsible for atmospheric auroras. For this reason, information about the production of O_2^+, NO^+, and CO^+ in specific rotational–vibrational (rovibronic) states by VUV photoionization of O_2, NO, and CO is relevant to detailed modeling of the chemistry in the ionosphere. The high sensitivity and high resolution of the photoelectron–photoion apparatus have made possible the measurement of rotationally resolved vibrational photoelectron bands for $O_2^+(X^2\Pi_{1/2,3/2g}$, $v^+=0$–38), $NO^+(X^1\Sigma^+$, $v^+=0$–32), and $CO^+(X^2\Sigma^+$, $v^+=0$–42). As examples, we show in Figures 3 and 4 the rotationally resolved PFI-PE bands for $O_2^+(X^2\Pi_{1/2,3/2g}$, $v^+=0$–38) and $NO^+(X^1\Sigma^+$, $v^+=0$–32), respectively. These spectra reveal that significant intensities of $O_2^+(X^2\Pi_{1/2,3/2g})$ and $NO^+(X^1\Sigma^+)$ ions are produced in highly excited v^+ states beyond the low v^+ ($\leq$6) states expected from the Franck–Condon photoionization of O_2 and NO. Thus, the involvement of these highly vibrationally excited ions in the ion chemistry of the ionosphere should be taken into account in the modeling of ionospheric processes.

We note that the high-resolution capability is important in resolving overlapping photoelectron bands at high vibrational levels. As an example, we show in Figure 5 the mixed PFI-PE band for $CO^+(X^2\Sigma^+$, $v^+=31)$ and $CO^+(A^2\Pi_{1/2,3/2}$, $v^+=28)$. The rotational structures resolved have allowed the unambiguous identification of individual bands by
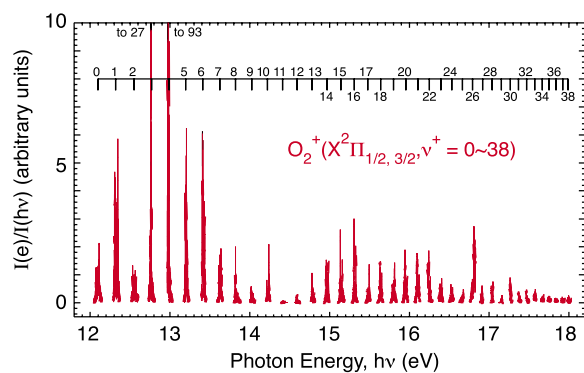
Figure 3

PFI-PE bands for $O_2^+(X^2\Pi_{3/2,1/2g}, v^+=0-38)$ in the energy range of 11.8–18.2 eV. The positions of these bands are marked. Note that the full scale for the PFI-PE intensity $[I(e)/I(h\nu)]$ is 10, but the maximum intensities of the $v^+=3$ and 4 are 27 and 93, respectively.

Figure 4

PFI-PE spectrum of NO in the range of 9.2–16.8 eV, showing the relative band intensities for the $NO^+(X^1\Sigma^+, v^+=0-32)$ states. The positions for the v^+ states are marked.

simulation. Panels (a) and (b) compare the experimental PFI-PE spectra (solid circles) with simulated spectra for $CO^+(X^2\Sigma^+, v^+=31)$ and for $CO^+(A^2\Pi_{1/2,3/2}, v^+=28)$, respectively. Panel (c) compares the experimental PFI-PE spectrum with the sum of the deconvoluted spectra for $CO^+(X^2\Sigma^+, v^+=31)$ and $CO^+(A^2\Pi_{1/2,3/2}, v^+=28)$.

Investigators

Y. Song, M. Evans, and C.Y. Ng (Ames Laboratory and Iowa State University); and C.-W. Hsu and G. Jarvis (Berkeley Lab).

Funding

Publications

1. Y. Song et al, "Pulsed field ionization photoelectron spectroscopy: Rotationally resolved photoelectron bands for $O_2^+(X^2\Pi_{3/2,1/2}, v^+=0-38)$," *J. Chem. Phys.* **111**, 1905 (1999).
2. G.K. Jarvis et al., "Rotational-resolved pulsed field ionization photoelectron study of $NO^+(X^1\Sigma^+, v^+ = 0-32)$ in the energy range of 9.24–16.80 eV," *J. Chem. Phys.* **111**, 3058 (1999).
3. M. Evans and C.Y. Ng, "Rotationally resolved pulsed field ionization photoelectron bands for $CO^+(X, v^+=0-42)$," *J. Chem. Phys.* **111**, 8879 (1999).

Figure 5

The mixed PFI-PE band for $CO^+(X^2\Sigma^+, v^+=31)$ and $CO^+(A^2\Pi_{1/2,3/2}, v^+=28)$. Panels (a) and (b) compare the experimental PFI-PE spectra (solid circles) and simulated spectra for $CO^+(X^2\Sigma^+, v^+=31)$ and for $CO^+(A^2\Pi_{1/2,3/2}, v^+=28$, respectively. Panel (c) compares the experimental PFI-PE spectrum with the sum of the deconvoluted spectra for $CO^+(X^2\Sigma^+, v^+=31)$ and $CO^+(A^2\Pi_{1/2,3/2}, v^+=28)$.

Fragmentation Reactions of Rydberg Molecules: Evidence of Inverse Born–Oppenheimer Processes

Molecular fragmentation is a chemical reaction that is important both for industry and for the science of the upper atmosphere and the vast space between the stars. In brief, absorption of short-wavelength ultraviolet (vacuum ultraviolet) light by the molecule increases its internal energy and also causes it to split into fragments. The chemical path of the molecule in this reaction depends on the details of the distribution of energy between the electron orbitals and molecular vibrations and rotations. A new way to study the energy distribution in molecules excited with vacuum ultraviolet light is to ionize the excited molecule and measure the intensity of electrons with just enough energy to be emitted as the ultraviolet wavelength changes. At the ALS, researchers have taken this method a step further and applied it to molecular fragmentation by measuring the intensity and the energy of the ion fragment formed in coincidence with the emitted electron.

The chemical reactivity of ions is important for understanding industrial discharge processes, reactions in the ionosphere, and the chemistry of interstellar space. The thermochemistry of molecular ions has generally been known with an accuracy of about 10 meV, but for a better understanding of the above-mentioned processes, at least one order of magnitude better accuracy is required. Significant progress in molecular spectroscopy over the last decade has been brought about by the development of the spectroscopy of electrons with zero kinetic energy (ZEKE spectroscopy), a technique that allows one to determine ionization potentials with resolution better than 0.1 meV or better, but the application of ZEKE spectroscopy has generally been limited to stable ground states of ions.

We have recently achieved a breakthrough in chemical dynamics by extending the ZEKE technique to the fragmentation thresholds of several molecules. With the goal of increasing the resolution of molecular ion spectroscopy, we have developed the pulsed-field-

ionization photoelectron–photoion coincidence technique (PFI-PEPICO). By combining PFI-PEPICO with the high spectral resolution of the 6.65-m Eagle-mounted monochromator in the chemical dynamics beamline (Beamline 9.0.2.2), we are able to study ionic reactions with sub-meV resolution.

In our experiments, neutral molecules are excited into high-lying Rydberg states by monochromatic synchrotron radiation. All prompt ionization events are discarded. After a certain delay time, the remaining neutral Rydberg molecules are pulsed-field ionized. Selecting only PFI electrons means that the internal state of the corresponding ions is precisely known and that the fragmentation reactions of the ions can be investigated in a mass spectrometer.

One of the first reactions studied with this technique was the predissociation of oxygen via the $b^4\Sigma_g^-$ state. Figure 6b shows the rotationally resolved PFI photoelectron (PFI-PE) spectrum of the $b^4\Sigma_g^-$ (v^+=4, N^+) state with peaks assigned to the O, Q, and S branches. Figure 6a shows the branching ratio of parent (O_2^+) and fragment (O^+) ion intensities, as determined in the PFI-PEPICO experiment. The simulated spectra (shown as lines) clearly prove that all oxygen ions with rotational angular momentum $N^+ \geq 9$ predissociate.

As an example of PFI-PEPICO applied to a polyatomic molecule, the formation of methyl cations (CH_3^+) from methane was investigated. Typical PFI-PEPICO ion time-of-flight (TOF) spectra of methane are shown in Figure 7. Evidently the warm (red) and the cold (green) parts of the sample have different dissociation characteristics. The variation of the ratio of green to red areas for the excitation energies shown, together with extensive analysis by simulation, gives unambiguous evidence that the formation of CH_3^+ from methane takes place by means of an inverse Born–Oppenheimer process, i.e., the Rydberg electron is only a spectator for the fragmentation of the molecular core (see equation). The same mechanism applies for O_2 and C_2H_2.

$$CH_4 + h\nu \longrightarrow CH_4^* \xrightarrow{\text{fragmentation}}$$

$$CH_3^* + H \xrightarrow{\Delta t,\ \text{field ionization}} CH_3^+ + e^- + H$$
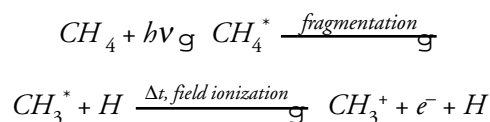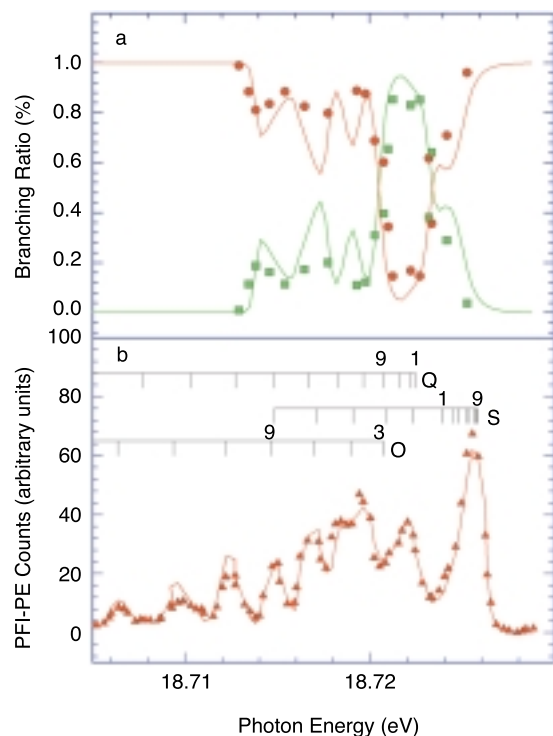
Figure 6

(a) Breakdown diagram for the formation of $O^+(^4S) + O(^3P)$ from O_2. The solid circles represent the branching ratios of O^+ and the solid squares are those for O_2^+. (b) PFI-PE spectrum (solid triangles) for $O_2^+(b^4\Sigma_g^-, v^+ = 4)$. The $\Delta N = -2, 0,$ and $+2$ (O, Q, and S, respectively) rotational branches are marked. The numbers given in (b) are N'' values. For further details of the simulations, see G.K. Jarvis et al., *Rev. Sci. Instrum.* **70**, 3892 (1999).

Figure 7

PFI-PEPICO TOF spectra of CH_4 at hν=13.9225, 14.3044, 14.3162, 14.3201, and 14.3240 eV. The TOF peaks centered at 14.10 and 14.35 μs are due to CH_3^+ and CH_4^+, respectively. The cold and the warm parts of the sample are marked in green and red, respectively.

The PFI-PEPICO experiment leads to thermochemical data with a precision of 1 meV or better. For example, the appearance energy of CH_3^+ from methane was determined to be 14.323 ± 0.001 eV. The data also yield important information on the dynamics of Rydberg-excited molecules that is difficult to obtain by any other technique.

Investigators

K.-M. Weitzel, M. Malow (Freie Universität Berlin, Germany); G. Jarvis (Berkeley Lab); T. Baer (University of North Carolina, Chapel Hill); and Y. Song and C.Y. Ng (Iowa State University).

Funding

Publications

1. G.K. Jarvis et al., "High Resolution Pulsed Field Ionization Photoelectron–Photoion Coincidence Spectroscopy Using Synchrotron Radiation," *Rev. Sci. Instrum.* **70**, 3892 (1999).
2. K.-M. Weitzel et al., "High-Resolution Pulsed Field Ionization Photoelectron–Photoion Coincidence Study of CH_4: Accurate 0 K Dissociation Threshold of CH_3^+," *J. Chem. Phys.* **111**, 8267 (1999).
3. G.K. Jarvis et al., "High-Resolution Pulsed Field Ionization Photoelectron–Photoion Coincidence Study of C_2H_2: Accurate 0 K Dissociation Threshold for C_2H^+," *Phys. Chem. Chem. Phys.* **1**, 5259 (1999).

Facility Report

Ben Feinberg
Division Deputy for Operations

A successful scientific program at a synchrotron light source depends directly on the reliability of operations the facility provides. High-quality beams delivered according to a published schedule, along with an efficient, effective safety program are required for researchers to make optimum use of their limited beamtime. In 1999, the ALS maintained its exemplary operations record while improving beam quality and increasing both the number of user hours and the number of beamlines. In addition, members of the Operations Group designed, constructed, and installed a set of third-harmonic cavities to increase the lifetime of the beam without sacrificing brightness (see "Accelerator Physics," p. 68).

Efficiency and Reliability

The research community at the ALS has become accustomed to high operational efficiency and reliability, and it was not disappointed during this period. As shown in Figure 1, the ALS delivered beam to the users more than 95% of the time scheduled for user operations in FY99, maintaining the efficiency of the last several years.

As commissioning of the third-harmonic cavities began, operations were briefly disrupted by a series of beam drop-outs that were caused by interactions between the newly installed third-harmonic cavities
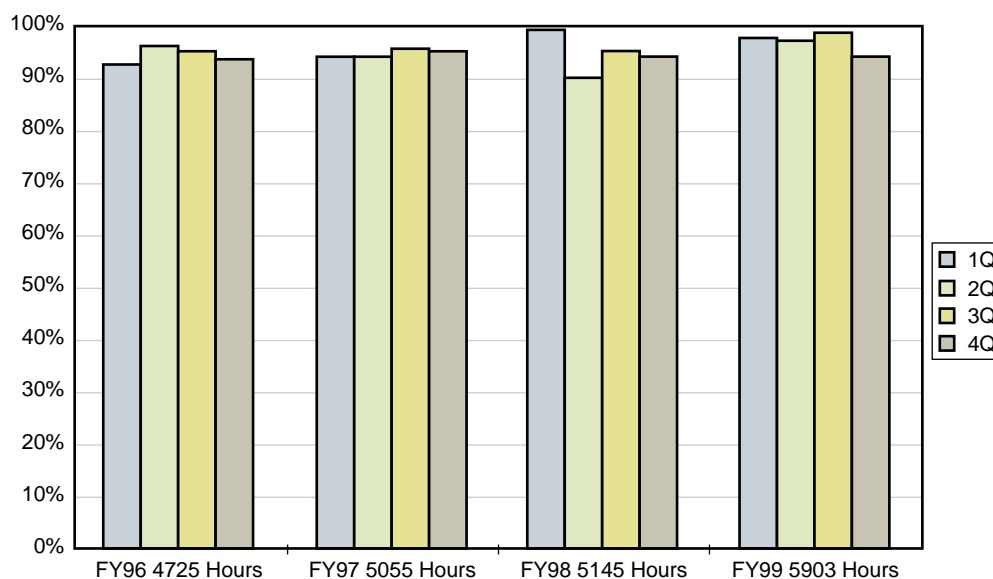
Figure 1

ALS operational efficiency (percentage of scheduled user beam time actually delivered).

Before   After

Time(h)
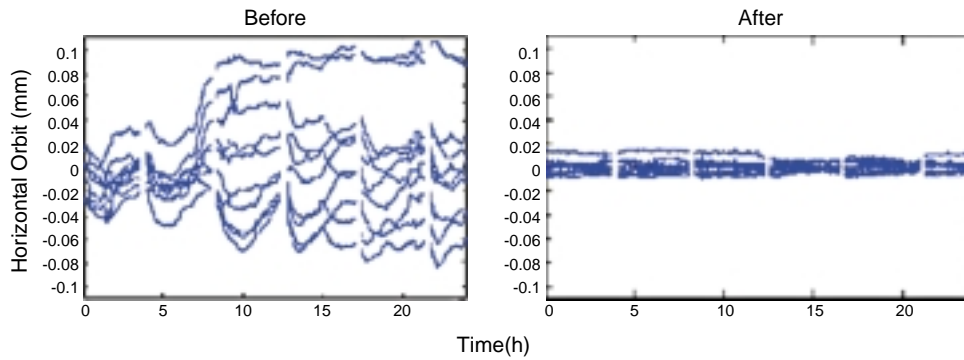
Figure 2

Comparison of orbit stability in the horizontal plane before and after slow orbit feedback operation.

and the feedback systems. While these drop-outs had a negligible effect on overall beam reliability (Figure 1), they did interrupt data taking during this period by shortening the average duration of the stored beam. The cause of these drop-outs has been corrected, and the cavities are now providing a 50% increase in beam lifetime, enabling a six-hour period between fills.

During this period, the beam orbit stability was greatly improved by the introduction of slow orbit feedback in both the horizontal and vertical planes. Figure 2 shows an example of the improved stability in the horizontal plane. The fill-to-fill reproducibility has been greatly increased with the beam stable to 10 μm in the horizontal plane and 5 μm in the vertical plane.

Growth in User and Instrument Hours

We were able to increase the number of scheduled operating hours significantly from 5,145 in FY98 to 5,903 hours in FY99. We continued to use the operating schedule established in 1997 that increased available user hours by reducing maintenance periods and limiting installation shutdowns to a single three-week period. In addition, we finished the year with a total of 21 beamlines operating simultaneously, up from 18 at the end of the previous fiscal year. The increases in the number of user hours and operating beamlines resulted in the delivery of 112,325 instrument hours (user hours multiplied by

the number of simultaneous beamlines that can accept beam), an increase of 47% over FY98.

Many events have contributed to the increasing number of delivered user hours and instrument hours shown in Figure 3. The completion of the initial complement of ALS beamlines was responsible for the large increase in instrument hours in FY95, while expanded operations due to funding of the Scientific Facilities Initiative (SFI) in FY 96 increased both user and instrument hours. The SFI also enabled us to build new beamlines, and the installation of these beamlines resulted in the increase in instrument hours in FY98. In FY99 we continued this large growth by increasing both the number of user hours and the number of beamlines.
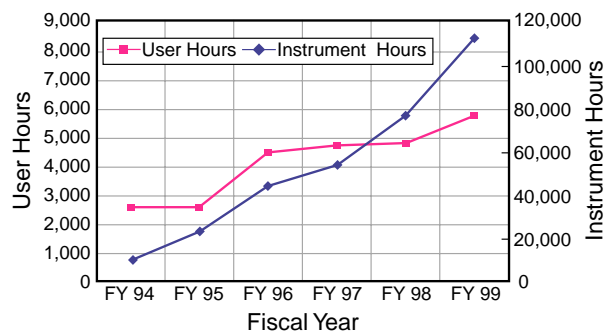
Figure 3

Number of delivered user hours and instrument hours from FY94 through FY99.

Facility Growth

One shutdown was scheduled during 1999 for the installation of new equipment. In June, five third-harmonic cavities were installed in the storage ring (Figure 4). The installation of the cavities was in response to user requests to lengthen the beam lifetime so that the time between fills could be increased from the standard four hours. The cavities are designed to extend beam lifetime by lengthening the orbiting electron bunches and reducing charge density. The cavities are now in the process of being commissioned.

In addition to the installation of the third-harmonic cavities, a number of beamlines began operations this year. These newly commissioned beamlines include the elliptically polarizing undulator (EPU) Beamline 4.0.1-2, installed last year, and two beamlines (12.0.1.2 and 11.3.2) designed and operated by the Center for X-Ray Optics (CXRO) for the industry/national laboratory consortium that is developing extreme ultraviolet (EUV) lithography.
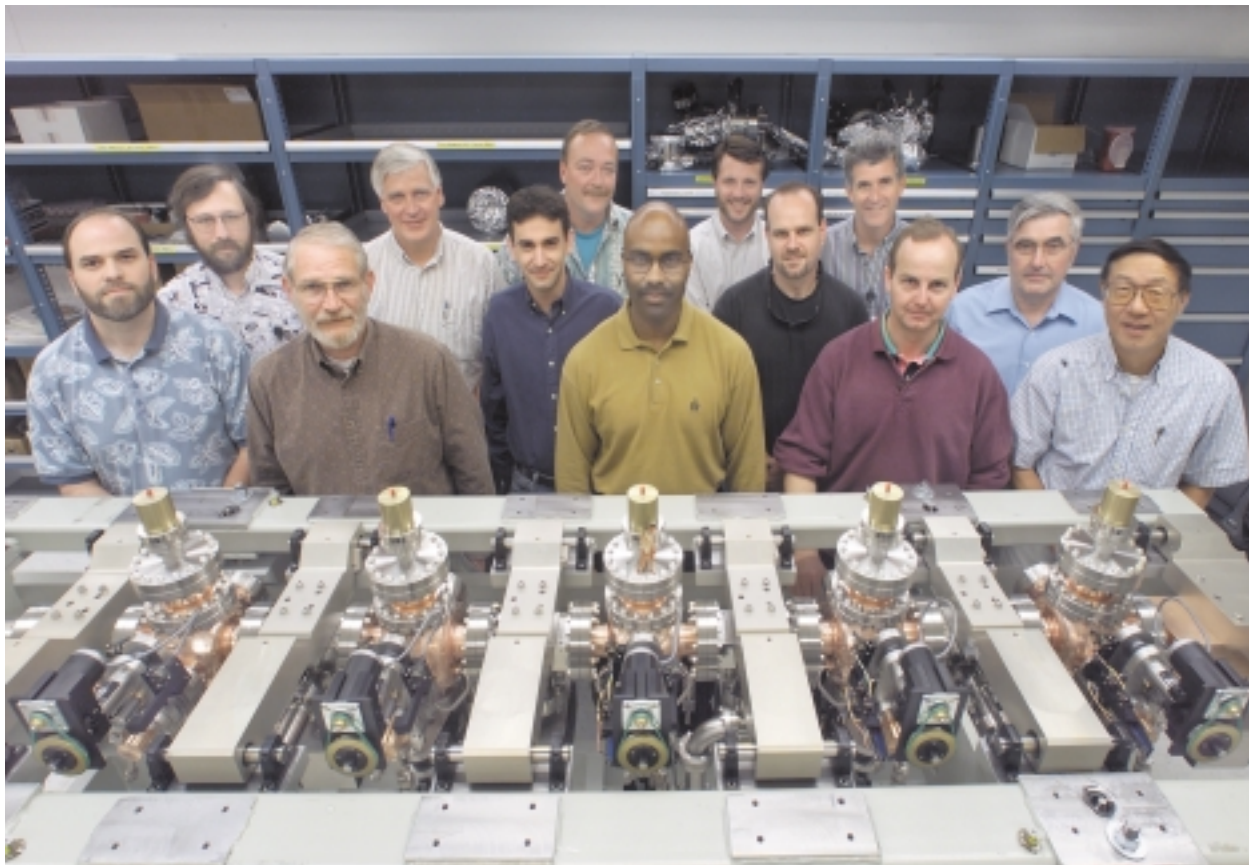
Figure 4

The third-harmonic cavities ready for installation into the ring, pictured with the project team.

ACCELERATOR PHYSICS

David Robin
Accelerator Physics Group Leader

As the ALS user community grows and becomes more diverse, the demands on the accelerator also grow. For instance, there are simultaneous demands for longer lifetimes, better beam stability, variable-polarization sources, more high-brightness, high-energy x-ray sources, high-brightness femtosecond x-ray pulses, etc. The challenge for the accelerator physics group is to meet and anticipate the demands of the community without compromising accelerator operation.

One of the main responsibilities of the accelerator physics group is to help ensure that the ALS continues to provide high-brightness synchrotron radiation to users in a stable and reliable manner. To this end, a large fraction of the weekly accelerator physics group meetings are devoted to examining archive data taken during the week prior to each meeting. Among the quantities examined are run times, lifetimes, beam sizes, and orbit motion. This allows us to assess the quality of the beam delivered to users and to identify and address problems early. In addition, we measure the distortion in the betatron functions on a weekly basis and adjust magnets to correct the distortion before it becomes large enough to affect operation.

This past year, we made significant advances in our understanding of the machine. Previously, the energy of the beam was inferred through magnet measurements. This is an indirect measurement and somewhat imprecise. This year, the electron-beam energy was measured much more precisely by resonant depolarization of the beam. The beam energy was measured to better than 1 part in 10,000. By using this method, the fill-to-fill reproducibility was measured and the energy found to be very stable.

In addition, a significant gain in our understanding of the single-particle dynamics in the ALS was revealed through the technique of frequency map analysis. Using a single-turn kicker (pinger) magnet and a turn-by-turn beam-position monitor, one could, for the first time, experimentally observe a web of excited betatron resonances. This tool provides a global vision of the dynamics and allows us to understand and tune the machine to improve its performance (both injection and lifetime).

We are continually trying to improve the performance of the accelerator. Over the years, there has been a constant demand for longer lifetimes in the ALS. To satisfy this demand without sacrificing the beam's brightness, a third-harmonic radiofrequency (rf) system was installed in the ring in June. Since then, much of the accelerator physics shift time has been devoted to commissioning the third-harmonic cavities and related systems. In some ways, the third-harmonic system has made operation of the ALS more complicated. Nevertheless, as of January 2000, the third-harmonic system has produced nearly a 50% increase in lifetime and allowed the multi-bunch run length to increase from four to six hours. We hope that further understanding and improvements will allow for even longer lifetimes and run lengths.

In addition to beam lifetime, advances were made in stabilizing the beam orbit with the introduction of a slow (0.1-Hz) vertical global orbit feedback system. This system works together with a previously existing horizontal orbit feedback system to prevent orbit drift of more than 5 μm during a run.

In 1999, work continued on the elliptically polarizing undulator (EPU), a device that can provide variably polarized light to users. Much of the effort was devoted to increasing the speed at which the device can shift between left and right circular polarization. The time to shift polarization has been reduced from 25 seconds to 8 seconds. (In the near future, we hope that the time can be reduced to 2 seconds, which is the limit of the motors.) Also, a new mode of operation of the EPU was successfully tested, where the

jaws of the device can move in such a manner as to provide arbitrary-angle linear polarization.

For the generation of high-brightness, high-energy radiation, a plan is in place to install three 5-Tesla superconducting dipoles (superbends) in the machine in 2001. Early in 1999, experiments were performed to test several key components of the cryosystem design. By the end of 1999, the design of the magnet and cryosystem was completed, and the contract for the first magnet/cryostat assembly was placed. Accelerator physics experiments have been ongoing to help ensure a smooth commissioning period.

Numerical tracking studies have shown that it is possible to modify the magnetic lattice of the ALS to include a narrow-gap insertion device in Straight 6 for the generation of femtosecond x rays. Such a source will be several orders of magnitude higher in flux than the present dipole sources and is a promising next step for the generation of femtosecond x rays.

Better Understanding of the Accelerator

Precision ALS Beam Energy Measurement Using Resonant Depolarization

The energy of the ALS electron beam can be calculated fairly accurately from a model of the integrated dipole fields around the storage ring. For several applications, however, it is useful to know the beam energy to much higher accuracy. Because the precession frequency of the electron spin around the vertical dipole fields depends only on the beam energy, it is possible to accurately find the beam energy by measuring the spin frequency. This is done in several other accelerators, particularly in high-energy colliders such as the Large Electron Positron (LEP) collider, by resonantly depolarizing a polarized beam. This requires measurement of the beam polarization and normally involves a fair amount of equipment, setup, and time.

Fortunately, for low- to medium-energy light sources like the ALS, it is possible to indirectly measure changes in the polarization and, from them, determine the beam energy. First, there is a process in the emission of synchrotron radiation called the Sokolov–Ternov effect that naturally polarizes any

lepton beam in the absence of depolarizing resonances. (For the ALS at a beam energy of 1.9 GeV, the polarization time is about 35 minutes.) Second, the ALS beam lifetime is dominated by large-angle intrabeam (Touschek) scattering. The cross-section for this scattering process is lower for electrons with parallel spins than for those with antiparallel spins. Therefore, a polarized beam will have fewer scattering events and a longer lifetime than an unpolarized beam. Thus we can use the beam lifetime, or equivalently a monitor of lost beam electrons, as a measure of changes in the polarization.

The resonant depolarization process is illustrated in Figure 1. A small horizontal magnetic field applied at step 4 shifts the polarization axis. If the magnetic field is varied resonantly with the spin precession, the axis of polarization will eventually flip. Because of the spread in spin frequencies within the beam due to the energy spread, this process results in a beam with no net polarization. We refer to this as a depolarized beam.
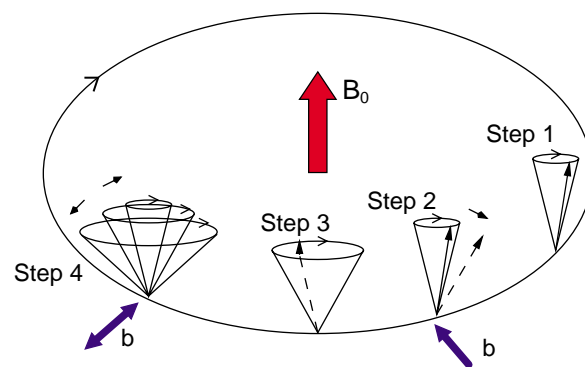
Figure 1

Depolarization of electrons in the storage ring. The magnetic field of the dipole magnets in the ring (B_0) is vertical. The individual spin vector of each electron precesses around the magnetic field and is represented by a circular arrow. If all electrons had the same spin (100% polarization) and were perfectly aligned with B_0, the precession cone would be infinitely narrow. To depolarize the beam, we start with an electron spin that has a small deviation from the vertical orientation in step 1. A small horizontal magnetic field (b) is applied at step 2, widening the precession cone (step 3). If the horizontal magnetic field is varied such that it is in phase with the spin precession (step 4), the precession cone for each electron will widen further and further. Since the electrons all have slightly different spin precession frequencies, they will ultimately run out of phase, yielding a beam with no net polarization.

In the ALS, we depolarize the beam by applying a time-varying horizontal magnetic field with a vertical stripline kicker normally used for exciting vertical betatron oscillations. We drive the kicker with a continuously swept excitation from a spectrum analyzer tracking generator (via an amplifier). We measure the beam lifetime from the rate of change of a DCCT current monitor or we use a beam loss monitor to measure relative changes in loss rate. The beam loss monitor consists of a scintillating material connected to a photomultiplier and is located outside the vacuum chamber just downstream of a small-gap insertion device. The counts are integrated over one second. The small-gap chamber is the minimum vertical aperture in the ring and the primary location where electrons are lost.

An example of the variation of lifetime with polarization is shown in Figure 2. Over the course of a 25-minute period, the beam was excited at the spin frequency. The time of depolarization is evident in both the lifetime and the count rate. As the lifetime decreases slightly, the count rate increases. Because of the higher sensitivity of the beam loss monitor and the faster time response, we used it as the primary monitor for changes in the lifetime.

Shown in Figure 3 is the normalized count rate from the beam loss monitors as the excitation is swept through the spin resonance at upper and lower sideband frequencies. In the limit of the Touschek-dominated lifetime, the normalized loss rate should be a constant, barring polarization effects.

One of the useful applications of the energy measurement is the precise determination of the lattice momentum compaction factor, α, given by

$$\frac{\Delta E}{E} = -\frac{1}{\alpha}\frac{\Delta f_{rf}}{f_{rf}}$$

where E is the beam energy and f_{rf} is the rf frequency. The momentum compaction factor is notoriously difficult to measure other than with a direct beam energy measurement. Shown in Figure 4 is a measurement of the relative change in beam energy (from the nominal energy) for several relative changes in rf frequency. The momentum compaction factor can be determined from the slope.

Figure 2

Beam lifetimes derived from the current monitor and count rates from the beam loss detector showing two partial spin depolarizations over a 25-minute period. The high sensitivity of the beam loss detector makes it better suited for detecting changes in the beam lifetime.
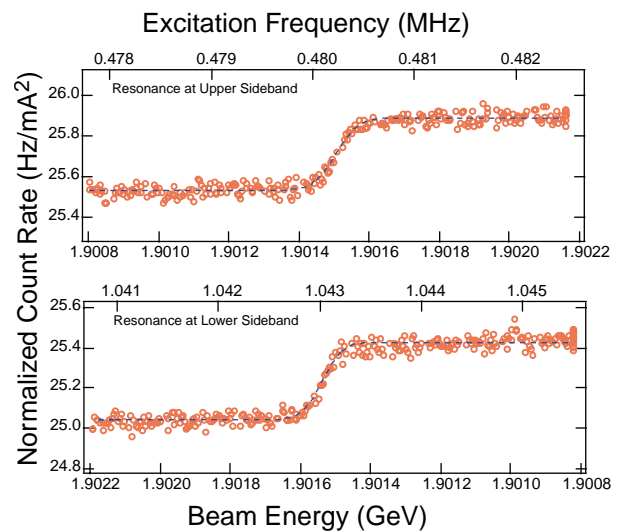
Figure 3

Normalized count rates from the beam loss detector as the excitation is swept through the spin frequency at an upper sideband and a lower sideband. The corresponding beam energy for each frequency is shown. The energy decreases while sweeping through the lower sideband.
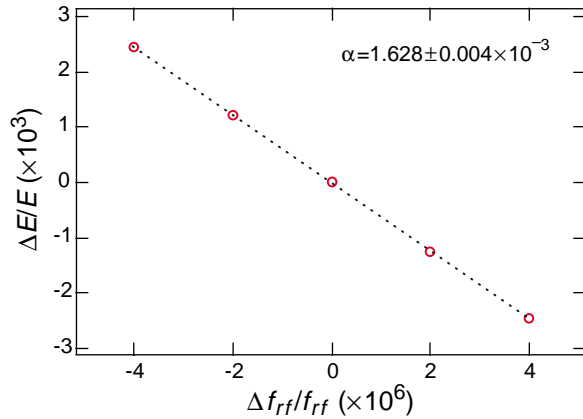
Figure 4

Measurement of the relative change in beam energy (from the nominal energy) for several relative changes in rf frequency. The slope is the momentum compaction factor.
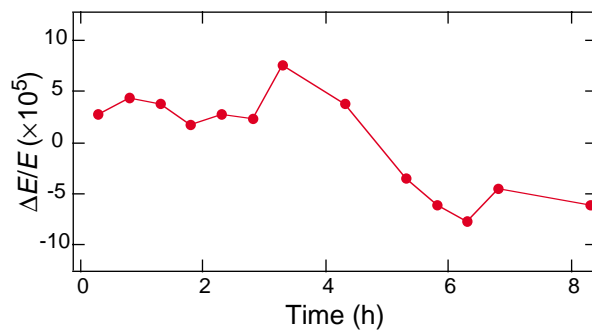
Figure 5

Stability of the storage-ring beam energy over an eight-hour period. Two beam injections and energy ramps occurred during this time.

Another application of interest is to measure the stability of the energy over time. Shown in Figure 5 is the relative beam energy variation measured every half hour over an eight-hour period during user operations. Because this process was automated, some measurements were invalid because they were made either during the injection process, during energy ramping, or during insertion device movement. During this particular measurement, two injections and energy ramps occurred.

This work was done with the help of Peter Kuske from BESSY II in Berlin.

Application of Frequency Map Analysis to the ALS

The performance (i.e., injection efficiency and beam lifetime) of a particle accelerator is limited by the stability of the particle motion. Therefore, to improve the performance, it is essential to understand the nonlinear particle dynamics. In order to obtain a good understanding of the dynamics, it is important to have a model that accurately describes the accelerator. One can obtain an accurate linear model of the accelerator by fitting measured orbit response matrix data (see Mini-Beta Lattice for Femtosecond X-Ray Source, below). One would like to know how well such a model, in combination with the nominal design sextupole settings, describes the nonlinear dynamics. Therefore, it is essential to have a method to measure dynamics in the accelerator and compare the measurements with the model predictions.

Frequency map analysis is a refined numerical method based on Fourier techniques that provides a clear representation of the global dynamics of a large class of multidimensional systems, and it is very effective for systems with three or more degrees of freedom. This method of analysis was developed by the French astronomer Jacques Laskar, and it has been applied to numerical simulations of physical systems (e.g., the solar system, galaxies, and particle accelerators). For several years, frequency map analysis has been applied to the ALS by using numerically generated data (from a model). In the last year, we have applied frequency map analysis to experimental ALS data.

Frequency maps generated from numerical data, for both the ALS with no errors and the ALS with calibrated linear errors, are shown in Figure 6. Diffusion rates (as defined by the change in betatron tune with time) are represented in color. The upper part shows the data in frequency (tune) space, revealing resonances and the tune footprints of particles at high amplitudes. The lower part shows the same data in configuration space. (An increase in horizontal displacement in the lower graph corresponds to a decrease in vertical tune on the upper graph. An increase in vertical displacement in the lower graph corresponds to a decrease in horizontal tune in the upper graph.) As seen in the figure, the dynamics of

IDEAL	**REAL**
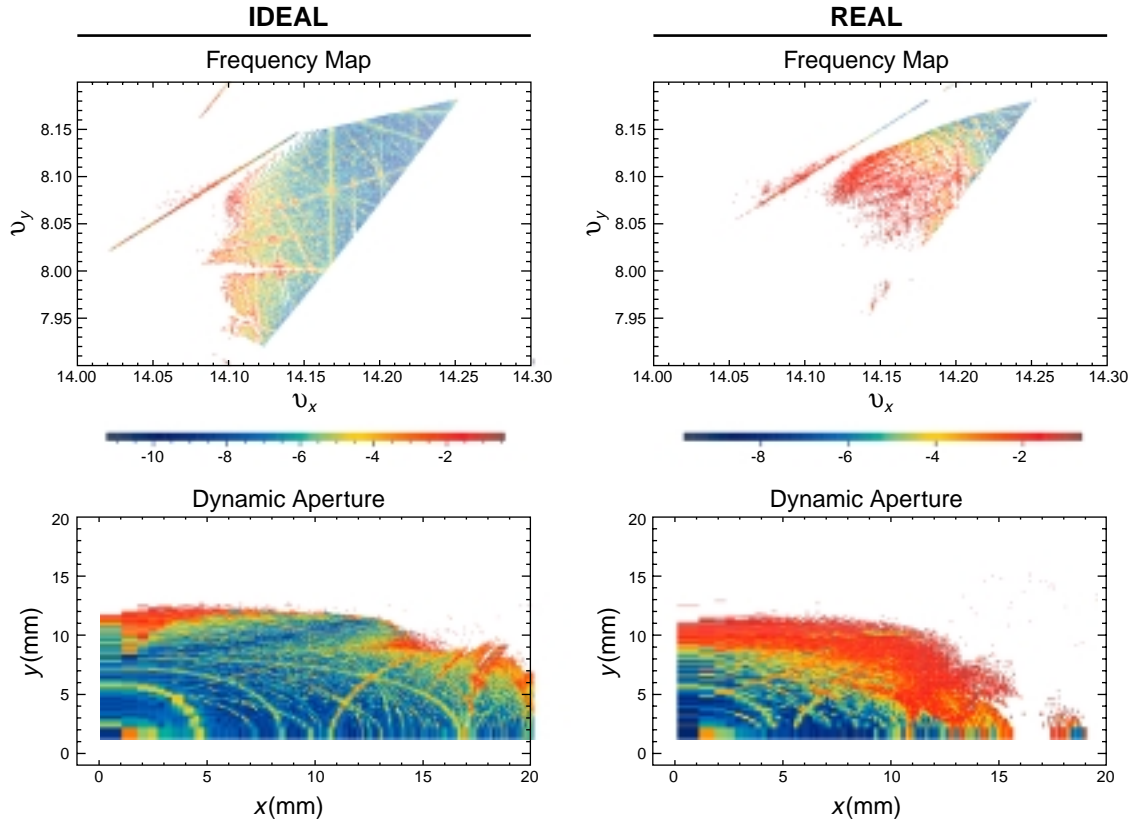
Figure 6

Frequency maps for the ideal lattice of the ALS (upper left) and for a lattice including measured gradient and coupling errors (upper right), from orbit response matrices. Blue areas represent electron trajectories with no diffusion (no change in betatron tune), and red areas represent particles with high rates of diffusion. The lower plots show the frequency map in configuration space (showing the transverse displacement of each electron from the closed orbit at the injection point).

the ideal accelerator and those of one with calibrated errors are significantly different. Not only does the dynamic aperture shrink with errors, but the regions of particle diffusion get closer to the origin and extend in size and further limit the dynamics.

The question that remains is how accurately our calibrated model describes the particle dynamics. This question can be answered by comparing the results of simulation (using the calibrated model) and measurement. The measurements at the ALS (Figure 7) clearly show the network of coupling resonances (uneven spacing in the frequency map). In

addition, comparison of the simulated and measured maps reveals that the machine is very sensitive to small field errors, which are responsible for the observed resonance excitation. Therefore, a model of the machine with no field errors ("ideal machine") is a poor model of the machine (compare Figure 6). On the other hand, a map generated by using a model that includes calibrated linear lattice errors is strikingly similar to the measured map (Figure 7).

This work was done in collaboration with Jacques Laskar and his student Laurent Nadolski from the Bureau des Longitudes in Paris.
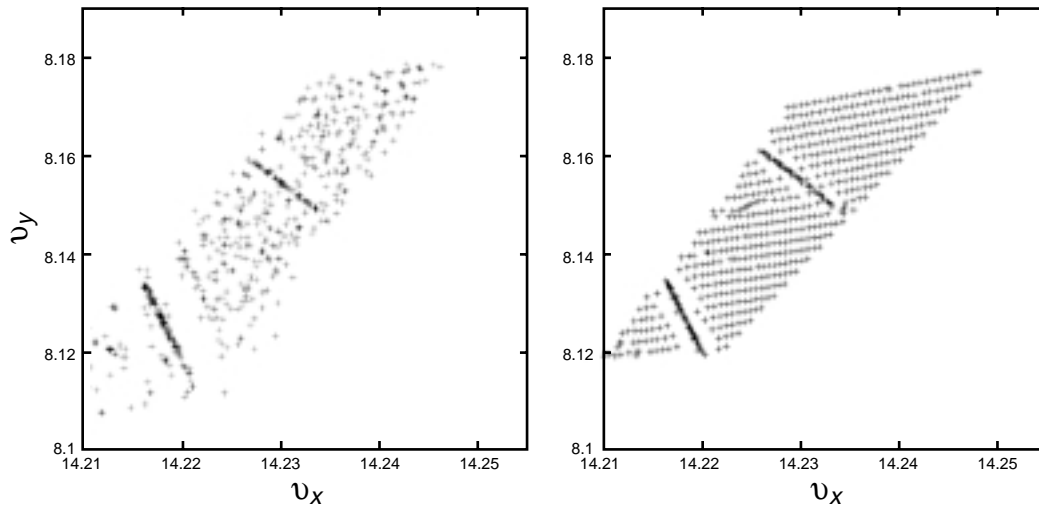
Figure 7

Comparison of a measured frequency map of the ALS (left) with a simulated one based on gradient and coupling errors measured from orbit response matrices (right).

Improvements in Machine Performance: Commissioning of the Third-Harmonic Cavities

The beam lifetime is one of the most important parameters to ALS users. The ALS beam lifetime is dominated by large-angle intrabeam (Touschek) scattering, which occurs when electrons within the bunch scatter and transfer enough momentum that they are knocked outside the momentum acceptance of the storage ring. For a given beam energy, we can improve the lifetime by either increasing the momentum acceptance of the ring or by reducing the charge density of the electron bunch.

One way to decrease the charge density without compromising the transverse beam brightness is to stretch the bunch longitudinally. This can be done by adding a higher-harmonic voltage to the main rf voltage such that the bunch is defocused at its center,

effectively increasing the bunch length. To introduce this voltage, we designed and constructed a prototype 1.5-GHz radiofrequency cavity in collaboration with Lawrence Livermore National Laboratory (Figure 8). The final cavities are intended to be operated initially in passive mode, where the cavity voltage is generated only by the beam. The cavity design includes an option to upgrade to an active mode, where the cavities are driven by an external generator.

In June 1999, we installed five harmonic rf cavities. In January 2000, we began running the harmonic cavities in operation, increasing the beam lifetime at 400 mA by about 50% and allowing user run times to increase to four to six hours between fills. During the commissioning process, we observed a number of interesting effects limiting the potential lifetime increase as well as affecting several other storage-ring systems. These are discussed below.
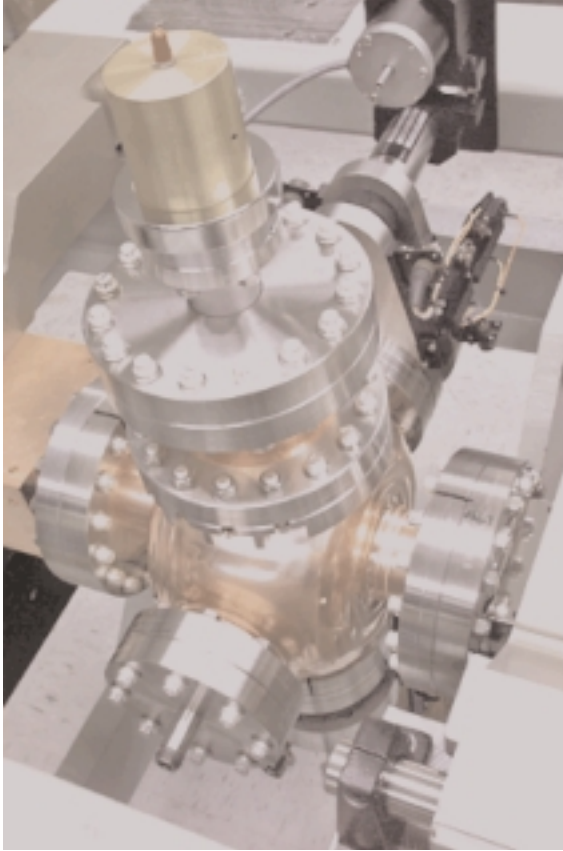
Figure 8

An ALS third-harmonic cavity. Beam ports are on the left and right. Tuners are located on the outer and bottom ports. The input port is located on the top.

Lifetime Improvements and Bunch Lengthening

During user operation with 272 (out of 328) bunches, we use two cavities in bunch-lengthening mode and reach lifetimes of about six hours at 400 mA with a 3% transverse emittance coupling. We are limited by transient beam loading effects, described below, which have strong influence on the multibunch feedback systems. During machine studies with a 320-bunch pattern, we have reached lifetimes of about nine hours. The limitation in this case is the optimization of the digital filter used in the longitudinal feedback system.

Because the harmonic voltage is generated only by the beam, rapid variations in the beam current can cause variations in the harmonic voltage. In the case of the ALS, a gap of 20-25% is left in the filling of

the ring in order to satisfy user requirements. This creates a transient loading of the harmonic cavities, resulting in a variable harmonic voltage along the bunch train. Although the variation in harmonic voltage is small, it can have a large effect on the beam because of the defocusing effect of the harmonic voltage. The net effect is a variation in both the synchronous phase along the bunch train and the relative amount of bunch lengthening.

The effect is apparent in streak-camera measurements of longitudinal bunch distribution, as shown in Figure 9 for the cases of 272 bunches and 320 bunches. The case of 272 bunches shows a variation of 100 picoseconds in the arrival time of the bunch from the head to the tail of the train, whereas the 320-bunch case shows a much smaller variation. Both the centroid position of the bunch and the bunch length as a function of position around the ring are shown for the two cases in Figure 10. The transient loading causes the bunch lengthening to vary along the bunch train, causing an overall reduction in the potential lifetime improvement.
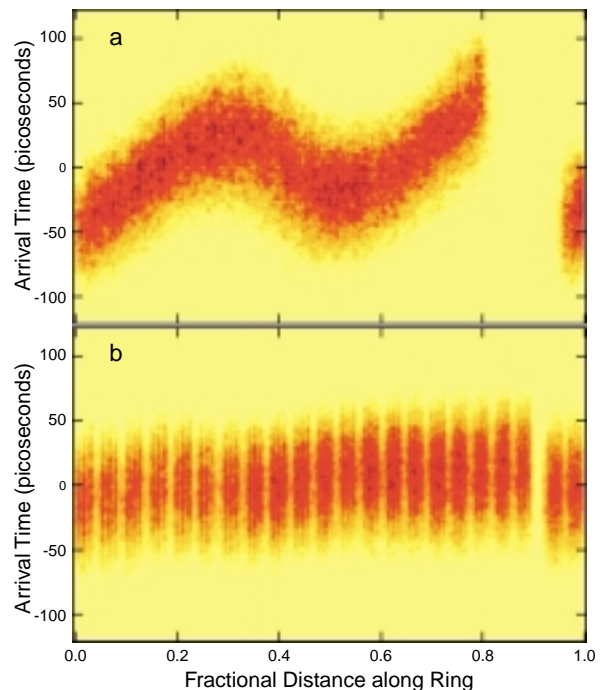
Figure 9

Streak camera images of the longitudinal bunch distribution along the length of (a) a bunch train of 272 bunches and (b) one of 320 bunches.
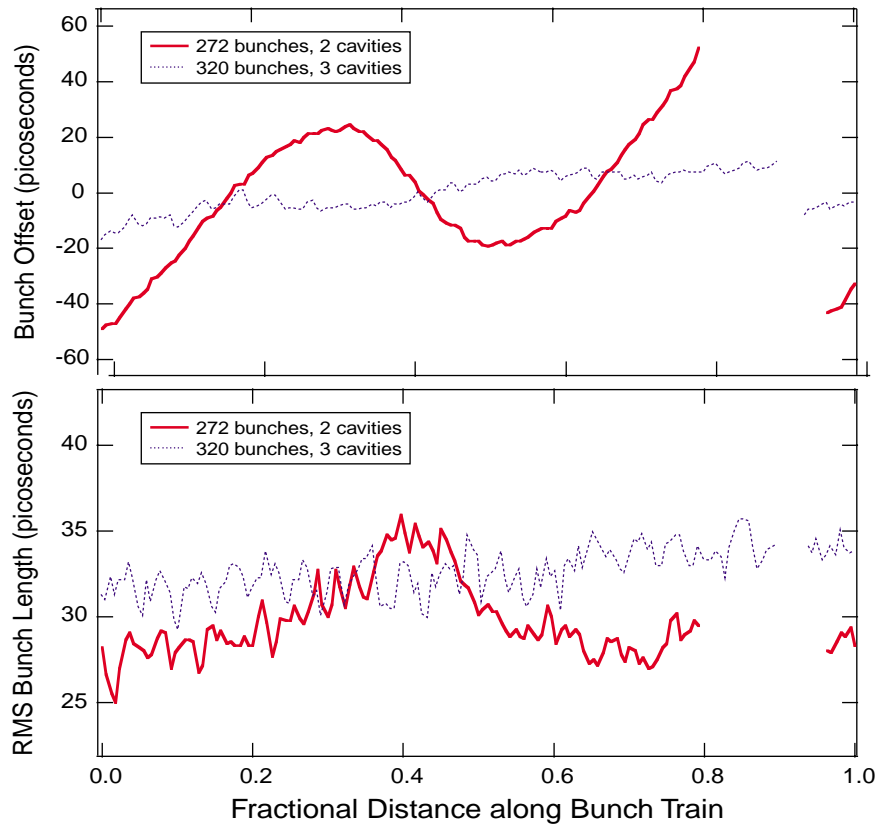
Figure 10

Longitudinal beam offset (top) and bunch length (bottom) along a bunch train of 272 bunches and one of 320 bunches. The variation in synchronous phase due to transient loading of the cavities is much larger in the case of 272 bunches. The transient loading also results in a variation of the bunch length along the train.

Effects on Multibunch Feedback Systems

In order to combat the effect of the gap-induced synchronous phase transient on the transverse system, a beam-synchronous, or "homodyne," demodulation technique was implemented to replace the existing heterodyne front-end demodulation system. The homodyne technique uses a bunch-by-bunch, beam-derived local oscillator that follows the phase transients. An automatic gain control loop stabilizes the amplitude of the reference throughout the fill.

The synchronous phase transients affect the front end of the longitudinal feedback system as well. Because the longitudinal system measures bunch phase at six times the rf frequency, the system can become unstable for bunches that experience transients of greater than ±15° at the rf frequency.

Currently, we are redesigning the longitudinal local oscillator to operate at three times the rf frequency so as to reduce the transient problems by a factor of two. In addition, a more accurate bunch-by-bunch synchronous phase correction technique for the longitudinal system is being designed as a long-term solution. This technology may have other applications for systems or experiments that require accurate bunch-specific timing. In addition, we have implemented a digital rf phase-control loop to keep the overall beam phase locked to the master oscillator.

HOM Damping

Our original intent in the cavity design was to damp the cavity higher-order modes (HOMs). With delays in the cavity schedule, however, we decided to

try and avoid the HOMs by using two tuners in each cavity. Following initial commissioning of the cavities, it became clear that this would be extremely difficult, especially given the high tuning sensitivity of the deflecting dipole HOMs. Fortunately, the cavity design included several extra ports through which we have been able to damp some of the HOMs.

Since we could not power test any of our damping schemes before installation in the storage ring, we took a conservative approach and did not insert any antennae into the cavity, since they could potentially overheat. Also, given the immediate need for some damping, we used the simple approach shown schematically in Figure 11. The input port was extended and terminated with in-vacuum ferrite. HOMs above the waveguide cutoff frequency of 2.5 GHz propagated up the input port and were damped in the ferrite while the fundamental mode at 1.5 GHz was unaffected. Shown in Figure 12 is the beam spectrum as measured from a cavity probe before and after installation of the HOM dampers.
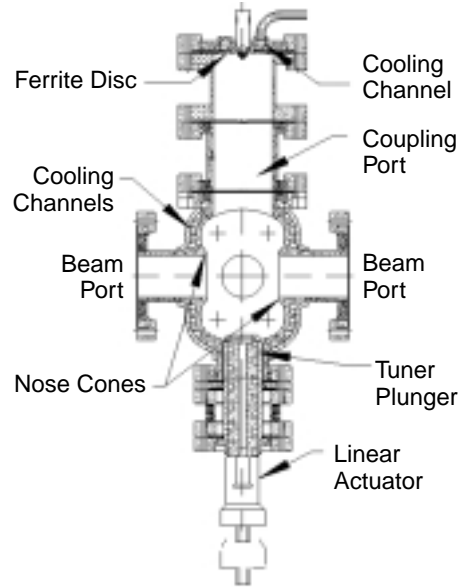
Figure 11

Schematic view of a harmonic cavity. Higher-order-mode damping was added by extending the coupling port and terminating the flange with microwave-absorbing ferrite.
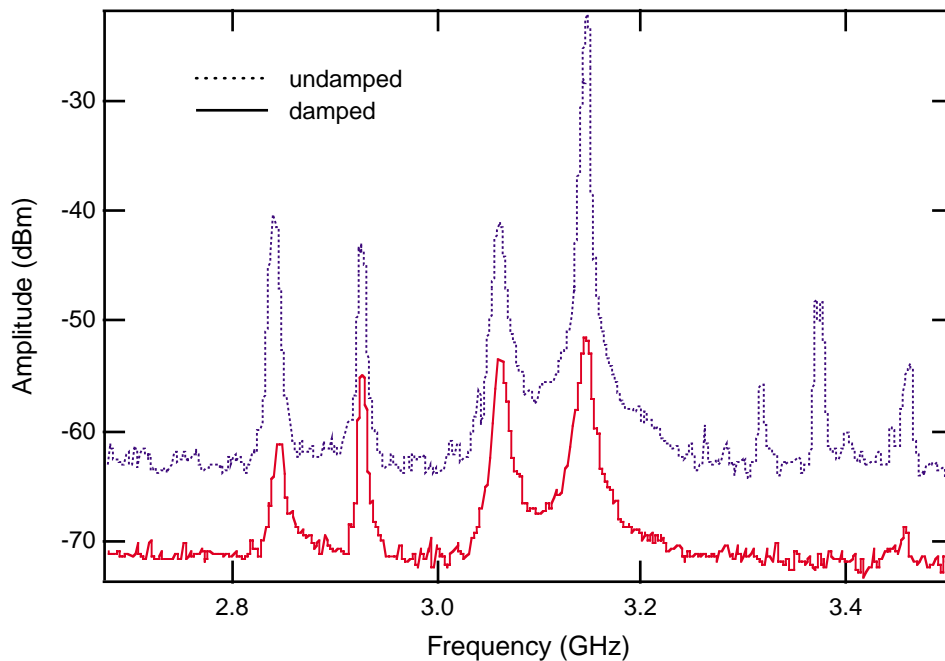
Figure 12

Beam spectra measured on one of the cavities before and after installation of the HOM damper. The vertical scale is logarithmic relative to milliwatts. Several of the HOMs are markedly damped.

Above the input port cutoff frequency, modes are markedly damped. While not all HOMs were damped, it became possible to tune the cavity fundamental mode and the HOMs. Following installation of dampers, the beam became much more vertically stable and more controllable by the vertical multi-bunch feedback system.

New Initiatives

Progress Update on the Superbend Project

The ALS is planning to install three five-Tesla superconducting magnets (superbends) in the storage ring in 2001. These magnets will be a bright source of higher-energy photons and will extend the capabilities of the ALS. Comparing the superbend sources to the normal-conducting dipoles (1.3 T) that are currently installed in the ring, the brightness and flux of the superbends will be an order of magnitude higher at 10 KeV and two orders of magnitude higher at 20 KeV.

In 1997, a prototype of the magnet core and coils (SB 4) was built and reached a design current without quenching. In 1998, a test cryostat was built, and static and dynamic magnetic fields were measured. Based on this work, it appears likely that a magnet can be built with a sufficiently robust operating margin.

One of the main accelerator physics tasks in 1999 was to determine the impact of the superbends on the performance of the accelerator. The impact was determined through particle-tracking studies. One of the issues in these studies was how precisely the superbend fields needed to be modeled. In many particle-tracking codes, one assumes a model of the magnet that has no longitudinal variation in field (an isomagnetic model). Tracking simulations performed in 1998 assumed an isomagnetic model for the superbends. The results showed no significant impact on the particle dynamics, but there was concern that the isomagnetic model was inadequate for tracking studies because the superbend field is far from isomagnetic. In 1999, we included a model of the superbend based upon a full three-dimensional field map of the magnet. Tracking studies were then done, and the results were not significantly different from the results obtained with the isomagnetic superbend model. Accelerator simulations were also done to study the effects of ramping and electron beam stability.

Also in 1999, a conceptual design for the superbend cryosystem was made. It was based upon two key features: a Gifford McMahon cryocooler and high-temperature superconducting (HTS) leads. The Gifford McMahon cryocooler was chosen because it is regarded as more reliable than cryocoolers with Joule–Thomson circuits. Compared to normal conducting leads, HTS leads have a very low heat leak, which is essential for operation with such a low-power cryocooler.

In FY99, a test cryosystem was built to test the performance of the cryocooler and the HTS leads. A 1.5-W Sumitomo cryocooler and a set of American Super Conductor (ASC) HTS leads were purchased. These were incorporated into a test cryostat that was constructed by Berkeley Lab in conjunction with Wang NMR. The system performed well in all aspects. The cryocooler was very easy to set up and operate, and it had sufficient capacity for cooling the superbend. Measured heat leaks from the leads were low and in agreement with the estimated heat leaks. The ASC leads (2223 with silver-alloy matrix) were found to be very stable and robust against temperature excursions. The results of these tests assure us that the design concept for the cryosystem is sound and that the system should perform reliably.

In addition to the cryocooler tests, a design package incorporating the new cryosystem features for the superbend magnet and cryosystem was completed. The design of the magnet can be seen in Figures 13 and 14.

This work was done in collaboration with the Berkeley Lab Accelerator and Fusion Research Division's Superconducting Magnet Program and Wang NMR.
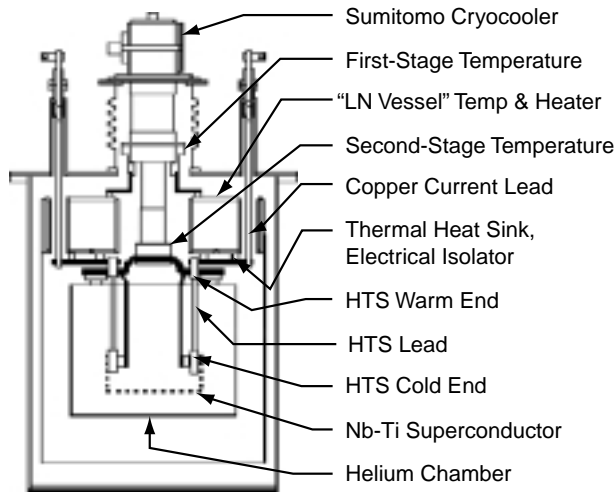
Figure 13

Diagram of the test cryostat for development of superconducting bend magnets.

Mini-Beta Lattice for a Femtosecond X-Ray Source

The inclusion of a narrow-gap insertion device in the ALS will result in a source of soft x rays that is several orders of magnitude brighter than the existing dipole and insertion-device sources. Having a brighter x-ray source is of particular interest for the generation of femtosecond x-ray pulses. Currently, femtosecond x rays are being generated from a dipole source, and the experiments are severely flux limited. To increase the brightness of the femtosecond x-ray source, the ALS is considering including a narrow-gap insertion device (with a five-millimeter full gap and a one-meter length) to be placed in Straight 6.

A 5-mm gap is almost a factor of 3 smaller than the current smallest magnetic gap (14 mm) and is nearly a factor of 2 smaller than the narrowest
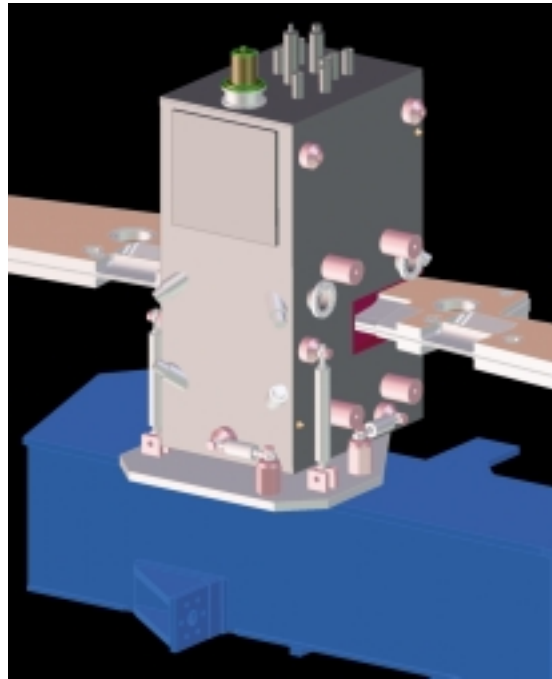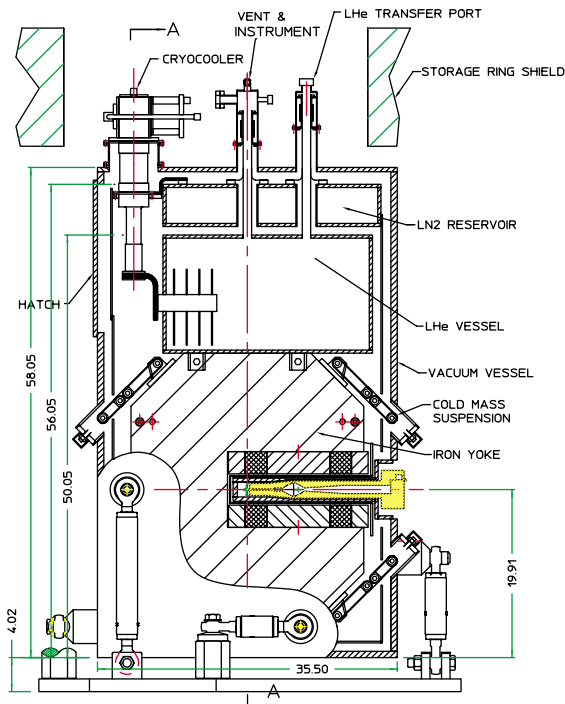
Figure 14

Two-dimensional (left) and three-dimensional (right) drawings of a superconducting bend magnet.

vacuum chamber (9 mm) that currently exists in the ring. Such a significant reduction in aperture could have a negative impact on the ring performance, particularly on injection and lifetime. It is therefore necessary to find a method of including such a narrow-gap device in the storage ring that will meet the needs of the femtosecond experiments without compromising the performance of the ALS. An investigation into the feasibility of the lattice modifications necessary to include a narrow-gap (5-mm full gap) insertion device in Sector 6 was therefore begun last year.

To optimize the performance of the undulator for the femtosecond experiments, the optics in the ring need to be modified to provide a small vertical beta function and a sizeable vertical dispersion (η) function at the location of the insertion device. The key requirements for this mini-beta lattice include

- β_y = 50 cm at the center of the straight section.
- η_y > 8.4 mm at the center of the straight section.
- a minimal impact on the single-particle beam dynamics (±10-mm horizontal dynamic aperture for injection).

A very simple mini-beta lattice was first designed by using two extra pairs of quadrupoles. However, particle tracking studies showed that the lattice modification caused a significant reduction in the dynamic aperture by breaking the twelve-fold symmetry of the ALS. To overcome this difficulty, we developed a novel technique to fully restore the beam dynamics while allowing a mini-beta lattice to be designed with a π phase advance in the vertical plane. This technique works for all storage rings employing only normal (not skew) multipoles, such as normal dipoles, quadrupoles, and sextupoles.

All normal multipoles contain only even-order powers of the vertical coordinate, y, in their vector potential. For example, the Lie map for a thin sextupole would be

$$\exp\left(:-b_2(x^3 - 3xy^2):\right)$$

Changing the sign of y does not affect the result. Therefore, the one-turn map for such rings is transparent to a local vertical phase advance of any odd-integer multiple of π if one keeps the local Twiss parameters matched.

With this technique, a mini-beta lattice with six quadrupoles has been designed with exactly the same dynamic aperture as the original ALS lattice (see Figures 15 and 16). To produce a sizeable vertical η function, essential for separating the femtosecond microbunch from the main bunch, we have developed two different methods. The first method generates an η bump by coupling the horizontal η in the arc to the vertical plane by using skew quadrupoles in the neighboring wiggler sector (Sector 5). The vertical η bump can be localized by using symmetric skew quadrupole bumps. As a result, the skew
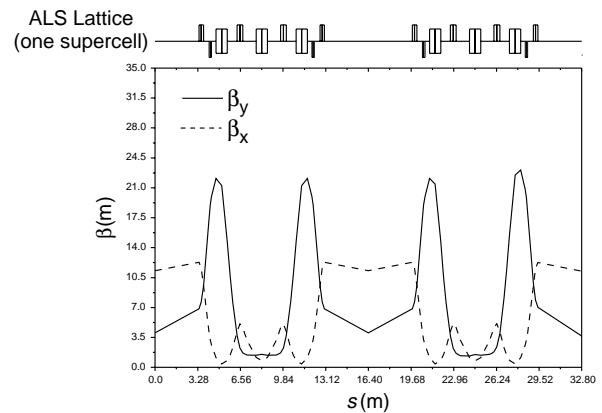
Figure 15

Lattice functions through two cells of the ALS lattice without the mini-beta straight.
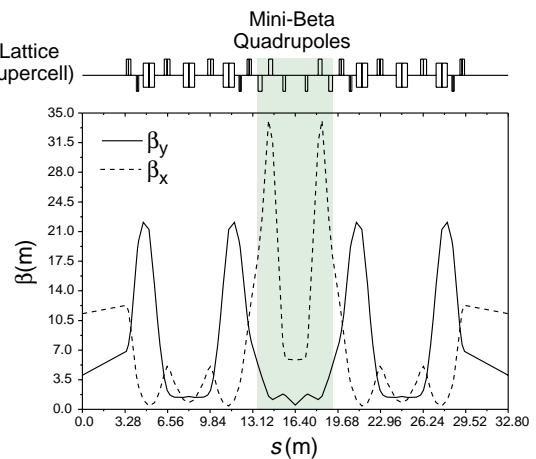
Figure 16

Lattice functions through two cells of the ALS lattice with the mini-beta straight.

quadrupoles change the global coupling, resulting in a sizeable vertical emittance. We have elected a 1% emittance coupling criteria for selecting the best combination of skew quadrupole bumps. Limited by their present maximum settings, an η_y of 16.8 mm can be generated in the wiggler sector, corresponding to an effective η_y of 5.6 mm in the mini-beta sector.

The second method generates the vertical η via a local vertical orbit bump around the mini-beta sector. Because strong quadrupoles are used in the mini-beta sector, the vertical local orbit bump has been found to be capable of generating an η_y of 3 mm in the mini-beta sector while keeping the vertical orbit distortion in the neighboring bends to less than 2 mm. Since the orbit bump is localized around Sector 6, it can be combined with the skew quadrupole bumps in Sector 5 to produce a larger-than-required

vertical beam separation at the center of the narrow-gap undulator. We are in the process of assembling a complete mini-beta lattice with the π phase advance trick and large vertical η bumps generated by both methods. To increase the separation even further would require either stronger skew quadrupoles or larger vertical orbit distortions or both.

Further work to be carried out for the mini-beta lattice includes designing mini-beta lattices with different operational tunes; conducting intensive dynamic-aperture studies, including energy-aperture calculations and the effects of the narrow-gap undulator, the superbends, and realistic magnetic errors; and studies of impedance and collective instabilities.

EXPERIMENTAL SYSTEMS

H. A. Padmore
Experimental Systems Group Leader

The range of work that the Experimental Systems Group covers is rather broad, so in this section we briefly report on the group's major programs and highlight four notable projects that have come to fruition during 1999. The work of the group covers construction of beamlines and endstations as well as pioneering new techniques of synchrotron radiation research that will have high scientific impact.

- Three protein crystallography beamlines now under construction, one for a University of California, Berkeley–University of California, San Francisco (UCB–UCSF) consortium and two for the Howard Hughes Medical Institute, will receive light from superconducting bend magnet sources. These will use high-power internally cooled invar premirrors, a double-plane-crystal monochromator with heavy internal water cooling for the first crystal, and a toroidal refocusing mirror operating at 2:1 horizontal demagnification. These systems will provide state-of-the-art performance, significantly superior to the current wiggler beamline used for protein crystallography. The first beamline, for UCB–UCSF, will be finished in late fall 2000.

- An aberration-corrected photoemission electron microscope, PEEM3, is under construction. The present PEEM2 system on Beamline 7.3.1.1 has achieved its design resolution of 20 nm, a record for systems of its type. To go beyond this resolution, however, the intrinsic spherical and chromatic aberrations of the electrostatic lenses need to be corrected, and in PEEM3 this correction will be carried out by an electron mirror. With aberration correction, the system should be capable of 2-nm resolution. The heart of the system will be a dipole separator magnet, which will separate the incoming and outgoing beams going to and from the electron mirror. The separator itself needs to be aberration free. The rest of the lens system will be similar to that for PEEM2. The whole system has already been designed, and major components are in manufacture. The new PEEM should be ready for off-line trials by summer 2001 and will then be installed on a branchline of the existing elliptically polarizing undulator (EPU) beamline. The plan is then to operate it there until a dedicated EPU is available. Funding for the latter is being sought from the U.S. Department of Energy.

- The molecular environmental science beamline is under construction and due for phase 1 completion in spring of 2002. It will be located in Sector 11 and will consist of an EPU, a plane-grating monochromator of the Petersen type, and two endstations. The 5-cm-period EPU and its beamline will cover the energy range from 70 to 1500 eV. In phase 2, a second, shorter-period undulator and smaller-grazing-incidence beamline will cover up to 4 keV. One endstation will be for scanning transmission x-ray microscopy (STXM), and the other will be for spectroscopy using both photoemission and energy-resolved x-ray fluorescence. The main characteristic of these stations will be the ability to look at samples in a wet environment. Photon-in–photon-out techniques such as fluorescence spectroscopy and STXM are well suited to this environment. In addition, the use of photoemission at high pressure is currently being pioneered at the ALS, and it is envisaged that experiments up to millibar pressures will be practical.

- We have investigated phase-contrast imaging at x-ray energies on Beamline 7.3.3. Whereas

absorption imaging at soft-x-ray energies is effective because of the high photoelectric cross-section, this becomes much less effective at keV-range energies because of the very low cross-sections of low-Z materials. In this range, however, phase contrast becomes a very good way to image. Phase information can be obtained in a number of ways. For example, it can be done by blocking part of the beam, shifting its phase with a thin foil, and then recombining the two waves to form an interference image. We have chosen in our first experiments to use dark-field imaging, where the direct beam transmitted through the object is completely blocked, and only the scattered beam is imaged. This enhances features where there is a large transverse change in the refractive index. We used the beamline's mirror system to illuminate the object and a high-resolution hard-x-ray zone plate to image at energies around 7 keV. The microscope produced a resolution of around 0.15 µm. The ultimate goal of this program is to extend this work to three-dimensional imaging, rotating the object about a fixed point in space. The initial applications have been in looking for cracks and defects in high-strength composite materials. Phase-contrast x-ray microscopy can play a prominent role in this area. Cracks are normally examined by sectioning, and apart from the difficulty of accurate sectioning, the sectioning process itself causes changes in stress state that propagate cracks. The noninvasive measurement of crack formation and propagation should have a large impact on materials science. Having carried out the test program on Beamline 7.3.3, we are helping to build a research team to construct a similar system on a superconducting bend-magnet source.

- The molecular environmental science beamline (Beamline 11.0), Beamline 7.0, and Beamline 5.3.2 all have or will have scanning transmission x-ray microscopes (STXMs). To extend the performance of the existing Beamline-7.0 STXM, and to build experience for the new systems on Beamlines 5.3.2 and 11.0, we are building a next-generation STXM in the laboratory. This will ultimately replace the Beamline-7.0 STXM when fully prototyped and tested. The new STXM has been constructed and is under intensive testing. Its main departure from existing STXMs is that the relative position of the zone plate to the sample stage is measured in real time by laser interferometers. This should allow accurate location of the focused beam, even during NEXAFS scans, where the zone plate can move up to hundreds of microns along the beamline but still must remain aligned laterally to a precision much better than the resolution. With increasingly high resolution zone plates from the Center for X-ray Optics Nanowriter, we have to keep improving the microscope to keep up with demands for increased performance.

- As mentioned above, one of the locations for a new STXM will be Beamline 5.3.2. This bend-magnet beamline is dedicated to polymer microscopy. The Participating Research Team is responsible for construction of the microscope system, which will be based on the STXM upgrade microscope described above. The ALS is responsible for the beamline. The prime requirement for this system is that it be stable and have as high an efficiency as possible. The extremely high brightness of ALS bend-magnet sources gives us the opportunity to use techniques such as STXM that are normally reserved for undulator sources, but it also means that high optical efficiency is crucial to good throughput. The system therefore has the minimum number of components. A horizontally deflecting toroidal premirror focuses light onto the entrance slit of a monochromator in the horizontal direction and onto the exit slit in the vertical direction. The monochromator is a simple spherical-grating device, and it disperses and deflects in the horizontal direction. The beam from the exit slit is refocused and demagnified by the zone-plate microscope, and the microscope and its operating infrastructure are to be enclosed in an acoustic hutch. This system will be operating in summer 2000.

Active Feedback on the Infrared Beamline

The infrared (IR) beamlines have proven to be the most sensitive to microscopic motions of the ALS beam, mainly because of the interferometric selection of wavelength. Even after a long series of beam noise abatement projects in collaboration with ALS accelerator physics and engineering staff[1–4], the IR photon beam still moves in angle with an rms magnitude of a few microradians. Because of the small (0.25-mm^2) size of the IR detectors and the nature of the FTIR data reduction, this motion places noise in the IR spectrum that manifests itself in two ways. The frequencies of the noise are reproduced in the spectrum as a function of the scanning mirror speed in the interferometer, and all frequencies of the noise contribute to an overall background noise. The higher-frequency noise, particularly in the 4- to 8-kHz region, has been largely eliminated by changing the storage ring's 500-MHz rf master oscillator to a unit that produces a narrower and more stable reference frequency. Despite large improvements to the low-frequency noise in our spectra, which came from the vibrations of pumps and other sources on the ALS floor, there remains some noise on the photon beam in the region below 500 Hz that is detrimental to the overall signal quality. Having attempted to remove as much noise as possible at the source, to reduce noise further, we have now introduced an active optical feedback system into the beamline. Preliminary results obtained by using a single two-axis feedback loop are described here.

The complete feedback system is shown in Figure 1. The system, based on one used at Lawrence
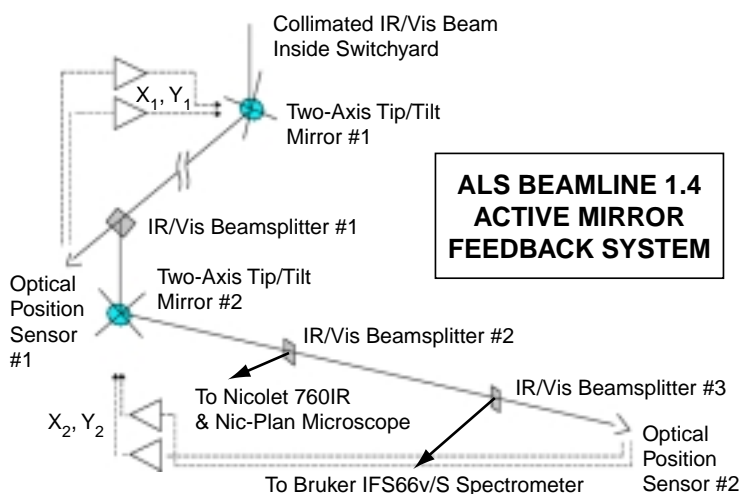
Figure 1

Schematic diagram of the planned optical active feedback system for the Beamline 1.4 complex. It consists of four feedback loops to lock the photon beam in x, y, θ, and ϕ.

[1] Byrd, J.M., M.C. Martin, and W.R. McKinney, in *1999 Particle Accelerator Conference*, edited by A. Luccio and W. MacKay (New York, 1999), p. 495.

[2] Byrd, J.M., in *1999 Particle Accelerator Conference*, edited by A. Luccio and W. MacKay (New York, 1999), p. 1806.

[3] Byrd, J.M., M. Chin, M.C. Martin, W.R. McKinney, and R. Miller, in *Accelerator-Based Sources of Infrared and Spectroscopic Applications*, edited by G.L. Carr and P. Dumas (SPIE Proceedings, Denver, 1999), Vol. 3775, p. 59.

[4] McKinney, W.R., M.C. Martin, J.M. Byrd, R. Miller, et al., in *Accelerator-Based Sources of Infrared and Spectroscopic Applications*, edited by G.L. Carr and P. Dumas (SPIE Proceedings, Denver, 1999), Vol. 3775, p. 37.

Livermore National Laboratory, employs a two-dimensional optical position sensor (Hamamatsu S1880) and a piezo-driven, two-axis, tip/tilt mirror stage (Physik Instrumente S-330). For initial testing, we used one detector and tip/tilt stage and two feedback loops in *x* and *y* corresponding to the positions of the #1 mirror and the #2 optical position sensor. Light is split off by a dichroic beam splitter (Spectra-Tech). The latter reflects 100% of the IR but transmits 50% of the visible light, which is then imaged by the optical position sensor. The electronics system is a hybrid of commercial systems and custom electronics designed by the ALS electrical engineering group.

The system performance with and without feedback is shown in Figure 2, and it can be seen that the dominant noise at 80 Hz has been reduced in intensity by a factor of 15. This correction is achieved in *x* and *y* alone, so to add correction in two-dimensional angle space requires another system. This will complete the full system as shown in Figure 1. It is

scheduled for installation shortly. This may well be a system that can usefully be employed around the ALS as our requirements for highly stable beams ever increase.

A New Instrument for Submicron X-Ray Diffraction

X-ray diffraction is a ubiquitous tool in the study of thin films, from measurements of average texture (orientation of microcrystallites) to determinations of average stress. With the millimeter-wide beams typically available, only average measurements are possible. Unfortunately, the properties of materials are often determined by the characteristics of single grains rather than the average. Although single-grain measurements are clearly of great importance for materials studies, no tool has been available until now, so we set out to build a system capable of submicron x-ray diffraction to address these important issues.
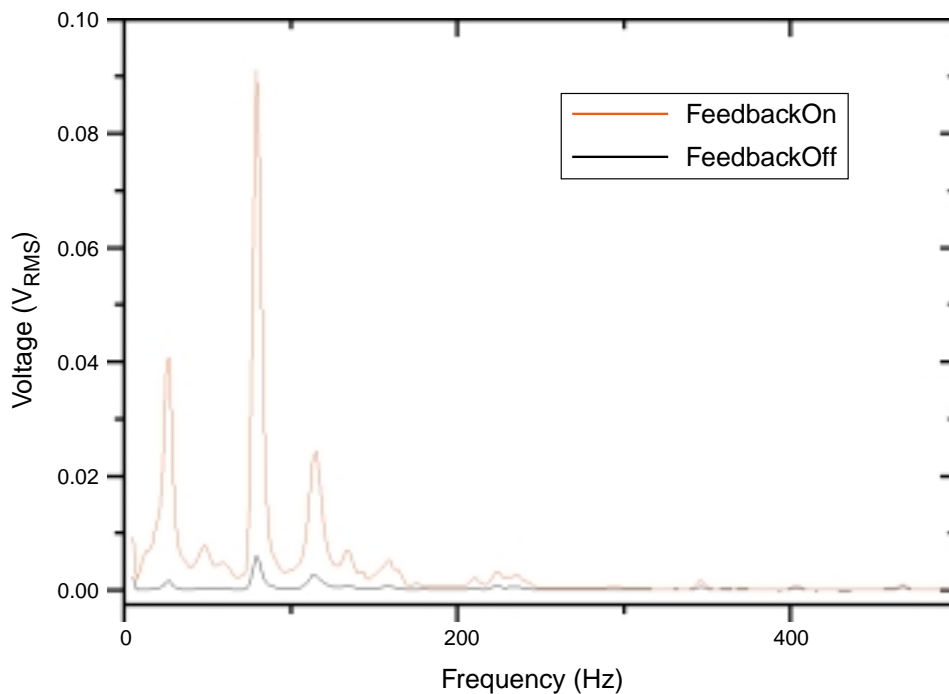
Figure 2

Measured noise spectrum for Beamline 1.4, showing horizontal beam motion at the first position-sensitive detector with and without one feedback loop.

Carrying out x-ray diffraction on the micron scale requires some special instrumental considerations that are not necessary with large beams. The main problem is that normal rotation crystallography, in which the sample rotates, is clearly impossible for submicron samples. We have circumvented this problem by the use of white light for location, indexing, and determination of orientation and deviatoric (distortional) stress, switching in a monochromator for determination of dilatational (hydrostatic) stress. The collinear beam required in white-light and monochromatic mode led to the choice of a four-crystal monochromator.

The beamline has a unity-magnification toroidal mirror that produces a 50-µm × 200-µm focus at an adjustable x–y slit inside a hutch. The toroidal mirror is followed by a four-bounce germanium or silicon monochromator and an elliptically bent Kirkpatrick–Baez mirror pair to image the beam from the x–y slits to submicron size (0.8×0.8 µm FWHM) at the sample. The sample is mounted on a precision translation stage to allow for characterization of different crystal regions or grains. The sample stage is supported on a state-of-the-art, six-circle diffractometer (Huber), and we use a $4K \times 4K$ x-ray CCD detector (Bruker) with a 9-cm × 9-cm view. This is mounted on a detector arm that can be positioned around the sample. The detector itself can translate away from the sample along the detector arm. The system is shown in Figure 3.

The technique consists of illuminating the sample with the submicron broad-bandpass (white) beam and collecting the Laue reflections with the large-area CCD detector. As the crystal structure of the sample is known, the Laue patterns yield the orientation of the microcrystals. Slight displacement of the Laue spots from their "correct" (distortionally free) positions allows for the full deviatoric (distortional) strain/stress tensor of the microcrystal to be directly derived. The dilatational (hydrostatic) component of the strain is obtained by switching to monochromatic beam and making energy scans on selected reflections.

Figure 4 shows an example of the unprecedented type of information that can be derived from the Laue patterns. A 3.8-µm-long single grain within a passivated aluminum interconnect (0.7 µm wide)
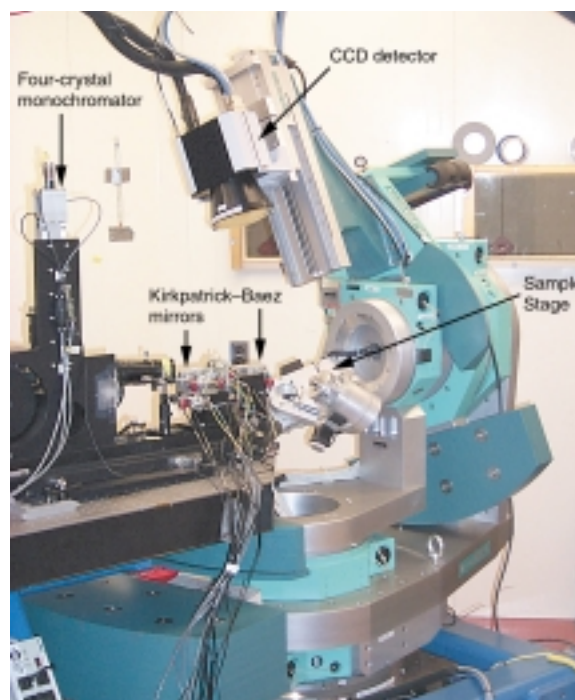
Figure 3

The new x-ray microdiffraction facility on Beamline 7.3.3.

was scanned with a micron-sized white beam. The changes in position, intensity, and shape of the Laue spots on the CCD reveal small changes in the orientation and distortional strain state of the sample under the beam. The analysis showed that this 3.8-µm-long grain is divided into subgrains (crystallites) about a micron in size. Since the complete orientation matrix of each subgrain is derived, the absolute
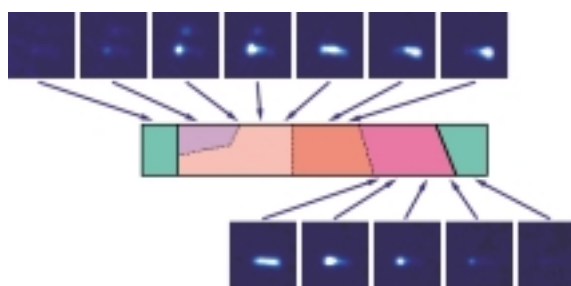
Figure 4

Diffraction spots from subgrains in a 3.8- × 0.7-µm grain of an aluminum interconnect studied at the x-ray microdiffraction facility. Data were obtained by following the position and shape of the (111) reflection in white x-ray microbeam mode.

misorientation between each crystallite can also be calculated, providing an estimate of the dislocation density at the boundaries.

Figure 5 plots the evolution of the deviatoric stress components in a single aluminum grain within an interconnect line during thermal cycling. The sample temperature was raised to 225°C, followed by cooling to room temperature. As the wire was cooled, a large tensile stress developed in the direction along the wire, whereas the normal component of the distortional stress became compressive. The data demonstrate the stability and sensitivity of the new instrument in its ability to measure the long-term stress on micron-sized samples over long periods.

X-ray microdiffraction presents many advantages compared to alternative techniques for microtexture study, such as backscattering electron microscopy/microdiffraction. X-ray microdiffraction has a much higher strain sensitivity and precision. The technique is nondestructive and can be applied to buried samples without need of special preparation. The technique is phase sensitive in the sense that it recognizes different crystalline structures and, with its high orientation sensitivity, allows the distinction of subgrains with angular misorientations of a fraction
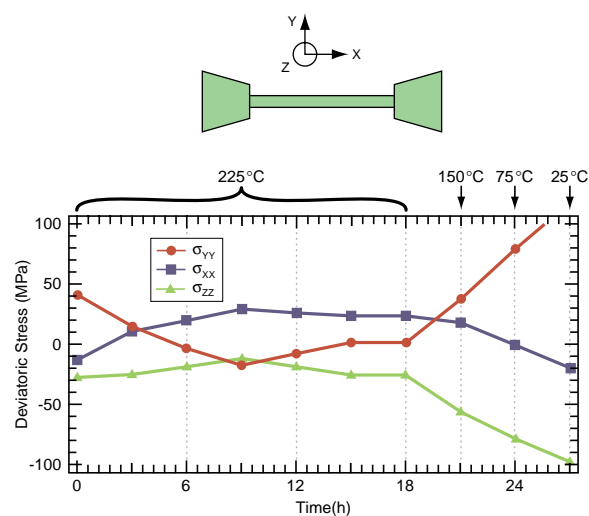
Figure 5

Evolution of the deviatoric stress components in a single aluminum grain within an interconnect line during a thermal cycling experiment. The schematic at the top represents the thin wire with its contact pads and the orientation vectors.

of a degree. One can take advantage of the penetrating property of x rays to study the stress and microstructure within bulk samples. This technique is therefore suitable for a host of problems in materials science, including the study of grain growth mechanisms and deformation.

Commissioning of the Elliptically Polarizing Undulator Beamline

This year marked the installation and first light for Beamline 4.0.2, the first ALS undulator beamline for the direct production of elliptically polarized x rays. Designed for the high-resolution spectroscopy of magnetic materials, this beamline incorporates several new innovations for the ALS. It is the first beamline to use a pure-permanent-magnet elliptically polarizing undulator (EPU). This type of insertion device allows user control of the polarization of the x rays, from elliptical (and circular) to linear polarization with arbitrary azimuth. It is also the first beamline to incorporate chicane magnets and shorter two-meter-long undulators in the insertion-device straight sections. This innovation will allow multiple undulators to be placed in a straight, increasing the number of possible undulator beamlines. Beamline 4.0.2 is also the first ALS beamline to use a variable-included-angle, plane-grating monochromator. This design provides several important performance enhancements, such as a wide tuning range with a single grating. Many of these design features will be incorporated into other new ALS beamlines. Together, these innovations produce a beamline which is a world-class facility for the study of magnetic materials.

The beamline consists of a horizontally deflecting toroidal mirror, which focuses light on the entrance slits of the monochromator in the vertical direction and on the sample in the horizontal direction, followed by a variable-included-angle, plane-grating monochromator with a fixed exit slit. This design incorporates a variable-incidence plane mirror, which rotates and translates, allowing the grating to have a variable scattering angle, and a horizontally deflecting cylinder mirror for vertical focusing. This

monochromator design provides a very wide energy range with a minimum number of gratings, good photon fluxes, and high spectral resolution. With the 5-cm-period EPU, the energy range of the beamline spans from 60 eV in linear horizontal mode (at a storage ring energy of 1.5 GeV) to beyond 1800 eV.

The most important characteristic of the beam-line is the control of the polarization of the x rays. With this type of insertion device, the polarization, from linear to elliptical to circular, is controlled by varying the "row phase" of the undulator magnets[5]. The insertion device, beamline, and control system have been designed to give direct control of the energy and polarization of the x rays to the experimenter. Both circular dichroism (to study ferromagnetic and paramagnetic species) and linear dichroism (to examine antiferromagnetic species) experiments can be performed.

To determine the polarization characteristics of the beamline, a multilayer reflection polarimeter[6] was used to analyze the x rays. Figure 6 shows the

results of measurements made at 460 eV with the undulator operating at the fundamental. As can be seen, the degrees of linear and circular polarization (P_L and P_C, respectively) vary as a function of the row phase of the EPU magnets. At a row phase of 0°, $P_L \approx 1$, showing that the x rays are linearly polarized, in this case horizontally. As the phase increases, P_L decreases while P_C increases, until at a row phase of 112°, $P_C \approx 1$ and $P_L \approx 0$, showing that the x rays are circularly polarized. As the row phase increases beyond 112°, the linearly polarized component increases until, at a phase of 180°, the beam is again completely linearly polarized. With this phase, how-ever, the direction of polarization is vertical rather than horizontal as it is when the phase is 0°. For row phases less than 0°, the pattern is repeated, but the circularly polarized component is of the opposite helicity (e.g., left circularly polarized instead of right circularly polarized).

Another important parameter of the beamline is the spectral resolution. This was evaluated by using the N_2 1s-π^* absorption at 401 eV. Figure 7 shows the experimental data and an eight-peak Voigt line-shape fit to the data. The structure in the spectrum is due to the vibrational states of the N_2. The natural linewidth (Lorentzian component) of the peaks was

Figure 6

Analysis of the x-ray polarization at Beamline 4.0.2. As the magnet row phase is varied from 0° to 180°, the polarization changes from completely linear (P_L =1 and P_C=0) to elliptical to purely circular (P_L =0 and P_C=1) and then back to linear.
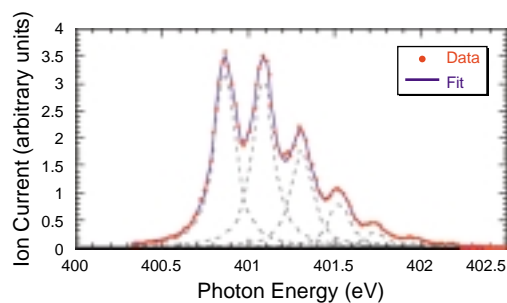
Figure 7

High-resolution spectrum of N_2 1s-π^* absorption, demon-strating a resolving power of ≥6000. The dots indicate the experimental data, and the line is an eight-peak Voigt line-shape fit to the data.

---

[5] Sasaki, S., *Nucl. Instrum. Meth. A* **347**, 83 (1994).

[6] Kortright, J.B., M. Rice, and K.D. Franck, "Tunable multilayer EUV soft x-ray polarimeter," *Rev. Sci. Instrum.* **66**(2), 1567–1569 (February, 1995).

fixed at 116 mV, while the Gaussian component of the fit was varied to determine the instrumental contribution to the linewidth. This analysis yields a spectral resolving power as expected of ≥6000, our design goal. The resolution could be further improved if necessary by closing the slits and by optimizing the monochromator refocus mirror. This spectrum was obtained under high-power conditions (1.9 GeV, >300 mA storage ring current and full illumination of the optics) with entrance and exit slit widths of approximately 25 μm.

The first experiments have now been performed, including studies ranging from the spin polarization of photoelectrons from gas-phase atoms and molecules to the fine structure in transition metal L-edge spectra of metalloproteins. These studies highlight the diversity of research to be conducted at the newest undulator beamline at the ALS, Beamline 4.0.2, a high-resolution beamline with polarization control.

Development of Picosecond X-Ray Diffraction as a Probe of Dynamic Phenomena in Solids

Short-pulse laser sources operating at infrared, visible, and ultraviolet wavelengths have been widely used in the last decade to study the dynamics of valence electrons in atoms, molecules, and solids. Evidence of the importance of this new area of dynamics research can be found in the award of this year's Nobel prize for chemistry to Zewail for pioneering studies of ultrafast chemical reactions performed with femtosecond (fs) lasers. However, to directly probe structural properties, e.g., the motion of nuclei, this methodology is insufficient, and the technique of choice is x-ray diffraction.

An apparatus has been developed for measuring time-dependent x-ray diffraction by combining bend magnet Beamline 7.3.3, time-resolved detectors, and a femtosecond laser system. This project is led by R. Falcone (University of California, Berkeley, Physics Department) in a collaboration with the Experimental Systems Group. The beamline uses a toroidal mirror to produce a 1:1 image of the source and employs a double-crystal monochromator. Laser pulses of 150 fs duration at a repetition rate of 1 kHz irradiate the sample, initiating the structural change to be studied. Two types of detectors are employed: an x-ray streak camera and an avalanche photodiode. The streak camera is driven by a photoconductive switch and has a 2-picosecond (ps) temporal resolution limited at present by trigger jitter[7]. A schematic layout of the system is shown in Figure 8.

Research topics include generation of coherent phonons during a laser-induced phase transition; the
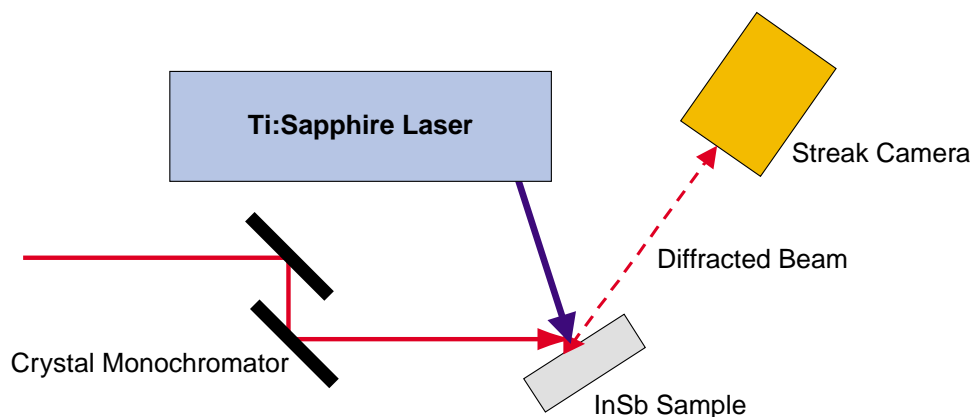
Figure 8

Schematic layout of the picosecond x-ray diffraction system on Beamline 7.3.3.

[7]Larsson, J., Z. Chang, E. Judd, R.W. Falcone, P.A. Heimann, H.A. Padmore, P.H. Bucksbaum, M. Murnane, H. Kapteyn, R.W. Lee, and J.S. Wark, *Opt. Lett.* **22**, 1012 (1997).

study of polarons in a colossal magnetoresistive material, $Nd_{1/2}Sr_{1/2}MnO_3$; photoabsorption in a laser-excited silicon foil; and production of photo-generated halogen radicals in aqueous solution. In one investigation, coherent acoustic phonons have been observed in the x-ray diffraction of a laser-excited InSb crystal (Figure 9)[8]. Modeling based on time-dependent dynamical diffraction theory has allowed the extraction of fundamental constants, such as the thermal electron–acoustic phonon coupling time. Above a critical laser fluence, the first step in the transition to a disordered state is the excitation of large-amplitude, coherent atomic motion. (See Science Highlights, p. 20.)

A dedicated beamline for time-resolved x-ray diffraction and spectroscopy, Beamline 5.3.1, is being developed with special consideration toward providing a wide spectral range and low optical scattering. This beamline will be a home for the experiments described above as well as the laser–electron beam modulation project led by R. Schoenlein (Berkeley Lab, Materials Sciences Division). The source for the beamline will be provided by this laser "slicing" technique, which works in the following way: A high-power laser beam propagates collinearly with the electron beam in Straight 5 of the ALS storage ring. The wiggler fundamental or third harmonic is tuned to the same energy as the laser, and the pulse from the laser is timed to directly overlap the electron beam. The pulse length of the laser is around 50 fs, and during this time, energy is exchanged between the laser and a short "slice" out of the relatively long 30-ps electron bunch. The energy kick given to the beam is many times the natural electron-beam energy. The electron beam now has an accelerated and retarded 50-fs "slice" of electrons, so these beams disperse radially in the field of a dipole magnet. In this case, we will observe this dispersion in the center dipole of Sector 5 (which illuminates Beamline 5.3.1), i.e., adjacent to the "energy modulator" in Straight 5.0.

Visible synchrotron pulses of 300 fs duration have been generated by this laser–electron beam modulation technique[9]. Proof-of-principle experiments have been carried out at Beamline 6.3.2 to observe optical wavelengths, but the new Beamline 5.3.1 is explicitly designed for time-resolved diffraction measurements and should achieve a time resolution as low as 80 fs. Beamline 5.3.1 will contain a visible-light diagnostic, a 1:1 toroidal mirror, a differential pumping section, a chopper, and a double-crystal monochromator. The spectral range of the beamline will include visible light and both soft and hard x rays. Horizontal scattering will be minimized by employing one vertically reflecting mirror. This project is scheduled for completion in May 2000.

Figure 9

X-ray diffraction in a laser-excited InSb crystal at crystal angles of 0, +20, and +40 arcseconds from the Bragg peak. The solid line shows experimentally measured intensity, and the dashed line shows simulated time-resolved diffracted intensity.

[8]Lindenberg, A.M., I. Kang, S.L. Johnson, T. Missalla, P.A. Heimann, Z. Chang, J. Larsson, P.H. Bucksbaum, H. Kapteyn, H.A. Padmore, R.W. Lee, J.S. Wark, and R.W. Falcone, *Phys. Rev. Lett.* **84**, 111 (2000).

[9]Zholents, A., and M. Zholotorev, *Proceedings of the 11th International Conference on Ultrafast Phenomena* (1998), pp. 390–392.

SCIENTIFIC SUPPORT

John Bozek
Scientific Support Group Deputy Leader

The Scientific Support Group (SSG) contributes to the mission of the ALS by supporting the efforts of researchers at the ALS through scientific and technical collaboration and scientific outreach. Depending on the needs of the user of ALS facilities, the degree of collaboration can range from technical assistance with the beamline to full partnership in developing new research programs and experimental endstations. The group was formed in 1998 from existing ALS staff in recognition of the changing needs of a maturing user facility and has continued to expand in size and scope. Several new permanent beamline scientists and associate beamline scientists were added to the group in 1999, and the group was given responsibility for the scientific and technical excellence of additional ALS beamlines.

Figure 1

Members of the Scientific Support Group: (front row) Zahid Hussain, Angela Garland, (back rows, left to right) Michael Martin, Jonathan Denlinger, Elke Arenholz, George Meigs, Xingxiang Zhou, John Bozek, Fred Schlachter, Scott McHugo, Eli Rotenberg, Scot Kellar, Wayne Stolte, Bruce Rude. Not picured: Glenn Ackerman, Tony Young.

Outreach

In addition to scientific and technical responsibilities, SSG strives to expand the scientific program of the ALS and broaden its user base through publications and presentations. A targeted weekly seminar series has been initiated to further these goals. Typically, a topic will be explored through a series of five to ten weekly lectures by world-renowned scientists in the field. Topics in 1999 included correlated electron systems (i.e., high-T_c materials) and photon-in–photon-out spectroscopies.

A workshop exploring the need for a new beamline to study complex and correlated phenomena was organized with the assistance of SSG and held in October. The participants discussed scientific frontiers in magnetism, nanostructures, and correlated-electron systems and concluded that a new experimental facility is required at the ALS. The consensus of the group was that a bright source with variable polarization, a beamline with high spectral resolution, and experimental stations for electron spectroscopy with high energy and momentum resolution and spin detection are required to advance the experimental frontiers.

To begin plans for the future of infrared research at the ALS, a simultaneous October workshop was held to discuss and investigate possibilities for a synchrotron-based, far-IR facility. The workshop produced much good scientific discussion and allowed attendees to compare ideas for far-IR sources. The overall conclusion and recommendation of the workshop was that a dedicated far-IR beamline should be built at the ALS. Dimitri Basov (University of California, San Diego), Zack Schlesinger (University of California, Santa Cruz), and Joe Orenstein (University of California, Berkeley) emerged as the most enthusiastic infrared scientists ready to help with making the scientific case for such a facility. The next step is to work through various designs for such a facility so that a full proposal can then be started.

Support

Members of SSG are also responsible for the operation, upgrade, and maintenance of most of the facility beamlines and many of the permanent endstations at the ALS. The undulator beamlines, Beamlines 4.0, 7.0, 8.0, and 10.0, each have at least one SSG staff member responsible for their continued operation. Several improvements were made to the operation of existing beamlines in 1999. For example, slit gaps were brought under computer control to make several of the spectroscopy beamlines more user friendly. The first such system, installed on Beamline 10.0.1, is now used continuously and has greatly simplified setting the slit gaps. In addition, an angle calibration scheme was devised and built for the ALS spherical-grating monochromators (SGMs). The scheme was based on a high-sensitivity electronic tiltmeter to ease difficulties with calibrating the photon energy when changing gratings. Installation of the first device is awaiting the venting of one of the three ALS SGMs (Beamlines 7.0, 9.3.2, and 10.0.1) and is expected to be installed and tested in March 2000. Finally, the mirror switch-yard on Beamline 10.0.1 was brought under remote control and, with the highly anticipated installation of a sensitive beam-position monitor on the High Energy Resolution Spectroscopy (HERS) endstation branch, is expected to greatly simplify the changeover from one branch of the beamline to the other.

Several new endstations were designed, constructed, and commissioned with the help of SSG personnel in 1999. A new endstation for EXAFS studies was commissioned on double-crystal bend-magnet Beamline 9.3.1 in collaboration with M. Klein and H. Frei (Berkeley Lab). A high-efficiency electron spin polarization detector capable of determining all three components of spin has been built and is in the process of being commissioned. It will be combined with an electron energy analyzer for the study of spin-resolved photoemission from complex materials at high energy resolution with both laser and synchrotron light. The x-ray photoelectron diffraction (XPD) chamber on Beamline 7.0.1 was upgraded with the replacement of the existing electron spectrometer with a new high-resolution, high-efficiency Scienta SES-100. The new spectrometer simultaneously measures spectra over an angular range of 8° with an angular resolution of 0.03°, greatly enhancing the efficiency of the research program. The XPD chamber will also incorporate an improved sample manipulator. The new manipulator has improved angle and position mechanisms and sample temperature controls (30–2000 K). A prototype one-dimensional, parallel, multichannel electron detector with a high count rate (1 GHz) has been successfully tested on the Beamline-9.3.2 APSD electron spectrometer (used by C. Fadley et al., University of California, Davis, and Berkeley Lab). Count rates were previously limited to 20 MHz on the best commercially available detectors. A successful implementation of such a detector on an electron energy analyzer will allow time-resolved (millisecond) photoemission experiments to be performed for the first time.

Off-line characterization capabilities were also improved with the addition of a reverse-angle Laue diffraction setup for sample crystal characterization. Further developments are anticipated to improve the effectiveness of all of the beamlines. Many other endstation and facility development projects involving SSG staff are in progress. Users are encouraged to contact an SSG member with any suggestions they might have for future beamline, endstation, or experimental facility improvements.

Scientific Contributions

Staff scientists within SSG are expected to maintain their scientific and technical excellence in areas of synchrotron radiation research. Participation in active scientific programs is essential for such development, and all of the SSG scientists are active members of research programs at the Advanced Light Source.

Beamline 1.4: Progress in Infrared Research

The Fourier-transform infrared (FTIR) spectro-microscopy beamline (Beamline 1.4.3) at the ALS has frequently been used to solve problems in environmental science. One outstanding example is the spatially resolved, time-dependent study giving

evidence for biogeochemical transformation of hexavalent chromium (Cr^{6+}), a widespread industrial contaminant. (See Science Highlights, p. 34.) The brightness of the infrared radiation at the ALS makes spatially resolved spectroscopy (spectromicroscopy) possible.

The diffraction-limited IR spatial resolution and high signal-to-noise ratio of the ALS is being applied to many other problems as well. For example, several users study individual human cells in order to analyze the biochemical changes that occur because of disease, oxidative damage, and environmental pollutants. Other users study the locations of toxins in sediments or the uptake of nutrients by root structures. An ongoing study of bacteriorhodopsin microcrystals endeavors to trap the protein in a light-induced intermediate structural conformation, which is then probed and verified by the IR beam. Another group studies the surface chemistry of water by using a microjet of water that is about 10 µm in diameter.

The IR beamlines, because of their interferometric selection of wavelength, have proven to be the most sensitive to microscopic motions of the ALS beam. To reduce this beam motion, an active optical feedback system was designed in cooperation with the Experimental Systems Group. (See Experimental Systems, p. 78.)

Beamline 9.3.2 : Photoelectron Spectroscopy at High Pressure

Atomic-level processes on surfaces have been studied with great success for many years in ultra-high-vacuum environments. Most relevant and important processes, however, take place in the presence of gases at high pressure (about one atmosphere or higher). Examples are catalysis (e.g., carbon monoxide and nitric oxide on rhodium in catalytic converters) and environmental science (e.g., water adsorption on mineral surfaces). Taking advantage of the high brightness and photon flux of the ALS, we have developed (with Laboratory Directed Research and Development funds awarded to principal investigators M. Salmeron, Z. Hussain, and C. Fadley) a new apparatus, a combination of electron optics and differential pumping systems, that makes it possible to obtain photoelectron spectra of materials under high pressure. The use of chemical shifts in x-ray photoelectron spectroscopy (XPS) allows one to conveniently separate out the signal from the surface of the sample and that from the gas phase that is in equilibrium with the sample surface.

Conventional XPS instruments normally operate below 10^{-5} Torr, for two reasons: (1) electrons are strongly scattered by gases at higher pressures (the mean free path of 100-eV electrons is only 1 mm in 1 Torr of oxygen), and (2) the detectors (channeltron or channel plates) of electron energy analyzers that are utilized in XPS experiments demand pressures below 10^{-6} Torr for stable operation. To overcome these obstacles, we have developed a high-pressure electron transfer system to carry out XPS at a pressure of about 1–20 Torr, i.e., about eight orders of magnitude higher than in conventional XPS instruments (Figure 2). Our lens system is differentially pumped in order to minimize the path length of the electrons in the high-pressure region. The differential pumping stages also help to maintain a sufficient vacuum in the electron energy analyzer. Electrostatic lenses image the electrons that are emitted from the sample surface onto the focal plane of a hemispherical energy analyzer.

Construction was completed during this past fiscal year, and the first successful tests were recently performed at pressures of up to 1.5 Torr. The example in Figure 3 shows an XPS survey of gold in 1.5 Torr of nitrogen gas. In this test, the electrostatic lens voltages of the transfer lenses had not yet been optimized for optimum transmission of the system. The system is currently going through active development.
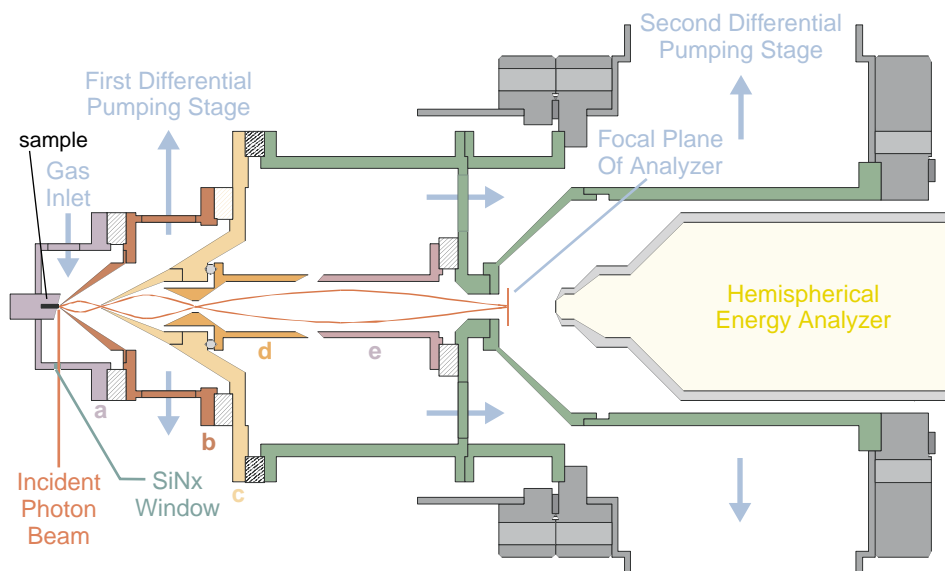
Figure 2

High-pressure electron transfer system for XPS experiments. The high-pressure cell (a) contains the sample. The incident photon beam is admitted to the cell via a silicon-nitride window, which separates the high pressure in the cell from the ultrahigh vacuum in the beamline. Electrons emitted from the sample are extracted through the orifice in the first skimmer (b). This skimmer serves also as the first differential pumping stage. The electrons then pass a second skimmer (second differential pumping stage (c) and another electrostatic lens (d). Four orthogonally arranged electrostatic deflection plates (e) steer the electron beam into the focal point of the hemispherical energy analyzer.
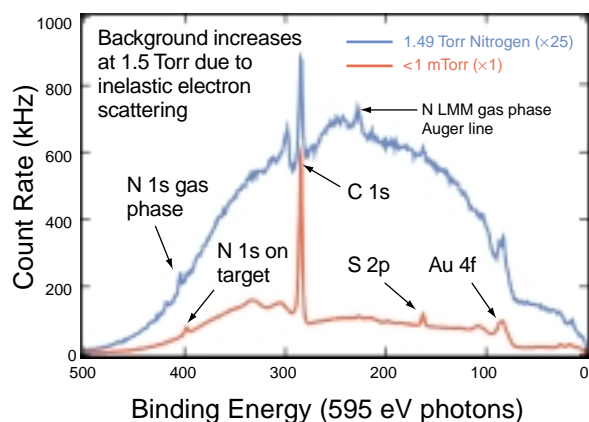
Figure 3

XPS spectra from a gold test sample (with some contamination) at low pressure and in the presence of 1.5 Torr of nitrogen gas.

Beamline 10.0.1: The Atomic and Molecular Facility and the High Energy Resolution Spectrometer

Beamline 10.0.1 is shared by the High Energy Resolution Spectrometer (HERS) and the Atomic and Molecular Facility (AMF), the latter with three permanent endstations and provisions for accommodating independent investigators. The AMF saw two new major installations in 1999: a quadruple-reflection phase retarder for the generation of circularly polarized radiation and the Ion Photon Beamline (IPB), both on this central branchline of Beamline 10.0.1.

The quadruple-reflection phase retarder (Figure 4) was purchased from the Physical Sciences Laboratory
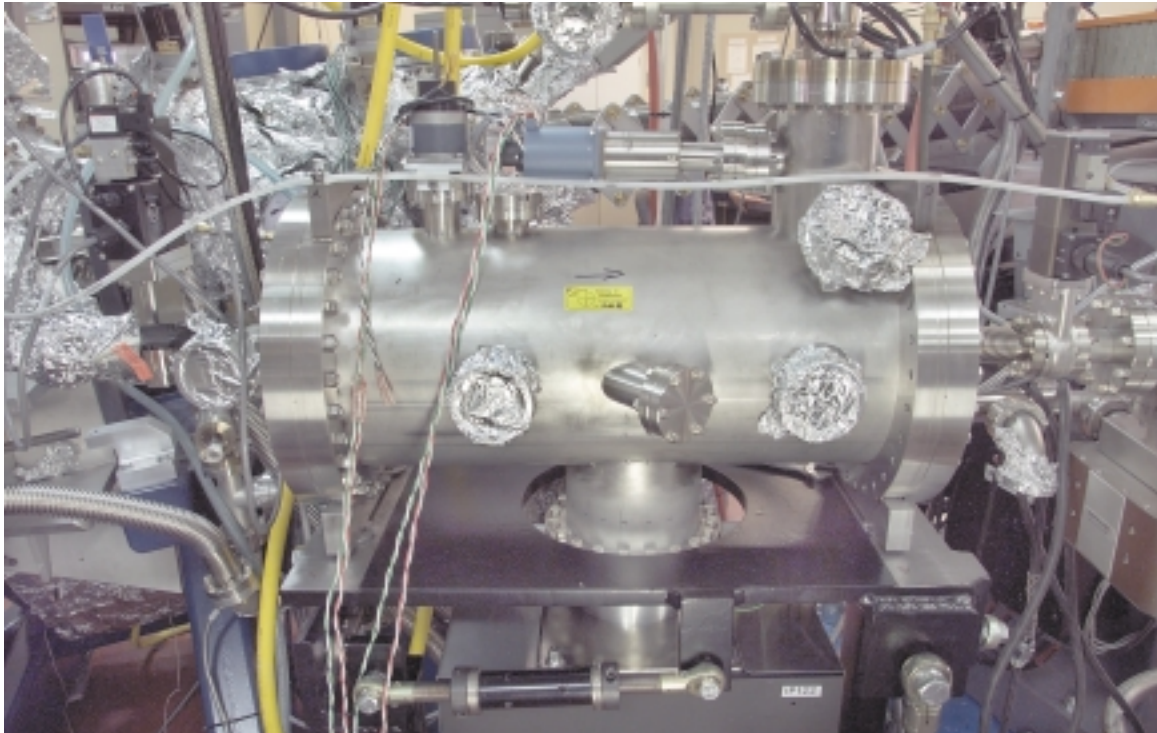
Figure 4

The quadruple-reflection phase retarder for the generation of circularly polarized radiation on Beamline 10.0.1.

of the University of Wisconsin, Madison, with funding from both the National Science Foundation (through D. Jaecks of the University of Nebraska, Lincoln) and the U.S. Department of Energy (DOE). The retarder was installed in the spring of 1999 with the assistance of SSG staff. The phase retarder uses four plane mirrors that rotate in two directions (α and θ) in vacuum to convert the linearly polarized incident radiation into circularly (elliptically) polarized light of any degree and hand. The angles of the mirrors are tuned for each photon energy to optimize either the degree of circular polarization or throughput, and the output is measured by using a plane-mirror polarization analyzer. The retarder has been used by two groups to provide circularly polarized photons for their research in 1999.

The Ion Photon Beamline (IPB), built at the University of Nevada, Reno, by R. Phaneuf and coworkers with funding from the DOE, was also installed and commissioned on Beamline10.0.1 in

1999 with the aid of SSG members. The IPB is used to study the photoionization of ions by using the intense beam of photons from Beamline 10.0.1. A colutron-ion-gun-assembly (CIGA) ion source from the University of Ceurnavaca, Mexico, provides an intense source of singly charged ions. An electron-cyclotron-resonance (ECR) ion source will soon be added to provide a source of multiply charged ions for the IPB. Initial tests of the experimental apparatus in May 1999 were followed by an aggressive schedule of experiments in the fall and winter of 1999 with many exciting results. Overall, the IPB is working well, providing much higher signal rates than any other similar experiment in the world (there are three other known competitive installations) at significantly better spectral resolution (Figure 5).

The HERS endstation was designed to study highly correlated materials, including high-temperature superconductors (HTS), colossal magnetoresistance (CMR) compounds, and heavy
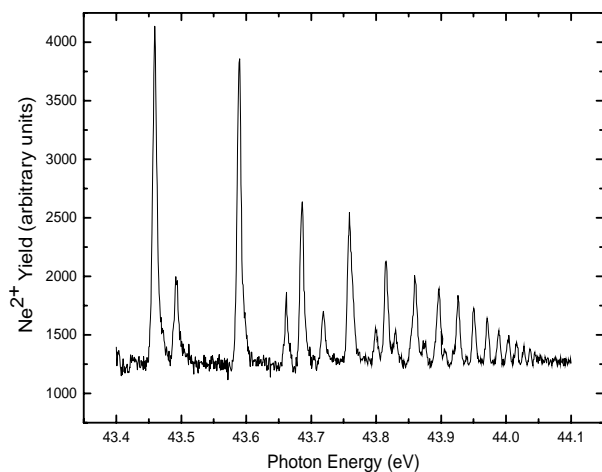
Figure 5

Photoionization spectrum for Ne$^+$ taken at the IPB endstation, showing a nominal resolution of 7.5 meV.

fermion compounds, with extremely high momentum and energy resolution. We have done this by bringing together a unique combination of high-performance components. The most obvious of these is the Scienta SES200 electron energy analyzer. With the proper image collecting hardware and lens configuration, we can simultaneously collect individual photoemission spectra from a 14° cone with angular resolution better than ±0.15°, without sacrificing the excellent energy resolution of better than 5 meV. We added to the analyzer's utility by mounting it to a chamber that allows us to rotate it 120° about the incoming synchrotron beam, making polarization-dependent studies possible.

As important to the success of the HERS endstation as the analyzer is the sample manipulator. This liquid-helium-cooled unit has three degrees of translational freedom, two rotational degrees of freedom, and a sample temperature range of 10 K to 450 K. The sample rotation is accurate to better than one-quarter degree, giving it accuracy comparable to the analyzer's angular resolution.

Because many samples cannot withstand the high-temperature bake-out necessary for ultrahigh-vacuum work, we developed an elaborate yet user-friendly load-lock system that allows one to move a fresh sample from atmospheric pressure onto the manipulator in the main chamber, where the

pressure is less than 4×10^{-11} Torr, in less than two hours without baking. The multistage load lock has parking spots for 39 different samples. For samples that cannot be cleaved and must be prepared in vacuum, the endstation is equipped with the standard surface science preparation tools (i.e., LEED, evaporators, ion sputtering guns, cleavers, and gas dosers) separated from the main analysis chamber by ultra-high-vacuum valves.

The endstation began full-scale operation in March 1999 and quickly earned its "stripes." One of the first experiments was an investigation of the electronic structure of $La_{1.28}Nd_{0.6}Sr_{0.12}CuO_4$, a stripe-phase compound. (See Science Highlights, p. 5.) The total data collection time was less than 3 hours. This was critical because the sample lifetime, even at 4×10^{-11} Torr and 20 K, was only 6 hours. Such experiments can only be done on the HERS endstation.

Beamline 10.3.1: The X-Ray Fluorescence Microprobe

The Participating Research Team (PRT) for Beamline 10.3.1 is currently being reorganized to transform the beamline into an external-user-directed facility. It is planned to combine the beamline's operation with that of Beamline 10.3.2 to provide a world-class microanalysis capability with instruments for both micro–x-ray fluorescence and micro–x-ray absorption spectroscopy. With this reorganization in mind, the SSG has worked to enhance the capabilities of the microprobe beamline and to encourage the involvement of scientists from outside institutions who could become part of the new PRT.

One of the major enhancements to the beamline has been the installation of a new sample stage and data acquisition system by the members of the present PRT, who are part of the Center for X-Ray Optics. These upgrades allow users to observe data acquisition in real time, as compared to the previous system, where the user was required to wait until the end of a scan before data visualization. This new capability minimizes time lost during undesirable scans. The time can be significant, since scan times

can run up to multiple hours. The SSG took part in the development of the new system by providing insight into user requirements for the new data-acquisition interface. This helped to define the needs of the new system in terms of hardware and software development.

Scientific outreach by the SSG has included direct collaboration with researchers from outside institutions. These direct collaborations were often initiated after conference presentations of demonstration experiments performed by the SSG. This type of interaction has been extremely successful with researchers involved with semiconductor materials, particularly those studying the use of silicon for solar cells (Figure 6) and integrated circuits as well as
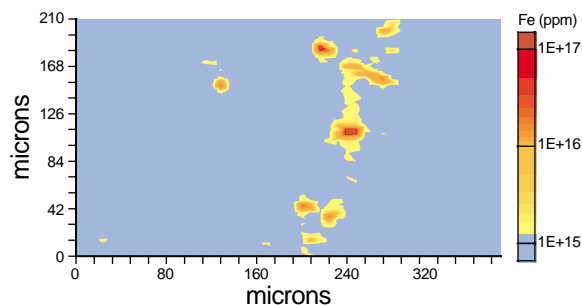
Figure 6

X-ray fluorescence image of Fe distribution in polycrystalline silicon used in the manufacture of solar cells.

III–V semiconductor materials for optoelectronics. The high sensitivity, large sampling volume, and micron-scale resolution provide unique capabilities that are unobtainable with the characterization techniques typically used by this community.

Another successful interaction has been with an aerosol contamination research group at the University of California, Davis. This research group is involved with monitoring of atmospheric contamination emanating from Asia. They had been using particle-induced x-ray emission (PIXE) to analyze the contamination with marginal sensitivity. After initial conversations with researchers at the ALS, the Davis group realized that a large enhancement in sensitivity could be gained with the use of Beamline 10.3.1. Over the initial months of work with the Davis investigators, we established methods of rapid sample analysis and data deconvolution needed by their research group. Furthermore, we were able to improve the sensitivity of the beamline by use of white-light radiation rather than the typically used "pink" radiation generated with the use of a multilayer mirror. This work has provided the impetus for the Davis group to become a lead member in the forthcoming PRT for Beamlines 10.3.1 and 10.3.2.

Demonstration studies have been conducted in several other research areas, including analysis of anthropogenic soil contaminants and cancerous lung tissue and development of x-ray optics.

USER SERVICES

Gary Krebs
User Services Group Leader

The goal of the ALS User Services Group is to provide our users with a friendly and efficient interface to the ALS. The group is organized into three sections: User Services Administration, Beamline Coordination, and Technical Information. These groups work together to provide ALS users with a wide range of services.

User Services Administration

The User Services Office, staffed by members of the User Services Administration Section (Figure 1) and conveniently located on the mezzanine of the ALS, assists users in a wide variety of ways. As a National User Facility, the ALS provides photons to independent investigators through a peer-review allocation process. User Services Administration manages

Figure 1

User Services Administration Section (left to right): Jane Tanamachi, Bernadette Dixon, Ruth Pepe, Barbara Phillips, and Sharon Fujimura.

the process to ensure equitable and efficient distribution of beamtime. Beamtime proposals are received through the ALS Web site, and twice a year these proposals are reviewed by a Proposal Study Panel under the direction of ALS Division Deputy for Science Neville Smith. Panel members are chosen in consultation with the Users' Executive Committee (UEC) to cover the wide range of sciences at the ALS. Protein crystallography beamtime requests are ranked by a separate panel, also twice annually. The proposal submission and beamtime allocation process is described in greater detail on the ALS Web site (www-als.lbl.gov).

The User Services Office also takes charge of helping new users through the required registration process before they begin work at the ALS. Each user receives a proximity card, which allows them access to the ALS experiment floor. All new users also watch a short safety video, which describes some of the potential safety hazards at the facility and outlines the experiment safety checkout process. New users can also take care of much of the advance processing before they arrive by using the ALS Web site.

The User Services Office also manages the ALS apartments, which are located near the Laboratory on the main shuttle-bus route (Figure 2). The apartments are available to all ALS users, and detailed information about costs and other factors can be found on the ALS Web site.

In another of its many roles, the User Services Office provides administrative and logistical support to the UEC and the Scientific Advisory Committee. The UEC serves as the users' voice and plays an important role in determining the direction of the ALS scientific program. The Scientific Advisory Committee provides scientific direction for the ALS and counsel to Berkeley Lab management. The User Services Administration Section is led by Ruth Pepe and includes Bernie Dixon, the User Services Office Manager; Sharon Fujimura; Jane Tanamachi; and Barbara Phillips.

Figure 2

The ALS apartments provide short-term and longer term accommodations for visiting users.

Beamline Coordination

The Beamline Coordination Section (Figure 3) provides endstation setup support on the experiment floor as well as shipping, receiving, and storage services. This group assists users in having their experimental setups checked for safety, working closely with various safety specialists in the areas of electrical, mechanical, chemical, radiation, and laser safety. This safety checkout process is required for each experiment and assures the safety of all users on the experiment floor. The Beamline Coordination Section also maintains a stock room of commonly needed parts and equipment for ALS users (Figure 4). The stock room, created by summer student Matthew

Figure 3

Beamline Coordination Section (left to right): student worker Ben Engel, Tony Marquez, Donna Hamamoto, (seated) Kelly Gonzalez, Gary Giangrasso, and Cheryl Hauck.

Figure 4

The ALS user stock room gives users easy access to commonly needed parts. Pictured is Matthew Krebs.

Krebs, is accessible by proximity card 24 hours a day. The Beamline Coordination Section is led by Donna Hamamoto and includes Cheryl Hauck, Gary Giangrasso, Tony Marquez, and Kelly Gonzalez.

Technical Information

The Technical Information Section (Figure 5) is responsible for the document you are reading as well as the annual Compendium of User Abstracts; special

Figure 5

Technical Information Section (left to right): Greg Vierra, Annette Greiner, Lori Tamura, Art Robinson, and Elizabeth Moxon.

brochures for new facilities such as the Atomic, Molecular, and Optical Facility and the Macromolecular Crystallography Facility; and countless workshop and conference posters. In addition, the section maintains and develops the ALS Web site and writes and edits the electronic newsletter, ALSNews. The section, composed of science writers along with graphics and web experts, provides the ALS scientific community as well as the general public with information about the scientific output of the ALS. The group maintains a strong tie to the educational community, both within the state of California and internationally. In conjunction with the User Services Office, this group coordinates tours for the thousands of visitors who come to see the ALS annually. The Technical Information section is led by Art Robinson and includes Annette Greiner, Elizabeth Moxon, Lori Tamura, and Greg Vierra.

Special Events

Shirley Symposium on Spectroscopy and the Structure of Matter

In March 1999, friends, colleagues, and former post-docs and students of David A. Shirley gathered at Berkeley Lab to celebrate his life and work on the occasion of his 65th birthday. The scientific scope of the day-long symposium included updates in research areas in which Dr. Shirley and his associates had been involved over the years. Topics included electron spectroscopy of solids, atomic and molecular physics, and hyperfine interactions. Highlights of the evening program were a scientific retrospective of Dr. Shirley's work and a special lecture given by T. Darrah Thomas about chemical information obtainable from inner-shell spectra.

Dave Shirley welcomed colleagues past and present during the opening ceremonies.

**Spectrosc[...]
and the
Structure o[...]
Matter**

Symposium on the occasion of David A. Shirley's 65th Bi[...]

March 28-29, 1999

Symposium participants paused for a group portrait.
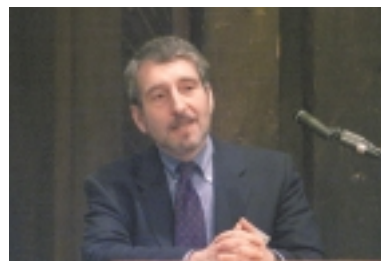
Speakers at the evening program included, from left, John Rasmussen, Professor Emeritus of Chemistry, UC Berkeley; Nicholas Stone, Oxford University; and Stephen Rosenblum, a former Shirley graduate student.

PEC 99

The Clark Kerr Campus of UC Berkeley was the site of the 59th Annual Physical Electronics Conference, held July 7–9. The international meeting, for scientists involved in the study of the physics and chemistry of surfaces and interfaces, offered a program of oral and poster presentations that highlighted recent research in atomic and molecular processes with a focus on applications in the microelectronics and magnetic recording industries. Other highlights of the conference included the awarding of the Nottingham Prize for the meeting's outstanding student presentation, an evening reception in Tilden Park, and a tour of the ALS.

59th Annual Physical Electronics Conference

July 7–9, 1999

Clark Kerr Campus
of the
University of California-Berkeley

Kalman Pelhos on his way to receive the Nottingham Prize for the best student paper presented at the conference.

An evening reception at nearby Tilden Park provided an informal venue for animated discussions.

XRM 99

The 6th International Conference on X-Ray Microscopy was held August 1–6, 1999, on the Clark Kerr Campus of UC Berkeley. Organized by the Center for X-Ray Optics and the ALS, the conference attracted researchers from around the world interested in advances in high-spatial-resolution x-ray imaging and its applications across a broad range of the sciences. A new award, for outstanding contributions in x-ray microscopy by a young scientist, was established this year in honor of the conference chair, Werner Meyer-Ilse, who died in an accident shortly before the1999 meeting. The winners were Jianwei Miao, recently of the State University of New York, Stony Brook, and Daniel Weiss of the Georg-August Universität, Göttingen.

Poster sessions gave conference participants the opportunity to view and discuss many topics relating to the applications of x-ray microscopy.
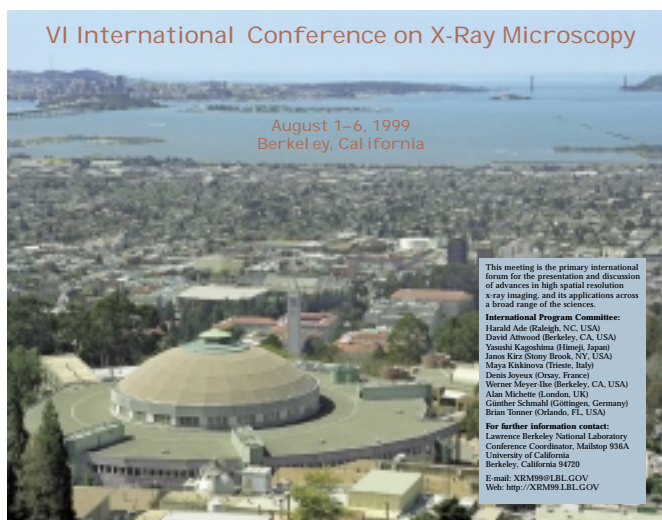
1998 ALS Users' Meeting

The October 1998 meeting of the ALS Users' Association attracted more than 225 users, staff, and vendors. The scope of this year's meeting included the full complement of oral and poster presentations as well as updates on the direction of the ALS scientific program and working-group sessions for new science initiatives. Other highlights included a session devoted to presentations by young researchers and the first-ever student poster competition.
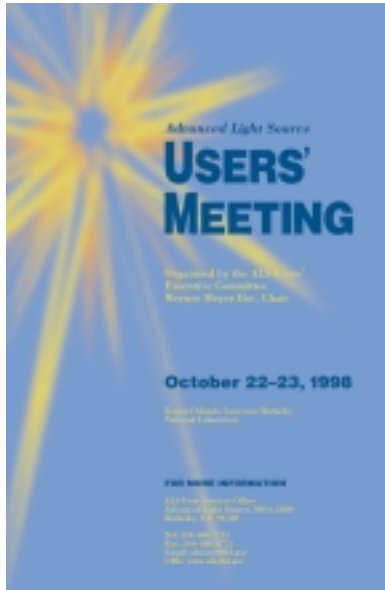
Elke Arenholz and Clemens Heske presented their work during the session for young researchers.

Lunchtime on the ALS patio was an opportune time for informal discussions.
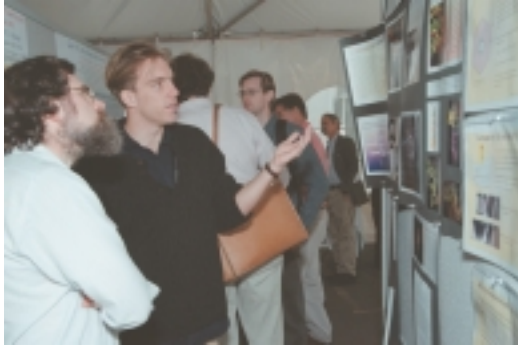
Seth Harris (second from left), the first winner of the student poster award, discussed his work during the poster session.

The Users' Executive Committee (UEC) honored administrative staff and conference organizers for their work in making the users' meeting a success. (From left: Sharon Fujimura, Ruth Pepe, Mollie Field, and Bernie Dixon. Not pictured: Elizabeth Moxon.)
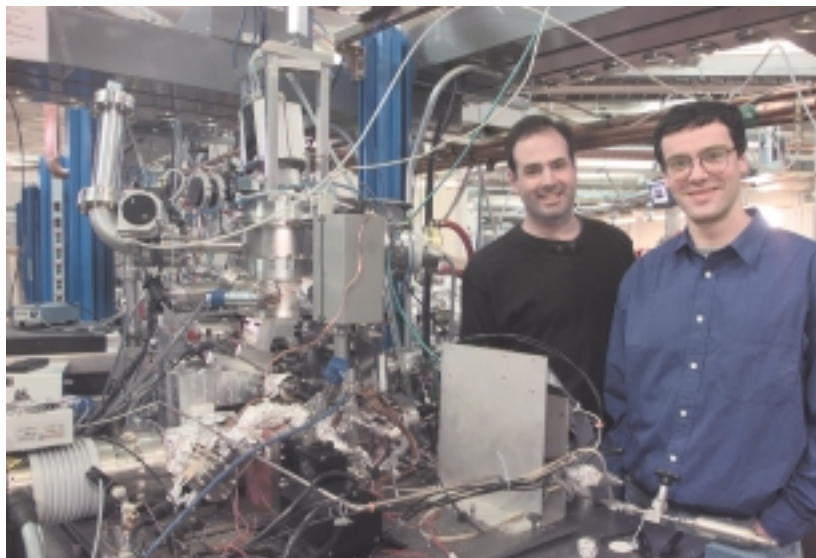
Klaus Halbach Award for Instrumentation. This award, presented annually at the ALS Users' Meeting, recognizes innovative work in instrument design at the ALS. This year's winners, Ken Goldberg (left) and Patrick Naulleau of the Center for X-Ray Optics, received the prize for their work in extreme-ultraviolet (EUV) interferometry. Goldberg and Naulleau led a team that commissioned a new phase-shifting point-diffraction interferometer based on coherent synchrotron radiation to measure the accuracies of cameras that are capable of imaging with EUV light. The team demonstrated that the interferometer could measure wavefront errors with an accuracy of 1/300 of the wavelength of the EUV radiation (13 nm), exceeding the design goal by a factor of two.

1999 ALS Users' Meeting

Reports on recent ALS scientific highlights and the growth of the facility took center stage at this year's busy ALS Users' Meeting. More than 225 users and staff attended oral presentations, poster sessions, and vendor exhibits. In addition, focused workshops were held to explore opportunities at the ALS in the fields of ultra-high-resolution spectroscopy of complex systems and far-infrared spectromicroscopy.

___ Advanced Light Source ___
USERS' MEETING

Organized by the ALS Users' Executive Committee
Stephen D. Kevan, Chair

October 18–20, 1999

Ernest Orlando Lawrence
Berkeley National Laboratory

FOR MORE INFORMATION

ALS User Services Office	TEL: 510-486-7745
Advanced Light Source	FAX: 510-486-4773
MS 6-2100	Email: alsuser@lbl.gov
Berkeley, CA 94720	URL: www-als.lbl.gov
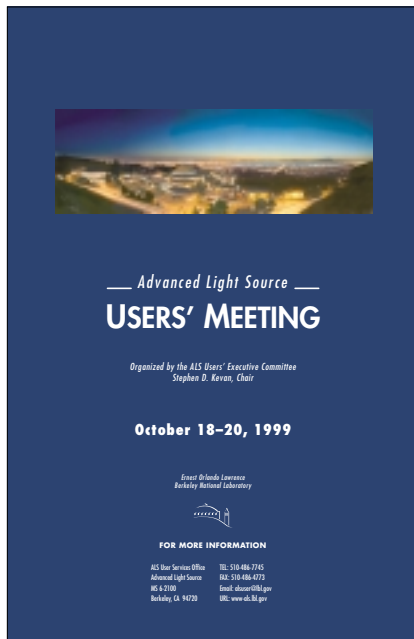
DOE Associate Director for Basic Energy Sciences Patricia Dehmer presented the view from Washington during the opening session.
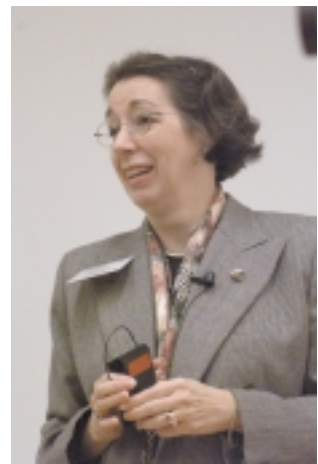
Users' Executive Committee Chair Steve Kevan presented ALS Director Daniel Chemla with a hand-drawn portrait in recognition of his efforts on behalf of the facility and the user community.
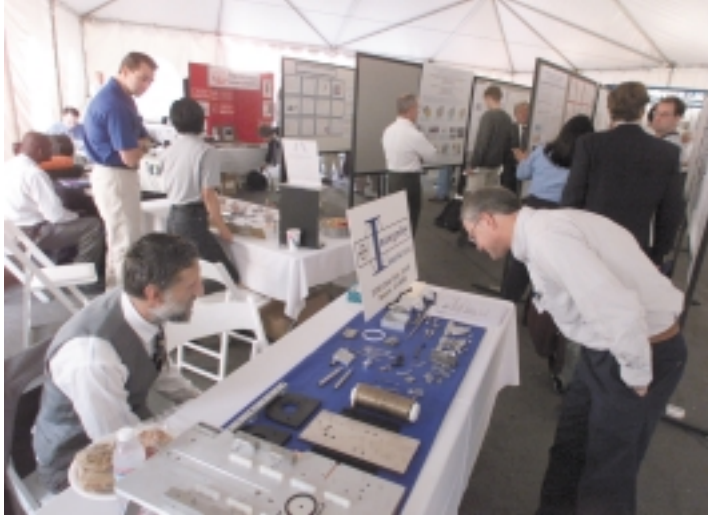
Poster sessions, held in conjunction with vendor exhibits, gave participants the chance to view recent research results and see the latest in beamline and vacuum components.

The well-attended evening reception on the campus of UC Berkeley featured award presentation ceremonies and a photo-collage slide show of ALS users and staff.
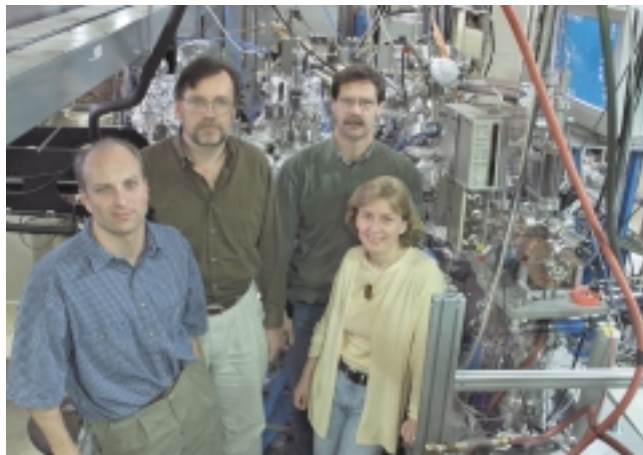
Klaus Halbach Award for Instrumentation. This year's annual award for significant accomplishment in instrumentation at the ALS went to the team responsible for the design and commissioning of the photoemission electron microscope, PEEM2. Developed by the team with collaborators from IBM, Arizona State University, and the ALS, the microscope uses the bright, focused x rays of the synchrotron to obtain images of solid surfaces with submicron resolution. The resulting image contains information about the magnetic structure, the elemental and chemical composition, and the topography of the sample. The microscope, installed on Beamline 7.3.1.1, has already achieved the theoretical resolution limit of 20 nm, and ALS users are now applying it to a variety of problems, in particular the structure of magnetic materials and polymers. Team members are, from left, Rob Duarte, Howard Padmore, Greg Morrison, and Simone Anders. Not pictured: Mike Scheinfein.

Distinguished Visitors

In September 1999, Dominican Republic President Leonel Fernandez Reyna (center) and an entourage of more than 60 people visited the ALS as part of a tour of Berkeley Lab. ALS Division Deputy for Science Neville Smith (right) led the tour, accompanied by Berkeley Lab Director Charles Shank (second from right). President Reyna was in the Bay area to forge new scientific collaborations between the developing research community in the Dominican Republic and local hi-tech industries and research institutions.

The Secretary of Energy Advisory Board (SEAB) visited Berkeley Lab in December 1999 to gain insight into the scientific programs at the ALS and other Lab facilities. ALS Division Deputy for Operations Ben Feinberg gave board members an overview of the ALS from atop the storage-ring shielding.

Ken Goldberg (top, center) of the Center for X-Ray Optics explained the applications of extreme-ultraviolet lithography to SEAB members.
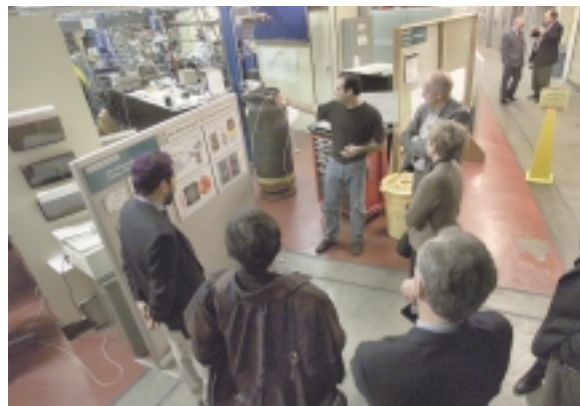
Educational Outreach

The ALS maintained its commitment to educational outreach to the local, national, and international communities over the last year. On-site student tours and special events like UC Berkeley's Cal Day and Berkeley Lab's Daughters and Sons to Work Day provided unique opportunities for members of the local community to learn about the ALS first hand. On a worldwide level, the interactive Web site MicroWorlds continued to educate and entertain teachers and students across the country and around the world.

During Berkeley Lab's Daughters and Sons to Work Day, (above) Thomas Earnest of the Macromolecular Crystallography Facility introduced young visitors to protein structures, while (right) ALS Environment, Health, and Safety Program Manager Georgeanna Perdue discussed the importance of a safe work environment.

The ALS opened its doors to the public again this year as a part of UC Berkeley's Cal Day. Here, David Attwood of the Center for X-Ray Optics conducts a tour around the ALS experiment floor.

ALS Advisory Panels 1999

Science Policy Board

Advises the Berkeley Lab Director on major policy issues concerning the ALS.

William Brinkman, Lucent Technologies/Bell Laboratories
John Carruthers, Intel Corporation
Chien-Te Chen, Synchrotron Radiation Research Center, Taiwan
Peter Eisenberger, Columbia Earth Institute
Paul Fleury, University of New Mexico
Franz J. Himpsel, University of Wisconsin-Madison
Yuan T. Lee, Academia Sinica, Taiwan
Albert Narath, Lockheed Martin Corporation (retired)
Yves Petroff, European Synchrotron Radiation Facility
Z.X. Shen (ex officio), Stanford University

Scientific Advisory Committee

Advises Berkeley Lab and ALS management on issues relating to ALS operations, resource allocation, strategic planning, and Participating Research Team proposals and performance.

David Agard, University of California , San Francisco
David Awschalom, University of California, Santa Barbara
Jeffrey Bokor, University of California, Berkeley
Gordon E. Brown, Jr., Stanford University
Chien-te Chen, Synchrotron Radiation Research Center, Taiwan
Wolfgang Eberhardt, Forschungszentrum Jülich, Germany
Graham Fleming, University of California, Berkeley
Thomas Gallagher, University of Virginia
Charles Harris, University of California, Berkeley
Stephen D. Kevan, University of Oregon
Janos Kirz, State University of New York, Stony Brook
Alan Manceau, Université Joseph Fourier and CNRS, France
Piero Pianetta, Stanford Synchrotron Radiation Laboratory
Zhi-xun Shen, Stanford University
Joachim Stöhr, IBM Almaden Research Center
Louis J. Terminello, Lawrence Livermore National Laboratory
Baylor B. Triplett, Intel Corporation

Users' Executive Committee

Elected by the members of the Advanced Light Source Users' Association to act as the official voice of the user community in its interactions with ALS management.

Paul Alivisatos, University of California, Berkeley
Nora Berrah (Vice Chair), Western Michigan University
Thomas Earnest, Berkeley Lab
Charles S. Fadley, University of California, Davis
Roger Falcone, University of California, Berkeley
David L. Hansen, University of Nevada, Las Vegas
Adam P. Hitchcock, McMaster University
Duane H. Jaecks, University of Nebraska-Lincoln
Stephen D. Kevan (Chair), University of Oregon
Werner Meyer-Ilse (Past Chair), Berkeley Lab
Rupert C. Perera, Berkeley Lab
James H. Underwood, Berkeley Lab

ALS Staff 1999

This is a cumulative list of all those who worked at the ALS at any time during the 1999 calendar year.

Management

D. Chemla	J. Krupnick
B. Feinberg	H. Padmore
Z. Hussain	N. Smith
G. Krebs	

Accelerator Physics

J. Byrd	H. Nishimura
T. Byrne	G. Portmann
S. DeSantis	D. Robin
A. Jackson	C. Steier
C. Kim	Y. Wu
D. Massoletti	

Administration

M. Fenner	J. Slatten
A. Garland	N. Tallcott
L. Howard	S. Vanecek
W. Mitchell	L. Williams
R. Pepe	M. Woods
S. Rossi	

Budget

J. Zelver

Environment, Health & Safety

K. Heinzelman
G. Perdue
R. Statam

Electrical Engineering

S. Austin	M. Chin	L. Jordan	K. Scott
B. Bailey	J. DeVries	J. Julian	L. Shalz
M. Balagot	M. Dwinell	R. Kerns	R. Slater
J. Bancroft	J. Elkins	A. Lindner	J. Spring
K. Baptiste	M. Fahmie	C.C. Lo	R. Steele
W. Barry	K. Fowler	J. Meng	G. Stover
M. Bell	R. Gassaway	P. Molinari	S. Stricklin
A. Biocca	R. Gervasoni	R. Mueller	M. Szabler
J. Bishop	A. Geyer	J. Nomura	B. Taylor
K. Bolin	J. Gregor	F. Ottens	C. Timossi
W. Brown Jr.	J. Hellmers	A. Ritchie	J. Tunis
J. Burch	J. Hinkson	A. Robb	J. Velasco
B. Candelario	C. Ikami	S. Rogoff	K. Woolfe
R. Candelario	S. Jacobson	D. Sandler	E. Yee
P. Casey			

Experimental Systems

H. Ade	E. Harvey	A. MacDowell	N. Tamura
S. Anders	P. Heimann	W. McKinney	A. Warwick
B. Batterman	M. Howells	F. Nolting	A. Young
R. Celestre	S. Irick	J. Patel	W. Yun
J. Feng	A. Lindenberg	A. Scholl	
T. Glover	S. Locklin	J. Spence	

Mechanical Engineering

J. Akre	D. Davis	E. Hoyer	T. Lauritzen	H. Nguyen	R. Schlueter
R. Armstrong	M. Decool	D. Hull	A. Lim	F. Ochoa	N. Searls
W. Baldock	R. DeMarco	D. Jones	B. MacDonell	W. Oglesby	K. Sihler
D. Baum	R. Duarte	N. Kelez	D. MacGill	A. Paterson	C. Stuart
L. Bonifas	K. Franck	N. Kellogg	S. Marks	R. Patton	W. Thur
D. Calais	S. Gavidia	S. Klingler	P. McKean	J. Pepper	E. Wong
D. Cambie	B. Gee	C. Knopf	H. Meyer	P. Piperski	R. Zager
D. Colomb	D. Gibson	J. Kregenow	V. Moroz	D. Plate	J. Zbasnik
C. Corradi	N. Hartman	M. Kritscher	G. Morrison	K. Rex	F. Zucca
C. Cummings	T. Henderson				

Operations

D. Bentsen	M. Monroy
E. Diaz	J. Pusina
O. Jones	B. Samuelson
J. McDonald	T. Scarvie
R. Miller	M. Wolfe

Procedure Center

R. Jones

Project Management

A. Catalano
J. Harkins

Quality Assurance

E. Lampo

Scientific Support

G. Ackerman	L. Erdong	G. Lamble	B. Rude
N. Berrah	Z. Hasan	E. Lu	A. Schlachter
P. Bogdanov	H. Hieslmair	M. Martin	G. Snell
J. Bozek	A. Hitchcock	S. McHugo	W. Stolte
C. Chang	A. Huan	G. Meigs	M. Van Hove
W.T. Cheng	R. Kawakami	E. Moler	Y. Wang
A. Covington	S. Kellar	R. Perera	X. Zhou
J. Denlinger	E. Kukk	E. Rotenberg	X. Zhou

User Services

B. Dixon	A. Greiner	L. Moxon	M. Sibony
S. Fujimura	D. Hamamoto	R. Pepe	L. Tamura
G. Giangrasso	C. Hauck	B. Phillips	J. Tanamachi
K. Gonzalez	A. Marquez	A. Robinson	G. Vierra

Facts and Figures

Using the Advanced Light Source

The ALS, a Department of Energy national user facility, welcomes researchers from universities, industry, and government laboratories. Qualified users have access either as members of participating research teams (PRTs) or as independent investigators. PRTs (groups of researchers with related interests from one or more institutions) construct and operate beamlines and have primary responsibility for experiment endstation equipment. They are entitled to a certain percentage of their beamline's operating time according to the resources contributed by the PRT. Through a peer-reviewed proposal process, the remaining beamtime is granted to independent investigators, who may provide their own endstation or negotiate access to a PRT-owned endstation.

The ALS does not charge users for beam access if their research is nonproprietary. Users performing proprietary research are charged a fee based on full cost recovery for ALS usage. All users are responsible for the day-to-day costs of research (e.g., supplies, phone calls, technical support).

The nominal operating energy of the ALS storage ring is 1.9 GeV, although it can run from 1.0 to 1.9 GeV, allowing flexibility for user operations. At 1.9 GeV, the normal maximum operating current is 400 mA in multibunch operation. The spectral range of undulator and wiggler beamlines extends from photon energies of roughly 5 eV to 21 keV. Bend magnets produce radiation from the infrared to about 20 keV.

The ALS is capable of accommodating approximately 55 beamlines and more than 100 endstations. The first user beamlines began operation in October 1993, and there were 28 operating beamlines, with several more under construction, by the end of 1999.
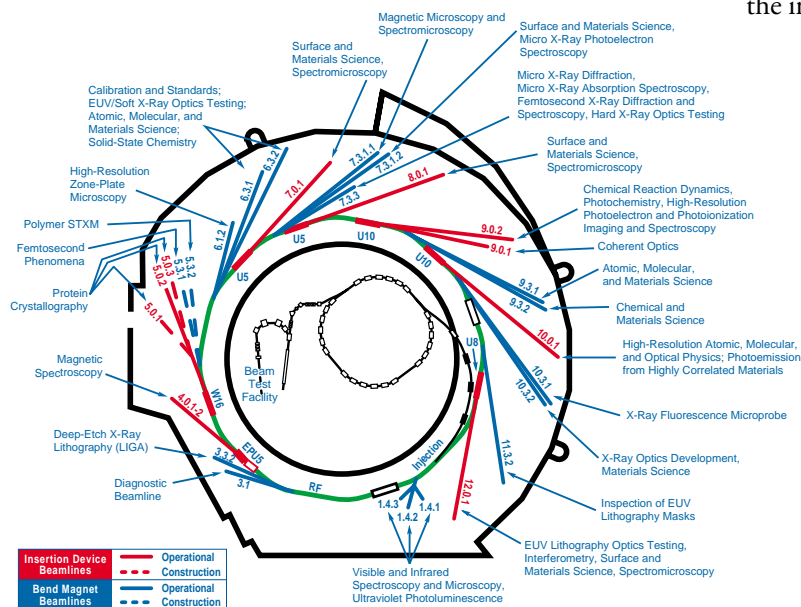
ALS Beamlines*

Beamline	Source	Areas of Research/Techniques	Energy Range	Monochromator	Available
BTF	ALS linac	Beam Test Facility	50 MeV (electrons)	None	Now
1.4.1	Bend magnet	Ultraviolet photoluminescence	1.6–6.2 eV	0.5 m, single grating	Now
1.4.2	Bend magnet	Visible and infrared Fourier transform spectroscopy	0.002–3 eV (15–25,000 cm^{-1})	Interferometer	Now
1.4.3	Bend magnet	Infrared spectromicroscopy	0.05–1 eV (450–10,000 cm^{-1})	Interferometer	Now
3.1	Bend magnet	Diagnostic beamline	200–280 eV	Mirror/filter	Now
3.3.2	Bend magnet	Deep-etch x-ray lithography (LIGA)	1–20 keV	None	Now
4.0.1-2	EPU5 Elliptical polarization undulator	Magnetic spectroscopy	60–1800 eV	Variable-included-angle PGM	Now
5.0.1	W16 Wiggler	Monochromatic protein crystallography	12.4 keV	Curved crystal	2000
5.0.2	W16 Wiggler	Multiple-wavelength (MAD) and monochromatic protein crystallography	3.5–14 keV	Double crystal	Now
5.0.3	W16 Wiggler	Monochromatic protein crystallography	12.4 keV	Curved crystal	2000
5.3.1	Bend magnet	Femtosecond phenomena	0.1–12 keV	Double crystal	2000
5.3.2	Bend magnet	Polymer STXM	150–650 eV	SGM	2000
6.1.2	Bend magnet	High-resolution zone-plate microscopy	300–800 eV	Zone-plate linear	Now
6.3.1	Bend magnet	Calibration and standards, EUV/soft x-ray optics testing, solid-state chemistry	500–2000 eV	VLS-PGM	Now
6.3.2	Bend magnet	Calibration and standards; EUV optics testing; atomic, molecular, and materials science	50–1300 eV	VLS-PGM	Now
7.0.1	U5 Undulator	Photoelectron spectroscopy and imaging (SPEM)	200–800 eV	SGM	Now
		Absorption-contrast near-edge x-ray absorption fine structure imaging (STXM)	180–900 eV	SGM	Now
		High-resolution, angle-resolved photoelectron spectroscopy (UltraESCA)	60–1200	SGM	Now
		Fluorescence spectroscopy	50–1200 eV	SGM	Now
7.3.1.1	Bend magnet	Magnetic microscopy, spectromicroscopy	175–1500 eV	SGM	Now
7.3.1.2	Bend magnet	Surface and materials science, micro–x-ray photoelectron spectroscopy	175–1500 eV	SGM	Now
7.3.3	Bend magnet	Micro–x-ray diffraction; micro–x-ray absorption spectroscopy; femtosecond laser-driven x-ray diffraction and absorption spectroscopy; hard x-ray optics testing	1.8–14 keV	White light, two or four crystal	Now
8.0.1	U5 Undulator	X-ray photoelectron spectroscopy, angle-resolved photoelectron spectroscopy, near-edge x-ray absorption fine structure spectroscopy	65–1400 eV	SGM	Now
		Soft x-ray fluorescence, near-edge x-ray absorption fine structure spectroscopy	65–1400 eV	SGM	Now
9.0.1	U10 Undulator	Coherent optics experiments	200–800 eV	None	Now
9.0.2	U10 Undulator	Chemical reaction dynamics, photochemistry	5–30 eV	None	Now
		High-resolution photoelectron and photoionization spectroscopy	5–30 eV	Off-plane Eagle	Now
		Photoelectron and photoionization imaging and spectroscopy	5–30 eV	Off-plane Eagle	Now
9.3.1	Bend magnet	Atomic, molecular, and materials science	2.2–6 keV	Double crystal	Now
9.3.2	Bend magnet	Chemical and materials science, circular dichroism, spin resolution	30–1500 eV	SGM	Now
10.0.1	U10 Undulator	Photoemission from highly correlated materials	17–340 eV	SGM	Now
		High-resolution atomic and molecular electron spectrometer	17–340 eV	SGM	Now
		Electron spin polarization analysis	17–340 eV	SGM	Now
		Photoionization of ions: cross-section and excitation spectrum measurements	17–340 eV	SGM	Now
10.3.1	Bend magnet	X-ray fluorescence microprobe	3–20 keV	White light, multilayer	Now
10.3.2	Bend magnet	X-ray optics development, materials science	3–20 keV	White light, four crystal	Now
11.3.2	Bend magnet	Inspectrion of EUV lithography masks	50–1000 eV	VLS-PGM	Now
12.0.1	U8 Undulator	Surface and materials science, spectromicroscopy	95&130 eV	VLS-PGM	Now
		EUV optics testing, interferometry, coherent optics	60–320 eV	VLS-PGM	Now
		EUV optics testing, interferometry, coherent optics	60–320 eV	VLS-PGM	Now

*This table is valid as of January 2000. The most current information on ALS beamlines is available on the World Wide Web (http://www-als.lbl.gov/als/als_users_bl/bl_table.html).

ALS Insertion Device Parameters

Device	Beamline	Status	Energy Range (at 1.5 GeV)	Energy Range (at 1.9 GeV)	Period Length	Number of Periods	Operating Gap Range	Peak Effective Field Range
U5 Undulator	8.0	Operational	130–1900 eV	210–3000 eV	5.0 cm	89	1.4–4.5 cm	0.46–0.10 T
U5 Undulator	7.0	Operational	50–1900 eV	80–3000 eV	5.0 cm	89	1.4–4.5 cm	0.85–0.10 T
U8 Undulator	12.0	Operational	18–1200 eV	30–1900 eV	8.0 cm	55	2.5–8.3 cm	0.80–0.07 T
U10 Undulator	9.0	Operational	5–950 eV	8–1500 eV	10.0 cm	43	2.4–11.6 cm	0.98–0.05 T
U10 Undulator	10.0	Operational	8–950 eV	12–1500 eV	10.0 cm	43	2.4–11.6 cm	0.80–0.05 T
EPU5 Elliptical Polarization Undulator	4.0	Operational	60–1000 eV*	100–1500 eV*	5.0 cm	37	1.45–5.5 cm	0.79–0.10 T (vertical field) 0.54–0.10 T (horizontal field)
W16 Wiggler	5.0	Operational	5–13 keV	5–21 keV	16.0 cm	19	1.4–18.0 cm	0.03–2.1 T

* Elliptical polarization mode

ALS Storage Ring Parameters

Parameter	Value
Beam particle	electron
Beam energy	1.0–1.9 GeV
Injection energy	1.0–1.5 GeV
Beam current	
multibunch mode	400 mA
two-bunch mode	2 × 30 mA
Filling pattern (multibunch mode)	272 bunches (variable) possibility of 10-mA "camshaft" bunch in filling gap
Bunch spacing	
multibunch mode	2 ns
two-bunch mode	328 ns
Circumference	196.8 m
Number of straight sections	12
Current number of insertion devices	7
Radio frequency	499.664 MHz
Beam size in straight sections, rms	250 microns horiz. × 20 microns vert. at 1.9 GeV
Natural emittance	5.5 nm-rad at 1.9 GeV
Energy spread ($\Delta E/E$, rms)	8×10^{-4} at 1.9 GeV

Parameter	Value at 1.5 GeV	Value at 1.9 GeV
Beam lifetime		
multibunch mode*	~4.0 hours at 400 mA	~6.0 hours at 400 mA†
two-bunch mode	not used	~1.0 hour at 40 mA
Horizontal emittance	3.5 nm-rad	5.5 nm-rad
Vertical emittance‡	0.3 nm-rad	0.2 nm-rad

*In multibunch mode, the storage ring is typically filled every six hours or as requested by our users.

†Using two of the third-harmonic cavities to increase the bunch length by 30–50%.

‡Vertical emittance is deliberately increased to improve beam lifetime.

1999 Publications

Beamline 1.4

Byrd, J.M., M.C. Martin, and W.R. McKinney, "Observing beam motion using infrared interferometry," in *Proceedings of the 1999 IEEE Particle Accelerator Conference* (New York, March 27–April 2, 1999).

Effey, B., "Neutron inelastic scattering from selenium-arsenic-germanium glasses," Ph.D. thesis, Ohio University, 1999.

Ghosh, U., R. Luthy, S. Gillette, R. Zare, and J. Talley, "Bioremediation technologies for polycyclic aromatic hydrocarbon compounds," in *In Situ and On-Site Bioremediation*, Proceedings of The Fifth International Symposium (San Diego, April 19–22, 1999).

Ghosh, U., R.G. Luthy, J.S. Gillette, R.N. Zare, and J.W. Talley, "Microscale characterization of PAH sequestration on sediments," in *In Situ and On-Site Bioremediation*, Proceedings of The Fifth International Symposium (San Diego, April 19–22, 1999).

Holman, H.-Y.N., D.L. Perry, M.C. Martin, G.M. Lamble, W.R. McKinney, and J.C. Hunter-Cevera, "Real-time characterization of biogeochemical reduction of Cr(VI) on basalt surfaces by SR-FTIR imaging," *Geomicrobiology J.* **16**(4), 307–324 (November 1999).

Holman, H.-Y.N., M. Zhang, R. Goth-Goldstein, M. Russell, M. Martin, W.R. McKinney, M. Ferrari, and J. Hunter-Cevera, "Detecting exposure to environmental organic toxins in individual cells: Towards the development of a micro-fabricated device," in *SPIE Photonics West BiOS'99 International Biomedical Optics Symposium* (San Jose, California, January 18–21, 1999).

Luthy, R., and U. Ghosh, "Analytical tools to assess sequestration and bioavailability of organic compounds," in *Proceedings of Association of Environmental Engineering and Science Professors, Research Frontiers Conference* (State College, Pennsylvania, August 1–3, 1999).

Raab, T.K., and M.C. Martin, "Can we see through the Black Box? Mid IR spectromicroscopy of intact root zones at a synchrotron light source," in *Proceedings of Biennial Soil Ecology Society Meeting* (Chicago, May 23–26, 1999).

Shan, W., J.W. Ager III, K.M. Yu, W. Walukiewicz, E.E. Haller, M.C. Martin, W.R. McKinney, and W. Wang, "Dependence of the fundamental band gap of $Al_xGa_{1-x}N$ on alloy composition and pressure," *J. Appl. Phys.* **85**(12), 8505–8507 (June 1999).

Beamline 3.1

Byrd, J., "Beam-based characterization of coupled-bunch instabilities," in *The Handbook of Accelerator Physics and Engineering* (World Scientific, Singapore, 1999).

Byrd, J., "Bunched-beam signals in time and frequency domain," in *Beam Measurement, Proceedings of the Joint US-CERN-Japan-Russia Accelerator School* (World Scientific, Singapore, 1999).

Byrd, J.M., "Effects of phase noise in heavily beam loaded storage rings," in *Proceedings of the IEEE Particle Accelerator Conference* (New York, March 27–April 2, 1999).

Byrd, J., "Maximizing integrated brightness in Touschek-dominated synchrotron light sources," *Nucl. Instrum. Methods* **427**(3), 614–621 (May 1999).

Byrd, J., "Spectrum and network analyzers," in *Beam Measurement, Proceedings of the Joint US-CERN-Japan-Russia Accelerator School* (World Scientific, Singapore, 1999).

Byrd, J., W.H. Cheng, S. De Santis, D. Li, G. Stupakov, and F. Zimmermann, "Nonlinear longitudinal dynamics studies at the Advanced Light Source," in *Proceedings of the IEEE Particle Accelerator Conference* (New York, March 29–April 2, 1999).

Byrd, J., M.C. Martin, and W.R. McKinney, "Beam diagnostics using infrared synchrotron radiation," in *Proceedings of the IEEE Particle Accelerator Conference* (New York, March 27–April 2, 1999).

De Santis, S., A. Mostacci, L. Palumbo, and B. Spataro, "Impedance of a long slot in a coaxial beam pipe," in *Proceedings of the IEEE Particle Accelerator Conference* (New York, March 27–April 2, 1999).

Decking, W., and D. Robin, "Dynamic aperture measurements at the Advanced Light Source," in *Proceedings of the IEEE Particle Accelerator Conference* (New York, March 27–April 2, 1999).

Forest, E., and D. Robin, "Maps for distributions and their time evolution," *Phys. Rev. E* **60**(4), 4793–4810 (October 1999).

Kamps, T., R. Lorenz, and S. De Santis, "Microwave characterization of the waveguuide BPM," in *Proceedings of the IEEE Particle Accelerator Conference* (New York, March 27–April 2, 1999).

Lo, C.C., K. Baptiste, J. Byrd, J. Julian, and R. Rimmer, "The rf system for the 3rd harmonic cavity of Advanced Light Source," in *Proceedings of the IEEE Particle Accelerator Conference* (New York, March 27–April 2, 1999).

Portmann, G.J., "Slow orbit feedback at the Advanced Light Source using Mat-lab," in *Proceedings of the IEEE Particle Accelerator Conference* (New York, March 27–April 2, 1999).

Robin, D., and H. Nishimura, "Impact of superbends at the Advanced Light Source," in *Proceedings of the IEEE Particle Accelerator Conference* (New York, March 27–April 2, 1999).

Robin, D., J. Safranek, and W. Decking, "Realizing the benefits of restored periodicity in the Advanced Light Source," *Phys. Rev. ST Accel. Beams* **2**(4), 044001 (April 1999).

Zholents, A.A., J. Byrd, S. Chattopadyay, H. Chong, T.E. Glover, P.A. Heimann, R.E. Schoenlein, C.V. Shank, and M. Zolotorev, "Development of a source of femtosecond x-ray pulses based on the electron storage ring," in *Proceedings of the IEEE Particle Accelerator Conference* (New York, March 29–April 2, 1999).

Zholents, A., P.A. Heimann, M. Zolotorev, and J. Byrd, "Generation of subpicosecond x-ray pulses using RF orbit deflection," *Nucl. Instrum. Methods Phys. Res. A* **425**(1), 385–389 (April 1999).

Beamline 3.3.2

Boehme, D., J. Hruby, W.D. Bonivert, M.A. Bankert, J.T. Hackman, A.M. Morales, D.M. Skala, S.K. Griffiths, A. Ting, T.E. Bennet, J.S. Krafcik Jr., S.D. Leith, and D. Chinn, "LIGA R&D and prototyping," in *Proceedings of SEMICONWEST* (San Francisco, July 14, 1999).

Griffiths, S.K., J.M. Hruby, and A. Ting, "Optimum doses and mask thickness for synchrotron exposure of PMMA resists," in *Symposium on Design, Test, and Microfabrication of MEMS and MOEMS*, Proceedings of SPIE Conference, (Paris, France, March 30–April 1, 1999).

Griffiths, S.K., A. Ting, and J.M. Hruby, "The influence of mask substrate thickness on exposure and development times for LIGA process," in *HARMST 1999*, Proceedings of Third International Conference on High Aspect Ratio Microstructure Technology (Chiba, Japan, June 13–15, 1999).

Hruby, J., M.A. Bankert, T.E. Bennett, D.R. Boehme, W.D. Bonivert, S.K. Griffiths, J.T. Hachaman, J.S. Krafcik Jr., A.M. Morales, and A. Ting, "LIGA prototyping at Sandia National Laboratories," in *HARMST 1999*, Proceedings of Third International Conference on High Aspect Ratio Microstructure Technology (Chiba, Japan, June 13–15, 1999).

Hruby, J.M., S.K. Griffiths, I.A. Domeier, A.M. Morales, D.R. Boehme, M.A. Bankert, W.D. Bonivert, J.T. Hachman, D.M. Skala, and A. Ting, "LIGA: metal, plastics, and ceramics," in *Micromachining and Microfabrication Process Technology V*, Proceedings of SPIE Conference (Santa Clara, California, September 20–22, 1999).

Kim, H.K., K. Jackson, W.S. Hong, I.J. Park, S.H. Han, J. Kadyk, V. Perez-Mendez, W. Wenzel, and G. Cho, "Application of the LIGA process for fabrication of gas avalanche devices," in *IEEE Transactions on Nuclear Science*, Proceedings of IEEE Nuclear Science and Medical Imaging Symposium (Seattle, October 26–28, 1999).

Beamline 4.0.1

Snell, G.P., B. Langer, E. Kukk, and N. Berrah, "Spin-resolved auger spectroscopy of xenon," in *Proceedings of XXI International Conference on the Physics of Electronic and Atomic Collision*s (Sendai, Japan, July 22–27, 1999).

Beamline 5.0.2

Bilwes, A., L.A. Alex, B. Crane, and M. Simon, "Structure of cheA, a signal-transducing histidine kinase," *Cell* **96**, 131–141 (January 1999).

Cate, J.H., M.M. Yusupov, G.Zh. Yusupova, T.N. Earnest, and H.F. Noller, "X-ray crystal structures of 70s ribosome functional complexes," *Science* **285**(5436), 2095–2104 (September 1999).

Chen, Y., C. Wiesmann, G. Fuh, B. Li, H.W. Christinger, P. McKay, A.M. de Vos, and H.B. Lowman, "Selection and analysis of an optimized anti-VEGF antibody: Crystal structure of an affinity-matured Fab in complex with antigen," *J. Mol. Biol.* **293**(4), 865–881 (November 1999).

Crane, B.R., R.J. Rosenfeld, A.S. Arvai, D.K. Ghosh, S. Ghosh, J.A. Tainer, D.J. Stuehr, and E.D. Getzoff, "N-terminal domain swapping and metal ion binding in nitric oxide synthase dimerization," *EMBO J.* **18**(22), 6271–6281 (November 1999).

Crowder, S.M., R. Kanaar, D.C. Rio, and T. Alber, "Absence of interdomain contacts in the crystal structure of the RNA recognition motifs of sex-lethal," *Proc. Natl. Acad. Sci. U.S.A.* **96**(9), 4892–4897 (April 1999).

Culver, G.M., J.H. Cate, G.Z. Yusupova, M.M. Yusupov, and H.F. Noller, "Identification of an RNA–protein bridge spanning the ribosomal subunit interface," *Science* **285**(5436), 2133–2136 (September 1999).

Dessen, A., J. Tang, H. Schmidt, M. Stahl, J.D. Clark, J. Seehra, and W.S. Somers, "Crystal structure of human cytosolic phospholipase A$_2$ reveals a novel topology and catalytic mechanism," *Cell* **97**, 349–360 (April 1999).

Galburt, E.A., B.L. Stoddard, et al., "A novel structural mechanism of DNA cleavage visualized by intermediate trapping: I-PpoI," *Nat. Struct. Biol.* **6**(12), 1096–1099 (December 1999).

Greenwald, J., W.H. Fischer, W.W. Vale, and S. Choe, "Three-finger toxin fold for the extracellular ligand-binding of the type II activin receptor serine kinase," *Nat. Struct. Biol.* **6**(1), 18–22 (January 1999).

Han, S., J.A. Craig, C.D. Putnam, N.B. Carozzi, and J.A. Tainer, "Evolution and mechanism from structures of an ADP-ribosylating toxin and NAD complex," *Nat. Struct. Biol.* **6**(10), 932–936 (October 1999).

Harris, S.F., and M.R. Botchan, "Crystal structure of the human papillomavirus type 18 E2 activation domain," *Science* **284**(5420), 1673–1677 (June 1999).

Hillier, B.J., K.S. Christopherson, K.E. Prehoda, D.S. Bredt, and W.A. Lim, "Unexpected modes of PDZ domain scaffolding revealed by structure of nNOS-syntrophin complex," *Science* **284**(5415), 812–815 (April 1999).

Huang, L., E.R.E. Kinnucan, G.L. Wang, S. Beaudenon, P.M. Howley, J.M. Huibregtse, and N.P. Pavletich, "Structure of an E6AP–UbcH7 complex: Insights into ubiquitination by the E2–E3 enzyme cascade," *Science* **286**(5443), 1321–1326 (November 1999).

Hwang, K.Y., C-S. Cho, S.S. Kim, H-C. Sung, Y.G. Yu, and Y. Cho, "Structure and mechanism of glutamate racemase from aquifex pyrophilus," *Nat. Struct. Biol.* **6**(5), 422–426 (May 1999).

Hymowitz, S.G., H.W. Christinger, G. Fuh, M.H. Ultsch, M.P. O'Connell, R.F. Kelley, A. Ashkenazi, and A.M. de Vos, "Triggering cell death: Crystal structure of Apo2L/TRAIL in complex with death receptor 5," *Mol. Cell* **4**(4), 563–571 (October 1999).

Iverson, T.M., C. Luna-Chavez, G. Cecchini, and D.C. Rees, "Structure of the E. coli fumarate reductase respiratory complex," *Science* **284**(5422), 1961–1966 (June 1999).

Lee, Y.-H., R.K. Deka, M.V. Norgard, J.D. Radolf, and C.A. Hasemann, "Treponema pallidum TroA is a periplasmic zinc-binding protein with a helical backbone," *Nat. Struct. Biol.* **6**(7), 628–633 (July 1999).

Li, H., C.S. Raman, C.B. Blasko, T.A. Young, J.F. Parkinson, M. Whitlow, and T.L. Poulos, "Crystal structure of zinc-free and -bound heme domain of human inducible nitric-oxide synthase," *J. Biol. Chem.* **274**(30), 21276–21284 (July 1999).

Lovejoy, B., A.R. Welch, S. Carr, C. Luong, C. Broka, R.T. Hendricks, J.A. Campbell, K.A.M. Walker, R. Martin, H. Van Wart, and M.F. Browner, "Crystal structures of MMP-1 and -13 reveal the structural basis for selectivity of collagenase inhibitors," *Nat. Struct. Biol.* **6**(3), 217–221 (March 1999).

Luecke, H., B. Schobert, H. Richter, J.-P. Cartailler, and J.K. Lanyi, "Structure of bacteriorhodopsin at 1.55 Å resolution," *J. Mol. Biol.* **291**(4), 899–911 (August 1999).

Luecke, H., B. Schobert, H.-T. Richter, J.-P. Cartailler, J.K. Lanyi, et al., "Structural changes in bacteriorhodopsin during ion transport at 2 Å resolution," *Science* **286**(5438), 255–260 (October 1999).

Malashkevich, V. et al ., "Core structure of the envelope glycoprotein GP2 from ebola virus at 1.9-Å resolution," *Proc. Natl. Acad. Sci. U.S.A.* **96**(6), 2662–2667 (March 1999).

McWhirter, S. , S. Pullen, J.M. Holton, J. Crute, M. Kehry, and T. Alber, "Crystallographic analysis of CD40 recognition and signaling by human TRAF2," *Proc. Natl. Acad. Sci. U.S.A.* **96**, 8408–8413 (July 1999).

Poulos, T.L., H. Li, and C.S. Raman, "Heme mediated oxygen activation in biology: Cytochrome c oxidase and nitric oxide synthase," *Curr. Opin. Chem. Biol.* **3**, 131–137 (January 1999).

Pratt, K.P., B.W. Shen, K. Takeshima, E.W. Davie, K. Fujikawa, B.L. Stoddard, et al., "Structure of the C2 domain of human factor VIII at 1.5 Å resolution," *Nature* **402**(6760), 439–442 (November 1999).

Prehoda, K., D. Lee, and W.A. Lim, "Structure of the enabled/VASP homology 1 domain–peptide complex: A key component in the spatial control of actin assembly," *Cell* **97**(4), 471–480 (May 1999).

Rice, L.M., and A.T. Brunger, "Crystal Structure of the vesicular transport protein Sec17: Implications for SNAP function in SNARE complex disassembly," *Mol. Cell* **4**(1), 85–95 (July 1999).

Robinson, R.C., M. Mejillano, V.P. Le, L.D. Burtnick, H.L. Yin, and S. Choe, "Domain movement in gelsolin: A calcium-activated switch," *Science* **286**(5446), 1939–1942 (December 1999).

Spiller, B., A. Gershenson, F.H. Arnold, and R.C. Stevens, "A structural view of evolutionary divergence," *Proc. Natl. Acad. Sci. U.S.A.* **96**(22), 12305–12310 (October 1999).

Thanos, C.D., K.E. Goodwill, and J.U. Bowie, "Oligomeric structure of the human EphB2 receptor SAM domain," *Science* **283**(5403), 833–836 (February 1999).

Wiesmann, C., M.H. Ultsch, S.H. Bass, and A.M. de Vos, "Crystal structure of NGF in complex with the ligand-binding domain of the TrkA receptor," *Nature* **401**(6749), 184–188 (September 1999).

Wiesmann, C., M.H. Ultsch, and A. de Vos, "Crystal structure of NGF in complex with the ligand-binding domain of the TrkA receptor," in *Proceedings of The 14th West Coast Protein Crystallography Workshop* (Pacific Grove, California, March 14–17, 1999).

Xiao, T., P. Towb, S.A. Wasserman, and S.R. Sprang, "Three-dimensional structure of a complex between the death domains of Pelle and Tube," *Cell* **99**(5), 545–555 (November 1999).

Ybe, J.A., F.M. Brodsky, K. Hofmann, K. Lin, S.H. Liu, L. Chen, T.N. Earnest, R.J. Fletterick, and P.K. Hwang,

"Clathrin self-assembly is mediated by a tandemly repeated superhelix," *Nature* **399**(6734), 371–375 (May 1999).

Yu, R.C., R. Jahn, and A.T. Brunger, "NSF N-terminal domain crystal structure: Models of NSF function," *Mol. Cell* **4**, 97–107 (July 1999).

Beamline 6.1.2

Denbeaux, G., "Soft x-ray full field spectromicroscopy," Ph.D. thesis, Duke University, 1999.

Gilbert, E.S., A.V. Khlebnikov, W. Meyer-Ilse, and J.D. Keasling, "Use of soft x-ray microscopy for analysis of early-stage biofilm formation," *Water Science and Technology* **39**(7), 269–272 (January 1999).

Kurtis, K.E., P.J.M. Monteiro, J.T. Brown, and W. Meyer-Ilse, "Analysis of deterioration products developed in large concrete dams by high resolution transmission soft x-ray microscopy," *Journal of Microscopy* **196**(1), 288–298 (December 1999).

Meyer-Ilse, W., "X-ray Microscopy and Microanalysis," in *Encyclopedia of Applied Physics*, edited by G.L. Trigg, (VCH, Weinheim, 1999), pp. 673–691.

Myneni, S.C., J.T. Brown, G.A. Martinez, and W. Meyer-Ilse, "Imaging of humic substance macromolecular structures in water and soils," *Science* **286**(5443), 1335–1337 (November 1999).

Beamline 6.3.2

Bajt, S., R.D. Behymer, P. Mirkarimi, C. Montcalm, M.A. Wall, M. Wedowski, and J.A. Folta, "Experimental investigation of beryllium-based multilayer coatings for extreme ultraviolet lithography," in *EUV, X-Ray and Neutron Optics and Sources*, Proceedings of SPIE Conference (Denver, July 21–23, 1999).

Burkhart, S., C. Cerjan, P. Kearney, P. Mirkarimi, C. Walton, and A. Ray-Chaudhuri, "Low-defect reflective mask blanks for extreme ultraviolet lithography," in *Emerging Lithographic Technologies III*, Proceedings of SPIE's 24th International Society for Optical Engineering (Santa Clara, California, March 14–19, 1999).

Folta, J., S. Bajt, T. Barbee, T.W. Grabner Jr., P.B. Mirkarimi, T. Nguyen, M.A. Schmidt, S.C. Spiller, C.C. Walton, M. Wedowski, C. Montcalm, et al ., "Advances in multilayer reflective coatings for extreme-ultraviolet lithography," in *Emerging Lithographic Technologies III*, Proceedings of SPIE's 24th International Society for Optical Engineering (Santa Clara, California, March 14–19, 1999).

Gullikson, E.M., and D.G. Stearns, "Asymmetric extreme ultraviolet scattering from sputter-deposited multilayers," *Phys. Rev. B* **59**(20), 13273–13277 (May 1999).

Kortright, J., D. Awschalom, J. Stöhr, S.D. Bader, Y.U. Idzerda, S.S. Parkin, I.K. Schuller, and H.-C. Siegmann, "Research frontiers in magnetic materials at soft x-ray synchrotron radiation facilities," *J. Magn. Magn. Mater.* **207**(1–3), 7–44 (December 1999).

Mangat, P.J.S., S.D. Hector, M.A. Thompson, W.J. Dauksher, J. Cobb, K. Cummings, D.P. Mancini, D.J. Resnick, G. Cardinale, C. Henderson, P. Kearney, and M. Wedowski, "Extreme ultraviolet lithography mask patterning and printability studies with a Ta-based absorber," *J. Vac. Sci. Technol. B* **17**(6), 3029–3033 (November–December 1999).

Mirkarimi, P., "Stress, reflectance, and temporal stability of sputter-deposited Mo/Si and Mo/Be multilayer films for extreme ultraviolet lithography," *Optical Engineering* **38**(7), 1246–1259 (January 1999).

Montcalm, C., R.F. Grabner, R.M. Hudyma, M.A. Schmidt, E.A. Spiller, C.C. Walton, M. Wedowski, and J.A. Folta, "Multilayer coated optics for an alpha-class extreme ultraviolet lithography system," in *EUV, X-ray and Neutron Optics and Sources*, Proceedings of SPIE Conference (Denver, July 21–23, 1999).

Montcalm, C., E. Spiller, M. Wedowski, E. Gullikson, and J. Folta, "Multilayer coatings of 10× projection optics for extreme-ultraviolet lithography," in *Emerging Lithographic Technologies III*, Proceedings of SPIE's 24th International Society for Optical Engineering (Santa Clara, California, March 14–19, 1999).

Sacchi, M., C.F. Hague, S. Gota, E. Guiot, M. Gautier-Soyer, L. Pasqualid, S. Mrowka, E.M. Gullikson, and J.H.

Underwood, "Resonant scattering of polarized soft x-rays for the study of magnetic oxide layers," *J. Electron Spectros. Relat. Phenom.* **103**, 407–412 (June 1999).

Sacchi, M., A. Mirone, C.F. Hague, J.-M. Mariot, L. Pasquali, P. Isberg, E.M. Gullikson, and J.H. Underwood, "Soft-x-ray resonant scattering from V/Fe(001) magnetic superlattices," *Phys. Rev. B* **60**(18), 12569–12572 (November 1999).

Soufli, R., S. Bajt, and E.M. Gullikson, "Optical constants of beryllium from photoabsorption measurements for x-ray applications," in *EUV, X-ray and Neutron Optics and Sources*, Proceedings of SPIE Conference (Denver, July 21–23, 1999).

Wedowski, M., S. Bajt, J.A. Folta, E. Gullikson, U. Kleineberg, L.E. Klebanoff, M.E. Malinowski, and W.M. Clift, "Lifetime studies of Mo/Si and Mo/Be multilayer coatings for extreme ultraviolet lithography," in *EUV, X-ray and Neutron Optics and Sources*, Proceedings of SPIE Conference (Denver, July 21–23, 1999).

Yamazaki, T., E.M. Gullikson, N. Miyata, M. Koike, Y. Harada, S. Mrowka, U. Kleineberg, J.H. Underwood, M.M. Yanagihara, and K. Sano, "Comparison of mechanically ruled versus holographically varied line-spacing gratings for a soft-x-ray flat-field spectrograph.," *Appl. Opt.* **38**(19), 4001–4003 (July 1999).

Yan, P., G. Zhang, P. Kofron, J. Chow, A. Stivers, E. Tejnil, G. Cardinale, and P. Kearney, "EUV mask patterning approaches," in *Emerging Lithographic Technologies III*, Proceedings of SPIE's 24th International Society for Optical Engineering (Santa Clara, California, March 14–19, 1999).

Beamline 7.0.1

Baumgartel, P., J.J. Paggel, M. Hasselblatt, K. Horn, V. Fernandez, O. Schaff, J.H. Weaver, A.M. Bradshaw, D.P. Woodruff, and E. Rotenberg, "Structure determination of $(\sqrt{3} \times \sqrt{3})R30°$ boron phase on the Si(111) surface using photoelectron diffraction," *Phys. Rev. B* **59**(20), 13014–13019 (May 1999).

Butorin, S.M., M. Magnuson, K. Ivanov, D.K. Shuh, T. Takahashi, S. Kunii, J.-H. Guo, and J. Nordgren, "Resonant inelastic soft-x-ray scattering at the 4d edge of Ce-based heavy-fermion materials," *J. Electron Spectros. Relat. Phenom.* **103**, 783–786 (June 1999).

Denlinger, J.D., G.-H. Gweon, J.W. Allen, J. Marcus, and C. Schlenker, "High-energy angle-resolved photoemission of $NaMo_6O_{17}$," *J. Electron Spectros. Relat. Phenom.* **101–103**, 805–810 (Spring 1999).

Denlinger, J.D., J.W. Allen, S.-H. Yang, S.-J. Oh, E.-J. Cho, W.P. Ellis, D.A. Gajewski, R. Chau, and M.B. Maple, "Fermi-energy 5f spectral weight growth in $Y_{1-x}U_xP_3$," *Physica B* **261**, 1130–1131 (January 1999).

Gunnelin, K.M., "A soft x-ray emission study of the electronic structure of molecules," Ph.D. thesis, Uppsala University, 1999.

Gunnelin, K.M., P.N. Glans, J. Rubensson, C. Såthe, J.E. Nordgren, Li Yang, F. Gel'mukhanov, and H. Ågren, "Bond-length-dependent core hole localization observed in simple hydrocarbons," *Phys. Rev. Lett.* **83**(7), 1315–1318 (August 1999).

Guo, J.H., W.T. Zheng, C. Såthe, N. Hellgren, J. Nordgren, et al., "Spectroscopic study of CN_x films grown by magnetron sputter deposition," *J. Electron Spectros. Relat. Phenom.* **103**, 551–554 (June 1999).

Hjörvarsson, B., J. Guo, G. Andersson, R.C.C. Ward, R. Ahuja, O. Eriksson, C. Såthe, A. Agui, S. Butorin, and J.E. Nordgren, "Probing the local electronic structure in the H induced metal-insulator transition of Y," *J. Phys.: Condens. Matter* **11**, 119 (March 1999).

Hochstrasser, M., F.O. Schumann, R.F. Willis, T. Cummins, G.D. Waddill, S.R. Mishra, J.G. Tobin, and E. Rotenberg, "Fermi surface study of pseudomorphic $Fe_{1-x}Ni_x$ and $Co_{1-x}Ni_x$ thin films on Cu(100)," *J. Vac. Sci. Technol. A* **17**(4), 1322–1325 (July 1999).

Hochstrasser, M., N. Gilman, R.F. Willis, F.O. Schumann, J.G. Tobin, and E. Rotenberg,

"Photoemission study of Fermi surfaces of pseudomorphic Co, Ni, and Co_xNi_{1-x} films on Cu(100)," *Phys. Rev. B* **60**(24), 17030–17036 (December 1999).

Kawakami, R., "Quantum confinement and symmetry breaking in layered magnetic nanostructures," Ph.D. thesis, University of California, Berkeley, 1999.

Kawakami, R.K., E. Rotenberg, H.-J. Choi, E. Escorcia-Aparicio, M.O. Brown, J. Wolfe, E. Arenholz, Z.D. Zhang, N.V. Smith, and Z.Q. Qiu, "Quantum-well states of the Cu/Co(100) system probed by a thin Ni layer," *Nature* **398**(6723), 132–134 (March 1999).

Kawakami, R.W., E. Rotenberg, E.J. Escorcia-Aparicio, H.-J. Choi, J.H. Wolfe, N.V. Smith, and Z.Q. Qiu, "Determination of the magnetic coupling in the Co/Cu./Co(100) system with momentum-resolved quantum well states," *Phys. Rev. Lett.* **82**(20), 4098–4101 (May 1999).

Kortright, J., M. Rice, S.-K. Kim, C.C. Walton, and T. Warwick, "Optics for element-resolved soft x-ray magneto-optical studies," *J. Magn. Magn. Mater.* **191**(1–2), 79–89 (January 1999).

Magnuson, M., J. Guo, S. Butorin, A. Agui, C. Såthe, J. Nordgren, and A. Monkman, "The electronic structure of polyaniline and doped phases studied by soft x-ray absorption and emission spectroscopies," *J. Chem. Phys.* **111**(10), 4756–4761 (September 1999).

Magnuson, M., J. Guo, C. Såthe, J. Rubensson, J.E. Nordgren, P.N. Glans, Li Yang, P. Salek, and H. Ågren, "Competition between decay and dissociation of core-excited carbonyl sulfide studied by x-ray scattering," *Phys. Rev. A* **59**, 4281–4288 (June 1999).

Magnuson, M., Li Yang, J. Guo, C. Såthe, A. Agui, J.E. Nordgren, Yi Luo, H. Ågren, N. Johansson, W. Salaneck et al ., "Resonant inelastic soft-x-ray scattering spectra at the nitrogen and carbon K-edges of poly(pyridine-2,5-diyl)," *J. Electron Spectros. Relat. Phenom.* **101–103**, 573–578 (May 1999).

Mishra, S.R., T.R. Cummins, G.D. Waddill, W.J. Gammon, J.G. Tobin, et al., "Linear dichroism and

resonant photoemission in Gd," *J. Magn. Magn. Mater.* **199**, 647–649 (June 1999).

Mishra, S.R., T.R. Cummins, W.J. Gammon, G. van der Laan, K.W. Goodman, and J.G. Tobin, "Investigation of resonant photoemission in Gd with x-ray linear dichroism," *J. Vac. Sci. Technol. A* **17**(4), 1313–1318 (July 1999).

Price, A.C., L.B. Sorensen, S.D. Kevan, J. Toner, A. Poniewierski, and R. Holyst, "Coherent soft-x-ray dynamic light scattering from smectic-A films," *Phys. Rev. Lett.* **84**(4), 755–758 (January 1999).

Püttner, R., I. Dominguez, T.J. Morgan, C. Cisneros, R.F. Fink, E. Rotenberg, T. Warwick, M. Domke, G. Kaindl, and A.S. Schlachter, "Vibrationally resolved O 1s core-excitation spectra of CO and NO," *Phys. Rev. A* **59**(5), 3415–3423 (May 1999).

Rotenberg, E., J.W. Chung, and S.D. Kevan, "Spin-orbit coupling induced surface band splitting in Li/W(110) and Li/Mo(110)," *Phys. Rev. Lett.* **82**(20), 4066–4069 (May 1999).

Rothe, J., E.M. Kneedler, K.H. Pecher, B.P. Tonner, K.H. Nealson, T. Grundl, W. Meyer-Ilse, and T. Warwick, "Spectromicroscopy of Mn distributions in micronodules produced by biomineralization," *Journal of Synchrotron Radiation* **6**(3), 359–361 (May 1999).

Schaefer, J.H., E. Rotenberg, G. Meigs, S.D. Kevan, P. Blaha, and S. Hufner, "Direct spectroscopic observation of the energy gap formation in the spin density wave phase transition at the Cr(110) surface," *Phys. Rev. Lett.* **83**(10), 2069–2072 (September 1999).

Schumann, F.O., M. Hochstrasser, R.F. Willis, K.G. Goodman, J.G. Tobin, et al., "On the magnetic instability of ultrathin FCC Fe_xNi_{1-x} films," *J. Magn. Magn. Mater.* **199**, 522–524 (June 1999).

Strietelmeier, B., P.A. Leonard, J. Terry, R. Villarreal, and T. Warwick, "Cell surface interactions of plutonium with WIPP halophiles," in *Proceedings of the Environment Management Science Program (EMSP) Actinide Research Workshop* (Albuquerque, New Mexico, November 9–10, 1999).

Terborg, R., J.T. Hoeft, R. Lindsay, O. Schaff, A.M. Bradshaw, R. Toomes, N.A. Booth, D.P. Woodruff, E. Rotenberg, and J.D. Denlinger, "Structural precursor to adsorbate-induced reconstruction: C on Ni(110)," *Phys. Rev. B* **60**(15), 10715–10718 (October 1999).

Tonner, B., T. Droubay, J. Denlinger, W. Meyer-Ilse, J. Rothe, E. Kneedler, K. Pecher, K. Nealson, T. Grundl, and Z.. Lewandowski, "Soft x-ray spectroscopy and imaging of interfacial chemistry in environmental specimens," *Surf. Interface Anal.* **27**(4), 247–258 (April 1999).

Urquhart, S.G., A.P. Hitchcock, A.P. Smith, H. Ade, W. Lidy, E.G. Rightor, and G.E. Mitchell, "NEXAFS spectromicroscopy of polymers: Overview and quantitative analysis of polyurethane polymers," *J. Electron Spectros. Relat. Phenom.* **100**, 119–135 (October 1999).

Urquhart, S.G., A.P. Smith, H. Ade, A.P. Hitchcock, E.G. Rightor, and W. Lidy, "NEXAFS spectroscopy of MDI and TDI polyurethanes," *J. Phys. Chem. B* **103**, 4603–4610 (May 1999).

Xu, S.H., Y. Yang, M. Keefe, G.J. Lapeyre, and E. Rotenberg, "High-resolution photoemission study of acetylene adsorption and reaction with the Si(100)-2×1 surface," *Phys. Rev. B* **60**(16), 11586–11592 (October 1999).

Yang, L., H. Agren, J. Guo, C. Såthe, A. Föhlisch, A. Nilsson, and J.E. Nordgren, "Core electron spectroscopy of chromium hexacarbonyl. A comparative theoretical and experimental study," *Phys. Scr.,* **T59**, 138 (January 1999).

Yeom, H.W., S. Takeda, E. Rotenberg, I. Matsuda, K. Horikoshi, J. Schaefer, C.M. Lee, S.D. Kevan, T. Ohta, T. Nagao, and S. Hasegawa, "Instability and charge density wave of metallic quantum chains on a silicon surface," *Phys. Rev. Lett.* **82**(24), 4898–4901 (June 1999).

Zheng, W.T., J.H. Guo, H. Sjostrom, and J.E. Sundgren, "The effect of substrate temperature on the structure and hardness of magnetron sputter deposited carbon nitride films," *Phys. Status Solidi A* **172**(2), 373–378 (April 1999).

Beamline 7.3.1.1

Ager, J.W., S. Anders, A. Anders, B. Wei, X.Y. Yao, I.G. Brown, C.S. Bhatia, and K. Komvopoulos, "Ion implantation post-processing of amorphous carbon films," *Diamond Relat. Mater.* **8**(2–5), 451–456 (March 1999).

Anders, S., H.A. Padmore, R.M. Duarte, T. Renner, T. Stammler, A. Scholl, M.R. Scheinfein, J. Stöhr, L. Seve, and B. Sinkovic, "Photoemission electron microscope for the study of magnetic materials," *Rev. Sci. Instrum.* **70**(10), 3973–3981 (October 1999).

Anders, S., H.A. Padmore, A. Scholl, and J. Stöhr et al ., "Imaging of magnetic domains and patterns using photoemission electron microscopy," in *Proceedings of the 1999 Materials Research Society Spring Meeting* (San Francisco, April 12–16, 1999).

Anders, S., H.A. Padmore, A. Scholl, J. Stöhr, J.M. Lüning, and M. Scheinfein et al ., "Photoemission electron microscopy for the study of magnetic materials," in *Proceedings of Annual Meeting of the American Physical Society* (Atlanta, March 22–25, 1999).

Anders, S., T. Stammler, W. Fong, C.-Y. Chen, D.B. Bogy, C.S. Bhatia, and J. Stöhr, "Study of tribochemical processes on hard disks using photoemission electron microscopy," *J. Tribol.* **121**(4), 961–967 (October 1999).

Anders, S., T. Stammler, W. Fong, D.B. Bogy, C.S. Bhatia, and J. Stöhr, "Investigation of slider surfaces after wear using photoemission electron microscopy," *J. Vac. Sci. Technol. A* **17**(5), 2731–2736 (September 1999).

Bhatia, C.S., W. Fong, C. Chen, J. Wei, D. Bogy, S. Anders, T. Stammler, and J. Stöhr, "Tribo-chemistry at the head/disk interface," *IEEE Trans. Magn.* **35**, 910–915 (June 1999).

Diaz, J., S. Anders, A. Cossy-Favre, M. Samant, and J. Stöhr, "Enhanced secondary electron yield from oxidized regions on amorphous carbon films studied by x-ray spectromicroscopy," *J. Vac. Sci. Technol. A* **17**(5), 2737–2740 (September 1999).

Slep, D., J. Asselta, M. Rafailovich, J. Sokolov, D. Winesett, A.P. Smith, H. Ade, and S. Anders, "The effect of interactive surface on the equilibrium contact angles in bilayer polymer blend films," in *Proceedings of Annual Meeting of the American Physical Society* (Atlanta, March 22–25, 1999).

Stöhr, J., A. Scholl, T. Regan, S. Anders, J. Luning, M.S. Scheinfein, H.A. Padmore, and R.L. White, "Images of the antiferromagnetic structure of NiO(100) surface by means of x-ray magnetic linear dichroism spectromicroscopy," *Phys. Rev. Lett.* **83**(9), 1862–1865 (August 1999).

Stöhr, J., H.A. Padmore, S. Anders, T. Stammler, and M. Scheinfein, "Principles of x-ray magnetic dichroism spectromicroscopy," *Surf. Rev. Lett.* **5**, 1297–1308 (October 1998).

Beamline 7.3.3

Heimann, P.A., T. Missalla, A. Lindenberg, I. Kang, S. Johnson, Z. Chang, H.C. Kapteyn, R.W. Lee, R.W. Falcone, R.W. Schoenlein, T.E. Glover, A.A. Zholents, M.S. Zolotorev, and H.A. Padmore, "Time-resolved x-ray photoabsorption and diffraction on timescales from ns to fs," in *Proceedings of the 18th International Conference on X-ray and Inner-Shell Processes*, X-99 (Chicago, August 23–27, 1999).

Heimann, P.A., T. Missalla, A. Lindenberg, I. Kang, S. Johnson, Z. Chang, H.C. Kapteyn, R.W. Lee, R.W. Falcone, R.W. Schoenlein, T.E. Glover, A.A. Zholents, M.S. Zolotorev, and H.A. Padmore, "Time-resolved x-ray photoabsorption and diffraction on timescales from ns to fs," in *Proceedings of SRI99* (Palo Alto, California, October 13–15, 1999).

Kim, K.H., C.-H. Chang, Y.M. Koo, and A.A. MacDowell, "Shape effect related to crystallographic orientation of deformation behavior in copper crystals," *Philos. Mag. Lett.* **79**(12), 919–924 (December 1999).

Tatchyn, R., M. Howells, et al ., "X-ray optics design studies for the 1.5–15 angstrom linac coherent light source," in *Proceedings of 20th Annual FEL Conference* (Williamsburg, Virginia).

Beamline 8.0.1

Carlisle, J.A., D.L. Ederer, L.J. Terminello, J.J. Jia, T.A. Callcott, R.C. Perera, and F.J. Himpsel, "Band-structure and core-hole effects in resonant inelastic x-ray scattering: Experiment and theory," *Phys. Rev. B* **59**(11), 7433–7445 (March 1999).

Carlisle, J.A., S.R. Blankenship, R.N. Smith, E.L. Shirley, L.J. Terminello, J.J. Jia, T.A. Callcott, and D.L. Ederer, "Soft x-ray fluorescence spectroscopy of solids," *J. Electron Spectros. Relat. Phenom.* **103**, 839–845 (June 1999).

Chang, G.S., K.H. Chae, C.N. Whang, E.Z. Kurmaev, D.A. Zatsepin, R.P. Winarski, D.L. Ederer, A.P. Moewes, and Y.P. Lee, "Mechanism for interfacial adhesion strength of an ion beam mixed Cu/polyimide with a thin buffer layer," *Appl. Phys. Lett.* **74**, 522–524 (January 1999).

Diaz, J., S. Anders, and A. Cossy-Gantner, "Enhanced electron emission from oxidized regions on amorphous carbon films studied by x-ray spectromicroscropy," *J. Vac. Sci. Technol. A* **17**(5), 2737-2740 (November 1999).

Ederer, D.L., E.Z. Kurmaev, S. Shin, A.P. Moewes, M.M. Grush, T.A. Callcott, R.C. Perera, J. van Ek, S. Stadler, R.P. Winarski, L.J. Terminello, and L. Zhou, "Examples of soft x-ray emission and inelastic scattering excited by synchrotron radiation," *J. Alloys Compd.* **286**(1–2), 47–55 (May 1999).

Finkelstein, L.D., E.Z. Kurmaev, M.A. Korotin, A.P. Moewes, B. Schneider, S. Butorin, J.-H. Guo, J.E. Nordgren, D. Hartmann, M. Neumann, and D.L. Ederer, "Band approach to the excitation-energy dependence of x-ray fluorescence of TiO_2," *Phys. Rev. B* **60**(4), 2212–2217 (July 1999).

Hamad, K.S., R. Roth, J. Rockenberger, T. van Buuren, and A.P. Alivisatos, "Structural disorder in colloidal InAs and CdSe nanocrystals observed by x-ray absorption near edge spectroscopy," *Phys. Rev. Lett.* **83**(17), 3474–3477 (October 1999).

Hansen, D.L., O. Hemmers, H. Wang, D.W. Lindle, P. Focke, I.A. Sellin, C. Heske, H.S. Chakraborty, P.C.

Deshmukh, and S.T. Manson, "Validity of the independent-particle approximation in x-ray photoemission: The exception, not the rule," *Phys. Rev. A* **60**(4), 2641–2644 (October 1999).

Heske, C., D. Eich, R.H. Fink, E. Umbach, T. van Buuren, C.F.O. Bostedt, L.J. Terminello, S. Kakar, M. Grush, T.A. Callcott, et al., "Observation of intermixing at the buried CdS/Cu(In,Ga)Se$_2$ thin film solar cell heterojunction," *Appl. Phys. Lett.* **74**(10), 1451–1453 (March 1999).

Heske, C., E. Eich, R. Fink, E. Umbach, S. Kakar, T. van Buuren, C. Bostedt, L.J. Terminello, M.M. Grush, T.A. Calcott, et al., "Localization of Na impurities at the buried CdS/Cu(In,Ga)Se$_2$ heterojunction," *Appl. Phys. Lett.* **75**(14), 2082–2084 (October 1999).

Heske, C., R. Treusch, F.J. Himpsel, S. Kakar, L.J. Terminello, and H.J. Weyer, "Band widening in graphite," *Phys. Rev. B* **59**(7), 4680–4684 (February 1999).

Izumi, H., T. Kaneyoshi, T. Ishihara, H. Yoshioka, H. Matsui, M. Motoyama, and Y. Muramatsu, "X-ray emission and absorption spectra of carbon nitride films prepared by laser ablation," *X-Ray Spectrom.* **28**(6), 509–514 (December 1999).

Jimenez, J., J. van Ek, D.L. Ederer, T.A. Callcott, J.J. Jia, J.A. Carlisle, L.J. Terminello, A. Asfaw, and R.C.C. Perera, "Dynamical behavior of x-ray absorption and scattering at the L edge of titanium compounds: Experiment and theory," *Phys. Rev. B* **59** (4), 2649–2655 (January 1999).

Kurmaev, E.Z., A.I. Poteryaev, V.I. Anisimov, I. Karla, A. Moewes, B. Schneider, M. Neumann, D.L. Ederer, and R.N. Lyubovskaya, "Electronic structure of superconducting inorganic polymer (SN)$_x$: Band structure calculations, x-ray fluorescence and pohotemission measurements," *Physica C* **321**, 191 (1999).

Kurmaev, E.Z., A.P. Moewes, M. Krietmeyer, K. Endo, T. Ida, S. Shimada, R.P. Winarski, M. Neumann, S.N. Shamin, and D.L. Ederer, "X-ray fluorescence study of organic–inorganic polymer conversion into ceramics

induced by ion irradiation," *Phys. Rev. B* **60**(22), 15100–15106 (December 1999).

Kurmaev, E.Z., D.A. Zatsepin, R.P. Winarski, S. Stadler, D.L. Ederer, A.P. Moewes, V.V. Fedorenko, S.N. Shamin, V.R. Galakhov, G.S. Chang, and C.N. Whang, "X-ray emission study of ion beam mixed Cu/Al films on polyimide," *J. Vac. Sci. Technol.* **17**(2), 593–596 (March 1999).

Kurmaev, E.Z., M.A. Korotin, V.R. Galakhov, L.D. Finkelstein, E.I. Zabolotzky, N.N. Efremova, N.I. Lobachevskaya, S. Stadler, D.L. Ederer, A.P. Moewes, S. Bartkowski, M. Neumann, J. Matsuno, A. Fujimori, and J. Mitchell, "X-ray emission of photoelectron spectra of Pr$_{0.5}$Sr$_{0.5}$MnO$_3$," *Phys. Rev. B* **59**(20), 12799–12806 (May 1999).

Kurmaev, E.Z., M.Z. Korotin, V.R. Galakhov, L.D. Finkelstein, E.I. Zabolotzky, N.N. Efremova, S. Stadler, D.L. Ederer, A.P. Moewes, S. Bartkowski, M. Neumann, J. Matsuno, T. Mizokawa, A. Fujimori, and J. Mitchell, "X-ray emission and photoelectron spectra of Pr$_{0.5}$Sr$_{0.5}$MnO$_3$," *J. Electron Spectros. Relat. Phenom.* **103**, 793–798 (June 1999).

Kurmaev, E.Z., R.P. Winarski, D.L. Ederer, J.-C. Pivin, S.N. Shamin, A.P. Moewes, G.S. Chang, and C.N. Wang, "Soft x-ray fluorescence measurements of irradiated polyimide and polycarbosilane films," *J. Electron Spectros. Relat. Phenom.* **103**, 565–571 (June 1999).

Kurmaev, E.Z., R.P. Winarski, K. Endo, T. Ida, A.P. Moewes, D.L. Ederer, J.-C. Pivin, S.N. Shamin, V.A. Trofimova, and Y.M. Yarmoshenko, "Radiation-induced degradation of polyethersulphone films studied by fluorescent x-ray emission spectroscopy," *Nucl. Instrum. Methods Phys. Res., Sect. B* **155**(4), 431–439 (September 1999).

Kurmaev, E.Z., S.N. Shamin, D.L. Ederer, U. Dettlaff-Weglikowska, and J. Weber, "Local and electronic structure of siloxene," *J. Mater. Res.* **14**(4), 1235–1237 (April 1999).

Kurmaev, E.Z., S.N. Shamin, Y.-N. Xu, W.Y. Ching, A.P. Moewes, D.L. Ederer, E.B. Yagubskii, and N.D. Kushch, "X-ray fluorescence measurements of organic

superconductors κ-(ET)$_2$Cu[N(CN)$_2$]Br and κ-(ET)$_2$Cu(NCS)$_2$," *Phys. Rev. B* **60**(18), 13169–13174 (November 1999).

Lindle, D.W., and O. Hemmers, "Breakdown of the dipole approximation in soft-x-ray photoemission," *J. Electron Spectros. Relat. Phenom.* **100**, 297–311 (October 1999).

Magnuson, M., A. Nilsson, M. Weinelt, and N. Mårtensson, "Angular-dependent resonant-photoemission processes at the 2p thresholds in nickel metal," *Phys. Rev. B* **60**(4), 2436–2440 (July 1999).

Moewes, A.P., A.V. Postnikov, B. Schneider, E.Z. Kurmaev, M. Matteucci, V.M. Cherhashenko, D. Hartman, H. Hesse, and M. Neumann, "Electronic structure of KNb0$_3$: Nb $M_{4,5}$ x-ray fluorescence measurements," *Phys. Rev. B* **60**(7), 4422–4425 (1999).

Moewes, A.P., M.M. Grush, T.A. Callcott, and D.L. Ederer, "Decay mechanisms of the 4d core hole through the 4d–4f resonance in dysprosium," *Phys. Rev. B* **60**(23), 15728–15731 (1999).

Moewes, A.P., R.P. Winarski, D.L. Ederer, M.M. Grush, and T.A. Callcott, "Study of 4f inner shell excitations in Gd and Tb using resonant inelastic soft x-ray scattering," *J. Electron Spectros. Relat. Phenom.* **101–103**, 617–622 (June 1999).

Moewes, A.P., S. Stadler, R.P. Winarski, D.L. Ederer, M.M. Grush, and T.A. Callcott, "Probing electron correlation, charge-transfer and Coster–Kronig transitions at the 3d and 4d thresholds of Nd by resonant inelastic scattering," *Phys. Rev. B* **59**, 5452. (February 1999).

Muramatsu, Y., H. Takenaka, T. Oyama, T. Hayashi, M. Grush, and R.C. Perera, "Valence Band Structure and Decay Process in the Inner-Shell Excitation of Boron Oxide," *X-Ray Spectrom.* **28**(6), 503–508 (November–December 1999).

Muramatsu, Y., Y. Tani, Y. Aoi, T. Kaneyoshi, M. Motoyama, J.J. Delaunay, T. Hayashi, M. Grush, T.A. Callcott, D.L. Ederer, et al., "High-resolution soft x-ray emission spectra of crystalline carbon nitride films

deposited by electron cyclotron resonance sputtering," *Jpn. J. Appl. Phys.* **38**, 5143–5147 (September 1999).

Qian, L., L. Norin, J. Guo, C. Såthe, A. Agui, U. Jansson, and J.E. Nordgren, "Electronic structure of Ti$_x$C$_{60}$ studied by x-ray spectroscopies," *Phys. Rev. B* **59**, 12667 (May 1999).

Winarski, R.P., D.L. Ederer, E.Z. Kurmaev, S.N. Shamin, K. Endo, T. Ida, A.P. Moewes, G.S. Chang, S.Y. Kim, and C.N. Whang, "Soft x-ray fluorescence measurements of polyimide films," *Thin Solid Films* **357**, 106 (1999).

Xu, S.H., M. Keeffe, Y. Yang, C. Chen, M. Yu, G.J. Lapeyre, E. Rotenberg, J. Denlinger, and J.T. Yates, Jr., "Photoelectron diffraction imaging for C$_2$H$_2$ and C$_2$H$_4$ chemisorbed on Si(100) reveals a new bonding configuration," *Phys. Rev. Lett.* **84**(5), 939 (January 1999).

Beamline 9.0.1

Bozek, J.D., N. Berrah, E. Kukk, T. Thomas, T.X. Carroll, L.J. Såthre, J.A. Sheehy, and P.W. Langhoff, "High resolution molecular inner-shell electron spectroscopies," in *Proceedings of XXI International Conference on the Physics of Electronic and Atomic Collisions* (Sendai, Japan, July 22–27, 1999).

Kukk, E., J.D. Bozek, T. Thomas, T.X. Carroll, L.J. Såthre, J.A. Sheehy, P. Langhoff, and N. Berrah, "New insights into molecular structure and dynamics using soft x-ray electron spectroscopy," in *Proceedings of XXI International Conference on the Physics of Electronic and Atomic Collisions* (Sendai, Japan, July 22–27, 1999).

Beamline 9.0.2

Bracker, A.S., E.R. Wouters, O.S. Vasyutinskii, and A.G. Suits, "Imaging the alignment angular distribution: State symmetries, coherence, and nonadiabatic dynamics in photodissociation," *J. Chem. Phys.* **110**, 6749 (April 1999).

Evans, M.D., "High-resolution photoionization studies performed utilizing third-generation synchrotron radiation at the Advanced Light Source," Ph.D. thesis, Iowa State University of Science and Technology, 1999.

Evans, M.D., and C. Ng, "Rotationally resolved pulsed field ionization photoelectron study of CO$^+$(X$^2\Sigma^+$, ν^+=0–42) in the energy range of 13.98–21.92 eV," *J. Chem. Phys.* **111**(19), 8879–8892 (November 1999).

Fedorov, D.G., M.D. Evans, Y. Song, M.S. Gordon, and C. Ng, "An experimental and theoretical study of the spin-orbit interaction for CO$^+$(A$^2\Pi_{3/2,1/2}$, ν^+ = 0–41) and O$_2^+$ (X$^2\Pi_{3/2,1/2g}$, ν^+ = 0–38)," *J. Chem. Phys.* **111**(14), 6413 (October 1999).

Hsu, C.-W., M.D. Evans, S.L. Stimson, and C.Y. Ng, "Rotationally resolved photoelectron study of O$_2^+$(B $^2\Sigma_g^-$, $^2\Sigma_u^-$; ν^+=0–7) at 20.2–21.3 eV," *J. Chem. Phys.* **110**(1), 315–327 (January 1999).

Jarvis, G., K.-M. Weitzel, M. Malow, T. Baer, Y. Song, and C. Ng, "High-resolution pulsed field ionization photoelectron-photoion coincidence spectroscopy using synchrotron radiation," *Rev. Sci. Instrum.* **70**(10), 3892 (October 1999).

Jarvis, G., K.M. Weitzel, M. Malow, T. Baer, Y. Song, and C. Ng, "High-resolution pulsed field ionization photoelectron–photoion coincidence study of C$_2$H$_2$: Accurate 0 K dissociation threshold for C$_2$H$^+$," *Phys. Chem. Chem. Phys.* **1**(22), 5259–5262 (1999).

Jarvis, G., M.D. Evans, C. Ng, and K. Mitsuke, "Rotational-resolved pulsed field ionization photoelectron study of NO$^+$(X $^1\Sigma^+$, ν^+ = 0–32) in the energy range of 9.24–16.80 eV," *J. Chem. Phys.* **111**(7), 3058 (August 1999).

Jarvis, G., Y. Song, and C. Y. Ng, "High resolution pulsed field ionization photoelectron spectroscopy using multi-bunch synchrotron radiation: Time-of-flight selection scheme," *Rev. Sci. Instrum.* **70**(6), (June 1999), 2615–2621.

Jarvis, G., Y. Song, and C.Y. Ng, "Rotationally-resolved pulsed field ionization photoelectron study of NO$^+$(*a* $^3\Sigma^+$,ν^+=0–16) in the energy range of 15.6–18.2. eV," *J. Chem. Phys.* **111**(5), 1937–1946 (August 1999).

Jarvis, G., Y. Song, C. Ng, and E.R. Grant, "A characterization of vibrationally and electronically excited NO$_2^+$ by

high-resolution threshold photoionization spectroscopy," *J. Chem. Phys.* **111**(21), 9568–9573 (December 1999).

Peterka, D., M. Ahmed, C. Ng, and A.G. Suits, "Dissociative photoionization dynamics of SF$_6$ by ion imaging with synchrotron undulator radiation," *Chem. Phys. Lett.* **312**, 108–114 (October 1999).

Shiell, R.C., M.D. Evans, S.L. Stimson, C. Hsu, C. Ng, and J.W. Hepburn, "A ZEKE photoelectron study of the D$^2\pi$ and 3$^2\Sigma^+$ satellite states of CO$^+$," *Chem. Phys. Lett.* **315**(5–6), 390–396 (December 1999).

Shiell, R.C., M.D. Evans, S.L. Stimson, C. Hsu, C. Ng, and J. Hepburn, "Characteristics of correlation satellites below 25 eV in xenon probed by pulsed-field ionization zero kinetic energy photoelectron spectroscopy," *Phys. Rev. A* **59**(4), 2903–2909 (April 1999).

Song, Y., M.D. Evans, C.Y. Ng, C. Hsu, and G. Jarvis, "Rotationally resolved pulsed field ionization photoelectron bands of O$_2^+$(*X* $^2\Pi_{1/2,3/2g}$, ν^+=0–38) in the energy range of 12.05–18.15 eV," *J. Chem. Phys.* **111**(5), 1905–1916 (August 1999).

Sorkhabi, O., Q. Fei, A.H. Rizvi, and A.G. Suits, "Ultraviolet photodissociation of furan probed by tunable synchrotron radiation," *J. Chem. Phys.* **111**(1), 100–107 (July 1999).

Sun, W., J. Robinson, K. Yokoyama, A.G. Suits, and D.M. Neumark, "Discrimination of product isomers in the photodissociation of propyne and allene at 193 nm," *J. Chem. Phys.* **110**, 4363 (March 1999).

Weitzel, K.-M., M. Malow, G. Jarvis, T. Baer, Y. Song, and C. Ng, "High-resolution pulsed field ionization photoelectron–photoion coincidence study of CH$_4$: accurate 0 K dissociation threshold for CH$_3^+$," *J. Chem. Phys.* **111**(18), 8267–8270 (November 1999).

Beamline 9.3.1

Hansen, D.L., J. Cotter, G.R. Fisher, K.T. Leung, R. Martin, P. Neill, R.C.C. Perera, M. Simon, Y. Uehara, B. Vanderford, S.B. Whitfield, and D.W. Lindle, "Multi-Ion coincidence measurements of methyl chloride

following photofragmentation near the chlorine K-edge," *J. Phys. B* **32**(11), 2629–2647 (June 1999).

Hemmers, O., H. Wang, D.W. Lindle, P. Focke, I.A. Sellin, J.D. Mills, J.A. Sheehy, and P.W. Langhoff, "Beyond the dipole approximation: Angular-distribution effects in the 1s photoemission from small molecules," in *Proceedings of the 18th International Conference on X-ray and Inner-Shell Processes, X-99* (Chicago, August 23–27, 1999).

Lindle, D.W., O. Hemmers, H. Wang, P. Focke, I.A. Sellin, J.D. Mills, J.A. Sheehy, and P.W. Langhoff, "Beyond the dipole approximation: Angular-distribution effects in the 1s photoemission from small molecules," in *Proceedings of the 21st International Conference on the Physics of Electronic and Atomic Collisions, ICPEAC-XXI* (Sendai, Japan, July 22–27, 1999).

Beamline 9.3.2

Denecke, R., J. Morais, R.X. Ynzunza, J.G. Menchero, J. Liesegang, and C.S. Fadley, "Magnetic circular dichroism in photoelectron angular distributions from Gd(0001)," *J. Electron Spectros. Relat. Phenom.* **101–103**, 263–269 (June 1999).

Diaz, J., S. Anders, X. Zhou, E.J. Moler, S.A. Kellar, and Z. Hussain, "Combined near edge x-ray absorption fine structure and x-ray photoemission spectroscopies for the study of amorphous carbon thin films," *J. Electron Spectros. Relat. Phenom.* **101–103**, 545–550 (June 1999).

Fadley, C.S., "Characterization of magnetic surfaces, interfaces, and nanostructures with soft x-rays and photo-electrons," in *Proceedings of IEEE Magnetics Society Meeting* (Milpitas, California, May 11, 1999).

Fadley, C.S., "From multiplet splittings to multi-atom resonant photoemission," in *Shirley Symposium on Spectroscopy and the Structure of Matter* (Berkeley, California, March 28–29, 1999).

Fadley, C.S., "Holography, interatomic resonance, and other interesting things to do in the next generation of x-ray photoelectron (and x-ray emission) spectroscopy," in

Proceedings of International Workshop "XPS: From Physics to Data," sponsored by the International Union for Vacuum Science, Technique, and Applications (Hortobagy, Hungary, April 26–30, 1999).

Fadley, C.S., "Multi-atom resonant photoemission," in *Proceedings of 24th International Conference on X-ray and Inner Shell Processes (X99)* (Chicago, August 23–27, 1999).

Fadley, C.S., "Photoemission and related techniques: Solids, surfaces, molecules, and atoms," in *Proceedings of International School on Synchrotron Radiation*, International Centre for Theoretical Physics (Trieste, May 17–21, 1999).

Faiz, M.M., X. Zhou, E. Moler, S.A. Kellar, Z. Hussain, N.M. Hamdan, and Kh.A. Ziq, "An x-ray absorption spectroscopic study of $YBa_2Cu_{3-x}Fe_xO_{7+y}$," *J. Electron Spectros. Relat. Phenom.* **103**, 707–711 (June 1999).

Garcia de Abajo, J., and C.S. Fadley, "Atoms talking to one another: Multi-atom resonant photoemission as a new materials characterization tool," in *Proceedings of Golden Gate Materials and Welding Technologies Conference* (San Francisco, February 4–5, 1999).

Garcia de Abajo, F.J., C.S. Fadley, and M.A. Van Hove, "Multi-atom resonant photoemission: Theory and systematics," *Phys. Rev. Lett.* **82**(20), 4126–4129 (May 1999).

Gessner, O., F. Heiser, N.A. Cherepkov, B. Zimmermann, and U. Becker, "Photoelectron scattering effects in molecular photoionization," *J. Electron Spectros. Relat. Phenom.* **101–103**, 113–118 (June 1999).

Kay, A.W., E. Arenholz, B.S. Mun, J. Garcia de Abajo, C.S. Fadley, R. Denecke, Z. Hussain, and M.A. van Hove, "Multiple atom resonant photoemission: A new technique for studying near-neighbor atomic identities and bonding," *J. Electron Spectros. Relat. Phenom.* **101–103**, 647–652 (June 1999).

Len, P., J. Denlinger, E. Rotenberg, B.P. Tonner, S.D. Kevan, M.A. Van Hove, and C.S. Fadley, "Holographic atomic images from surface and bulk W(110) photoelectron diffraction data," *Phys. Rev. B* **59**(8), 5857 (February 1999).

Shimomura, M., H. Yeom, B. Mun, C.S. Fadley, S. Hara, S. Yoshida, and S. Kono, "Surface core-level-shift photoelectron diffraction study of the β-SiC(001)-*c*(2 × 2) surface," *Surf. Sci.* **438**(1–3), 237–241 (September 1999).

Spring, J.A., "Design and construction of a transform soft x-ray fourier interferometer," Master's thesis, Lawrence Berkeley National Laboratory, 1999.

Thevuthasan, S., Y.J. Kim, S.A. Chambers, J. Morais, R. Denecke, C.S. Fadley, P. Liu, T. Kendelewicz, and G.E. Brown, Jr., "Surface structure of MBE-grown α-Fe_2O_3(0001) by intermediate-energy x-ray photoelectron diffraction," *Surf. Sci.* **425**(2–3), 276–286 (April 1999).

Yeom, H.W., M. Shimomura, J. Kitamura, S. Hara, K. Tono, I. Matsuda, B.S. Mun, W.A.R. Huff, S. Kono, T. Ohta, S. Yoshida, H. Okushi, K. Kajimura, and C.S. Fadley, "Atomic and electronic-band structures of anomalous carbon dimers on 3*C*-SiC(001)-*c*(2 × 2)," *Phys. Rev. Lett.* **83**(8), 1640–1643 (August 1999).

Ynzunza, R., H. Daimon, J. Palomares, E.D. Tober, Z. Wang, Y. Chen, M.A. Van Hove, and C.S. Fadley, "Structure determination for saturated (1 × 1) oxygen on W(110) from full-solid-angle photoelectron diffraction with chemical-state resolution," *Surf. Sci.* **442**(1), 27–35 (November 1999).

Ynzunza, R., E. Tober, J. Palomares, Z. Wang, H. Xiao, F. Zhang, H. Daimon, Z. Hussain, and C.S. Fadley, "Full-solid-angle photoelectron diffraction from bulk and surface atoms of clean W(110)," *Surf. Sci.* **441**(2–3), 301–310 (November 1999).

Beamline 10.0.1

Bawagan, A.D.O., J.D. Bozek, E. Kukk, and E.R. Davidson, "Peculiar non-adiabatic effects in the photoelectron spectrum of allene (1,2-propadiene)," in *Proceedings of Annual Meeting of the American Physical Society* (Atlanta, March 22–25, 1999).

Berrah, N., B. Langer, A.A. Wills, E. Kukk, J.D. Bozek, A.H. Farhat, and T.W. Gorczyca, "High-resolution angle-resolved measurements in atoms and molecules using advanced photoelectron spectroscopy at the Advanced

Light Source," *J. Electron Spectros. Relat. Phenom.* **103**, 1–11 (June 1999).

Borve, K., L.J. Saethre, J.D. Bozek, J.E. True, and T. Thomas, "Molecular-field splitting and vibrational structure in the phosphorus 2p photoelectron spectrum of PF_3," *J. Chem. Phys.* **111**(10), 4472–4477 (September 1999).

Bozek, J.D., E. Kukk, N. Berrah, J.A. Sheehy, and P.W. Langhoff, "Angular distributions in the S 2p photoelectron spectrum of OCS with molecular-field, vibrational and spin-orbit splitting," in *Proceedings of Annual Meeting of the American Physical Society* (Atlanta, March 22–25, 1999).

Bozek, J.D., E. Kukk, W.-T. Cheng, and N. Berrah, "Resonance auger spectra of the C $1s^{-1} 2\pi_u$ excited CO_2," in *Proceedings of Annual Meeting of the American Physical Society* (Atlanta, March 22–25, 1999).

Carroll, T.X., N. Berrah, J.D. Bozek, J.A. Hahne, E. Kukk, L.J. Saethre, and T. Thomas, "Carbon 1s photoelectron spectrum of methane: Vibrational excitation and core-hole lifetime," *Phys. Rev. A* **59**(5), 3386–3393 (May 1999).

Diehl, S., "Studies of Hollow Li," Ph.D. thesis, Universite Paris-Sud, 1999.

Domke, M., K. Schulz, R. Püttner, G. Kaindl, A.S. Schlachter, and J.D. Bozek, "Photoionization study of double-excited states in He at ultra-high resolution," *Poverkhnost* **8**, 158–161 (January 1999).

Farhat, A.H., A.A. Wills, B. Langer, and N. Berrah, "Resonant Auger decay studies in Kr $3d_{3/2,5/2}^{-1}$ np states using angle-resolved electron imaging spectroscopy," *Phys. Rev. A* **59**(1), 320–329 (January 1999).

Kukk, E., J.D. Bozek, W.-T. Cheng, R.F. Fink, A.A. Wills, and N. Berrah, "Auger decay of the C $1s^{-1}2\pi^*$ resonance in carbon monoxide: Vibrationally and angularly resolved spectra," *J. Chem. Phys.* **111**(21), 9642–9650 (December 1999).

Kukk, E., J.D. Bozek, A. Wills, W.-T. Cheng, B. Langer, G. Snell, and N. Berrah, "Fully vibrationally resolved

auger electron spectra following the C 1s → π excitations in CO," in *Proceedings of Annual Meeting of the American Physical Society* (Atlanta, March 22–25, 1999).

Lopes, M.C.A., A.J. Yencha, G.C. King, J.D. Bozek, and N. Berrah, "High resolution (6–12 meV) threshold photoelectron spectroscopy of argon from 28 to 49 eV," *Chem. Phys. Lett.* **310**(5–6), 433–438 (September 1999).

Ohrwall, G., J.D. Bozek, and P. Baltzer, "Very high resolution electron spectroscopy with third generation synchrotron radiation sources: The resonant Auger decay spectrum of the Xe $4d_{5/3}$-16p site," *J. Electron Spectros. Relat. Phenom.* **104**(1–3), 209–212 (June 1999).

Ohrwall, G., P. Baltzer, and J.D. Bozek, "Photoelectron spectra of N_2^+: Rotational line profiles studied with He I-excited angle-resolved spectroscopy and with synchrotron radiation," *Phys. Rev. A* **59**(3), 1903–1912 (January 1999).

Ohrwall, G., "UV-photoelectron spectroscopy of free atoms and molecules at near 1 meV resolution," Ph.D. thesis, Uppsala University, 1999.

Ohrwall, G., P. Baltzer, and J.D. Bozek, "Synchrotron radiation excited photoelectron spectrum of H_2^+ with rotational resolution," *J. Phys. B* **32**(3), 51–56 (June 1999).

Ohrwall, G., S. Sundin, P. Baltzer, and J.D. Bozek, "Inner-valence states of CO^+: Comparison of photoelectron and resonant auger spectra," *J. Phys. B* **32**(2), 463–473 (July 1999).

Snell, G., B. Langer, J. Viefhaus, E. Kukk, J.D. Bozek, and N. Berrah, "First spin-resolved gas-phase studies at the Advanced Light Source," in *Proceedings of Annual Meeting of the American Physical Society* (Atlanta, March 22–25, 1999).

Thomas, T.D., N. Berrah, J. Bozek, T.X. Carroll, J. Hahne, T. Karlsen, E. Kukk, and L.J. Såthre, "Photon energy dependence of the $^1\sigma_u/^1\sigma_g$ intensity ratio in carbon 1s photoelectron spectroscopy of ethyne," *Phys. Rev. Lett.* **82**(6), 1120–1123 (February 1999).

Yencha, A.J., G.C. King, M.C.A. Lopes, J.D. Bozek, and N. Berrah, "Photo-double ionization of deuterium

chloride studied by threshold photoelectron coincidence spectroscopy," *Chem. Phys. Lett.* **315**(1–2), 37–42 (December 1999).

Zhou, X.J., P. Bogdanov, S.A. Kellar, T. Noda, H. Eisaki, S. Uchida, Z. Hussain, and Z.-X. Shen, "One-dimensional electronic structure and suppression of d-wave node state in $(La_{1.28}Nd_{0.6}Sr_{0.12})CuO_4$," *Science* **286**(5438), 268–272 (October 1999).

Beamline 10.3.1

Cahill, T.A., S.S. Cliff, K.D. Perry, M.P. Jimenez-Cruz, and S. McHugo, "Size and time resolved anthropogenic components of aerosols via synchrotron x-ray fluorescence: Application to Asian aerosol transport," in *Proceedings of American Geophysical Union Fall Conference* (San Francisco, December 13–17, 1999).

Cahill, T.A., K.D. Perry, and S.S. Cliff, "Transport of Asian dust and anthropogenic pollutants to Hawaii and the eastern Pacific," in *Proceedings of Climate Monitoring and Diagnostics Lab Annual Meeting* (Boulder, Colorado, May 12–13, 1999).

Chuchalin, A.G., O.A. Lyaskina, P.G. Plashanov, E.P. Plashanova, D. Sayers, W. Zhou, S. McHugo, et al., "Concentration of heavy elements and their compounds in the cells from BAV and pulmonary tumors in radiation-exposed subjects," *Terapeticheskii Arkhiv* **71**(4), 47-51 (September 1999).

Flink, C., H. Feick, S. McHugo, A.J. Mohammed, W. Seifert, H. Hieslmair, T. Heiser, A. Istratov, and E.R. Weber, "Formation of copper precipitates in silicon," *Physica B* **274**, 437–440 (December 1999).

Koshka, Y., S. Ostapenko, I. Tarasov, S. McHugo, and J.P. Kalejs, "Scanning room-temperature photoluminescence in polycrystalline silicon," *Appl. Phys. Lett.* **74**(11), 1555–1557 (April 1999).

McHugo, S., and H. Hieslmair, "Gettering in Silicon," in *Wiley Encyclopedia of Electrical and Electronics Engineering*, edited by J. Webster (John Wiley and Sons, New York, 1999), Vol. 8, p. 388.

McHugo, S., A.C. Thompson, C. Flink, G. Lamble, and E.R. Weber, "Metal impurity precipitates in silicon: Chemical state and stability," *Physica B: Condensed Matter* **274**, 371–374 (December 1999).

McHugo, S., A.C. Thompson, and G. Lamble, "Synchrotron-based impurity mapping," in *Proceedings of 8th International Conference on Defects-Recognition, Imaging and Physics in Semiconductors* (Narita, Japan, September 15–18, 1999).

Beamline 10.3.2

Jeong, S., M. Idir, L. Johnson, Y. Lin, P.J. Batson, R.A. Levesque, P. Kearney, P. Yan, E. Gullikson, J.H. Underwood, and J. Bokor, "Actinic detection of EUVL mask blank defects," in *Proceedings of BACUS Symposium on Photomask Technology and Management '99* (Monterey, California, September 15–17, 1999).

Reeder, R.J., G.M. Lamble, and P.A. Northrup, "XAFS study of the coordination and local relaxation around Co^{2+}, Mn^{2+}, Pb^{2+}, and Ba^{2+} trace elements," *Am. Mineral.* **84**(7–8), 1049–1060 (July–August 1999).

Shin, N.S., Y.M. Koo, C.H. Chang, and H.A. Padmore, "Photoelectron bremsstrahlung spectrum in synchrotron radiation excited total reflection x-ray fluorescence analysis of silicon wafers," *J. Appl. Phys.* **86**(2), 902–908 (July 1999).

Beamline 11.3.2

Cardinale, G.F., J.E.M. Goldsmith, A.K. Ray-Chaudhuri, S.D. Hector, J. Bokor, S. Jeong, S.C. Burkhart, C.C. Walton, C. Larson, P. Yan, and G. Zhang, "Comparison of at-wavelength inspection, printability, and simulation of nm-scale substrate defects in extreme ultraviolet lithography EUVL," in *Proceedings of BACUS Symposium on Photomask Technology and Management '99* (Monterey, California, September 15–17, 1999).

Jeong, S., C. Lai, S. Rekawa, C.C. Walton, E. Tejnil, and J. Bokor, "At-wavelength detection of 100-nm defective from EUVL mask blank," in *Proceedings of BACUS Symposium on Photomask Technology and Management '99* (Monterey, California, September 15–17, 1999).

Jeong, S., M. Idir, Y. Lin, L. Johnson, S. Rekawa, M. Jones, P. Denham, P.J. Batson, R.A. Levesque, P. Kearney, P. Yan, E. Gullikson, J.H. Underwood, and J. Bokor, "At-wavelength detection of EUVL mask blank defects," *J. Vac. Sci. Technol. B* **16**(6), 3430–3434 (November–December 1999).

Jeong, S., L.E. Johnson, Y. Lin, S. Rekawa, P.Y. Yan, J.H. Underwood, and J. Bokor, "Actinic EUVL mask blank defect inspection system," in *Emerging Lithographic Technologies III*, Proceedings of SPIE's 24th International Society for Optical Engineering (Santa Clara, California, March 14–19, 1999).

Jeong, S., L.E. Johnson, S. Rekawa, C. Walton, S.T. Prisbrey, E. Tejnil, J. Underwood, and J. Bokor, "Actinic detection of sub-100 nm defects on EUVL mask blanks," *J. Vac. Sci. Technol. B* **17**(6), 3009–3013 (November–December 1999).

Pu, N.-W., J. Bokor, S. Jeong, and R.-A. Zhao, "Nondestructive picosecond-ultrasonic characterization of Mo/Si EUV multilayer reflection coatings," *J. Vac. Sci. Technol. B* **17**(6), 3014–3018 (November–December 1999).

Pu, N.W., S. Jeong, R.A. Zhao, and J. Bokor, "Nondestructive ultrasonic characterization of Mo/Si EUV multilayers," in *Emerging Lithographic Technologies III*, Proceedings of SPIE's 24th International Society for Optical Engineering (Santa Clara, California, March 14–19, 1999).

Beamline 12.0.1

Attwood, D.T., *Soft X-Rays and Extreme Ultraviolet Radiation: Principles and Applications* (Cambridge University Press, Cambridge, 1999).

Attwood, D.T., P. Naulleau, K. Goldberg, E. Tejnil, C. Chang, R. Beguiristain, P.J. Batson, J. Bokor, E. Gullikson, M. Koike, H. Medecki, and J.H. Underwood, "Tunable coherent radiation in the soft x-ray and extreme ultraviolet spectral regions," *IEEE J. Quantum Electron.* **35**(5), 709–720 (May 1999).

Goldberg, K.A., "Testing extreme ultraviolet optical systems at-wavelength with sub-angstrom accuracy," in

Fabrication and Testing of Aspheres, Topics in Optics Series, Vol. 24, edited by J.S. Taylor, M. Piscotty, and A. Lindquist (Optical Society of America, 1999).

Goldberg, K., P. Naulleau, and J. Bokor, "EUV interferometric measurements of diffraction-limited optics," *J. Vac. Sci. Technol. B* **17**(6), 2982–2986 (November–December 1999).

Goldberg, K., P. Naulleau, R. Gaughan, H. Chapman, J. Goldsmith, and J. Bokor, "Direct comparisons of EUV and visible-light interferometrics," in *Emerging Lithographic Technologies III*, Proceedings of SPIE's 24th International Society for Optical Engineering (Santa Clara, California, March 14–19, 1999).

Goldsmith, J., K. Berger, D. Bozman, G. Cardinale, D. Folk, C. Henderson, D. O'Connell, A. Ray-Chaudhuri, K. Stewart, D. Tichenor, H. Chapman, R. Gaughan, R. Hudyma, C. Montcalm, E. Spiller, J. Taylor, J. Williams, K. Goldberg, E. Gullikson, P. Naulleau, and J. Cobb, "Sub-100-nm imaging with the EUV 10× microstepper," in *Emerging Lithographic Technologies III*, Proceedings of SPIE's 24th International Society for Optical Engineering (Santa Clara, California, March 14–19, 1999).

Gullikson, E., S. Baker, J.E. Bjorkholm, J. Bokor, K. Goldberg, J. Goldsmith, C. Montcalm, P. Naulleau, E. Spiller, D.G. Stearns, J.T. Taylor, J.H. Underwood, et al., "EUV scattering and flare of 10× projection cameras," in *Emerging Lithographic Technologies III*, Proceedings of SPIE's 24th International Society for Optical Engineering (Santa Clara, California, March 14–19, 1999).

Kim, H.K., K.H. Jackson, J. Lee, I. Park, et al., "Gas electron multiplier development using LIGA," in *IEEE Transactions on Nuclear Science*, Proceedings of IEEE Nuclear Science and Medical Imaging Symposium (Seattle, October 26–28, 1999).

Naulleau, P., and K. Goldberg, "Dual-domain point diffraction interferometer," *Appl. Opt.* **38**(16), (June 1999) 3523–3533.

Naulleau, P., K. Goldberg, E. Gullikson, and J. Bokor, "Interferometric at-wavelength flare characterization of extreme ultraviolet optical systems," *J. Vac. Sci. Technol. B* **17**(6), 2897–2991 (November–December 1999).

Naulleau, P., K. Goldberg, S. Lee, C. Bresloff, D.T. Attwood, and J. Bokor, "An EUV projection lithography system alignment and qualification tool," in OSA Technical Digest Series, 1999.

Naulleau, P., K. Goldberg, S. Lee, C. Chang, D.T. Attwood, and J. Bokor, "The EUV phase-shifting point diffraction interferometer: A sub-angstrom reference-wave accuracy wavefront metrology tool," *Appl. Opt.* **38**(35), 7252–7263 (December 1999).

Naulleau, P., K. Goldberg, S. Lee, C. Chang, P. Batson, D.T. Attwood, and J. Bokor, "Recent advances in EUV phase-shifting point diffraction interferometry," in *EUV, X-ray and Neutron Optics and Sources*, Proceedings of SPIE Conference (Denver, July 21–23, 1999).

Porter, M., "Soft x-ray speckle patterns from rough surfaces," Ph.D. thesis, University of Oregon, 1999.

Solak, H.H., G. Lorusso, S. Singh-Gasson, and F. Cerrina, "An x-ray spectromicroscopic study of electromigration in patterned Al–Cu lines," *Appl. Phys. Lett.* **74**(1), 22–24 (January 1999).

Yang, Y., S.R. Mishra, F. Cerrina, S.H. Xu, H. Cruguel, G.J. Lapeyre, and J.F. Schetzina, "Photoemission spectromicroscopy studies on epitaxial lateral overgrowth GaN surfaces," *J. Vac. Sci. Technol. B* **17**(4), 1884–1890 (Jul–Aug 1999).

Beam Test Facility

Chin, A.H., R.E. Schoenlein, T.E. Glover, P. Balling, W. Leemans, and C.V. Shank, "Ultrafast structural dynamics in InSb probed by time-resolved x-ray diffraction," *Phys. Rev. Lett.* **83**(2), 336–339 (July 1999).

Govil, R., W.P. Leemans, E. Yu. Backhaus, and J.S. Wurtele, "Observation of return current effects in a passive plasma lens," *Phys. Rev. Lett.* **83**(16), 3202–3205 (October 1999).

FOR MORE INFORMATION

Ernest Orlando Lawrence Berkeley National Laboratory
One Cyclotron Road
Berkeley, California 94720